Université du Québec
Institut National de la Recherche Scientifique
Centre Énergie Matériaux Télécommunications

Study on the structural and dielectric properties of epitaxial Barium Strontium Titanate (BST) for Tunable Microwave applications.

Par

Marwa Ahmed Mohamed Ismail

Thèse présentée pour l'obtention du grade de
Philosophiae doctor (Ph.D.)
en sciences de l'énergie et des matériaux

Jury d'évaluation

Président de jury et examinateur interne	Serioja Tatu Professeur, INRS-ÉMT
Examinateur externe	Richard Clergereaux Professeur, Université Paul Sabatier
Examinateur externe	Nadi Braidy Professeur, Université de Sherbrooke
Directeur de recherche	Mohamed Chaker Professeur, INRS-ÉMT

ABSTRACT

The future generation of active telecommunication devices may benefit a lot from components based on ferroelectrics. These tunable microwave devices require thin film ferroelectrics with specific material characteristics such as high dielectric constant that allows reducing the size of the devices, high tunability typically more than 50% for few kV.cm^{-1}, low dielectric loss lower than 0.01 in order to minimize signal attenuation, high Figure-of-Merit (FOM) at microwave range of frequencies (300 MHz to 300 GHz). In order to achieve these characteristics, high quality thin films, better understanding of the material properties and improvement of device designs are needed.

The challenge in the recent years is the difficulty to obtain thin films with low dielectric loss and high tunability at the same time. This step is crucial for integrating thin film in tunable microwave devices such as phase shifters, tunable resonators, filters, and tunable antenna. The most promising ferroelectric for this kind of applications is Barium Strontium Titanate, $Ba_{0.6}Sr_{0.4}TiO_3$ (BST) that can have a Curie temperature around room temperature and a dielectric constant that can be varied by more than an order of magnitude under an electric field, but that generally exhibit a relatively high level of losses at high frequency.

In this thesis high quality of BST thin films were deposited on MgO substrates by mean of pulsed laser deposition (PLD), in order to study the influence of the film microstructure on the microwave characteristics of the material. We investigated the influence of the deposition parameters such as laser fluence, laser repetition rate, substrate temperature, oxygen background pressure, substrate material type and orientation, and BST target composition on the BST thin films characteristics. Base on this first extensive study, we try to optimize the BST thin film properties by using buffer layers and doping with different elements (Mg, Ni, Mo, Fe, and Ti) in order to obtain low dielectric loss (tan δ) and high tunability at the same time.

These extended studies yielding to epitaxial, textured, and polycrystalline BST films revealed that there is a strong correlation between the microstructure properties and the microwave properties of BST thin films, that highlights the important influence of the crystal quality and lattice parameter on the microwave characteristics of the films, such correlation found between the lattice parameter and rocking curve FWHM, the rocking

curve FWHM and tunability, the lattice parameter and tunability, and dielectric loss and tunability. These observations helped to better understand the correlations between the dielectric characteristics and the material structural properties. The relation between the tunability and the material lattice parameter was found to obey to the Landau-Devonshire theory whereas the dielectric losses are found to be either intrinsically linked to the tunability or influenced by the presence of a large stress gradient at the substrate interface.

The optimum conditions for depositing epitaxial BST thin films on MgO (100) substrates were found to be at 10 Hz for laser repetition rate, 1 J/cm^2 for laser fluence, 65 mm for target substrate distance, 10 mTorr oxygen pressure, 800°C deposition temperature and post annealing conditions of 1050°C for 3 hours. In these conditions the rocking curve full-width at half-maximum obtained is of ~0.3, one of the best obtained so far for BST thin films. Interestingly, the BST Figure of Merit (FOM, ratio of tunability on the dielectric losses) of epitaxial and polycrystalline films are found to be comparable, due to high level of losses on highly epitaxial films. For example, the film deposited at 500°C is polycrystalline with a low tunability of 20%, low dielectric loss of 0.025, and a FOM of ~7.5; while the best crystal quality film ($\Delta\omega$ of 0.23°) has the highest tunability of 75% and also the highest dielectric loss of 0.1 but it has a FOM of ~7.

The BST-0.6 epitaxial thin film characteristics were further improved using specific design of experiments, intended to reduce the level of stress of epitaxial films. Using, for the first time, ion implantation of Mg on epitaxial thin films and post-implantation annealing, the BST Figure of Merit was improved from ~10 to 17 (tunability of 60% and dielectric loss of 0.035 at 3 GHz and 10 V.μm^{-1}). Our results proves that whereas tunability and losses seem to be intrinsically linked for BST alone, ion implantation gives the opportunity to decrease the level of losses while maintaining a relatively high tunability of the material. This work provides a better understanding of the performance of BST material at microwave frequency and will help to reach the targeted ferroelectric properties for its integration into functional tunable microwave devices.

ACKNOWLEDGEMENTS

Contents

Chapter 4.

Correlation between microstructure and microwave properties of BST thin films

List of Figure

CHAPTER 2

CHAPTER 3

CHAPTER 4

List of Tables

Glossary

Pulsed laser deposition   PLD

Barium Strontium Titanate   BST

Micro-electrical-mechanical systems   MEMS

Monolithic microwave integrated circuits   MMIC

Interdigital capacitor   IDC

Barium titanate   BTO

X-ray diffraction   XRD

Scanning electron microscopy   SEM

Rutherford backscattering spectroscopy   RBS

Physical vapor deposition   PVD

Chemical vapor deposition   CVD

Coplanar waveguide   CPW

Scattering parameters   S-parameters

Conformal mapping method   CMM

Partial-capacitance technique   PCT

LIST OF TERMS

ε	Dielectric constant
Φ	Tunability
FOM	Figure-of-merit
tan δ	Dielectric loss
a	Lattice parameter
$\Delta\omega$	FWHM of the rocking curve
T_c	Curie temperature
E	Electric field
P	Dielectric polarization
ε_0	Permittivity of free space
χ_e	Electric susceptibility
u_m	Misfit strain
a_1	Dielectric stiffness
Q_{ij}	Electrostrictive coefficients
S_{ij}	Elastic compliances
σ_i	Stress coefficients
γ_{i3}	Stress-related flexoelectric coupling coefficients
η_{i3}	Converse flexoelectric coefficients
μ	Flexoelectric coefficient
T_c^*	Strained-modified Curie temperature
T_{ferro}	Temperature for the ferroelectric transition
T_m	Temperature of the maximum dielectric constant
h	Plank's constant
v	Oscillation frequency
α	Thermal expansion coefficient
F	Laser fluence
D	Diffusion coefficient
C	Capacitance

INTRODUCTION

Telecommunication domain

Telecommunication is one of the great revolutions of modern times. Nowadays telecommunication includes a large variety of wired and wireless technologies such as radio and microwave devices as well as cable and fiber optics. This growing network of satellites, phones and computers allow the exchange of voice, image, data and video at an increasing speed. The telecommunications domain is still expanding and the industry's revenue represent a huge share of the global economy with service revenue, for the global telecommunications industry, estimated to be 5 trillion US$ in 2013. [1]

Digital mobile communication is a great achievement of recent years because it gave people an extraordinary level of mobility with the rest of the world at its fingertip. The mobile revolution has started and the next generation of mobile and wireless communications technology is emerging. The new 3G and 4G services offer the opportunity for true broadband mobile services. The requirement for future mobile and wireless networks will include new technologies able to integrate device electronics and new material technologies at the same time. This implies new research challenges in order to optimize material properties and improvement of device design for the circuits integrating these materials.

Fig. I.1 shows the position of microwave spectrum and the repartition of the different microwave bands (from 0.3 to 300 GHz) with the corresponding applications. This frequency range regroups most of wireless communication systems such as satellite communication or cellular phones which use microwave signals as a carrier. These electromagnetic waves correspond to electric length of few centimeters to few millimeters which allow compact device sizes and signal processing at high data speed. The signal processing in these devices is done through different element such as oscillators, amplifiers and tuners that uses dielectric resonators. With the recent evolution of transmitters and receivers towards more efficient bandwidth usage, the development of new dielectric material has become a large domain of research. [2]

As illustrated on Fig. I.2, the number of papers published on dielectric resonator materials and technology and the number of patents filed during the last 40 years as constantly increased. More than 5000 papers have been published from 1969 to 2005 and more than 1000 patents were filed from 1975 to 2005 on the subject.
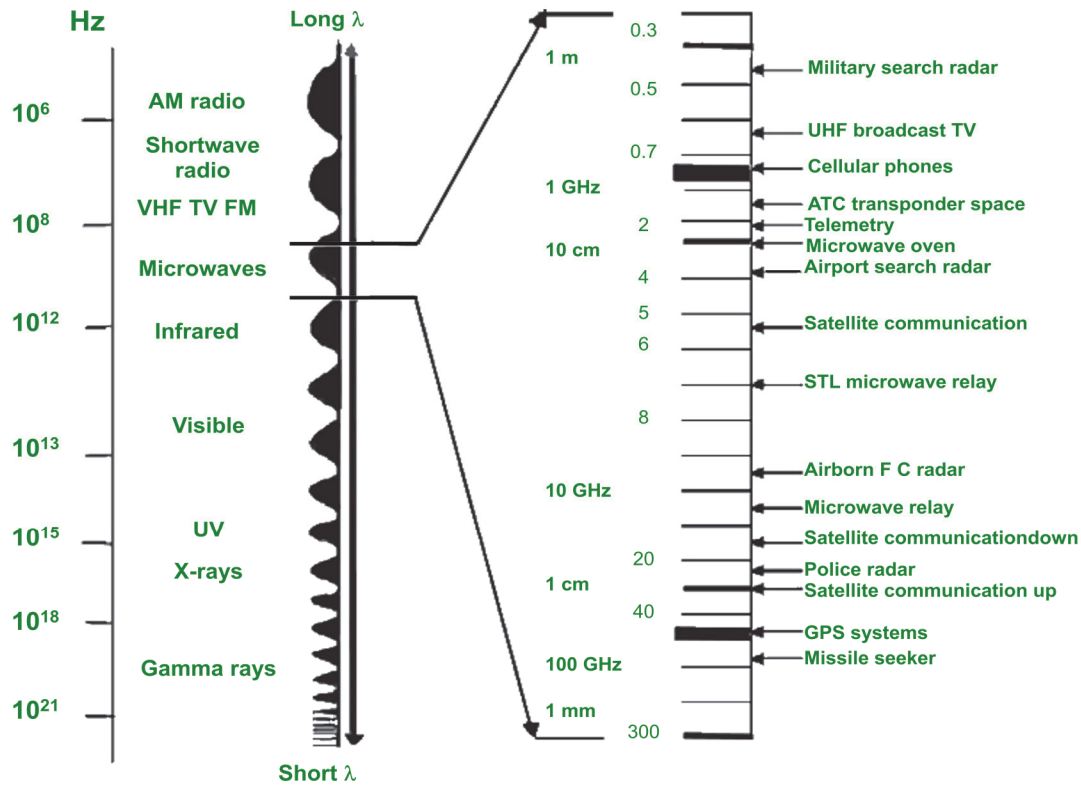
Figure.I.1: Microwave spectrum and application.[2]
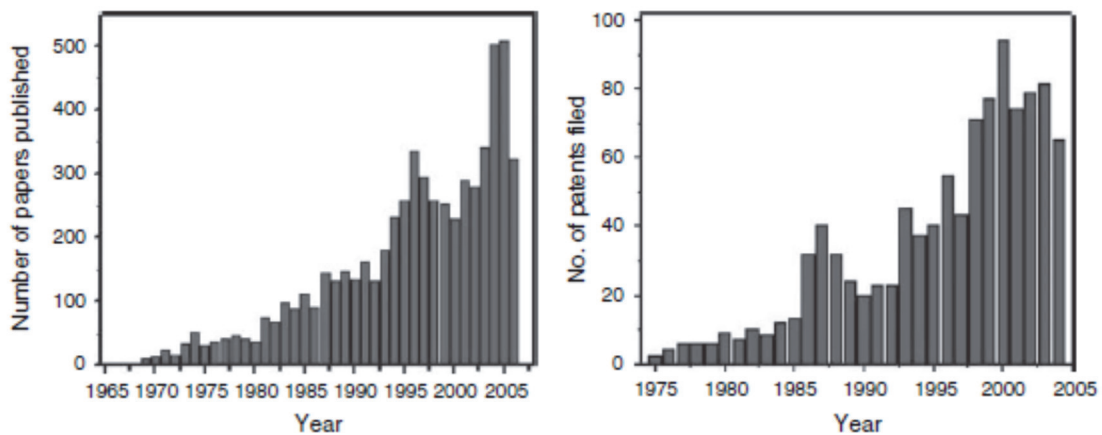
Figure I.2: The number of papers published versus year of publishing, and the number of patents versus the year. [2]

A large portion of today's research lies in the development of functional microwave materials in order to develop a new class of active devices for telecommunications. This research is mainly devoted to the synthesis and characterization of smart materials such as ferroelectrics which offer tunable dielectric constant under the application of an external field. These developments first require a clear understanding of the relation between structural and electrical characteristics of these materials, in particular deposited in thin film [3,4].

Ferroelectrics for telecommunications

In the quest for high-performances frequency agile (tunable) devices, ferroelectrics have many advantages such as: [5]

1- Enabling the miniaturization of microwave components (dimensions are in mm), due to their high dielectric constant;

2- Enabling the integration in the thin film form with semiconductor microelectronic circuits;

3- Enabling functionalization of microwave components by the use of an external electric field which offers continuous and reversible variation of the material dielectric properties;

4- They also present high power handling and fast switching time.

Due to these unique properties, ferroelectric materials found applications in different field over the years (and particularly since the late 80s, as described in Table I.1).

For the case of tunable microwave applications, other technologies are explored, including ferrite, micro-electrical-mechanical systems (MEMS), and semiconductors. All these technologies present disadvantages that restrict their integration, especially for high frequency applications. Ferrites require the application of a magnetic field which is a technological challenge that increases the fabrication costs and the component size. They also offer slow tuning speeds and hysteresis on the material response. MEMS varactors have very low dielectric losses, however their response time is relatively slow compared to ferroelectrics or semiconductors and requires high operating voltage; they are also sensitive to environmental conditions such as air moisture, temperature and vibrations. Semiconductor technology such as GaAs varactors is presently dominant but present losses that are linearly increasing with frequency, thus limiting their applications

in tunable filters above 20 GHz. Even if semiconductor diodes have good tunability, fast tuning speed, small size and compatible with monolithic microwave integrated circuits (MMIC), they also present a large cost and low power handling capabilities.

Table I.1: Development and applications of ferroelectric materials over the years. [6, 7]

1912	Ferroelectricity first described as a property of solids.
1944	Ferroelectricity discovered in ABO_3-type perovskite $BaTiO_3$.
1960s and 1970s	FE semiconductor (PTC) devices developed. FE thin films processing techniques started to emerged.
mid-1980s	Advancements in processing of complex ferroelectric oxides and discovery of the high temperature superconductive oxides.
late 80s	- Ferroelectric memory integrated with silicon complementary metal-oxide semiconductor (CMOS). - Integration of microsensors with microelectronics, emergence of the micro electro mechanical systems (MEMSs) area.
late 1990s	- Introduction of polar thin films in portable telephone technologies. Mobile phones become a mass product. - Development of BST ferroelectric material.
2010	A new family of ferroelectric materials: $Me_2Nb_4O_{11}$ (Me = Na and Ag) are developed.
2012	The first columnar ferroelectric liquid crystal is synthesized.
Nowadays	Ferroelectric films are being used in a number of commercial, widespread products; these applications include memories, microwave electronic components, and micro-devices with pyroelectric and piezoelectric micro-sensors/actuators.

In practice the choice of a particular technology will depend on the type of application, economic factors and material properties. Table I.2 shows a comparison between ferroelectric (BST thin film) and other competing technologies, namely semiconductor (GaAs) and MEMS.

Up to now, ferroelectric technology seems to present the most attractive characteristics with high tuning range at low voltages, high power handling, fast tuning speed and operation in a very large frequency range. The only drawback of these materials is their relatively high dielectric losses in the thin film form. For example, Barium Strontium Titanate thin films (BST) [5,8] , which is the most promising ferroelectric material for microwave applications exhibit dielectric loss of about 0.04-0.05 in the GHz range whereas most of applications will require losses lower than 0.01 to be integrated in functional microwave devices. [9,10,11]

Table I.2: **Comparison of the properties of semiconductor GaAs, MEMs, and ferroelectric BST thin film varactors.** [5]

	Semiconductor	MEMS	BST
Tunability	$\sim$ 2-6: 1[a]	$\sim$ 1.5-3: 1[b]	$\sim$ 2-4: 1
RF Loss (Q = 1 / loss tangent)	$\sim$ 20-50 at 10GHz	Very high	$\sim$ 20-100 at 10GHz
Control voltage	<15 V[a]	<50 V[b]	<15 V (parallel plate type)
Tuning speed	$\sim$ 10^{-6} S	$\sim$ 10^{-5} S	$\sim$ 10^{-9} S[c]
Reliability	Good[a]	Poor	Good
Cost	High	High	Low
Power handling	Poor	Good	Good[c]

a taken from http://www.mbelectronique.fr/
b taken from Peroulis *et al MTT-S Int. Microwave Symp. Digest* Vol 2, p. 1117 (2003).
c taken from Kozyrev *et al Integr. Ferroelectr. Vol.* 22, 329 (1998).

Statement of purpose

The current challenge for integrating ferroelectric thin film material such as Barium Strontium Titanate (BST) into microwave devices is to obtain low dielectric loss (tan δ) BST thin film and a large electric-field induced tuning at the same time. In this context, the main objective of this thesis is to study the influence of the film microstructure on the microwave characteristics of the BST material in order to better understand the mechanism behind dielectric losses and tunability and try to improve them.

In order to achieve this goal, we need first to understand the microstructure of the BST thin film and find out how the crystal quality (epitaxial, textured, or polycrystalline) influences the Figure of Merit (FOM, the ratio between the tunability and dielectric loss). We need to obtain different thin film characteristics using specific design of experiments and study the general correlation between microstructural and microwave properties of BST with 60% of barium (BST-0.6) thin film. This work will help to understand the mechanisms of dielectric loss and tunability and try to find ways to improve them for microwave devices applications.

This project is facing two major difficulties:
- First, achieving growth of epitaxial BST thin films. This requires careful optimization of the pulsed laser deposition (PLD) parameters in order to find the set of conditions for epitaxial growth.
- Second, fabricating interdigital capacitor (IDC) with small dimension (3 μm gap) and large thickness (2 μm thick) by photolithography, metallization and lift-off processes in order to characterize the dielectric properties of the fabricated BST thin films. This step requires an optimization of the microfabrication process in order to obtain high quality electrodes with a large aspect ratio.

Presentation of the thesis

This thesis starts with a general presentation of the telecommunication domain and briefly describes the new materials for telecommunications, and more specifically the ferroelectrics.

Chapter 1 presents the general properties of Barium Strontium Titanate, a ferroelectric material, in the context of microwave applications. The electrical properties of ferroelectrics, the mechanism of polarization and paraelectric/ferroelectric phases are presented in details. This chapter also compares the microwave properties of bulk and thin films (dielectric constant, tunability), and presents a review on Landau–Devonshire phenomenological model which provides a quantitative prediction for the dielectric properties of ferroelectrics. It also presents a phenomenological model for flexoelectricity, a theory developed to explain the dielectric constant behavior of inhomogeneously strained ferroelectric thin films. An introduction on the dielectric loss properties of BST (intrinsic and extrinsic contributions) can be found in the last part of the chapter.

The second chapter, entitled "epitaxial growth of BST thin films", introduces the deposition of BST thin films. This chapter presents different growth modes (epitaxial and polycrystalline), the influence of the substrate, and different deposition techniques used for the epitaxial growth of BST on MgO single-crystal substrate in the literature. This section is followed by a description of the Pulsed Laser Deposition method (PLD), used to synthesize BST-0.6 thin films in this study, this includes the experimental setup and the influence of the different deposition technique parameters. The second part of this chapter concerns the material characterization methods, where the different diagnostics used to characterize the microstructural properties of the BST films are exposed. These diagnostics include scanning electron microscopy (SEM), atomic force microscopy (AFM), Rutherford backscattering spectroscopy (RBS) and X-ray diffraction (XRD) techniques. The last part of the second chapter presents experimental results on the microstructural properties of films deposited under different PLD conditions, namely the laser fluence, laser repetition rate, BST target composition, substrate temperature, oxygen background pressure, substrate material type and orientation.

The following chapter (Chapter 3, entitled "Microwave characterization of BST thin films") is divided into three parts. The first part presents the domain of microwave with introductions to waveguides, scattering parameters, and thin film microwave parameters. The second part describes the microwave characterization device and method used in the present study to extract the dielectric constant, dielectric loss, tunability, and Figure

of Merit of BST thin film. This section includes devices fabrication (photolithography process optimization, microfabrication process), microwave diagnostic calibration, and interdigital capacitor (IDC) diagnostic description. In the last part of the chapter, the measured microwave properties of the films will be presented at the end of the chapter 2 and discussed. These results present the influence of different PLD deposition parameters (laser fluence, laser repetition rate, BST target composition, substrate temperature, oxygen background pressure, substrate material type and orientation) on the microwave properties of BST thin film.

The chapter 4 ("Correlation between microstructure and microwave properties of BST thin films") presents general correlations between microstructural properties and the microwave properties of BST-0.6 thin film presented at the end of chapter 2 and 3. Different correlations (between the lattice parameter and rocking curve FWHM, the rocking curve FWHM and tunability, the lattice parameter and tunability and between dielectric loss and tunability) are presented and discussed in order to better understand the important material parameters for the tunability and a better understanding of the origin of the dielectric loss in BST-0.6 thin film. These observations are then used as a guide to optimize the BST-0.6 thin film for microwave applications, the goal being to obtain BST lattice parameter as close as possible to the bulk value while minimizing the film stress. This optimization, presented in the second part of the chapter, consists in the deposition of a buffer layer (thickness of a Barium Titanate (BTO) buffer layer, influence of the buffer layer material) and doping (through co-deposition of BST and a doping material by PLD and by ion implantation) and the related structural and microwave properties of epitaxial BST thin film. This chapter ends with a general synthesis on BST thin film properties (structural and electrical characteristics) regrouping all the different BST thin films synthesized during this study.

The thesis ends with the presentation of the conclusions and perspective of the presented work.

CHAPTER 1: Barium Strontium Titanate, a ferroelectric material for microwave applications

Barium Strontium Titanate is part of the ferroelectrics, a class of high dielectric permittivity materials characterized by a transition from a polar (ferroelectric) phase to a nonpolar (paraelectric) phase at a temperature at which their dielectric permittivity presents a maximum (called the Curie temperature). The term ferroelectricity was chosen by analogy with ferromagneticity: while ferromagnetic effect occurs in presence of a magnetic field, the ferroelectric phenomenon happens in the presence of an electric field. Below the Curie temperature (T_c) ferroelectrics exhibit a spontaneous electric polarization and a hysteresis loop of the dielectric constant as a function of the electric field E; above T_c they present a continuous change of the dielectric constant as a function of E. These unique properties make ferroelectrics very attractive for the conception of microwave devices and especially active devices in which the microwave signal could be controlled by an external voltage.

1.1. General properties of ferroelectrics

1.1.1. Pyroelectricity, Piezoelectricity, Ferroelectricity

Pyroelectrics are a class of materials in which heat can generate electricity or electricity can generate heat. Pyroelectricity is a phenomenon known for a very long time: the philosopher Theophrast described it in 314 bc in relation to a stone (supposedly tourmaline) that was able to attract bits of wood when heated. It took more than 20 centuries to relate this phenomenon to electricity and few more centuries to develop a theory explaining the observed effect. It is now well known that pyroelectricity is closely related to the crystallographic structure of the material. Many physicists studied this kind of materials and discovered other related properties. In 1880 Pierre and Jacques Curie discovered piezoelectrics, a class of materials in which mechanical stress can generate electricity or electric filed can generate mechanical stress. In 1921, Valasek discovered the ferroelectric phenomena in the Rochelle salt (potassium-sodium tartrate tetrahydrate, $KNaC_4H_4O_6$–4 H_2O), a colorless crystalline compound with an orthorhombic structure discovered by Rochelle in the 17th century. Few years later, in 1935, a second

ferroelectric compound was identified: Potassium-Dihydrogen Phosphate (KDP). And another decade later barium titanate ($BaTiO_3$) was added to the list of ferroelectric materials that is still growing nowadays.

Pyroelectric, piezoelectric or ferroelectric materials are characterized by a net electric polarization. In general, all materials undergo a small change in dimension when exposed to an external force, such as an electric field, a mechanical stress, or a change in temperature. Depending on the material structure, such a small change in dimension may result in a change in electric polarization and hence give rise to the occurrence of the ferroelectric, piezoelectric, or pyroelectric effects. Materials exhibiting these effects are polar and crystalline, or polycrystalline. The specific symmetry of the unit cell determines whether the crystal exhibits ferroelectric, piezoelectric, pyroelectric, or electro-optic effects.

```
                    ┌──────────────────┐
                    │   32 symmetry    │
                    │   Point groups   │
                    └──────────────────┘
                       ↙            ↘
        ┌──────────────────┐   ┌──────────────────┐
        │       21         │   │ 11 centosymmetric│
        │ Noncentrosymmetric│   └──────────────────┘
        └──────────────────┘
                 ↓
        ┌──────────────────┐
        │  20 piezoelectric │
        │ Polarized under stress│
        └──────────────────┘
                 ↓
        ┌──────────────────┐
        │  10 pyroelectric  │
        │ Spontanously polarized│
        └──────────────────┘
                 ↓
        ┌──────────────────┐
        │Subgroup Ferroelectric│
        │ Reversible Polarization│
        └──────────────────┘
                 ↓
        ┌──────────────────┐
        │    Peroviskite   │
        │       ABO₃        │
        └──────────────────┘
                 ↓
        ┌──────────────────┐
        │  Ba₀.₆ Sr₀.₄ Ti O₃ │
        └──────────────────┘
```
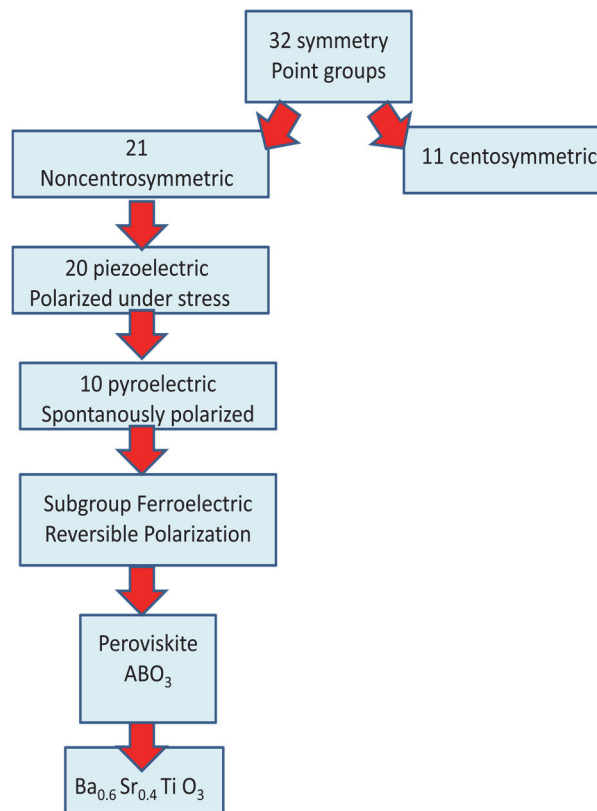
Figure 1.1: Classification of crystals showing the classes with piezoelectric, pyroelectric, and ferroelectric effects.

The existence of pyroelectricity in a material requires that its molecular structure have a nonzero dipole moment, no center of symmetry and must have either no axis of

rotational symmetry or a single axis of rotational symmetry that is not included in an inversion axis. On the basis of the symmetry elements, there are 32 point groups or classes. The 32 point groups are subdivisions of seven basic crystal systems, these seven basic crystal systems are triclinic, monoclinic, orthorhombic, tetragonal, trigonal (rhombohedral), hexagonal, and cubic.[12] Of these 32 classes, 11 classes are centrosymmetric and 21 classes are noncentrosymmetric possessing no center of symmetry. Only 20 classes of noncentrosymmetric crystals exhibit piezoelectric effects. Only 10 of these 20 classes possess spontaneous polarization, being permanently polar and thus exhibiting piezoelectric as well as pyroelectric effects. There is a subgroup within these 10 classes that possesses spontaneous polarization and reversible polarization and that can have ferroelectric, piezoelectric, and pyroelectric effects.

As shown on Fig. 1.1, Barium Strontium Titanate (or BST of formula $Ba_xSr_{1-x}TiO_3$) has a perovskite structure and is one of the few ferroelectric materials that exhibit spontaneous polarization with applied electrical field due to the atomic displacement of the body-centered atom (Ti) in the perovskite (ABO_3) structure.

Figure 1.2: Perovskites ABO_3 with the atomic orbitals that contribute to covalent bonding (oxygen atoms in the unit cell are labeled O_1, O_2, O_3, the remaining oxygen atoms are related to those by the repeat vectors of the crystal, indicated as a_1, a_2, a_3). The p_x, p_y, p_z orbitals of the three O atoms and the dx^2-y^2, $d_3z^2-r^2$ orbitals of the B atoms that participate in the formation of covalent bonds in the octahedron are shown schematically.[8]

The chemical formula of perovskites is ABO_3, where A is the easily ionized element (in the case of BST, Ba or Sr atoms occupy the site A) and B is the element located at the center which is bonded to oxygen atoms (in case of BST, Ti atom occupies the site B). The basic unit cell is shown in Fig. 1.2 with the corresponding atomic orbitals. Bonding in the xy plane is accomplished through the overlap between the p_x and p_y orbitals of the first (O_1) and second (O_2) oxygen atoms, respectively, and the $d_{x^2-y^2}$ orbital of B; bonding along the z axis is accomplished through the overlap between the p_z orbital of the third (O_3) oxygen atom and the $d_{3z^2-r^2}$ orbital of B. The A atoms provide the necessary number of electrons to satisfy all the covalent bonds. Thus, the overall bonding involves both strong covalent bonds between B and O, as well as ionic bonds between the B–O units and the A atoms [8].

1.1.2. Mechanisms of polarization

In a dielectric subject to an electric field **E,** the dielectric polarization density **P** is defined as:

$$P = \varepsilon_0 \chi_e E \quad \text{...Eq. 1.1}$$

where $\boldsymbol{\varepsilon_0}$ is the electric permittivity of free space ($\varepsilon_0 = 8.85 \times 10^{-12} \ F/m$) and $\boldsymbol{\chi_e}$ is the electric susceptibility.

The electric susceptibility $\boldsymbol{\chi_e}$ of a medium is hence a measure of how easily it polarizes in response to an electric field. It is related to the relative permittivity of the material $\boldsymbol{\varepsilon_r}$ by

$$\chi_e = \varepsilon_r - 1 \quad \text{.. Eq. 1.2}$$

The electric displacement **D** is related to the polarization density **P** by

$$D = \varepsilon_0 E + P = \varepsilon_0(1 + \chi_e)E = \varepsilon_r \varepsilon_0 E \quad \text{..................... Eq. 1.3}$$

The polarization **P** of a dielectric material with the density $\boldsymbol{N_j}$ is the sum of all the individual dipole moments $\boldsymbol{p_j}$:

$$P = \sum_j N_j p_j \quad \text{.. Eq. 1.4}$$

The dipole moment induced by an electric field **E** can be expressed as:

$$p = \alpha E \quad \text{... Eq. 1.5}$$

where α is the polarizability of an atomic dipole.

The relation between the susceptibility (χ) and the polarizability (α) is given by:

$\varepsilon_0\chi = N_j\alpha_j$. …………….......................................…… Eq. 1.6

In general, there are five different mechanisms of polarization which can contribute to the dielectric response:

- **Electronic polarization**

This mechanism is common in all dielectric materials. By applying an electric field, the center of the negative charge within the atomic structure is shifted relatively to the position of the positive nucleus and creates a dipole. The electronic polarizability α_e is temperature-independent. And large atoms have a large electronic polarizability.

- **Ionic polarization**

This mechanism is observed in ionic crystals. By applying an electric field, the cations and anions will be displaced in opposite direction and will cause a net dipole moment.

- **Orientation polarization**

This mechanism only exists in materials that contain permanent dipoles moments. As an electric field is applied the dipole moments rotate to align themselves with the field. This type of polarization (due to alignment of permanent dipoles) is sensitive to thermal vibrations and will decrease as the material is heated.

- **Space charge polarization**

This mechanism could exist in dielectric materials which show spatial inhomogeneities of charge carrier densities. It occurs when mobile charges within the material are impeded by interface such as grain boundaries and are not discharged at an electrode.

- **Domain wall polarization**

The domain walls separate regions of different oriented polarization. The motion of a domain wall takes place when a strong electric field is applied to the material that favor domains orientation along the electric field lines.

In a dielectric, the total polarization comes from the different mechanism contributions and is dependent on the frequency. Fig. 1.3 shows the typical polarizability of materials as a function of frequency.[13] Electronic and ionic polarization are called intrinsic contributions, they show contributions up to very high frequencies and exhibit resonance effects. The other mechanisms (orientation, domain walls, and space charge polarizations) are called extrinsic contributions and have a relaxation behavior. They tend to vanish as the frequency increases: above few tens of GHz, only the intrinsic contributions are present.
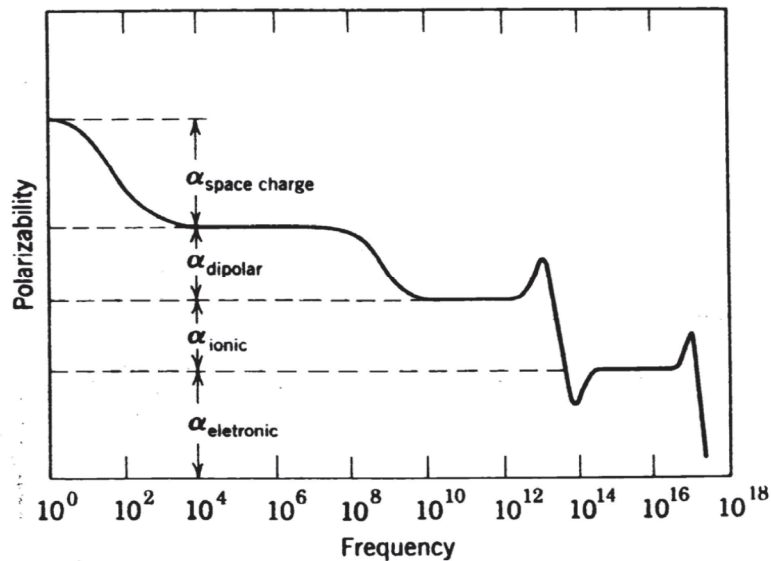
Figure 1.3: **Polarizability as a function of frequency for a typical dielectric material.**
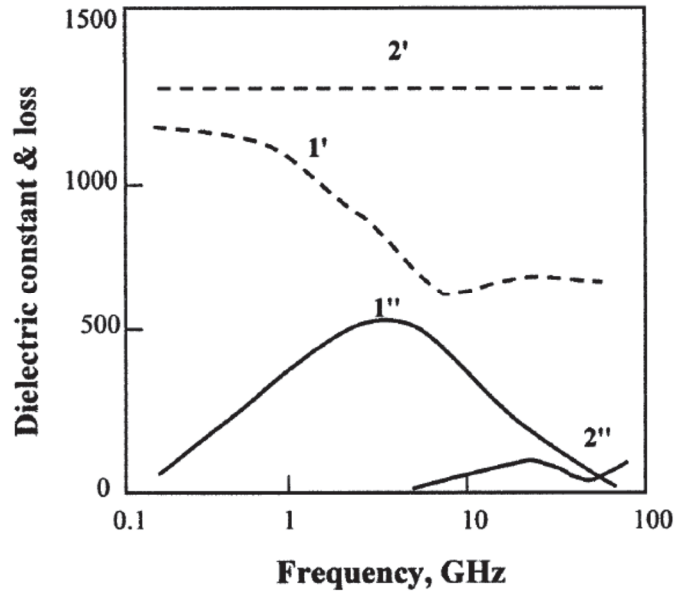
Figure 1.4: Real (dash line) and imaginary (plain line) part of the dielectric constant of BaTiO$_3$ bulk ferroelectric ceramics (identified as 1) and Ba$_{0.25}$Sr$_{0.75}$TiO$_3$ (BST) bulk paraelectric ceramics (identified as 2) as a function of frequency [from ref. **14**]).

The dispersion of the dielectric response of each contribution leads to dielectric losses of the matter which can be mathematically expressed by a complex dielectric permittivity:

$$\varepsilon = \varepsilon' + i\varepsilon'' \dots\dots\dots\dots\dots\dots\dots\dots\dots\dots\dots\dots\dots\dots\dots\dots \text{Eq. 1.7}$$

Dielectric losses are usually described by the loss tangent:

$$tan\delta = \frac{\varepsilon''}{\varepsilon'} \dots\dots\dots\dots\dots\dots\dots\dots\dots\dots\dots\dots\dots\dots\dots\dots \text{Eq. 1.8}$$

Fig. 1.4 shows the real (ε') and imaginary (ε'') parts of the BaTiO$_3$ and Ba$_{0.25}$Sr$_{0.75}$TiO$_3$ bulk ceramics, measured as a function of the frequency (from 200 MHz to 60 GHz). It is evident from this figure that large variations of the dielectric properties are observed as a function of frequency with the presence of maxima with positions depending on the material composition.

1.1.3. Electrical properties of ferroelectrics
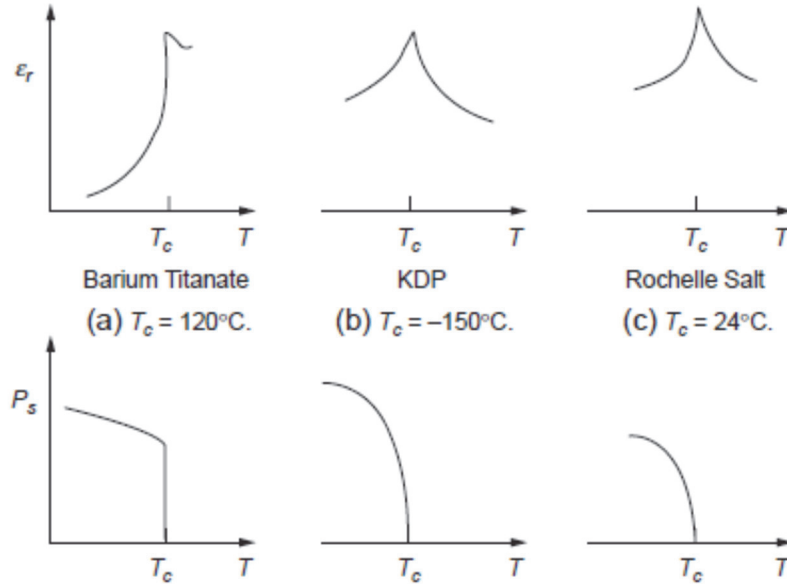
Figure 1.5: **Schematic illustration of the variation of the dielectric constant** εr **and the spontaneous polarization of spontaneous polarization (Ps) as a function of temperature for three typical ferroelectric crystals: (a) Barium titanate (BaTiO$_3$) with** Tc **= 120°C, (b) Potassium dihydrogen phosphate (KDP, KH$_2$PO$_4$) with** Tc **= -150°C, and (c) Potassium Sodium tartrate-tetrahydrate (Rochelle Salt, KNaC$_4$H$_4$O$_6$-4H$_2$O) with** Tc **= 24°C.** [15]

Ferroelectrics are pyroelectrics with a reversible spontaneous polarization. The direction of their polarization can be reversed by a sufficiently large electric field. They are characterized by their Curie temperature T_C, which marks the transition between a polar state (below T_C, where they can exhibit pyroelectricity) and a nonpolar state (also called paraelectric state, above T_c).[15]

The typical dielectric constant–temperature and polarization–temperature characteristics curves of three different ferroelectrics (BTO, KDP, and Rochelle salt) are shown in Fig. 1.5. This figure shows that the dielectric constant of these ferroelectric increases very rapidly to reach a maximum value at T_c and that this transition temperature can be very different from one material to the other.

In the ferroelectric state (T < T_c), the material spontaneous polarization P_s usually increases rapidly just below the transition point and then gradually reaches a saturation

value at lower temperatures. When an electric field is applied on a ferroelectric in the ferroelectric state, the polarization P presents nonlinearities and a hysteresis as a function of the applied electric field E as shown on Fig. 1.6:

- Starting from the unpoled state and applying a small electric field, all the spontaneous dipoles will align in the direction of the field and the polarization increases linearly with the field (from origin to point A).

- By further increasing the electric field all domains start to orient toward the direction of the field (from point A to point B) and the polarization increases nonlinearly.

- Above a certain field (and below the breakdown field), the polarization will reach a saturation state (from point B to point C), where almost all domains are aligned toward the direction of the poling field.

This process, inducing alignment of domain walls in the ferroelectric state is often called material poling.

- When the material is poled and if the electric field is gradually decreased to zero, the polarization will not go to zero but follow the path CBD, down to the remnant polarization value P_r (point D on the figure). The spontaneous polarization value P_s is defined as the intersection of line CB and the polarization axis.
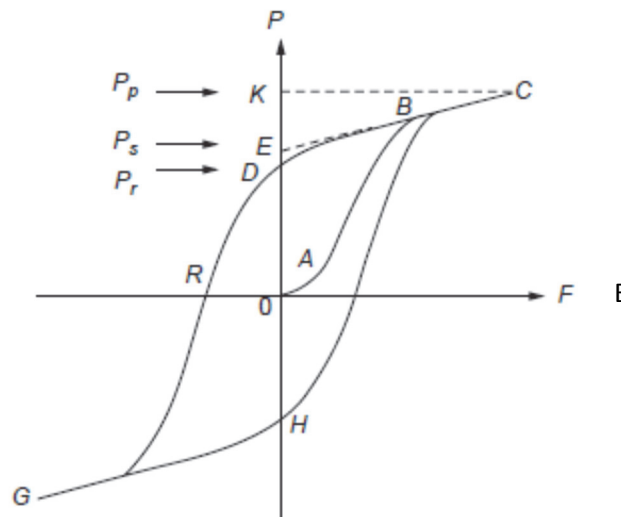
Figure 1.6: Typical ferroelectric hysteresis loop.[15]

Going from positive electric fields to negative ones, the P-E plot will follow a hysteresis loop characterized by the remnant polarization P_r and the coercive field E_c values. E_c corresponds to the field required to bring the polarization back to zero (distance 0R on the electric field axis). When the field is increased from negative values to zero, the

remanant polarization is reversed (point H), indicating a change in the direction of the material polarization. The hysteresis arises from the energy needed to reverse the metastable dipoles during each cycle of the applied field.

In the paraelectric state (T > T_c), the material has no spontaneous polarization and its dielectric constant follows the Curie–Weiss relation $\varepsilon_r = C / (T-T_C)$, where *C* is known as the Curie constant.[16] When an electric field is applied, the polarization presents a continuous increase (the dielectric constant decreases), followed by a saturation below material breakdown and goes back to zero when the applied field is removed.

1.1.4. Paraelectric and Ferroelectric phases

The basic electric field tuning mechanism of the permittivity can be represented by a simple mechanical spring model [17], as depicted in Fig1.7:

- In the paraelectric phase (Fig.a,b)
  I. The central ion oscillates about the equilibrium position and the free energy is characterized by a parabolic dependence.
  II. An external electric field will shift the central ion from its equilibrium position to a new position and induce an electrical dipole.
  III. When the external field is switched off the ion will go back to the equilibrium position.

- In ferroelectric phase (Fig.c,d,e)
  I. The central ion will shift left or right and the free energy is minimum at these positions.
  II. The ion will remains in the new position (left or right) as long as no external forces are applied.
  III. Under external DC field the central ion shift from left to right changing the direction of the polarization.
  IV. Changing the direction of the external field will brings the ion back to its left position.
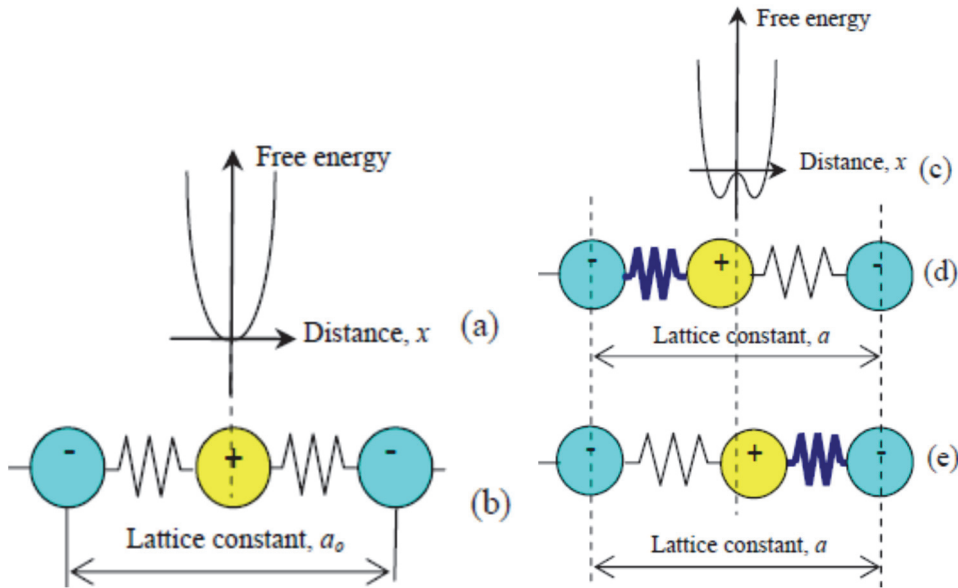
Figure1.7: Free energy of perovskites ABO$_3$ in paraelectric (a, b) and in ferroelectric (c, d, e) phases.[17]

1.2. Dielectric constant properties of BST

The two inverse permanent polarization states of ferroelectrics are very useful for applications such as non-volatile memory devices (the two states being used as the 0 and 1 binary states). But in the case of microwave devices, it is preferable to obtain a continuous change of the material properties as a function of the electric field, which occurs in the paraelectric state only. Moreover, dielectric losses are much higher in the ferroelectric state than in the paraelectric state.

The other key parameter for room temperature microwave applications is the tunability, defined as the ratio of the dielectric permittivity at zero electric field to the permittivity at a given electric field E$_0$. The tunability Φ is commonly described by:

$$\Phi(E_0) = \frac{\varepsilon_r(0) - \varepsilon_r(E_0)}{\varepsilon_r(0)} \dots\dots\dots\dots\text{Eq 1.9}$$

Among all the ferroelectric materials, Barium Struntium Titanate or BST-x of formula Ba$_x$Sr$_{1-x}$TiO$_3$ is considered as the most promising material for electrically tunable microwave devices applications. BST is a solid solution of SrTiO$_3$ (STO) and BaTiO$_3$ (BTO), two ferroelectric materials with a Curie temperature of -168°C and 120°C

respectively. The adjustment of the fraction x of $BaTiO_3$ into the solid solution is a way to precisely define the T_c of BST. As the Ba atom substitute the Sr atoms in the STO unit cell, the lattice parameter and Curie temperature linearly increase. In order to obtain a large tunability at room temperature, one needs to be just above ferroelectric-paraelectric phase transition. This corresponds to x fraction between 0.5 and 0.6. For instance the T_C of $Ba_{0.6}Sr_{0.4}TiO_3$ (BST-0.6) is about 5°C.[18]

1.2.1. Dielectric constant and tunability of bulk BST

Fig 1.8 shows the permittivity of bulk $Ba_{0.6}Sr_{0.4}TiO_3$ material as a function of the electric field at room temperature. The dielectric constant ε_r of the ferroelectric material has strong dependence on the applied electric field E_0, it varies from about 10000 to 1000 (a ratio of 1:10 corresponding to a tunability of 90%) for an electric field of 25 kV/cm (=2.5 V/μm).
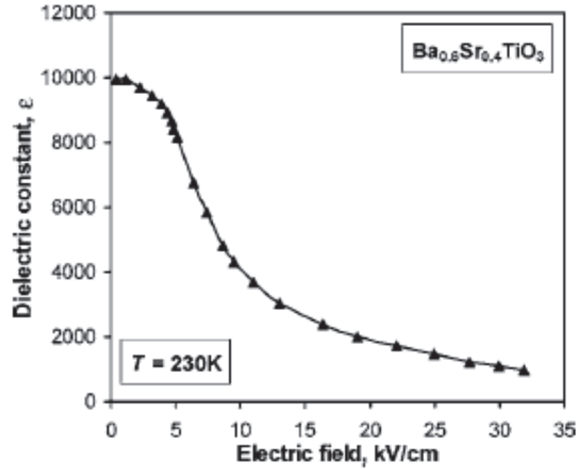
Figure 1.8: Typical field dependence of the dielectric permittivity of $Ba_{0.6}Sr_{0.4}TiO_3$ on the electric field.[19]

1.2.2. Landau theory [19]

The Landau theory gives a model for the dielectric response of a bulk ferroelectrics, it is based upon an expansion of the Helmholtz free energy **F** with respect to the vector polarization **P**. For the situation where the polarization is in the direction of the electric field **E** applied to the material, the first two terms of this expansion are:

$F = \frac{\alpha}{2} P^2 + \frac{\beta}{4} P^4$ ....Eq. 1.10a

And from the equation of state

$\frac{\partial F}{\partial P} = E$ ....Eq. 1.10b

it is possible to obtain a relation between the polarization and the electric field:

$E = \alpha P + \beta P^3$ Eq.1.11

From Eq. 1.1 and 1.2, the material susceptibility is given by:

$P = \varepsilon_0 \chi_e E$ such that $\chi_e = \frac{1}{\varepsilon_0} \frac{\partial P}{\partial E}$.....................Eq.1.12

Hence, the relative dielectric permittivity of the material can be expressed as:

$\chi_e = \frac{1}{\varepsilon_0} \frac{\partial P}{\partial E} = \frac{1}{\varepsilon_0} \frac{1}{\alpha+3\beta P^2} = \chi_e(0) \frac{1}{1+3\beta \chi_e(0)\varepsilon_0 P^2}$.................Eq.1.13

Where $\chi_e(0)$ (at E=0) is the susceptibility given by

$\chi_e(0) = (\varepsilon_0 \alpha)^{-1}$.................Eq.1.14

According to the Landau theory, the coefficient α of a ferroelectric is assumed to be a linear function of temperature and vanishes at the Curie-Weiss temperature T_c, it has the expression:

$\alpha = \frac{1}{\varepsilon_0} \frac{|T-T_c|}{C}$ ....Eq. 1.15

where T_c and *C* are the Curie temperature and the Curie-Weiss constant respectively.

For ferroelectrics the Curie-Weiss constant *C* is about 10^5 K. Such a value implies high values of the dielectric permittivity even far from the T_c. For example, at $T = T_c$ +200 K, from Eqs. 1.13 and 1.14 one can obtain $\chi_e(0)$=500. This implies that the susceptibility of ferroelectrics ($\chi_e = \varepsilon_r - 1$) can be approximated by ε_r.

From the value of $\chi_e(E = 0)$ (or $\varepsilon_r(E = 0)$), the Eq.1.13 gives the expression of χ_e as a function of P. This equation can also be expressed as a function of E (since $P = \varepsilon_0 \chi_e E$, Eq. 1.1), which leads to a polynomial expression of the 3d order for $\chi_e(E)$:

$3\beta\varepsilon_0^3 E^2 . \chi_e^3 + \varepsilon_0 \alpha . \chi_e - 1 = 0$.................Eq.1.16
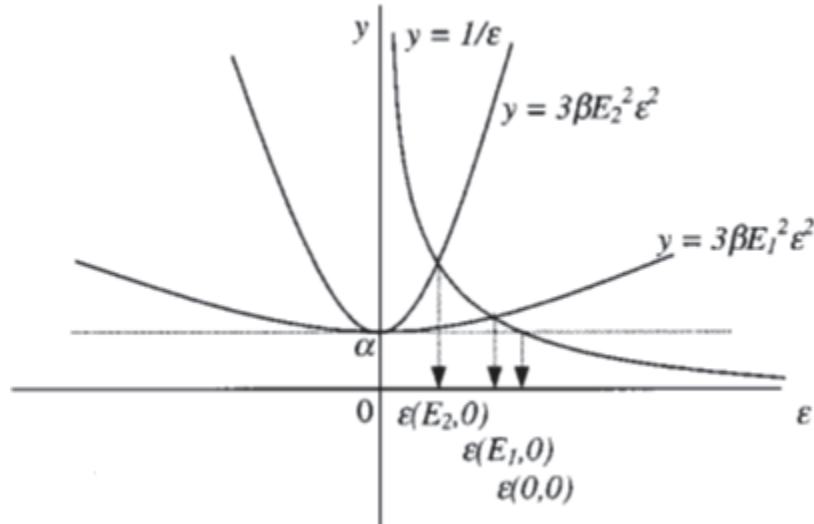
Figure 1.9: Dependencies of electric-field and the dielectric constant for BST film.[20]

The parameters α and β being positive constants at a given temperature, this cubic equation has a negative discriminant and hence only one real solution for each electric field E. Fig. 1.10 graphically illustrates the calculation of $\varepsilon_r(E)$ for two values of $\varepsilon_r(0)$ and a β of 8 × 10⁹ J.C⁻⁴ m⁻⁵ (typical value for SrTiO₃). It shows that the Landau theory gives a good representation of the dielectric constant variation as a function of the dielectric field for SrTiO₃, with a fast decrease of the dielectric constant up to ~40 kV/cm, which slows down above this value. It also shows that the amplitude of the variation depends on the starting value of the dielectric constant (at E=0): the higher $\varepsilon_r(E=0)$ is, the higher is the variation (corresponding to the tunability).
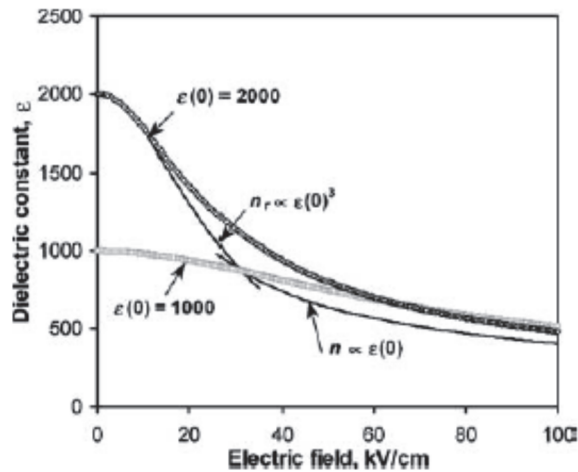
Figure. 1.10: Field dependence of the dielectric permittivity plotted for β = 8×10⁹ JC⁻⁴m⁵ and for the values of $\varepsilon_r(0)$ 2000 and 1000. [from ref.[19]]

22

If we state that $\chi_e \approx \varepsilon_r$ the tunability $\Phi(E_0)$ (Eq. 1.9) can be written as:

$$\Phi(E_0) \approx \frac{\chi_e(0) - \chi_e(E_0)}{\chi_e(0)} \Leftrightarrow$$

$$\Phi(E_0) \approx 1 - \frac{\chi_e(E_0)}{\chi_e(0)} = 1 - \frac{1}{1 + 3\beta\chi_e(0)\varepsilon_0 P^2} = 1 - \frac{1}{1 + 3\beta\chi_e(0)\varepsilon_0{}^3\chi_e(E_0)^2 E_0^2} \quad \dots\dots\dots\dots\dots\dots\dots \text{Eq.1.17}$$

This expression has the form $\Phi(E_0) \approx \frac{n-1}{n}$ where

$$n = \frac{\chi_e(0)}{\chi_e(E_0)} = 1 + 3\beta\chi_e(0)\varepsilon_0{}^3\chi_e(E_0)^2 E_0^2 \quad \dots\dots\dots\dots\dots\dots\dots\dots\dots\dots\dots \text{Eq.1.18}$$

For weak electric fields $\chi_e(E_0) \approx \chi_e(0)$, n $\rightarrow$ 1 and $\Phi(E_0)$ is close to zero. For large electric fields n >> 1, $\Phi(E_0)$ gets closer to 1 (or 100 %). Since χ_e (or ε_r) can be calculated for a given value E_0, it is also possible to calculate $\Phi(\text{E})$ knowing the parameters α and β of the ferroelectric. α being temperature dependent, the Landau theory also allows calculating the tunability as a function of the temperature for a given electric field. In any case, it is sure that the tunability will be maximum for a given E_0 when the temperature is as close as possible to the Curie temperature, the factor n being proportional to $\chi_e(0) = \frac{C}{|T - T_c|}$.

1.2.3. Dielectric constant and tunability of BST thin films

Although ferroelectrics have found many applications in the bulk form (such as bulk acoustic wave resonators), in most of wireless applications, they need to be integrated as thin films in order to reduce the size and the cost of production of the active components. The problem until now for thin-film applications is that the material thin film properties are far from the one of bulk ceramics.

Dielectric Permittivity

Many groups have synthesized ferroelectric thin films since the last twenty years, and BST was one of the most investigated materials, but most of the BST thin films obtained present dielectric properties well below the ones of bulk ceramics. Fig. 1.11 compares the temperature dependence of the dielectric permittivity in BST-0.7 ceramic and thin film form. Whereas the bulk form presents a sharp peak at the Curie temperature, reaching dielectric constant values of ~20000, the thin film presents almost no transition or one that is completely flatten out and well below the expected Curie temperature with

23

a maximum value of ~300. There are many papers reporting degradation of the thin film dielectric permittivity, and this effect that is thought to be related to film stress is often called the "clamping effect".
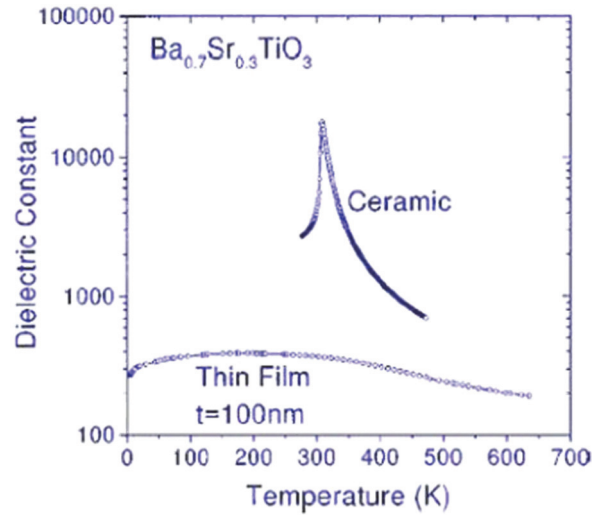
Figure 1.11: Temperature dependence of the dielectric permittivity in ceramic and thin film.[21]

Many reasons have been discussed to explain this phenomenon including strain due to the lattice mismatch between the film and the substrate, thermal strain or defects.

Li *et al.*[22] studied the effect of thickness on the properties of epitaxial $Ba_{0.5}Sr_{0.5}TiO_3$ thin films grown on MgO. They found that as the thickness is increased from 14 to 500nm, the in-plane misfit strain decreases and the dielectric constant and tunability also decrease.

Xiao *et al.*[23] led a similar study but on epitaxial $Ba_{0.5}Sr_{0.5}TiO_3$ thin films grown on $SrTiO_3$ (001). They found that as the thickness varies from 160 to 1000 nm the biaxial compressive strain decreased from 2.54% to 1.14% and the Curie temperature is shifted to lower temperature. Their results show that large in-plane compressive strain decreases the out-of-plane dielectric constant but also enhances the ferroelectric properties of the films, the Curie temperature being shifted to values closer to room temperature.

Zhu *et al.* [24] found large dielectric anisotropy in BST films strained along the in-plane direction (with higher dielectric permittivity and tunability) compared to those strained along the out-of-plane direction. The strains along the in-plane and out-of-plane directions are influenced by the interfacial low-dielectric layer between the BST film and

the substrate (a metal electrode). They explained qualitatively the anisotropic dielectric responses in terms of a thermal strain effect.

Ito *et al*. [25] *also* studied the effect of the residual strain induced by the thermal strain on the dielectric tunability of polycrystalline $Ba_{0.5}Sr_{0.5}TiO_3$ thin films. The films, grown on various substrates with different thermal expansion coefficients, exhibit a dielectric tunability that linearly increases with increasing thermal expansion coefficients. Their results demonstrate that large BST-0.5 dielectric tunability can be achieved by using residual thermal strain.

1.2.4. Landau–Devonshire model: [26]

All these studies show that the Landau theory model developed for bulk ferroelectric is not sufficient to describe the dielectric properties of ferroelectric thin films. In order to take the influence of the film strain into account, another model was developed. It is based on Landau–Devonshire phenomenological model and derived from the expression of the thermodynamic potential $\tilde{G}$ of the material.
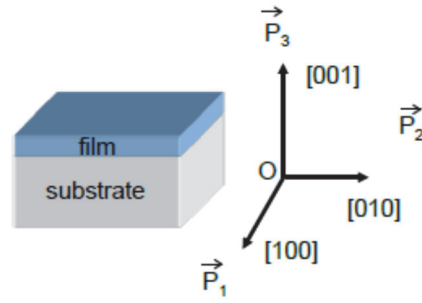
Figure 1.12: **Definition of the crystallographic directions with respect to the film and the substrate.**[26]

If we consider a polarization *Pi* applied on a pseudocubic BST film such as P_1//[100], P_2//[010], P_3//[001] (as shown on Fig.1.12) the thermodynamic potential $\tilde{G}$ of a pseudocubic BST film as a function of the polarization *Pi*, the applied field *Ei* and the misfit strain $u_m=(a_{BST} - a_{Bulk}) / a_{BST}$ (where a_{BST} is the BST thin film lattice parameter and a_{Bulk} is the BST bulk lattice parameter) can be expressed as:

$$\tilde{G} = a_1^* (P_1^2 + P_2^2) + a_3^* P_3^2 + a_{11}^* (P_1^4 + P_2^4) + a_{33}^* P_3^4 + a_{13}^* (P_1^2 P_3^2 + P_2^2 P_3^2) + a_{12}^* P_1^2 P_2^2 +$$
$$a_{111}(P_1^6 + P_2^6 + P_3^6) + a_{112}[P_1^4(P_2^2+P_3^2) + P_3^4(P_1^2+P_2^2) + P_2^4(P_1^2+P_3^2)] + a_{123}P_1^2 P_2^2 P_3^2 +$$
$$\frac{u_m^2}{s_{11}+s_{12}}(E_1 P_1 + E_2 P_2 + E_3 P_3).$$

<div align="right">Eq.1.19</div>

Where

$$a_1^* = a_1 - u_m \frac{Q_{11} + Q_{12}}{S_{11} + S_{12}}$$ Eq.1.20

$$a_3^* = a_1 - u_m \frac{2Q_{12}}{S_{11} + S_{12}}$$ Eq.1.21

$$a_{11}^* = a_{11} - \frac{1}{2} \frac{1}{S_{11}^2 + S_{12}^2} [(Q_{11}^2 + Q_{12}^2)S_{11} - 2Q_{11}Q_{12}S_{12}]$$ Eq.1.22

$$a_{33}^* = a_{11} + \frac{Q_{12}^2}{S_{11} + S_{12}}$$ Eq.1.23

$$a_{12}^* = a_{12} - \frac{1}{S_{11}^2 + S_{12}^2} [(Q_{11}^2 + Q_{12}^2)S_{12} - 2Q_{11}Q_{12}S_{11}] + \frac{Q_{44}^2}{2S_{44}}$$ Eq.1.24

$$a_{13}^* = a_{12} + \frac{Q_{12}(Q_{11} + Q_{12})}{S_{11} + S_{12}}$$ Eq.1.25

a_1 is the dielectric stiffness, a_{ij} is higher order stiffness coefficients at constant stress, Q_{ij} are the electrostrictive coefficients (relates the strain and polarization), and S_{ij} the elastic compliances (the inverse of the stiffness) of the film.
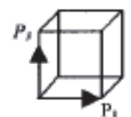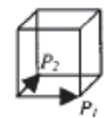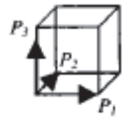
Table 1.1: The parameters for the calculation of the renormalized coefficients for BST films.

parameter	BST-0.6
Tc (°C)	5
C (10^5 °C)	1.22
a_{11} (10^6 m^5/C^{2}F)	2.16 T +462 (T in °C)
a_{12} (10^8 m^5/C^{2}F)	7.98
S_{11} (10^{-12} m^2/N)	5.12
S_{12} (10^{-12} m^2/N)	-1.65
S_{44} (10^{-12} m^2/N)	5.86
Q_{11}(m^4/C^2)	0.1
Q_{12}(m^4/C^2)	-0.034
Q_{44}(m^4/C^2)	0.029

The temperature dependence of the dielectric stiffness a_1 is given by the Curie–Weiss law, $a_1 = (T - T_0)/2\varepsilon_0 C$, where T_0 and C are the Curie–Weiss temperature and constant of a bulk ferroelectric, respectively, and ε_0 is the vacuum permittivity.

The parameters used for the calculation of the renormalized coefficients for BST-0.6 films are given in Table 1.1.

Table 1.2: **Polarization components of the theoretically predicted phases in epitaxial ferroelectric thin films.**[26]

Phase	Polarization components	
Paraelectric	$P_1 = P_2 = P_3 = 0$	
c phase	$P_1 = P_2 = 0,\ P_3 \neq 0$	
a phase	$P_1 \neq 0,\ P_2 = P_3 = 0$	
ac phase	$P_1 \neq 0,\ P_2 = 0,\ P_3 \neq 0$	
aa phase	$P_1 = P_2 \neq 0,\ P_3 = 0$	
r phase	$P_1 = P_2 \neq 0,\ P_3 \neq 0$	

The polarization components of the six phases for a given temperature and misfit strain are listed in Table 1.2. Only the *c* phase, the paraelectric phase, and the *aa* phase are the stable ones. The polarization components as a function of the applied field can be obtained from the relation $\dfrac{\partial \tilde{G}}{\partial P_i} = 0$, such that:

$$\frac{\partial \tilde{G}}{\partial P_1} = 2(a_1^* + a_{13}^* P_3^2 + a_{12}^* P_2^2)P_1 + 4a_{11}^* P_1^3 - E_1 = 0 \dots\dots\dots\dots\text{Eq.1.26}$$

$$\frac{\partial \tilde{G}}{\partial P_2} = 2(a_1^* + a_{13}^* P_3^2 + a_{12}^* P_1^2)P_2 + 4a_{11}^* P_2^3 - E_2 = 0 \dots\dots\dots\dots\text{Eq.1.27}$$

$$\frac{\partial \tilde{G}}{\partial P_3} = 2\left[(a_3^* + a_{13}^*(P_1^2 + P_2^2)]P_3 + 4a_{33}^* P_3^3 - E_3 = 0 \dots\dots\dots\dots\text{Eq.1.28}$$

The electric field dependent relative dielectric constants along [001] and [100] directions can be determined by

$$\frac{\varepsilon_{33}(E_3)}{\varepsilon_0} = \left(\varepsilon_0 \frac{\partial^2 \tilde{G}}{\partial P_3^2}\right)^{-1} = \frac{1}{2\varepsilon_0[a_3^* + a_{13}^*(P_1^2 + P_2^2) + 6a_{33}^* P_3^2]} \qquad\qquad \text{Eq.1.29}$$

$$\frac{\varepsilon_{11}(E_1)}{\varepsilon_0} = \left(\varepsilon_0 \frac{\partial^2 \tilde{G}}{\partial P_1^2}\right)^{-1} = \frac{1}{2\varepsilon_0[a_1^* + a_{13}^* P_3^2 + (a_{12}^* + 6a_{11}^*)P_1^2]} \qquad\qquad \text{Eq.1.30}$$

The tunability;

$$\Phi = \begin{cases} 1 - \varepsilon_{33}(E_3)/\varepsilon_{33}(E_3 = 0) & for\ E//[001] \\ 1 - \varepsilon_{11}(E_1)/\varepsilon_{11}(E_1 = 0) & for\ E//[100] \end{cases}$$

Eq. 1.31

Eq. 1.32

Different groups have found experimental validation of the Landau-Devonshire model [27,28] where the tunability is generally plotted as a function of the thin-film stress or misfit strain.

Among these studies, we can note that Sharma *et al.*[29] theoretically investigated the dependence of the tunability on thermally induced internal stresses in highly textured BST films using this model. They found that the deposition temperature and the thermal expansion coefficient of the substrate can be used as design parameters to achieve desirable tunability of ferroelectric thin films.

Delprat *et al.* [30] extended the model validation to polycrystalline BST-0.5 films deposited on Alumina. They found a correlation between the tunability and the lattice parameter, the later being varied by different deposition parameters (deposition temperature and pressure, annealing temperature, doping). This correlation was fitted with a Landau-Devonshire model of the thin film, expressed as a function of the lattice parameter of the films.

1.2.5. Flexoelectricity [31]

Another phenomenon occurring in ferroelectric is flexoelectricity. Flexoelectricity is the coupling between strain gradient and polarization. For instance, if a mechanical stress is applied on a ferroelectric it will greatly affect its dielectric properties. This phenomenon has gain more and more attention over the years since its impact could explain the dielectric behavior of thin films in relation to stress gradients in the films. Flexoelectric coefficient was found to be quite important for BST (μ_{12} ~ 100 µC/m), and it was observed that it reaches a maximum near the dielectric peak associated with the ferroelectric phase transition.[32]

A phenomenological theory of flexoelectricity was developed [31] based on the Landau–Ginzburg–Devonshire free energy (ΔG) considering a thin single-domain perovskite ferroelectric single crystal, epitaxially grown onto a cubic substrate, with in-plane elastic stresses due to lattice mismatch between the film and substrate. Beside the conventional free energy expression (as in the Landau-Devonshire model) two terms are added: a flexoelectricity term for the coupling between the polarization and stress gradient, and a converse flexoelectricity term taking into account for the coupling between the stress and polarization gradient. If one considers a polarization only allowed in the z direction (P₃), the free energy ΔG can be expressed as:

$$\Delta G = \frac{1}{2} a P_3^2 + \frac{1}{4} \beta P_3^4 - \frac{1}{2} S_{ij}(\sigma_i \sigma_j) - Q_{i3}\sigma_i P_3^2 - \gamma_{i3}\frac{d\sigma_i}{dZ}P_3 - \eta_{i3}\sigma_i \frac{dP_3}{dz} + G\left(\frac{dP_3}{dZ}\right)^2 + K\left(\frac{d\sigma_i}{dZ}\right)^2 - E_3 P_3 + \sigma_i \varepsilon_j \dots\dots\dots\dots\text{Eq.1.33}$$

where σ_i are the stress coefficients, γ_{i3} the stress-related flexoelectric coupling coefficients, η_{i3} the converse flexoelectric coefficients and Q_{ij} the electrostrictive coefficients.

Considering only in-plane stresses arising from the lattice mismatch (which are thickness dependent), the mismatch-induced stress are $\sigma1 = \sigma2 = \sigma(z)$ and all other stress components are 0; likewise $\varepsilon1 = \varepsilon2 = \varepsilon(z)$. Both the correlation term $G\left(\frac{dP}{dZ}\right)^2$ and the flexoelectric coupling $K\left(\frac{d\sigma}{dZ}\right)^2$ mean that the polarization is thickness dependent, thus $P_3=P(z)$. The actual total free energy corresponds to the integral of Eq. 1.33 with respect to *z.* Thus,

$$\Delta G = \int \left(\frac{1}{2} aP(z)^2 + \frac{1}{4} bP(z)^4 \right) dZ - \frac{1}{2} (S_{11} + S_{12}) \int \sigma(Z)^2 \, dZ - Q \int \sigma(Z)P(Z)^2 dZ -$$

$$\gamma \int P(Z) \frac{\delta\sigma(Z)}{\delta Z} dZ - \eta \int \sigma(Z) \frac{\delta P(Z)}{\delta Z} dZ + \frac{1}{2} G \int \left(\frac{\delta P(Z)}{\delta Z} \right)^2 dZ + \frac{1}{2} K \int \left(\frac{\delta\sigma(Z)}{\delta Z} \right)^2 dZ -$$

$$E \int P(Z) dZ + \int \sigma(z)\varepsilon(Z) dZ \ \text{.........Eq.1. 34}$$

Assuming a symmetric system with zero boundary conditions, the derivative with respect to polarization (*P*) and stress (*σ*) are:

$$E = aP(Z) + bP(Z)^3 - 2Q_{13}P(Z)\sigma(Z) - \gamma_{13} \frac{\delta\sigma(Z)}{\delta Z} - \frac{d}{dZ} \left[-\eta_{13}\sigma(Z) + G \frac{\delta P(Z)}{\delta Z} \right] \text{......Eq.1.35}$$

$$-\varepsilon(Z) = -(S_{11} + S_{12})\sigma(Z) - Q_{13}P(Z)^2 - \eta_{13} \frac{\delta P(Z)}{\delta Z} - \frac{d}{dZ} \left[-\gamma_{13}P(Z) + K \frac{\delta\sigma(Z)}{\delta Z} \right] \text{....Eq.1.36}$$

Hence,

$$\sigma(Z) = \frac{Y}{1-v} \left(+\varepsilon(Z) - Q_{13}P(Z)^2 - \eta_{13} \frac{\delta P(Z)}{\delta Z} - \frac{d}{dZ} \left[-\gamma_{13}P(Z) + K \frac{\delta\sigma(Z)}{\delta Z} \right] \right) \text{.........Eq.1.37}$$

where the elastic compliances (S_{ij}) are related to the Young's modulus (*Y*) and the Poisson's ratio (*v*).

Considering a situation where $\frac{d}{dZ} \left[K \frac{\delta\sigma(Z)}{\delta Z} \right]$ is ignored, we can substitute (Eq.1.37) into (Eq.1.36) and obtain the following equation:

$$E = P(Z) \left[a - 2Q_{13} \frac{Y}{1-v} \varepsilon(Z) \right] + P(Z)^3 \left[b - 2Q_{13}^2 \frac{Y}{1-v} \right] - (\gamma - \eta) \frac{Y}{1-v} \frac{d\varepsilon(Z)}{dZ}$$
$$- \left[G - \frac{Y}{1-v} (\gamma - \eta)^2 \right] \frac{d^2 P(Z)}{dZ^2} \text{..........Eq.1.38}$$

For conventional ferroelectrics we have $\quad a = \alpha(T - T_C) \text{..........Eq.1.39}$

Where: *α* is the Curie constant and *T*c is the critical temperature for the ferroelectric transition (the Curie temperature);

The first coefficient of Eq 1.38 can be conveniently redefined as

$$a^*(Z) = \alpha \left(T - T_C^*(Z) \right) \text{.........Eq.1.40}$$

Where, $\quad T_C^* = T_C + \frac{2}{\alpha} \frac{Y}{1-v} Q_{13}\varepsilon(z) \text{...............Eq.1.41}$

given that Q_{13} is negative, the Curie temperature will shift depending on whether the in-plane strain is negative (compressive) or positive (tensile).

We can also redefine the second and last coefficient of Eq. 1.34 as

$$b^* = \left[b + 2Q_{13}^2 \frac{Y}{1-v} \right] \text{........Eq.1.42}$$

and

$$G^* = \left[G - \frac{Y}{1-\upsilon}(\gamma - \eta)^2\right]...............\text{Eq.1.43}$$

This yields to the simplified expression

$$E = a^* P(Z) + b^* P(Z)^3 - (\gamma - \eta)\frac{Y}{1-\upsilon}\frac{d\varepsilon(Z)}{dZ} - G^*\frac{d^2 P(Z)}{dZ^2}....................\text{Eq.1.44}$$

The inverse permittivity can be then expressed as:

$$\chi^{-1} = \frac{dE}{dP} = \frac{d^2(\Delta G)}{dP^2} = 3b^* P^2 + \alpha(T - T_C^*) - \frac{d}{dP}\left[G^*\frac{d^2 P}{dZ^2}\right]...................\text{Eq.1.45}$$

The G* value measured experimentally for bulk ceramics or single crystals is about 10^{-9} J m^3 C^{-2}, therefore this term can be ignored in Eqs 1.44 and 1.45 and the Eq.1.45 becomes:

$$\chi^{-1} = 3b^* P^2 + \alpha(T - T_C^*).........\text{ Eq.1.46}$$

Substituted back into the Eq. 1.44, the following expression is obtained:

$$E = \chi^{-1}P(Z) - 2b^* P(Z)^3 - (\gamma - \eta)\frac{Y}{1-\upsilon}\frac{d\varepsilon(Z)}{dZ}...................\text{ Eq.1.47}$$

Thus, setting E = 0, the flexoelectric polarization as a function of strain gradient in a bulk paraelectric is giving by the expression (the polarization being very small in the paraelectric state, the P^3 term can be ignored):

$$P(Z) = \chi(\gamma - \eta)\frac{Y}{1-\upsilon}\frac{d\varepsilon(Z)}{dZ}..........\text{ Eq.1.48}$$

Eq. 1.48 allows relating the phenomenological coefficients $(\gamma - \eta)$ to the empirically measured coefficient, μ:

$$\mu = \chi(\gamma - \eta)\frac{Y}{1-\upsilon}......................\text{ Eq.1.49}$$

Eq. 1.49 shows that if the flexoelectric coefficient μ is measured as the derivative of the polarization with respect to the strain gradient, it will be proportional to the permittivity.

Typical μ values for BST are of the order of 10^{-4} C m^{-1}, this means that the BST flexoelectric coefficients in the model are of the order of $(\gamma - \eta) \sim 10^{-9}$ m^3 C^{-1}.

Further development of this model also shows that the reversible polarization does not actually happen at Tc (or at the strain-modified T_c^*), but at the temperature T_{ferro} defined as:

$$T_{ferro} = T_C^* - \frac{3b^*}{\alpha}\left(\frac{C}{2b^*}\right)^{2/3} \ldots\ldots\ldots\ldots \text{Eq.1.50}$$

Thus, the ferroelectric transition will take place at a temperature lower than the Curie temperature.

This model predicts that, in the presence of strain gradients, there is a splitting of the bulk Curie temperature into three important temperatures, namely, the strained-modified Curie temperature T_c^*, the temperature for the ferroelectric transition T_{ferro} and the temperature of the maximum dielectric constant T_m, where ($T_m>T_c>T_{ferro}$). It shows that for ferroelectrics exhibiting relatively large flexoelectric coefficient (such as BST), a stress gradient (due for instance to a lattice mismatch) will have a major impact on the dielectric properties and Curie temperature of the material.

1.3. Dielectric loss properties of BST

The integration of ferroelectric into active microwave devices requires three major material characteristics. In the previous section, we presented the dielectric constant and tunability of ferroelectrics which are crucial for the optimization of tunable device size and low voltage response. The other important parameter is the dielectric loss of the material, which is important to avoid the use of signal amplification and reduce the influence of noise. Losses lower than 0.01 are typically required for material integrated into microwave devices. If the real part of the dielectric constant (ε') is well modelized by thermodynamical models (as a function of temperature, stress), very few models exists for the imaginary part of the dielectric constant (ε") or the corresponding dielectric losses (tan δ defined as ε"/ε').

1.3.1. Dielectric Loss of bulk BST [17]

Fig. 1.13 shows the different loss mechanisms associated with ferroelectrics. All losses can be divided into intrinsic loss, which represent the lower limit of the loss, and extrinsic loss due to different type of impurities and defects.
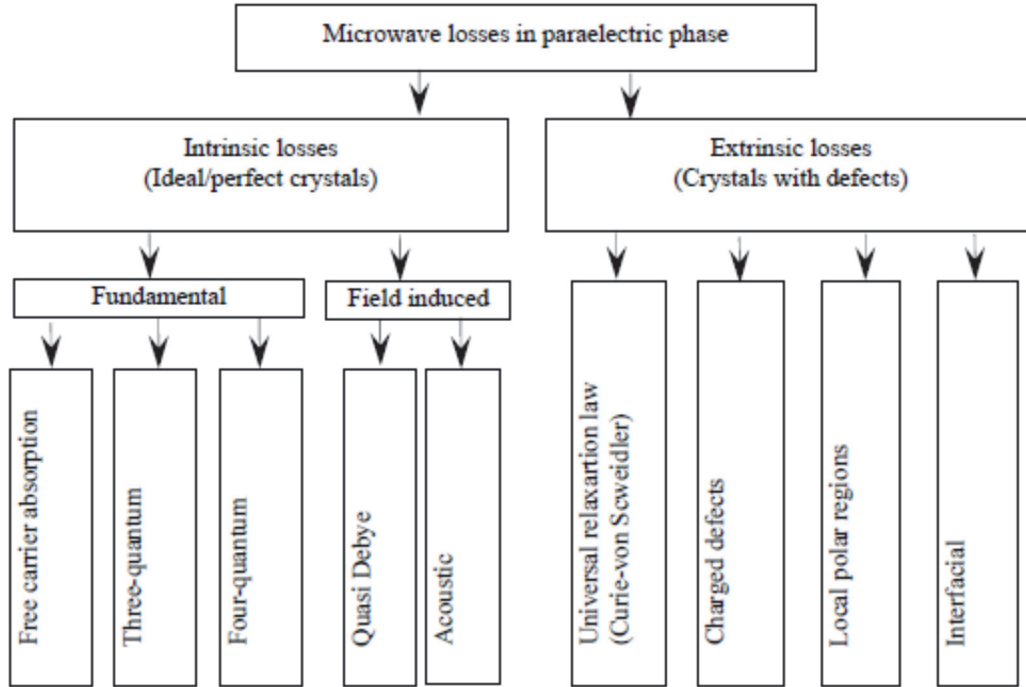
Figure 1.13: **classification of the loss mechanisms.**[17]

Intrinsic Loss theory

The fundamental losses are associated with the interactions of the electromagnetic (microwave) energy with phonons. Phonons correspond to thermal oscillations of ions, their energy equal to hv (h being the Planck's constant and v the oscillation frequency). When microwave energy is absorbed by thermal oscillations (phonons) of the crystal, the dissipated energy heats up the crystal.

The energy of phonons, hv, is much higher than the microwave energy quantum hf (where f is the frequency of microwave field), this results in three different collision schemes : three quantum, four quantum and quasi-Debye mechanism.

In the three quantum case the absorption process involves one microwave quantum *hf* and two phonons having a small energy difference (close to *hf)*. The predicted frequency and temperature dependence of losses in that case (for microwave and near room temperature regions) is:

$$tan\delta_{ph} \propto \omega\varepsilon^{3/2}T^2 \quad ....Eq.\ 1.51$$

Where, ω is the microwave frequency and ε is the relative permittivity of the ferroelectric.

In the case of four-quantum process one microwave quantum *hf* interacts with three phonons of the crystal. In perfect crystals, besides the fundamental phonon losses, extra microwave losses appear due to free charge carriers and under the external electric field.

In a crystal with a symmetric lattice structure (i.e. cubic) the external field shifts the centers of the positive and negative charges. The induced non-center symmetric unit cell of the crystal lattice becomes polarized with an external field dependent dipole moment.

The induced electric dipole initiates two extra mechanisms of the microwave losses:
 i) DC field induced Quasi-Debye, and ii) Microwave to acoustic transformations. For small tunability (Φ <<1) the losses associated with this mechanism are characterized by the following functional dependences of the loss tangent on the frequency and electric field:

$$tan\delta_{QD} = Al\ (E)\omega\ \Phi\ (E) \ ....Eq.\ 1.52$$

where Φ *(E)* is the tunability of the dielectric permittivity *A* is a material related constant.

Extrinsic Loss

Extrinsic losses are mainly coming from structural defects of the material. Even in the case of chemically pure bulk single crystals ferroelectrics, impurities, charge defects or lattice distortion could create energy dissipation. In ferroelectric materials, the intrinsic and extrinsic contributions are usually comparable at microwave frequencies. Three major loss mechanisms are associated with extrinsic losses, namely losses due to charged defects, universal-relaxation-law mechanism and local polar regions.

Charged defects are one of the most common defects. In ferroelectrics any charged point defects and charged dislocations, such as oxygen vacancies, create local static

electric field. The neutral defects may also locally distort the crystal symmetry and create local dipoles and static fields around them that will enhance the energy dissipation.

Since the ferroelectric requires being just above the Curie temperature to exhibit large tunability, the material could present local polar regions at the interfaces between the phases, grains/ columns, electrodes and other layers (i.e. dielectric and metallic buffer layers).[33] The ferroelectric phase being much more dissipative than the paraelectric phase, these polar regions will be a source of extrinsic losses.

1.3.2. Dielectric Loss of BST thin films

Understanding and distinguishing different sources of dielectric loss at microwave frequencies in thin films is crucial for the integration of BST in microwave devices. These applications require the use of thin films with low dielectric loss in order to minimize signal attenuation. Compared to bulk material, the dielectric loss in thin films is roughly one order of magnitude higher, and it is believed that it mainly comes from extrinsic origin. Possible reasons for high losses in thin films are local stress, oxygen vacancies, and interfacial effects.

Intrinsic Loss

Intrinsic losses are the lower limit of loss that exists in defect-free single crystals and it depends on the crystal symmetry. As for bulk material, the intrinsic loss mainly corresponds to the absorption of the energetic quantum of the electromagnetic field by collisions with thermal phonons. The fundamental phonon loss mechanisms of the dielectric loss in thin film are strongly dependent on the dielectric permittivity and the frequency.[19]

Extrinsic Loss

Extrinsic losses are due to interaction between charged defects and the microwave field. These losses are associated with imperfections in the crystal lattice and can be reduced by proper material processing. The understanding of the extrinsic loss mechanism is useful in optimization of the device design but, to date, there is no model that correlates material processing conditions and/or the type of defects to the dielectric loss of thin film.

It is only usually reported that structural defects such as oxygen vacancies in the films leads to a degradation of the electrical properties of the films, and in particular an increase of the material losses.

The distinction between the contributions of intrinsic and extrinsic loss mechanisms is important for the materials development but it is a non-trivial task to experimentally separate the two mechanisms since the intrinsic and extrinsic contributions are comparable in most of the cases. Astafiev et al.[34] analyzed the behavior of dielectric loss in $SrTiO_3$ thin films at different microwave frequencies and under an applied dc bias voltage. Their experimental results pointed to a crossover between extrinsic and intrinsic losses in the thin films. They stated that the crossover is driven by the applied dc bias field and that at weak fields the loss is governed by extrinsic mechanisms whereas, at higher fields, the contribution of an intrinsic mechanism becomes predominant.
Vorobie et al.[35] studied $Ba_{0.25}Sr_{0.75}TiO_3$ thin film and found that the oxygen vacancies within the grain boundaries of ferroelectric film act as charged defects and cause extrinsic microwave losses. They also found that the loss for frequencies above 2 GHz and no dc field are mainly due to the charged defects and could be described as $\tan\delta_{ch} \propto \varepsilon\omega^{1/3}$, where ε is the real part of relative dielectric permittivity and ω is the angular frequency.

Many studies have shown that the thin film extrinsic dielectric loss strongly depends on the processing conditions. Zhu et al.[36] theoretically studied the evolution of dielectric loss with processing temperature. Experimental results show a common dielectric loss behavior in ferroelectric and dielectric thin oxide films such as BST0.7 which shows a maximum as the processing temperature is gradually raised. They proposed that in the initial stage of crystallization, the transformation from amorphous to crystalline phase increases the dielectric loss due to the enhancement of dielectric polarization and the higher dissipation energy induced. With further increase of the processing temperature, the coalescent growth of small crystalline grains into big ones is believed to results in the reduction of dielectric loss by lowering grain boundary densities.

What is common to all the papers reporting studies on BST thin films is the high dielectric loss value for films exhibiting a reasonable tunability. Typical values for tan δ are about 0.04 in the GHz range, which is about one order of magnitude higher than the bulk BST value, and no major improvement have been done on this aspect within the

last decade. Crystal quality, surface roughness, stress and stoechiometry are parameters influencing dielectric extrinsic losses, but since these parameters have also an important role on the dielectric constant of the films, it is usually very difficult to isolate the origin of the extrinsic losses. A clear model on the origin of losses and ways to improve them without degrading the material tunability remains to be developed.

Conclusion

The conception of tunable microwave devices based on ferroelectrics requires the integration of ferroelectric thin films with specific dielectric properties, in particular a large variation of the dielectric constant as a function of the applied electric field (tunability Φ) and low losses, typically $\Phi > 50\%$ for few kV.cm^{-1} and tan $\delta < 0.01$.[5] Many groups have studied ferroelectric materials and it appears that Barium Strontium Titanate (BST) is one of the best candidates for these applications. But one of the major difficulties is that, whereas bulk material exhibits the expected dielectric characteristics, in the case of thin films it is very hard to obtain at the same time large tunabilities and low losses.

The dielectric constant and its variation as a function of different parameters, such as the tunability, is well documented and different theories exist that fits well the experimental data for either bulk or thin film materials. It is now well-known that the stress or misfit strain, the so-called "clamping effect" is responsible for the degradation of the dielectric constant properties. Concerning the dielectric losses, different hypotheses exist on the origin of the large extrinsic losses observed in the case of thin films, but there is no clear conclusion yet on the subject. Even if one knows that crystal defects, oxygen vacancies and local polar region could increase the dielectric losses, experimental data shows that even highly epitaxial thin films, annealed in oxygen and presenting minimized stress present an abnormally high level of dielectric losses.

Today, the relatively high loss of BST thin films in the GHz range (tan $\delta \sim 0.04$) is the major bottleneck to its integration into commercial wireless products such as electrically controlled phase shifters, bandpass filters or adjustable antennas. To overcome this difficulty, a better understanding on the origin of extrinsic losses in BST thin films is necessary.

CHAPTER 2: Epitaxial growth of BST thin films

As presented in the previous chapter, the dielectric properties of BST are closely related to its crystal structure. It is hence very important to control the BST synthesis and try to reach high crystal quality and minimal stress in order to optimize the dielectric properties of the material. In this chapter, we will first present different deposition techniques used for the epitaxial growth of BST and in particular the Pulsed Laser Deposition method that was used in this study to grow BST on MgO single-crystal substrates. We will also present the different diagnostics used to characterize the microstructural properties of the BST films such as X-ray diffraction (XRD), and Rutherford backscattering spectroscopy (RBS). The last part will present experimental results on the influence of different PLD parameters such as laser fluence, laser repetition rate, BST target composition, substrate temperature, oxygen background pressure, substrate material type and orientation, on the microstructural properties of the deposited films.

2.1. Deposition conditions of epitaxial BST

Understanding the different mechanisms affecting the growth mode is necessary to control the film crystallinity during thin film growth. There are different forms of crystallization: polycrystalline, textured and epitaxial growth which mainly depend on the deposition conditions.

2.1.1. Growth mode

The growth mode is governed by the balance between the free energy of the film surface, the substrate surface and the interface between the film and the substrate. Deposition rate and substrate temperature are two important factors that control the structure and the morphology of film growth. These factors determine the degree of diffusivity of the adatoms on the substrate surface, which seek minimum energy positions. The diffusivity of the adatoms is also strongly dependent on the ratio between the substrate temperature and the film bond strength.

2.1.1.a. Polycrystalline thin film [37]

Fig. 2.1 illustrates the various stages of growth of a thick polycrystalline film on a substrate. It shows that cluster formation and growth leads to impingement of cluster to form grain boundaries. The development of grain structure and subsequent film growth is determined largely by surface mobility of adatoms relative to the deposition rate and by the substrate temperature relative to the melting temperature of the film material. When the growth flux is very large and the substrate temperature is moderate, the common mode of film growth initiation is the 3D island (Volmer Weber) mode. Polycrystalline film growth starts with thermally activated nucleation of film material islands on the substrate surface.

The growth of polycrystalline films will occur at either low substrate temperature and low deposition rate, or for a material that present a high melting point and low surface diffusivities. The first case will lead to large initial grain size as the islands join to form a polycrystalline film. The second mechanism will develop smaller initial grain sizes during island impingement. During the growth the grain always try to reduce total grain boundary surface area.
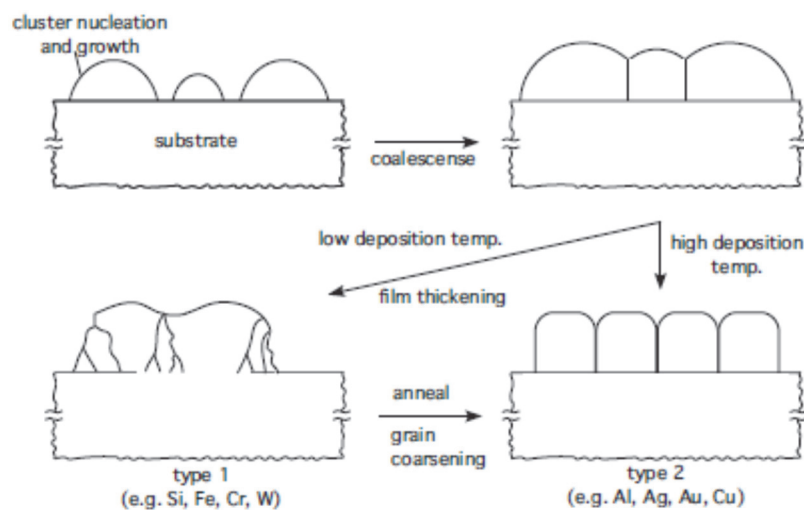
Figure 2.1: A schematic representation of several stages in the formation of a thick polycrystalline film on a substrate. [37]

2.1.1.b. Epitaxial thin film

The term epitaxy comes from the Greek roots epi (επί) and taxis (τάξις), meaning «above in ordered manner» and refers to the growth of a material grown on top of a substrate with a structure close to a perfect crystal. There are two main types of epitaxy: heteroepitaxy (growth of a material on a substrate of a different material), and homoepitaxy (growth of a material on a substrate of the same material).[38] The matching of symmetry and lattice parameters between the substrate and the thin film is the most important consideration in epitaxy. The mismatch in the lattice parameter, is called misfit (u_m) and expressed as $u_m = (a_s - a_f / a_s)$, where a_s is the substrate lattice parameter, a_f is the film lattice parameter. It is also important to consider matching of the thermal expansion coefficient between the film and the substrate, as unmatched thermal expansion coefficient will lead to thermal strain or film cracking. The strain usually degrades the thin film properties.[39]

Heteroepitaxial growth first requires a lattice matching between the film and the substrate, but the compatibility of the crystal structures, the symmetry, and unit cell dimensions need to be considered as well. For small mismatch and very thin film the mismatch is accommodated by homogenous strain in the film, and the film unit cell either expands or contracts uniformly in plane to fit the one of the substrate. Above a certain critical thickness, crystal defects such as dislocation becomes more energetically favorable than homogenous strain and the film relaxes to its equilibrium.

The thermodynamic approach is used to describe crystal growth close to equilibrium. A supersaturated gas phase is a prerequisite for the formation of nuclei, which will be formed once a critical density is reached. From this point onwards the nuclei will grow and crystallization will take place. In the thermodynamic approach, the balance between the free energies of film surface (γ_F), substrate surface (γ_s) and the interface between film and substrate (γ_i) is used to determine the film morphology. The surface free energies for the substrate and film materials influence the growth mode.

For heteroepitaxy, four types of growth modes are observed, as illustrated on Fig. 2.2: layer-by-layer growth (Frank-van der Merwe growth or "FM" mode), three-dimensional 3D islands (Volmer-Weber growth or "VW" mode), 3D island layer growth (Stranski-Krastanov growth or "SK" mode), and step-flow mode.
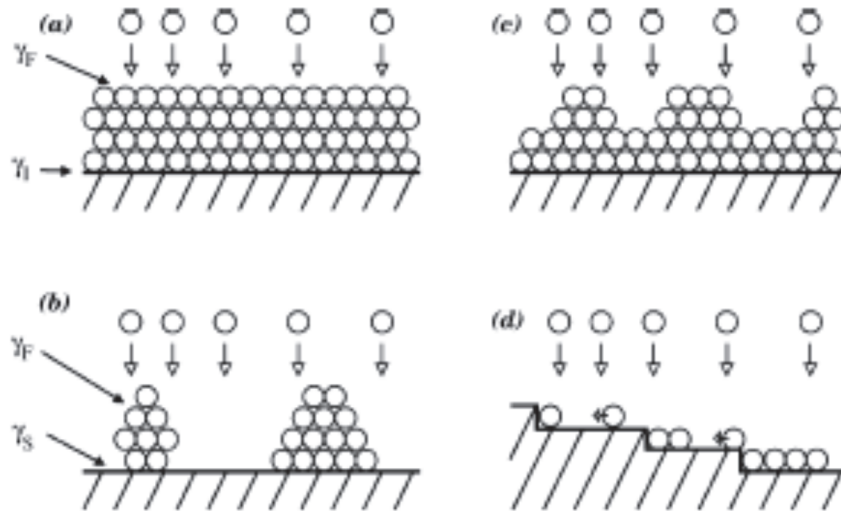
Figure 2.2: **Film growth modes: a) Layer-by-layer (Frank-Van der Merwe), b) 3D island (Volmer–Weber), c) 3D island layer (Stranski–Krastanov) and (d) step flow.**

In FM growth, the interactions between substrate and deposited atoms are stronger and more attractive than those between the different atomic species within the film material, which result in a layer arrangement at the first stage of the growth. In VW growth, it is the opposite case which results in the formation of organized 3D islands on the substrate that tends to decrease as the film grows. The SK growth is an intermediate case between the two previous modes.[40] Step flow growth is a special case where the incident atoms are deposited on a terraced surface, resulting in the arrangement of atoms along the different atomic steps of the substrate material.

2.1.2. Choice of the substrate

Heteroepitaxy is the method of choice to obtain the epitaxial growth of BST, but substrates having the same crystallographic structure and lattice parameters as close as possible as the one of BST are very limited. Other considerations have to be taken into account in the case of BST and microwave applications: this substrate will need to sustain high temperature in an oxidizing atmosphere, exhibit low microwave losses in the GHz range and being available as a polished substrate with a size larger than a cm (in order to fabricate microwave waveguides on top of it). BST-0.6 has a lattice parameter of 3.96 Å and a cubic structure. The available materials corresponding to these characteristics are mainly limited to two materials: $LaAlO_3$ (LAO) and MgO.[5,41,42]

The characteristics of these substrates are shown on Table 2.1. LAO have a quasi cubic structure (Rhombohedral with α = 90°5'), a lattice parameter of 3.79 Å and microwave losses of about $3\text{x}10^{-5}$. MgO have a cubic structure, a lattice parameter of 4.21 Å and losses between 2 and $3\text{x}10^{-5}$ in the GHz range. Sapphire could be also considered for its good dielectric properties but its crystal structure is octahedral with lattice constants very far from BST (a=4.785Å and c=12.991Å), and it is thus uncertain if epitaxial growth of BST is possible on top of this substrate.

Table 2.1: **Physical parameters of substrate materials commonly used in BST varactors. Note that the data are the room-temperature values.**

Substrate	Lattice parameter (Å)	Relative permittivity ε_r	Dielectric loss tanδ (at 10 GHz)	Thermal expansion coefficient α (K^{-1})
MgO	a= 4.213	9.8	< 3 x 10^{-5}	10.8 x 10^{-6}
LaAlO$_3$	a= 3.793	~25	~ 3 x 10^{-5}	11 x 10^{-6}
Sapphire	a= 4.758 c= 12.993	a:9.4 c: 11.58	a: < 2 x 10^{-5} c: < 5 x 10^{-5}	7.3 x 10^{-6}
BST-0.6	a=3.96	~1000	~0.04-0.05	10.5 x 10^{-6}

2.1.3. Deposition method

There are two main thin film vapor deposition methods: Physical vapor deposition (PVD) and chemical vapor deposition (CVD). Vapor deposition describes any process in which a material is transferred to a solid surface through a vapor state. If the vapor is created by physical means and not a chemical reaction, the process is called PVD.[43]

In the case of CVD, the vapor phase is created from precursors and/or from the decomposition of liquid or gas precursors, which limits a lot the material that can be deposited with this technique. The thermal evaporation process comprises evaporating source materials in a vacuum chamber below 1 × 10^{-6} Torr and condensing the evaporated particles on a substrate. Since the evaporation of ferroelectric ceramics require high energies, the main PVD preparation methods used for fabricating epitaxial

ferroelectric thin films are pulsed laser deposition (PLD) and sputtering (DC magnetron, and ion beam).

For complex oxides such as BST, the sputtering method, which consists in bombarding a ceramic target with energetic accelerated ions, leads to low deposition rates because of the high sputtering yield and the large bonding energies in this material.[44] To overcome these limitation the Pulsed laser deposition (PLD) will be preferred. In this method, a high-power pulsed laser is focused onto a target of the source material and atoms ablated from the target surface are collected on the substrate to form a thin film. This is the best method for the deposition of BST and the control of its crystal structure. In this work all the BST thin films (epitaxial, textured, and polycrystalline) were obtained using the PLD technique, details about the technique are given in the next section.

2.2. Pulsed Laser Deposition

Pulsed laser deposition (PLD) is a thermal process that consists in evaporating a material under low pressure or vacuum conditions through the use of laser pulses. The first laser ablation experiment was done in 1965 by Smith and Turner using a Ruby laser on different materials.[45] Ruby lasers produce pulse at 694 nm (red) but most of the materials exhibit stronger absorption in the UV range (generally, the shorter the wavelength, the higher the absorption coefficient). Later, with the development of Excimer lasers that can produce short and intense laser pulses in this part of the spectrum (248 nm for KrF), laser ablation became more and more used in the research community since it offers an excellent experimental technique for thin-film synthesis. The process setup of this film deposition method is shown on Fig. 2.3. This setup is generally simple; however, the physical phenomena related to the laser ablation and plasma formation are complex and are still a matter of discussion. [46]
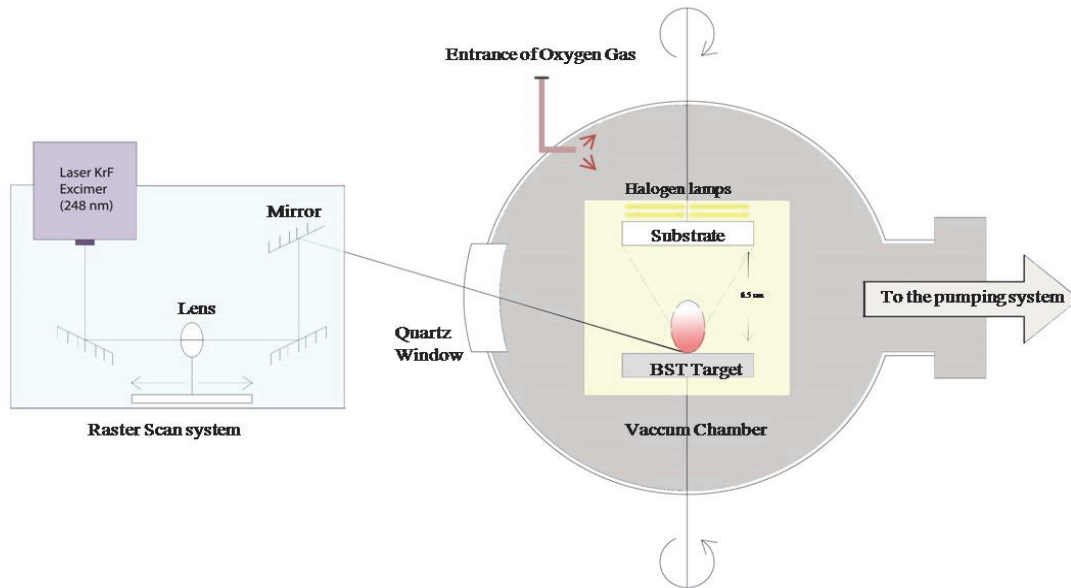
Figure 2.3: PLD setup used for synthesis of BST thin films on MgO.

2.2.1. Mechanism of pulsed laser deposition

When a laser beam hits the surface of a target, it will create excited electrons that will transfer their energy to the lattice and heating begins within the optical absorption depth of the material $1/\alpha$, where α is the optical absorption coefficient. When the laser fluence (laser energy per unit area) exceeds the ablation threshold of the material, the temperature of the target surface is increased instantaneously to a temperature above the vaporization temperature; this causes a local evaporation of the target. Above this threshold (which depends on the absorption coefficient of the material and its vaporization temperature) the ablation of atoms, ions, electrons, molecules, and particulates occurs and forms a plasma at the surface of the target. This plasma will expand in the vacuum chamber and flows towards the substrate to form the deposited material. This plasma, that is clearly visible as a bright cone in front of the target, is called the plasma plume. The mechanism of the energy transfer from the laser pulse to the target depends strongly on the properties of the laser (fluence, frequency, pulse

duration and wavelength).[46] The energy and the nature of the ejected species will depend on the laser energy and the background pressure of the process chamber, as the ejected particles can interact with the background gas.

The main parameters of PLD deposition are: the fluence (the laser energy density on the target), the background gas pressure, the target-substrate distance, the substrate temperature. It is important to note that the prerequisite to PLD deposition is also the quality of the target material. PLD target should be as dense and homogeneous as possible to ensure a good quality of the deposition and the target must be polished frequently to avoid the generation of particulates during the deposition.

2.2.2 Advantages and drawbacks of PLD

The important advantage of PLD over other techniques is the stœchiometric transfer of the target material to the substrate for most of the materials. PLD is able to produce species with electronic states outside chemical equilibrium which enable the production of metastable materials which will not be possible under normal thermal conditions. Almost any condensed matter material can be ablated and the use of a pulsed laser allows good control on the growth rates. All types of materials such as metals, dielectrics, semiconductors, superconductors, simple or complex oxides, etc….can be deposited by PLD. It is also important to note that, in PLD, it is possible to get excellent adhesion between the film and the substrate although the substrate is at room temperature. PLD is a technique that gives an opportunity to coat heat sensitive materials like polymers. [46]

The main drawback of PLD, is the control of thickness uniformity on large surfaces and the production of particulates during the thin films deposition. Since the plasma plume has a narrow distribution, the control of thickness uniformity requires a combination of target and substrate scans and rotations to obtain uniformity on large surfaces that will generally lead to low deposition rates. During the ablation process, the laser pulse will sometimes eject large aggregates called 'droplets' that will cause large defects (particulates of few tens of microns) on the film surface. These droplets can be reduced by properly adjusting the laser fluence and background pressure during deposition. These drawbacks are also less critical in applications where metal electrodes are deposited on top of a dielectric stack (as in the case of coplanar microwave waveguides) compared to Metal/Insulator/Metal (MIM) structures.

2.2.3. Deposition parameters of BST film grown by PLD

In this section, results of the influence of the deposition parameters of PLD on BST films will be presented.

The laser used in our PLD system (a PVD 3000 system) is an excimer KrF laser (PM-800 from Lumonics) with a wavelength of 248 nm, a pulse duration of 15 ns and a repetition rate between 1 and 100 Hz. The beam has a uniform distribution across the beam intensity profile cross section. Optical components that are used to guide, shape and focus the laser beam are located outside the deposition chamber. The focused beam size on the target can be varied by adjusting the position of a focal lens from 1 mm^2 (at focal length) to few mm^2.

Laser fluence (laser energy divided by the laser spot area on the target) can be typically varied from 0 to 5 J/cm^2. There are two ways to vary the laser fluence, either by increasing the laser energy at constant laser spot size, or by decreasing the laser spot size at constant laser energy.

The substrate temperature has a major role in controlling structure of the film. The thermal energy that the condensing species reach the substrate surface allows increasing the surface mobility, the energy for nucleation, and growth rate of the film. In the PVD 3000 system, the substrate temperature is controlled by 4 halogen lamps and can be set from room temperature to ~900°C.

For the deposition of complex oxides such as BST, the use of oxygen background pressure helps the formation of multications. Interaction of ablated species with this background oxygen pressure produces molecular species and compensate for the loss of oxygen in the plasma plume. The background pressure has also a major influence on the kinetic energies of the ablated species. This pressure can be controlled from 0 to 100 mTorr by a gas flow meter and the opening of a throttle valve at the bottom of the process chamber.

The target-substrate-distance provides an opportunity to control the deposition rate, as well as the energy of the particles hitting the substrate. In any case, the plasma plume being directional, the material deposition will have a Gaussian distribution. Uniformity of the coating thickness requires rotation and/or translation motion of the laser beam and/or the substrate during the deposition. PLD system (PVD3000) (schematic shown on Fig

2.3) has a raster scan system, where the laser beam scanning on the rotating target surface is controlled by changing the position of the focusing lens with a linear motor and different settings for the inner, middle and outside rings of the target. Raster scan allows the deposition of uniform thickness of thin film on large substrate surfaces up to 3" but requires adjustment of the different parameters for each target-substrate distance, background pressure and ablated material.

In order to obtain a good uniformity on the 1 inch square substrates used, a fixed 6.5 cm distance was chosen for the deposition and different scan settings where tested with an oxygen background pressure of 10 mTorr. Fig 2.4. shows the thickness profile of BST (measured on the cross-section of a 3 inch Si wafer, using a scanning electron microscope) as a function of the distance from a 3 inch Si wafer center. According to the thickness measurements, the most uniform scan is the one with constant raster speed (0.25 cm/sec) that shows thickness variation of 13% (red line) over a 3 inch wafer.
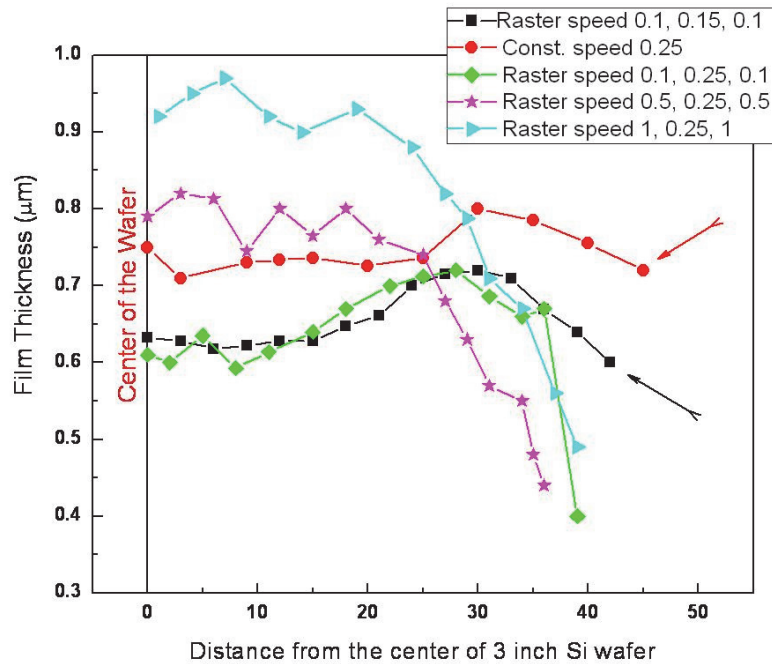
Figure 2.4: **thickness of BST thin film (deposited on 3" diameter Si wafer) versus the distance traveled from the center of the 3" diameter of Si wafer. The thickness was measured by taken SEM images of the wafer cross section.**

2.3. Material characterization methods

Many techniques where employed in this study to characterize the BST thin film grown on MgO substrate: X-ray diffraction (XRD) for the structure analysis, and Rutherford backscattering spectroscopy (RBS) for the chemical analysis. In this part of the chapter a brief introduction of each technique will be presented, including some results of BST analysis done with them.

2.3.1. Rutherford backscattering spectroscopy (RBS)

Rutherford backscattering spectroscopy (RBS) is an analytical technique used to determine the structure and composition of materials by measuring the backscattering of a beam of high energy ions impinging on a sample. RBS allows quantification of the different elements composing the analyzed sample, without the use of a reference standard. It is also a nondestructive method of analysis that allows quantitative analysis of all elements simultaneously except for hydrogen. It has a typical resolution depth of about 10 nm and its sensitivity is about 100 ppm for heavy elements (although it is not so precise for light elements). Measurement times are typically as short as several minutes.

An RBS instrument generally includes three essential components: (1) an ion source, usually alpha particles (He+ ions) or, less commonly, protons; (2) a linear particle accelerator capable of accelerating incident ions to high energies, typically in the range 1-3 MeV and (3) a detector capable of measuring the energies of backscattered ions over some range of angles.
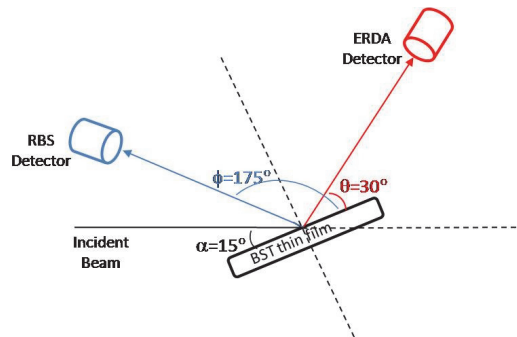
Figure 2.5: RBS and ERDA set up.[47]

When the target material is bombarded by low mass ions (H or He) at high energy, the energy of the backscattered ions will depend on the mass of the atoms encountered. These RBS spectrum can be interpreted knowing the following parameters:

1. The kinematic factor of the elastic scattering which describes the reduction of incident energy in a collision between the probe ion and the target atom. The resulting energy of the scattered ion increases with the target atom mass. This allows identification of the target atom by measuring the scattered ion energy. The fundamental equation that describes the scattering process is:

$$E_1 = \left\{ \frac{\left(M^2 - M_0^2 \sin^2\theta\right)^{1/2} + M_0 \cos\theta}{M_0 + M} \right\}^2 E_0 \quad \ldots\ldots\ldots\ldots\ldots\ldots..\text{Eq. 2.1}$$

where E_1 is the ejected ion energy, E_0 and M_0 are the incident ion energy and atomic mass, M the atomic mass of ejected ion and θ the scattering angle.

2. The differential scattering cross-section which gives the probability of scattering. This allows basic quantitative analysis without a standard sample.
3. The stopping power which is defined as the ion energy loss per unit path length inside the target. The energy of the backscattered ion depends on the depth from which the ion is scattered since the path length is proportional to the depth. This allows the depth profiling of elements inside the target.

This characterization method will give quantitative measurements of the BST thin film stœchiometry.

Fig 2.6 shows the measured RBS spectrum of a $Ba_{0.6}Sr_{0.4}TiO_3$ thin film deposited on MgO substrate. The continuous blue line is the fitted RBS spectrum that includes the different element contribution to the spectrum (corresponding to the convolution of the other continuous lines of the different elements). The mesured stœchiometry of BST-0.6 extracted from this spectrum is Ba : 0.113%, Sr : 0.087%, and Ti : 0.2%, which matches the expected atomic composition.
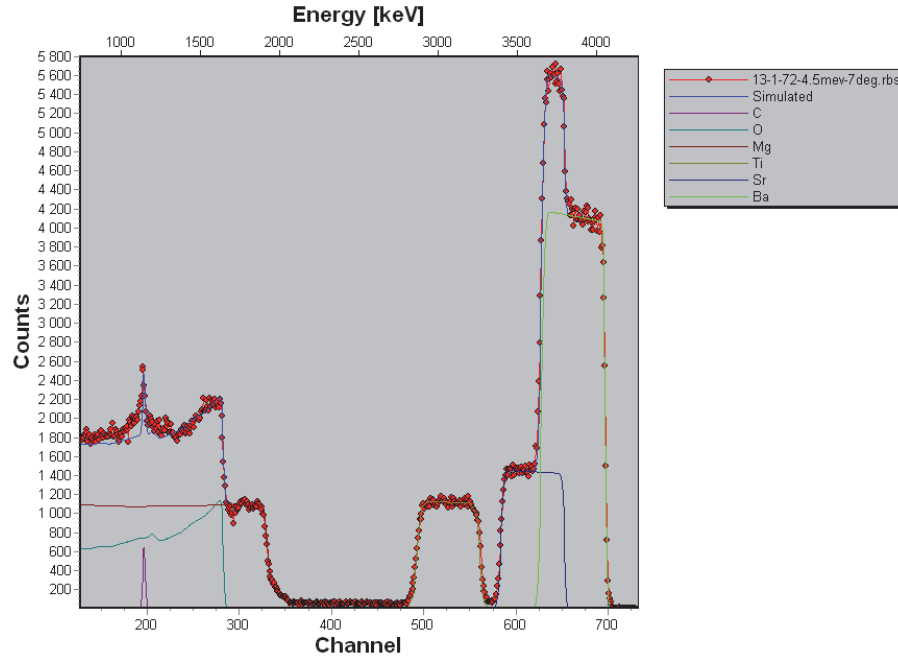
Figure 2.6: RBS spectra simulated and measured of $Ba_{0.6}Sr_{0.4}TiO_3$ thin film deposited on MgO substrate.

2.3.2. X-ray diffraction - (XRD)

X-ray diffraction (XRD) consists of exposing a sample to a monochromatic X-Ray radiation and interpreting the generated diffraction pattern. Diffraction is obtained from constructive and destructive interference of X-ray as it interacts with the crystal lattice of the sample. XRD is an important method for structure characterization that is able to quantify different crystal properties from the X-ray scans obtained by rotating the sample or the detector along different axes (theta, phi, omega and psy) as shown in Fig 2.7. The resulting scans performed using XRD will be named according to the measurement angle: θ-2θ scans, ω-scan (or rocking curves) and phi scans, which are described in this section.
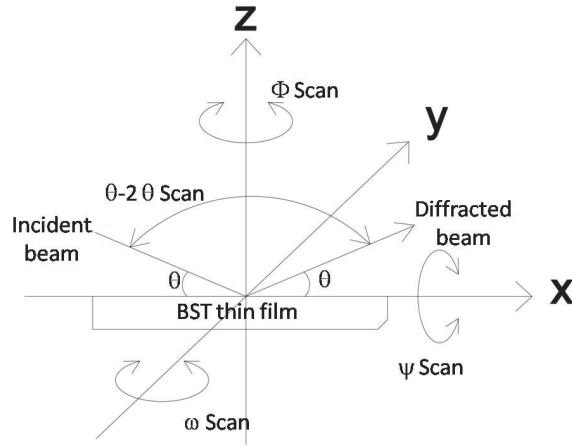
Figure 2.7: schematic diagram of different types of scans using XRD.

2.3.2.a. θ-2θ scan

In the θ-2θ scan configuration, the X-ray hits the sample at an incident angle θ. As the different rows of the material crystal planes will reflect the incident beam, a path difference between two reflections will exist (one reflected by a row, the other one by the row below) that is a function of the interplanar spacing d (= 2d sinθ). If the path difference between the two rays is an integer multiplier (n) of the wavelength the two reflected signals will be in phase and result in constructive interference at angle θ. As the incident angle changes, constructive interferences will appear at peak positions obeying to the Bragg's law:

$$n\lambda = 2d_{hkl} \sin \theta \dots\dots\dots\dots\dots\dots\dots\dots\dots\dots\dots\dots\text{Eq.2.2}$$

Where λ is the wavelength of the incident X-ray beam, d is the interplanar spacing and n is an integer.

The different constructive interference found will correspond to the different plane orientation (hkl) of the crystal structure. The interplanar distance of these planes, for a cubic structure, can be found using the following relation:

$$\frac{1}{d_{hkl}^2} = \frac{h^2}{a^2} + \frac{k^2}{b^2} + \frac{l^2}{c^2} \dots\dots\dots\dots\dots\dots\dots\dots\dots\dots\dots\dots\dots\text{Eq.2.3}$$

52
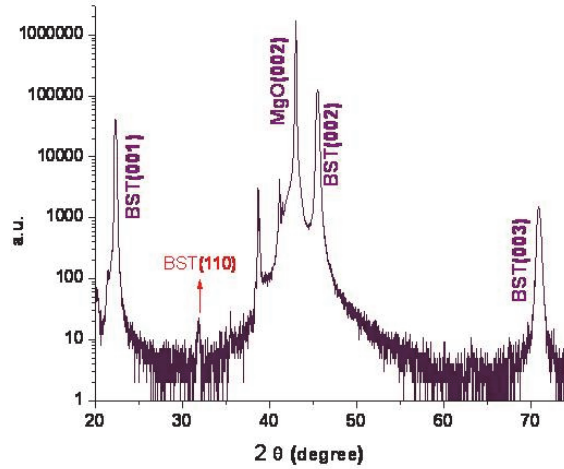
Figure 2.8: XRD spectra of (θ–2θ) scan of single phase BST-0.6 thin film grown on MgO single crystal substrate.

Fig 2.8 shows a (θ –2θ) scan of a single phase BST-0.6 thin film with (001) orientation with respect to MgO (001) single crystal substrate. This figure shows a very strong (002) MgO diffraction peak in addition to the (001), (002), and (003) BST peaks. A very small (110) peak is also visible, demonstrating that this thin film is not strictly epitaxial but is highly oriented (textured) in the (001) direction.
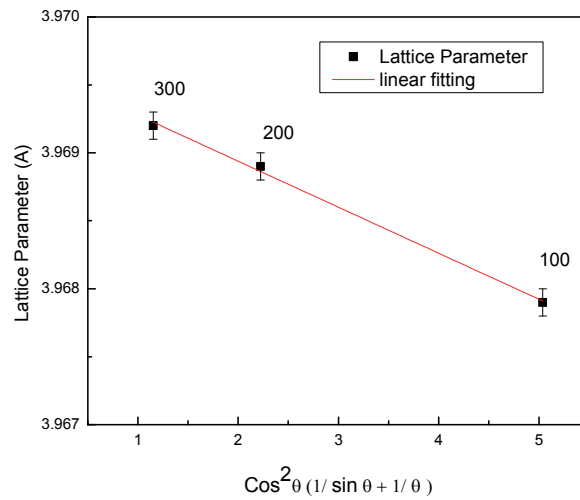
Figure 2.9: lattice parameter for BST thin film on MgO substrate.

From the peaks positions, it is possible to calculate the in-plane lattice parameter of BST-0.6 thin film (a_0) using the Nelson – Riley function.

$$\frac{a_{\cos\theta} - a_0}{a_0} = c \; cos^2\theta \left(\frac{1}{sin\theta} + \frac{1}{\theta} \right)$$ ....Eq. 2.4

Where $a_{\cos\theta}$ is the interplanar distance calculated from the Bragg peak position at 2θ and C is a fitting coefficient. Fig. 2.9 shows the lattice parameters $a_{\cos\theta}$ calculated from (001), (002) and (003) Bragg reflections for BST considering a cubic cell. The extrapolation at zero gives the lattice parameters a_0, found here to be 3.9696 Å.

2.3.2.b. Rocking curve (ω- scan)

Rocking curve scans are used to analyze highly oriented or epitaxial thin films. In this configuration, the detector remains fixed at the location of a Bragg diffraction peak (2θ) while the sample is tilted at an angle ω. Since misalignment of certain crystallographic plane with respect to the C axis will induce spreading of the peak around its expected position, the full-width at half maximum (FWHM) will be an indication of the crystal quality (or degree of perfection). Rocking curves of perfect crystals gives a sharp peak with a very small FWHM, while crystals with mosaicity, dislocation or curvature gives a broader peak. Fig.2.10 shows a comparison between rocking curves of epitaxial and textured BST thin film for the (002) reflection, one can clearly see the broader ω-scan peak for the textured film (0.67°) compared to the epitaxial one (0.25°).

2.3.2.c. Phi Scan

Phi scans are used to analyze the in-plane texture of an epitaxial thin film. In this configuration, the detector and the source are aligned to satisfy the diffraction condition for the selected plane and they remain fixed while the sample is rotated along ϕ from 0 to 360° (see Fig 2.7). Phi scans are used to characterize the crystallographic relation (alignment) between the substrate and the thin film. Fig 2.11 shows the phi scans of the MgO substrate and of an epitaxial BST thin film deposited on MgO. The presence of four symmetry related peaks in phi scan proves the epitaxial relation between the film and the substrate and confirms the cubic structure of the film. The presence of BST peaks at

the same position as the MgO substrate peaks indicates a cube on cube in-plane alignment between BST film and the MgO substrate.
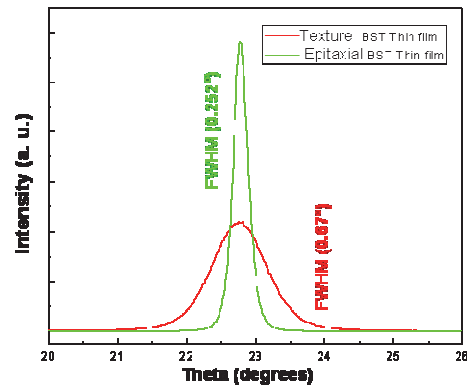
Figure 2.10: Rocking curves of epitaxial and textured BST thin film deposited on MgO.
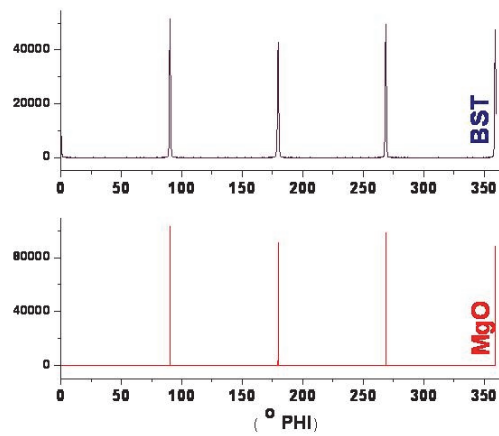
Figure 2.11: Phi scan of BST thin film and MgO single crystal substrate showing cube on cube in-plane alignment.

2.4. PLD parameters study, influence on microstructure

In pulsed laser deposition (PLD), the BST film microstructure can be influenced by many processing parameters, the main ones being the laser fluence, the repetition rate, the substrate temperature and oxygen pressure, the type of substrate and the BST-x composition. Our goal being to study the influence of microstructure on the microwave properties of BST thin films, we led an extensive study on the microstructure and stœchiometry of BST films processed in a broad range of deposition conditions.

2.4.1. Effect of Laser fluence (Laser energy density)

Laser fluence (F) is the ratio between laser energy (E) and laser spot area (A), (F=E/A) and it affects the deposition rate but also the nature of the created plasma.

The ablation volume (V_a) can be expressed as

$V_a = k \cdot A \cdot ln \, (F \, / \, F_s)$ …………………………………………..Eq.2.5

Where, (F) is the Laser fluence, (F_s) the ablation threshold, (k) is a constant (between 0.3 and 0.4 J.cm^{-2} for BST), and (A) is the laser spot area.[68]

At a fixed spot size and with increasing laser energy above the material threshold, the ablated volume will increase and yield to higher plasma densities and deposition rates.

There are a number of publications that discuss the effect of laser fluence on the quality of deposited films. For example Bu *et. al.*[48] studied the effect of the laser fluence on the microstructures and electrical properties of polycrystalline $SrBi_2Ta_2O_9$ thin films and they found that high quality films with good electrical properties are obtained in a narrow laser fluence range of 1 to 1.5 J/cm^2. Dam *et.al.*[49] found that low fluence affects the (Sr/Ti) ratio of $SrTiO_3$ films, while at higher fluence (above 1.3 J/cm^2), stœchiometric $SrTiO_3$ films are obtained. Furthermore, Han *et.al.*[50] found that the laser fluence strongly influences the structural and electrical properties of $(Pb_{0.72}La_{0.28})TiO_3$ (PLT) thin films.

Experimental conditions: In order to investigate the effect of the laser fluence on the microstructures and dielectric properties of BST-0.6, three different sets of films were prepared. All the films were deposited on MgO (100) single crystal substrates by pulsed

laser deposition (PLD) technique. As described in the previous section, the KrF excimer laser (λ=248nm) beam is focused on a BST-0.6 target using a lens and a quartz window (positioned outside the vacuum chamber). The repetition rate of the laser was set to 10 Hz, and the deposition was done under 10 mTorr O_2 background pressure, and a temperature of 700 °C. After deposition, all films were annealed in O_2 background at 1050°C for 3h.

The different sets are:

- Set # 1: the laser fluence is varied by varying the laser spot area while the laser energy is maintained fixed at 110 mJ such that the obtained fluences are of 1, 2, 3.5 and 7.5 J/cm^2.
- Set # 2: the laser fluence is varied by varying the laser energy while the laser spot area is maintained fixed at 11 mm^2 yielding to fluences of 1, 2 and 4 J/cm^2.
- Set # 3: both the laser spot area and laser energy were varied in order to keep a laser fluence of 1 J/cm^2, the value used are reported in Table 2.2.

The deposition rates were measured in all conditions, in order to obtain films of 600 nm thickness for all the samples. Fig 2.12a and 12b show these deposition rates measured as a function of the fluence, varying the laser energy and the spot area respectively. In the first case, the deposition rate increases as the laser fluence increase (i.e. the laser energy E increases from 110 to 440 mJ with a spot size of 11 mm^2). This result is in agreement with Eq. 2.5 that shows that for a constant area (A) and above F_s, the ablated volume (and so the deposition rate) will be proportional to ln (E). On the other case (Fig 2.12b) the deposition rate decreases as the Laser fluence increases (i.e. the Laser spot size decreases from 11 to 1.5 mm^2 with laser energy of 110 mJ). According to Eq. 2.5, at constant laser energy and with a decreasing laser spot area, the ablated volume will be proportional to A ln (A^{-1}) which will decrease as A decreases (i.e. as the laser fluence E/A increases).
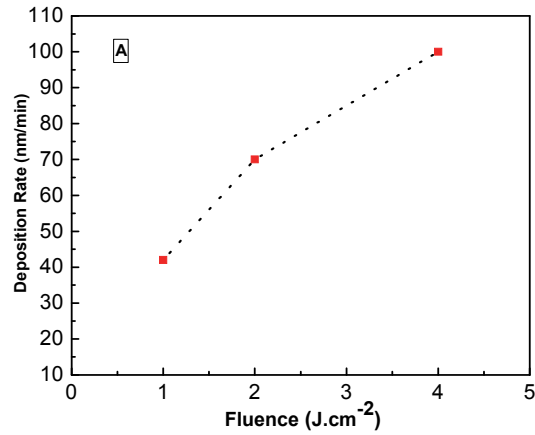
Figure 2.12.a: Deposition rate as a function of laser fluence (by increasing the laser energy at constant laser spot area).
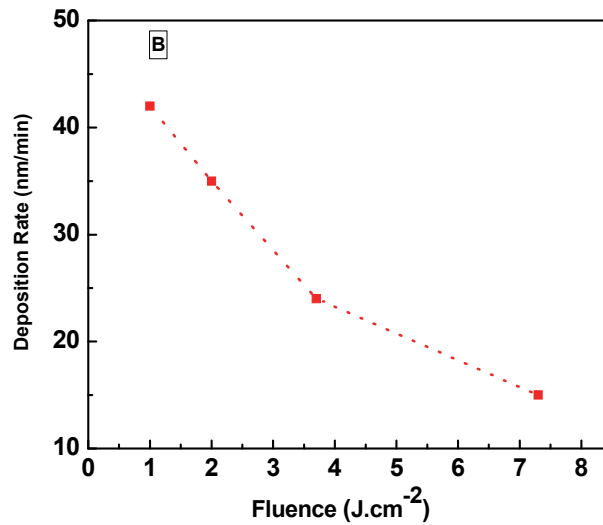
Figure 2.12.b: Deposition rate as a function of laser fluence (by decreasing the laser spot area at constant laser energy).

2.4.1.a. Varying Laser spot area

First, the Laser fluence was varied by decreasing the laser spot area (with values of 1, 2, 3.5 and 7.5 J/cm^2) while the laser energy was maintained at 110 mJ. The obtained films were characterized by XRD. Fig. 2.13 shows the rocking curve (FWHM) and the

lattice parameter of BST-0.6 as a function of the laser fluence (going from 1 J/cm^2 to 7.5 J/cm^2). The BST lattice parameter starts slightly higher than the bulk value (3.96 Å) and almost linearly increases as a function of the laser fluence (up to 4.03 Å). The rocking curve FWHM follows the same behavior: it goes from 0.57° at low laser fluence (1 J/cm^2) to 0.87° at the highest laser fluence investigated (7.5 J/cm^2).
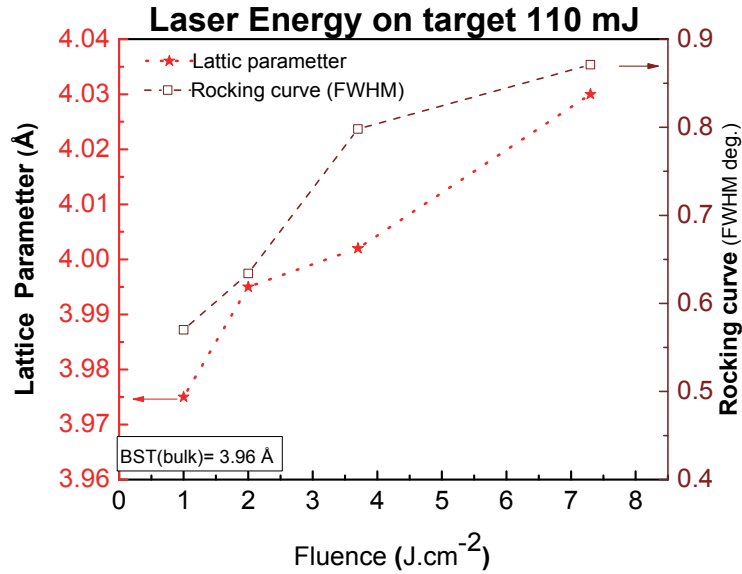
Figure 2.13: lattice parameter and rocking curve FWHM as a function of laser fluence.

2.4.1.b. Varying Laser energy

Fig. 2.14 shows the lattice parameter and rocking curve FWHM as a function of the Laser fluence, when the Laser fluence is varied by increasing the Laser energy (values set at 110, 220 and 440 mJ) while laser spot area is maintained fixed at 11 mm^2. This figure shows that the rocking curve FWHM is almost unchanged while the lattice parameter increases with increasing laser fluence. The FWHM value stays around 0.56° while the lattice parameter goes from 3.975 Å at 1 J/cm^2 to 4.03 Å at 4 J/cm^2. As observed in Fig. 2.13, a better structural properties and a lattice parameter closer to the bulk value are obtained at low laser fluence (1 J/cm^2).

It is known that, in PLD the laser fluence can modify the stœchiometry of BST-0.6.[51] In order to investigate the origin of the lattice parameter increase, RBS measurements were performed on the samples. The parameter found to be dependent on the fluence was the (Ba+Sr)/Ti ratio (that should be equal to one for BST-0.6 stœchiometry).

Fig. 2.15 shows the effect of the laser fluence on the measured (Ba+Sr)/Ti ratio. This figure shows that the stœchiometry is only equal to one at 1 J/cm². As the fluence increases, the (Ba+Sr)/Ti ratio is decreasing down to 0.82 for 7.5 J/cm². Since cation non-stœchiometry can induce larger lattice,[52] this deviation from the correct BST-0.6 stœchiometry can be responsible for the observed lattice parameter increase (observed on Fig. 2.13 and 2.14). Since high laser energy or small laser spot area will result in a non-stœchiometric transfer of BST-0.6 material the chosen fluence for all the further deposition was set to 1 J/cm².
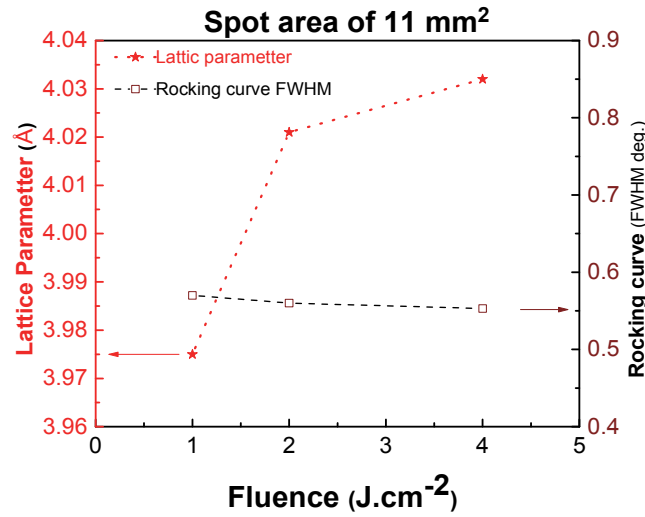
Figure 2.14: lattice parameter and rocking curve FWHM as a function of laser fluence.
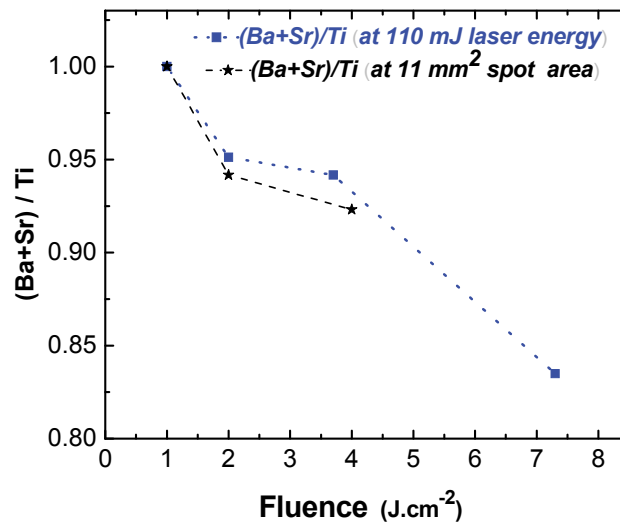
Figure 2.15: (Ba+Sr)/Ti ratio as a function of the laser fluence.

2.4.1.c. Constant laser fluence (1 J/cm^2)

Table 2.2: Laser spot area and laser energy were varied to maintain fixed laser fluence at 1 J/cm^2.

Laser spot area (mm^2)	4	5	11	20	30
Laser Energy (mJ)	40	50	110	200	300

Based on the results from set# 1 and set #2 (fluence varied by either the laser spot area or the laser energy), the optimum laser fluence in terms of microstructure was found to be 1 J/cm^2. In the set #3, the laser fluence was set to 1 J/cm^2 while both the laser spot area and laser energy are varied, following the values reported on Table 2.2. All the deposited films were analyzed by XRD and RBS. Fig 2.16 shows the lattice parameter and the (Ba+Sr)/Ti ratio as a function of the laser spot size (and the corresponding laser energy on the target), the fluence being kept at 1 J/cm^2. As observed for the set#1 and 2, there seems to be a correlation between the (Ba+Sr)/Ti ratio and the lattice parameter, the later being closer to the bulk value when the ratio is closer to one. The 1 J/cm^2 fluence obtained with 110 mJ energy and 11 mm^2 laser spot size gives the best result in terms of stœchiometry and lattice parameter for the deposited film.
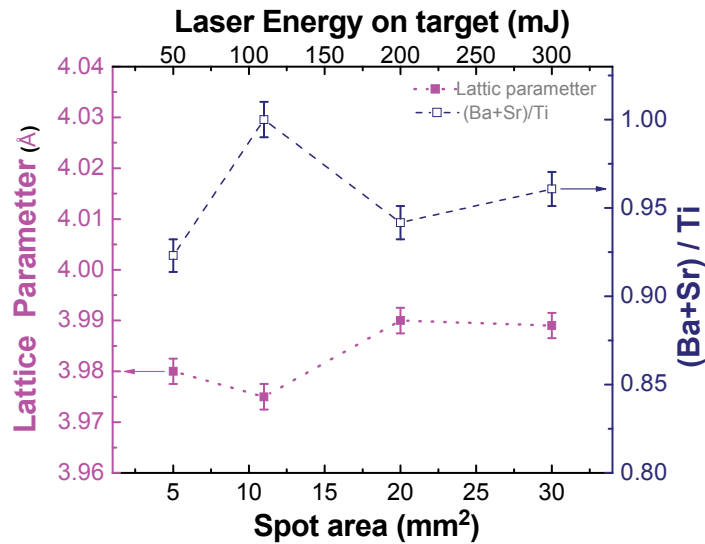
Figure 2.16: lattice parameter and (Ba+Sr)/Ti ratio as a function of spot area for 1J/cm^2 laser fluences.

This study demonstrates that, not only the laser fluence but also the way this fluence value is obtained (i.e. the corresponding laser spot size and energy) are important parameters of the BST-0.6 deposition on MgO substrates. Among all the fluence conditions explored, the best deposition conditions found, in terms of film stœchiometry, lattice parameter value compared to the bulk is a fluence around 1 J.cm^{-2} obtained with a 110 mJ laser energy and a 11 mm^2 laser spot size. In these conditions, epitaxial BST thin film with an ω-scan FWHM of 0.56°, a (Ba+Sr)/Ti ratio close to one and a lattice parameter of 3.975 Å. For higher fluences, especially when it increases by increasing the laser energy, the crystallinity of the BST films degrades and the measured stœchiometry (measured through the ratio ((Ba+Sr)/Ti) deviates from the normal value. An increase of the lattice parameter is also observed and correlated with the change of stœchiometry and related to cationic vacancies inside the crystal structure.[53]

2.4.2. Effect of Laser Repetition Rate

Apart from the fluence, the other laser parameter influencing the growth mode is the laser repetition rate.[54] In epitaxial growth, it is usually observed that the lower is the repetition rate, the higher is the crystal quality. Guan *et. al.*[55], studied the role of pulse repetition rate in film grown by pulsed laser deposition, they found that at a low pulse repetition rate (longer pulse interval) gives islands more time to form. The total of island density thus reduces and the film aggregation tends to be more compact. In contrast, the island density will increase at a high pulse repetition rate, and islands may be in dispersed mode. On the other hand, the deposition rate will be directly proportional to the repetition rate. Hence, one has to keep the repetition rate high enough to obtain reasonable growth rates. The optimal conditions will be a tradeoff between these two effects.

Experimental conditions: In order to study the influence of the laser repetition rate on the microstructure and dielectric properties of BST-0.6 thin film, a series of BST-0.6 films were prepared by PLD with laser repetition rates of 2, 10, 20, and 50 Hz. All BST-0.6 films were deposited on MgO single crystal substrates with a laser fluence of 1 J/cm^2 (obtained with 110 mJ laser energy and 11 mm^2 laser spot area), the substrate temperature was fixed at 800 °C and the oxygen pressure was maintained at 10 mTorr.

After deposition, all the films were annealed at 1050°C for 3h in an O_2 background atmosphere.

Structural properties: Through the structural analysis of XRD θ/2θ scan, ω-scan, and Phi scan, it is clear that changing laser repetition rate between 2, 10, 20, and 50 Hz has a direct influence on the microstructure of BST-0.6 thin film. Fig. 2.17a and 2.17b shows the rocking curve (ω-scan) and the Phi scans of the 2 and 50 Hz films. Both scans show large differences between the two extreme repetition rates. Whereas the film grown at 2 Hz is epitaxial the one grown at 50 Hz laser repetition rate is textured. This demonstrates that, as the laser repetition rate increases the growth kinetics is changing. At 2 Hz, and 10 Hz the XRD spectra showed epitaxial BST films reflecting a layer-by-layer-growth, while at 20 Hz and 50 Hz the XRD spectra showed textured BST films, certainly caused by a 3D island growth.
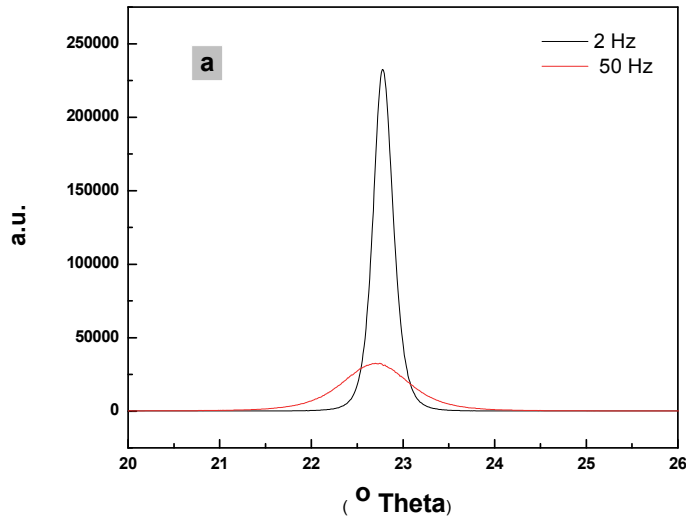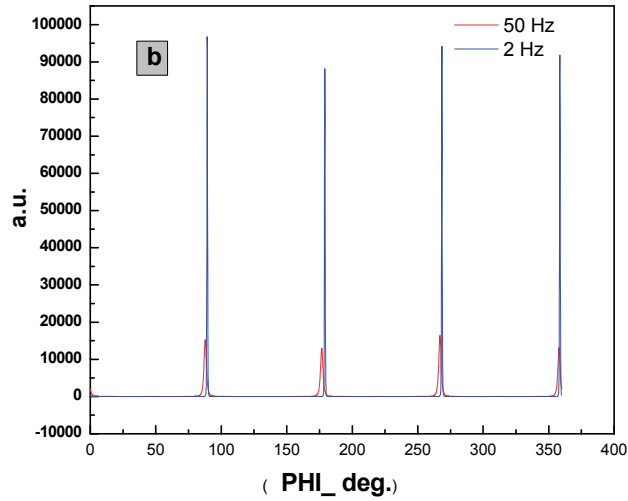
Figure 2.17: XRD patterns of, a.) rocking curve (ω-scan), b.) Phi scan, of BST-0.6 thin film on MgO single crystal substrate deposited by PLD at 2 Hz and 50 Hz laser repetition rate.

Fig. 2.18 a, b shows the FWHM of the rocking curve, Phi scan, and lattice parameter extracted from the XRD measurements as a function of the laser repetition rate. Fig. 2.18 a shows that both FWHM of the rocking curve, and Phi scan increase as the laser repetition rate increases, which means that the quality of epitaxial structure degrades as the laser repetition rate increases. Also Fig. 2.18 b shows the lattice parameter variation from the bulk value as the laser repetition rate increases. The variation of growth kinetics through laser repetition rate has a direct effect on the microstructure that could, in turn, affect the electric properties of the BST films.[56]
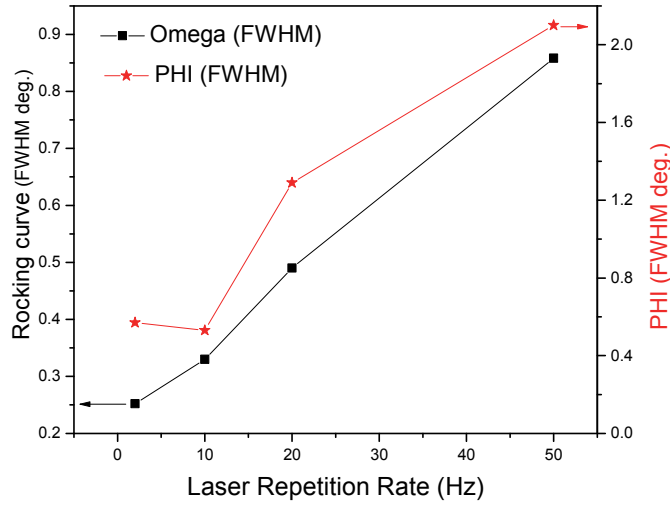
Figure 2.18.a: BST films rocking curve and Phi scan FWHM as a function of laser repetition rate (2, 10, 20, and 50 Hz).
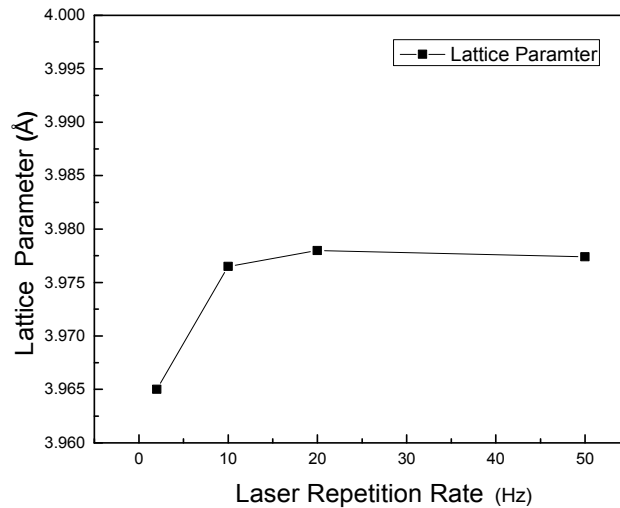
Figure 2.18.b: BST films lattice parameter as a function of laser repetition rate (2, 10, 20, and 50 Hz).

On the other hand, the deposition rate at 2Hz is about 1 nm/min, which is a bit too slow for reasonable deposition time knowing that the required deposition thickness for devices application is between 500nm and 1 μm thick. As the loss in terms of crystal quality between 2Hz and 10Hz is not that important, the repetition rate was chosen to be 10Hz for the film deposition.

2.4.3. Effect of BST-x Composition (x=0, 0.3, 0.5, 0.6, 0.7, 1)

BST-x ($Ba_xSr_{1-x}TiO_3$) is a solid solution of Barium Titanate ($BaTiO_3$) and Strontium Titanate ($SrTiO_3$). At room temperature, by changing the concentration of Ba from x=0 (STO) to x=1 (BTO), the BST-x material will go from a paraelectric material having a cubic structure with a lattice parameter of 3.9 Å to a ferroelectric material having a tetragonal structure with lattice parameters of a=3.99 Å and c=4.03 Å. For bulk material, this phase transition will occur around x=0.7 and will correspond to a maximum in the dielectric constant (ε_r) and the tunability of the material. In the case of thin films, because of the material strain and stress, this maximum can be shifted to higher or lower values. On the other hand, for tunable microwave devices applications, it is preferable to use paraelectric phase material because ferroelectric phase usually present higher dielectric losses and dielectric constant hysteresis as a function of the electric field. It is hence important to choose the right material concentration having these restrictions in mind.

Experimental conditions: In order to verify the influence of the fraction x of the BST-x material on its structural properties, a series of $Ba_xSr_{1-x}TiO_3$ thin films were prepared with x=0 (STO), 0.3, 0.5, 0.7and 1 (BTO). All the thin films were deposited by PLD on MgO (100) single crystal substrates, the laser fluence being 1 J/cm^2 (obtained with 110 mJ laser energy and 11mm^2 laser spot area). During the deposition the substrate temperature was fixed at 800 °C and the oxygen pressure was maintained at 10 mTorr. After deposition, all the films were annealed in O_2 background atmosphere at 1050°C for 3h.

Structural properties: The X-ray patterns (θ–2θ) of all the deposited thin films are showing that BST films are single phase. The structure of the films is epitaxial for x=1 to x=0.3 (BTO, BST-0.7, BST-0.6, BST-0.5 and BST-0.3) and polycrystalline for x=0 (STO) films, with a degradation of the epitaxial quality from x=1 to x=0.3.
Fig. 2.19a shows ω-scan (rocking curve) of (002) reflection of the BTO, BST-0.7, BST-0.6, and BST-0.3 thin films obtained and Fig. 2.19b shows ω-scan (rocking curve) FWHM values and Phi scan FWHM values of BTO, BST-0.7, BST-0.6, BST-0.5, and BST-0.3. One can observe on Fig. 2.19a that there is a shift of the (002) peak to higher angles going from BTO to BST-0.3. This is due to the expected decrease in the material lattice parameter from x=1 to lower concentration values.

The observed phi scan and ω-scan FWHM (Fig. 2.19b) increase going from BTO to BST-0.3 indicate that the epitaxial relation between the film and the substrate is degrading as the Ba concentration increases. The in-plane alignment with respect to MgO substrate is degrading as well. This effect is directly related to the lattice mismatch between BST-x and MgO. The lattice mismatch between BTO thin film (a_{BTO} = 4.012 Å) and MgO substrate (a_{MgO} = 4.212 Å) is 4.74% and the lattice mismatch between STO thin film (a_{STO} = 3.915 Å) and MgO substrate is 7.05%. This difference makes it easier to grow epitaxial BTO thin film on MgO than STO. As a consequence, the epitaxial growth gets more and more stressed as the BST-x concentration increases, yielding to more and more defects on the material growth which ends up with a polycrystalline film in the case of STO growth.
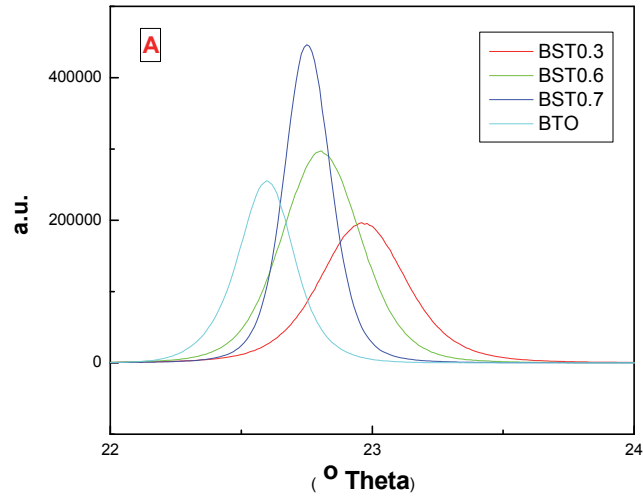
Figure 2.19.a: **Rocking curve of BTO, BST-0.7, BST-0.6, and BST-0.3 grown on MgO substrate.**
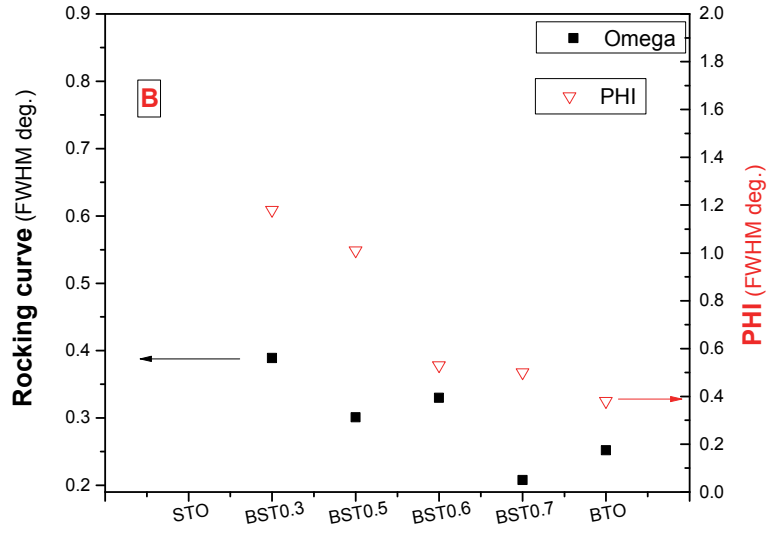
Figure 2.19.b: ω Scan (rocking curve) FWHM and Phi scan FWHM of BTO, BST-0.7, BST-0.6, BST-0.5, and BST-0.3 grown on MgO substrate.
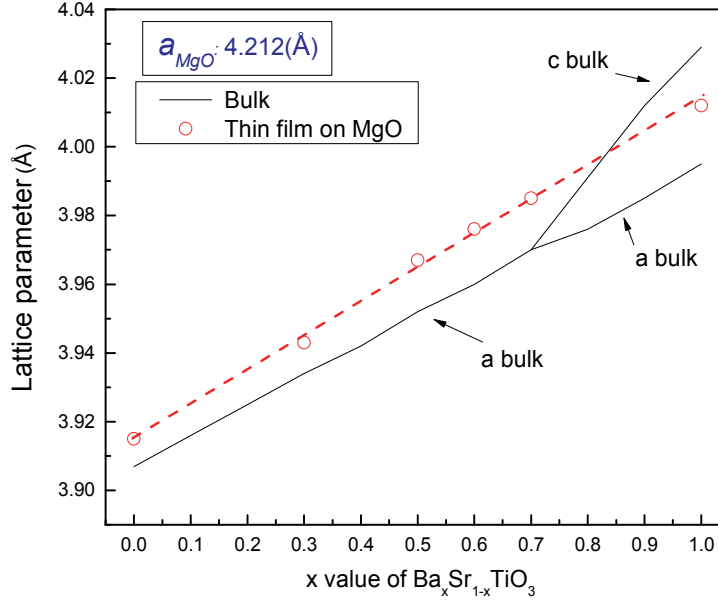
Figure 2.20: Lattice parameter of (BTO, BST-0.7, BST-0.6, BST-0.5, BST-0.3, STO) thin films grown on MgO substrate.

Fig. 2.20 shows the lattice parameter of all the deposited samples, extracted from the XRD analysis. These values are compared to the bulk values of the different BST concentrations (data taken from Gim *et al.* [57]). One can observe that, for all the samples, the value of lattice parameter of the deposited thin film is higher than the bulk value. The difference between the bulk and thin film value seems to be a bit lower for low x values which may indicate that the presence of defects act as a strain reliever on the unit cell, but it is difficult to conclude.[58] It is also important to note that since BST is supposed to become tetragonal above x=0.7, and the calculation being made considering a cubic cell on in-plane measurements, the XRD calculations are just an indication of the unit-cell evolution.

These results show that the higher is the x concentration of Ba into the BST solid solution, the better is the epitaxial quality. At the same time, the lattice parameter tends to deviate more from the bulk value as x increases. This effect is certainly a consequence of the lattice mismatch between the MgO substrate and the grown BST-x film. For low mismatch (case of BTO) the epitaxial growth contains a low level of defects but with a lattice volume that is larger than the material bulk due to the presence of mismatch stress. In the case of higher mismatchs the growth contains a higher level of defects or even becomes polycrystalline (in the case of STO). The defects degrade the epitaxial quality of the film but relax the stress on the cell, ending up with lattice parameters closer to the one of the bulk.

2.4.4. Effect of substrate temperature

Substrate temperature is a crucial parameter in material growth dynamic; it directly controls the energy and mobility of the adatoms arriving on the substrate and hence has a direct impact on the crystallization process. Deposition temperature also plays a role on the level of thin film stress through the difference in thermal expansion coefficient between the substrate and the grown material. The higher is this difference, the higher will the induced thermal stress be as the sample cools down to room temperature.

Experimental conditions: In order to study the effect of deposition temperature, BST-0.6 thin films were deposited onto MgO single crystal substrates at different deposition

temperatures ranging from room temperature to 950 °C using a laser fluence of 1 J/cm^2 (110 mJ laser energy and 11mm^2 laser spot area), the oxygen pressure being maintained at 10 mTorr. After deposition, all the films were annealed in a furnace at 1050°C for period of 3 hours with O$_2$ background atmosphere.

Structural properties: XRD patterns of BST thin films deposited on MgO substrate (θ/2θ scan at grazing incidence) showed large microstructure differences across the range of temperature investigated. Below 700 °C, the resulting films are polycrystalline while at 750 °C the films are textured along the c-axis (with a small contribution of (111) peak in addition to the (100) X-ray reflections). For temperatures going from 800 °C to 950 °C, the XRD patterns show highly c-axis oriented films. These observations were confirmed by phi-scans that demonstrate an epitaxial growth of the films along the substrate crystal orientation.

Rocking curve measurements (ω-scan spectra for the (002) reflection of BST) were done on the textured and epitaxial films deposited on MgO. Fig. 2.21 shows these rocking curves for the different deposition temperatures investigated in the range going from 700 °C to 950 °C. It is clear on this figure that the deposition temperature has a major influence on the BST crystal quality, this one being optimal around 800-850 °C. Below or above this temperature there is a large broadening of the peak, revealing an increasing number of structural defects and/or misalignment of the crystallographic planes.

The full-width at half-maximum of the different peaks were measured and plotted as a function of the deposition temperature. The result is presented on Fig. 2.22 that also shows, in addition to the rocking curve FWHM, the corresponding BST Phi scan FWHM as a function of deposition temperature.
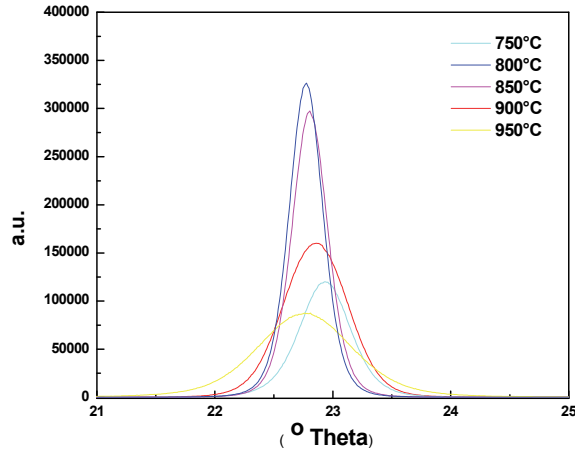
Figure 2.21: rocking curve (ω-scan) of BST thin films deposited on MgO substrate at deposition temperature 750, 800, 850, 900, and 950°C.
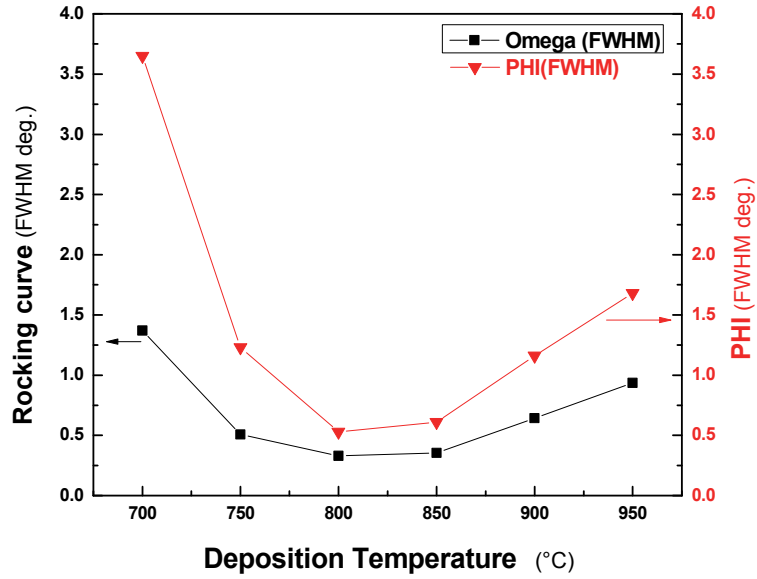
Figure 2.22: rocking curve (FWHM), and Phi scan (FWHM) of BST thin films deposited on MgO substrate as a function of deposition temperature.

This figure shows that, as the deposition temperature increases between 700°C to 800°C, both the rocking curve FWHM and Phi scan FWHM decrease from 1.37° and 3.65° to 0.33° and 0.53°, respectively, which indicate improvement in the BST structure

with increasing the deposition temperature. At 800°C, both the rocking curve and Phi scan FWHM reach a minimum (optimal value). Above 800°C and up to 950°C, both parameters increase up to 0.67°and 1.68° respectively for the rocking curve and Phi scan FWHM. This indicates that the quality of epitaxial structure is optimal around 800°C and degrades at higher or lower temperature.

Increasing the substrate temperature influences the surface mobility of the adatoms that will diffuse through several atomic distances before sticking to a stable position. The diffusion coefficient (D) is typically observed to depend on temperature as:

$$D = D_0 \, exp\left(\frac{-E_d}{KT}\right)$$ ....Eq. 2.6

Where, E_d is the activation energy for diffusion, k the Boltzmann's constant, T the absolute temperature, and D_0 is a temperature-independent factor that depends on the physical properties of the surface and of the particular materials involved.[59] At too high temperatures the adatoms will constantly move and re-evaporation of the elements could happen, this will induce the formation of vacancies that will degrade the quality of the epitaxial growth.

The optimum deposition temperature corresponds to system in which the surface diffusion is sufficient to allow the atoms to minimize their surface energy and to attain positions of thermodynamic stability.[62] As a consequence; there is always a critical temperature for epitaxial growth that requires a good control. In the case of the BST-0.6 epitaxial growth studied here, this temperature was found to be 800°C. This deposition temperature leads to FWHM value that are good and better than the previously reported value on BST thin film. [60]

The deposition temperature has also an impact on the lattice parameter of the BST films. Fig. 2.23 shows the variation of the lattice parameter (calculated from the XRD spectra) as a function of the deposition temperature. This curve presents a maximum corresponding to the transition temperature between polycrystalline and epitaxial films (750°C) whereas all the samples show lattice parameter values higher than the BST-0.6 bulk value (3.96 Å). Between room temperature and 750°C, the measured lattice parameter slowly increases up to 3.98 Å and then drastically decreases between 750°C and 850°C. There are two conditions where the lattice parameter difference between the thin film and the bulk value is minimal: the first one at room temperature, where the film

is completely polycrystalline, and the other one at 850°C, corresponding to a highly epitaxial film.
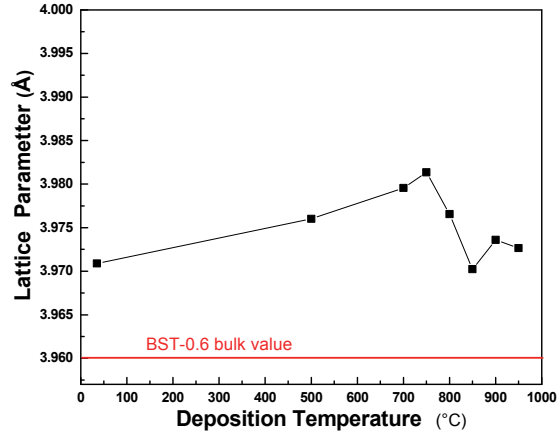
Figure 2.23: lattice parameter of BST thin films deposited on MgO substrate as a function of deposition temperature.

A larger lattice parameter could have different origins: the lattice mismatch between the film and the substrate, the presence of oxygen vacancies (that is known to increase the unit cell dimension) [61] and/or the expansion coefficient mismatch (the films being, in all cases, annealed at 1050°C in oxygen). What is observed here is certainly due to a combination of opposite effects coming from the thermal stress, which will increase as the deposition temperature increase, and the crystallization dynamic, which will be optimal at a given temperature.

2.4.5. Effect of oxygen background pressure

Oxygen background pressure is usually an influential parameter in multicomponent oxides growth by PLD.[62,63] In vacuum or low background pressures, the plasma expands freely. However, as the background pressure increases, an interpenetration of the background gas into the plasma plume takes place. Thus, energy and momentum exchange between the plasma plume and the interpenetrating background gas occurs via scattering, collisions, and charge exchange interactions, resulting in reduction in the effective deposition rate. However, this interaction is a complex dynamic process due to presence of several physical processes involved such as deceleration, attenuation, recombination of the ablated species, and formation of shock waves.

Experimental conditions: A series of BST-0.6 films were prepared with varied oxygen background pressure (10, 50, and 100 mTorr). All BST-0.6 films were deposited on MgO single crystal substrates by PLD, the laser fluence being 1 J/cm^2 (110 mJ laser energy and 11mm^2 laser spot area), and the substrate temperature was fixed at 700 °C. The deposition time was adjusted to obtain film thickness of 600 nm in all cases. After deposition, all films were annealed in O$_2$ background at 1050°C for 3h.

Zhu *et al.* [18] showed that the film deposited in absence of oxygen background pressure has higher lattice parameter and lower dielectric properties than other films deposited in presence of oxygen background pressure. So we started this study with a film grown at 10 mTorr, this is because oxygen background pressure compensates for the loss of oxygen in oxide films grown by PLD.

Structural properties: XRD patterns of BST thin films deposited on MgO substrate at 10, 50, and 100 mTorr showed that all films are single phase with a crystal structure going from textured to polycrystalline. Whereas the films grown at 50 and 100 mTorr are polycrystalline, the one deposited at 10 mTorr exhibits intense (100) diffraction peaks, with a very small (110) peak, suggesting that the film is textured along the (100) direction. It is also observed that the intensities of (100), (200) and (300) diffraction peaks increased as the background oxygen pressure decreases. Since film thicknesses are the same, this may indicate a higher degree of crystallization for lower deposition pressure.

The BST lattice parameters were extracted from these spectra, as reported in Table 2.3. In all case, the lattice parameter of BST-0.6 thin films grown on MgO substrate is larger than the lattice parameter of the bulk material (3.96 Å). The smaller difference compared to the bulk value is obtained for the film grown at higher oxygen pressure (100 mTorr) but its value is not significantly different from the other samples.

This shows that the deposition pressure has little influence on the lattice parameter. The main influence of the deposition pressure is on the crystal form of the film: as the deposition pressure increase, the growth mechanism goes from a texture film to polycrystalline and a lower degree of crystallization. This effect is directly related to the lower the energy of the atoms landing on the substrate surface as the pressure increases.

Table 2.3: **variation of lattice parameters and microstructure of the BST-0.6 thin films grown under different oxygen pressures.**

Oxygen pressure (mTorr)	structure	Lattice parameter (A°)
10	Nearly epitaxial	3.975
50	polycrystalline	3.976
100	polycrystalline	3.971

2.4.6. Effect of substrate material and orientation (MgO, LAO, Al_2O_3)

The choice of the substrate is important because the structural and dielectric properties of BST films may change significantly depending on the substrate used. Horwitz *et al.*[42] deposited BST onto $LaAlO_3$ and MgO substrates. They found that the structure and dielectric properties are strongly affected by the substrate material. Films deposited on MgO and annealed have usually better structural and microwave properties. They explained the observed difference in terms of film stress, arising from the lattice mismatch and the differences in the thermal expansion coefficient between the film and the substrate.

Experimental conditions: Two series of BST-0.6 films were deposited by PLD on different substrates (MgO, $LaAlO_3$ and Sapphire) and different MgO orientations ((100), (110) and (111)) using a laser repetition rate of 10 Hz, a laser fluence of 1 J/cm^2 (110 mJ laser energy and 11mm^2 laser spot area), and an oxygen pressure of 10 mTorr. The substrate temperature was set at 800 °C for MgO and $LaAlO_3$ single crystal substrates, 700°C for sapphire, and 500°C for alumina ceramic substrate (higher temperature yielding to film cracking on these substrates). After deposition, all the films were annealed in O_2 background at 1050°C for 3h.

2.4.6.a. Influence of the substrate material

MgO, LaAlO$_3$, and Sapphire are the most frequently used single crystal substrate in microwave application because their lattice parameters are close match to BST which enable epitaxial growth; they have also low permittivity and dielectric loss at microwave frequencies as shown in Table 2.1. Fig. 2.24a and 2.24b show respectively the XRD (θ–2θ) spectra of single phase BST-0.6 grown on LaAlO$_3$ (100) and sapphire (0001) substrates. The diffractogram for the film grown on alumina is shown on Fig. 2.25, whereas the one deposited on MgO (100) was presented earlier (Fig. 2.12). These figures show similar spectra for the films grown on MgO and LAO and a large difference for the one deposited on Sapphire. Film on LAO is single-phase without contribution of the (110) peak whereas the film deposited on Sapphire is highly oriented along the (111) direction. As shown on the left part of Fig. 2.24b, this orientation is due to the hexagonal structure of sapphire that creates a pseudo-cubic BST growth. As a comparison, BST-0.6 grown on polycrystalline alumina ceramic substrate is shown on Fig. 2.25. As expected, the obtained BST-0.6 is polycrystalline, with an XRD pattern (and peaks relative intensity) very close to the XRD powder standard.

These measurements were treated to extract the lattice parameter values, the results are shown on Table 2.4 together with the measured rocking curve FWHM (for epitaxial films). Again, this table shows that, except for the film deposited on LaAlO$_3$ (a = 3.962 Å), the films obtained on the different substrate exhibit lattice parameters larger than the bulk BST (3.960 Å). The rocking curves FWHM also shows better film quality for BST/LAO than BST/MgO films, with values of 0.273° and 0.33° respectively.
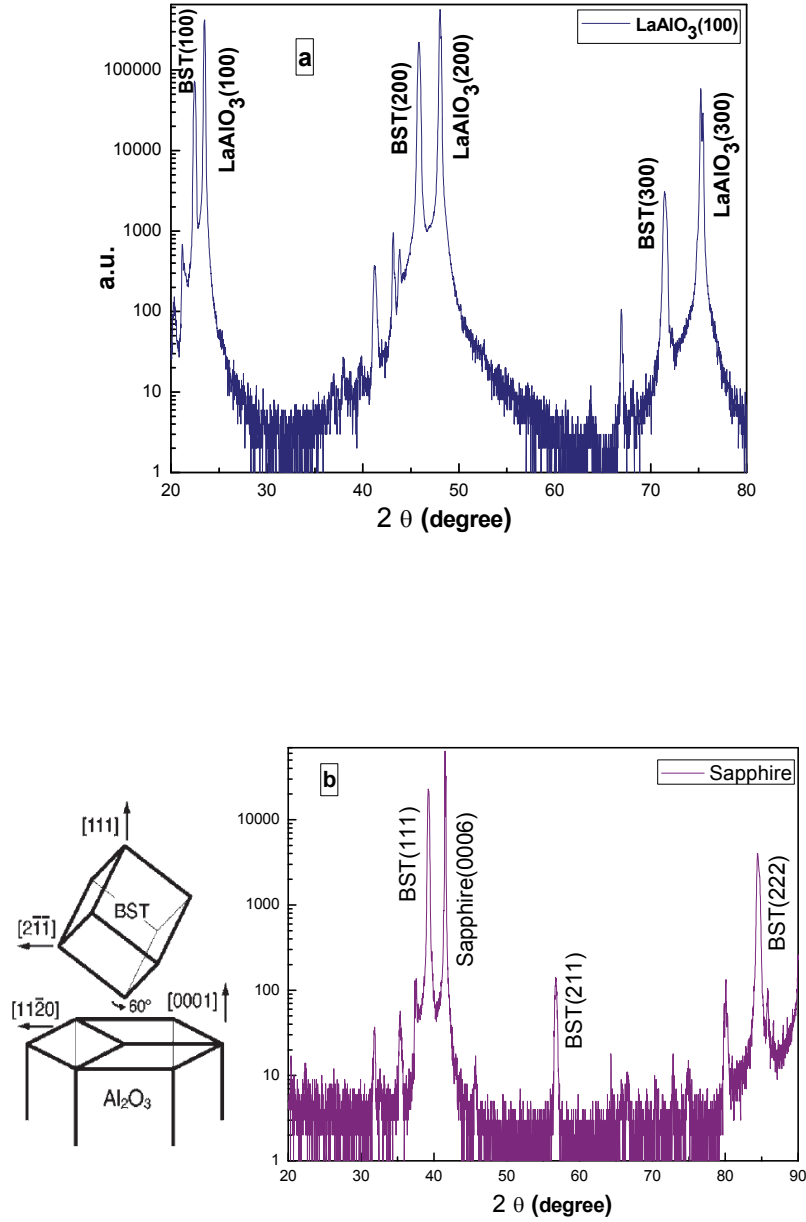
Figure 2.24: XRD (*θ–2θ*) spectra of, a.) BST-0.6 grown on LaAlO₃(100) substrate, and b.) BST-0.6 grown on Sapphire (0001) single crystal substrates. Also schematic diagram of the observed BST on Al₂O₃(0001).[64]
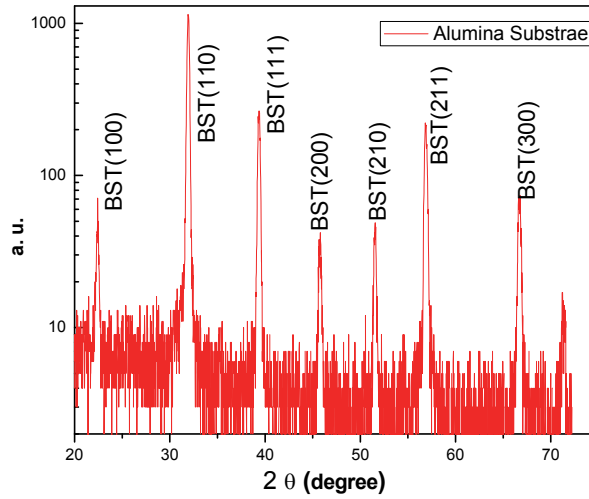
Figure 2.25: XRD (*θ–2θ*) of BST-0.6 grown on alumina substrate.

Table 2.4: Structural properties of BST-0.6 thin films grown on different substrate types (MgO), (LaAlO₃), (Sapphire), and (alumina).

Substrate	BST Lattice parameter (Å)	BST Structure	BST ω-scan FWHM (°)
MgO (100)	3.975	Nearly epitaxial	0.33
LaAlO₃ (100)	3.962	Epitaxial	0.273
Sapphire (0001)	3.972	Textured	-
Alumina (poly)	3.97	Poycrystalline	-

2.4.6.b. Influence of MgO substrate orientation

Fig. 2.26a and 2.26b show the XRD (θ–2θ) spectra of BST-0.6 deposited on MgO (110) and (111) single crystal substrate respectively, the film deposited on MgO (100) was previously reported on Fig. 2.8. These graphs show that films are epitaxial with no secondary orientation and that each film orientation matches the orientation of the substrate. Table 2.5 reports the lattice parameter of these films, extracted from the XRD

spectra, together with the rocking curve FWHM (measured from the (200), (220), and (222) peaks). These values show that the substrate orientation has little influence on the lattice parameter, this one being 3.976 Å, 3.972Å, and 3.975Å for the BST (100), (010) and (111) respectively, but plays an important role on the crystal quality, the ω-scan FWHM being 0.33°, 0.54°, 1.58° respectively.
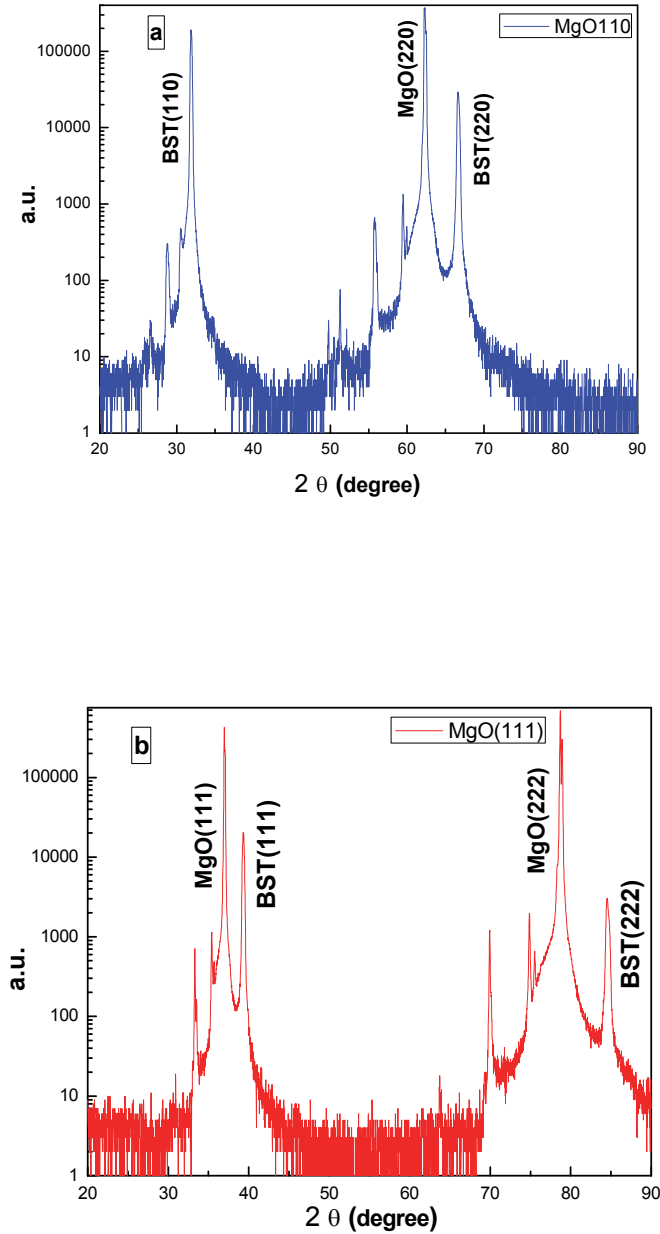
Figure 2.26: XRD (*θ–2θ*) spectra of a.) BST-0.6 grown on MgO (110) substrate, and b.) BST-0.6 grown on MgO (111) substrate.

Table 2.5: **Structural properties of BST-0.6 thin films grown on different MgO substrate orientation (100), (110), and (111).**

Substrate	Lattice parameter (Å)	Omega FWHM (°)
MgO(100)	3.976	0.33
MgO(110)	3.972	0.54
MgO(111)	3.975	1.58

These results show that the choice of substrate is affecting a lot the crystalline structure of the deposited thin films. Different crystal structure going from polycrystalline to epitaxial films can be obtained with very small changes in the lattice parameter of the film (except for the LAO substrate). For the different substrate orientation, the effect is quite the same but more subtle: the obtained film orientation is found to follow exactly the one of the substrate with a small degradation of the epitaxial quality going from (100) to (010) and (111) substrate (and thin film orientation).

Based on the results of chapter 2, Table 2.6. summarizes the optimum PLD conditions for epitaxial growth of BST thin film.

Table 2.6: **PLD conditions for epitaxial BST thin film.**

PLD Parameter	value
Laser repetition rate	10 Hz
Laser fluence	1 J/cm^2
Oxygen background pressure	10 mTorr
Deposition temperature	800°C
Target substrate distance	6.5 cm
Post annealing conditions	1050 °C for 3 hours.

Conclusion

In this chapter high quality BST thin films have been deposited by pulsed laser deposition (PLD) and conditions for obtaining BST epitaxial growth were determined. A large number of deposition parameters and their influence on the material crystallinity, stœchiometry and epitaxial quality were investigated.

First, the laser fluence was studied in details (using a parametric study, by varying the laser energy only, the laser spot area only or both parameters at the same time while keeping the laser fluence constant). This study demonstrates that for the BST epitaxial growth, the laser energy, spot size and fluence have an important impact on the BST microstructure. Films obtained with different fluence conditions goes from polycrystalline to epitaxial depending on the fluence. Among all the fluence conditions explored, the best deposition conditions found, in terms of film stœchiometry, lattice parameter value compared to the bulk and in terms of crystal quality of the films is a fluence around 1 J.cm^{-2} obtained with a 110 mJ laser energy and a 11 mm^2 laser spot size. In these conditions, the BST growth is epitaxial with an ω-scan FWHM of 0.56°, a (Ba+Sr)/Ti ratio close to one and a lattice parameter of 3.975 Å. For higher fluences, especially by increasing the laser energy, the crystallinity of the BST films degrades and the measured stœchiometry (measured through the ratio (Ba+Sr)/Ti) deviates from the BST-0.6 value. In the case of fluence increase through larger laser energies, an increase of the lattice parameter is also observed which can be correlated with the change in stœchiometry and related to cationic vacancies inside the crystal structure.

The influence of the laser repetition rate was also studied. It shows that the rocking curve FWHM and the lattice parameter both increase as the laser repetition rate increases, which indicates that the quality of epitaxial structure degrades with increasing the laser repetition rate. The best epitaxial films were obtained with a repetition rate of 2 Hz, but between 2 Hz and 10 Hz, in order to keep deposition rate reasonably high, this parameter was set at 10 Hz for further experiments.

Different Ba concentrations of $Ba_xSr_{1-x}TiO_3$ solid solution were deposited on MgO. The films obtained show that the higher is the x concentration of Ba into the BST target, the better is the epitaxial quality. At the same time, the lattice parameter tends to present a larger deviation from the bulk value as x increases. This effect is certainly a

consequence of the lattice mismatch between the MgO substrate and the grown BST-x film. For low mismatch (case of BTO) the epitaxial growth contains a low level of defects but with a larger lattice volume than the bulk material, due to the presence of mismatch stress. In the case of higher mismatch the growth contains a higher level of defects or become polycrystalline in the case of STO (x=0). These defects degrade the epitaxial quality of the film but relax the stress on the lattice, ending up with lattice parameters closer to the one of the bulk.

The effect of deposition temperature was found to have a large influence on the BST-x microstructure. The lattice parameter (calculated from the XRD spectra) as a function of the deposition temperature presents a maximum corresponding to the transition temperature between polycrystalline and epitaxial films (occurring around 750°C) whereas all the samples show lattice parameter values higher than the BST-0.6 bulk value. Between room temperature and 750°C, the measured lattice parameter slowly increases up to 3.98 Å and then drastically decreases between 750°C and 850°C. There are two conditions where the lattice parameter difference between the thin film and the bulk value is minimal: one at room temperature, where the film is completely polycrystalline, and the other one at 850°C, corresponding to a highly epitaxial film.

The influence of the oxygen pressure on the deposited film lattice parameter is not significant. The main influence of the pressure is appearing on the growth mechanism of the film: the higher is the pressure, the lower the energy of the atoms landing on the substrate surface. This causes the growth mechanism to go from textured to polycrystalline films and a lower degree of crystallization.

Finally, the choice of substrate was found to affect a lot the structural properties of the deposited films. Different substrates (MgO, LAO and Al_2O_3 Sapphire) and different MgO substrate orientation were used. It was found that film structure going from polycrystalline to epitaxial films can be obtained depending on the substrate, with very small change of the film lattice parameter (except for the LAO substrate). For the different MgO substrate orientation, the obtained film orientation is found to follow exactly the one of the substrate with a small degradation of the epitaxial quality going from (100) to (010) and (111) films.

The main objective of this thesis is to study the influence of the film microstructure on the microwave characteristics of the material. With all the deposition conditions explored

and all the different films obtained (polycrystalline, textured, epitaxial, different orientation and lattice parameters values), we have in hands a very broad range of BST-0.6 sample that can be used to study the influence of microstructure on microwave properties of these films. The result of this study is presented in the next chapter, where the microwave characterization of all these samples will be presented.

Chapter 3: Microwave characterization of BST thin films

Ferroelectric thin films are promising materials for monolithic microwave integrated circuits (MMIC). They can be used in tunable microwave devices, such as tunable resonators, filters, and phase shifters. The use of ferroelectrics has two main advantages: their tunability that is driven by the application of an electric field that allows fabricating voltage-controlled devices and their high dielectric constant that allows reducing the size of the devices. The development of such devices requires first the characterization of the ferroelectric thin films dielectric properties (i.e., the dielectric constant, tunability and the dielectric loss), to optimize the material properties for such applications and to improve the device design using the proper characteristics of the films.

The characterization of the dielectric constant and loss factor at low frequencies (in kHz or MHz range) can be directly obtained by measuring the capacitance of metal-insulator-metal capacitor structure. At microwave frequencies (in GHz range) these measurements are much more complex and require special methods and techniques. This chapter describes the measurement method that was used for the microwave characterization of BST thin films. All the deposited samples described in the previous chapter were characterized in the GHz range, their dielectric constant, dielectric losses, tunability and Figure of Merit will be presented.

3.1. Microwave domain

3.1.1. Waveguides / Devices [65]

The first microwave guiding structures used were rectangular waveguides. But, due to their cut-off frequency characteristic and the use of air as a medium, these guides have a narrow bandwidth and a large size. With the development of telecommunication systems, new components such as ridge waveguides and coaxial lines emerged, providing greater bandwidth and the possibility of miniaturization. Further development brought planar transmission lines (namely strip transmission line or Stripline), a concept that evolved over the years to allow higher operation frequencies and smaller size.

Fig. 3.1 presents the different types of planar transmission lines. Stripline, Microstrip Line, Suspended Stripline, Slotline, Coplanar Waveguide, and Finline, are all planar

transmission lines which consist of strip metallic conductors on a nonconducting substrate. These designs require three conductors where the middle conductor carrying the signal is commonly called the "hot conductor," while the other two, connected to the signal ground, are called "cold" or "ground" conductors. The hot conductor can be embedded in a homogeneous and isotropic dielectric or rely on a dielectric, surrounded by air. These coplanar structures present the advantage of being broadband while providing compact dimensions with light weight; they are readily adaptable to hybrid and monolithic integrated circuit fabrication technologies. Nowadays, the microstrip line and the coplanar waveguide (CPW) are the most used transmission lines.
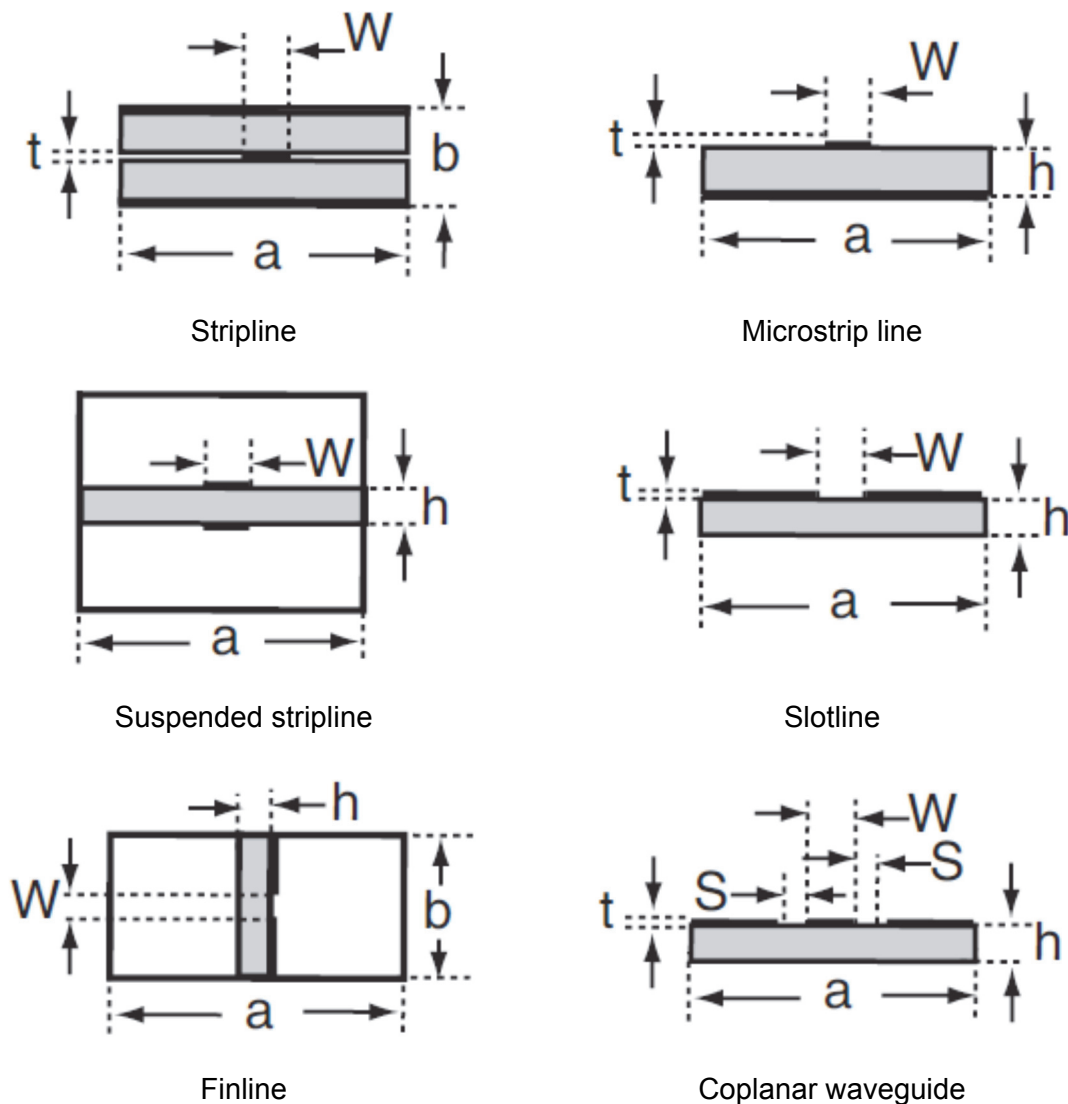
Figure 3.1 : **Commonly used types of planar transmission lines (the material is denoted by gray areas, and conductors and ground planes by bold lines.**

85

Microstrip line

Microstrip is the printed circuit version of a wire standing over a ground plane, and thus it tends to radiate as the spacing between the ground plane and the strip increases. Dispersion becomes more pronounced with the decreasing ratio of strip width W to substrate thickness h, W/h. Dispersion is less pronounced as the strip width becomes wider (as the Microstrip line physically starts to approach an ideal parallel-plate capacitor). Waveguides and Striplines have no radiation losses, while in Microstrip case (since the Microstrip is an open transmission line) radiation effects are present at any discontinuity section. For Microstrip using high dielectric materials and accurate conductor shape, conductor and dielectric losses are predominant compared to the radiation losses.

The Microstrip line is the most popular planar transmission line for RF and microwave circuits. This popularity and its widespread use are due to its planar nature, ease of fabrication using various processes, ease of integration with solid-state devices, good heat dispersion, and good mechanical support.

Coplanar Waveguide

Coplanar Waveguide (CPW) is an alternative to Microstrip and Stripline that consist of placing both the signal and grounds on the same layer. The conductors formed a center strip separated by a narrow gap from two larger ground planes placed on each side. The dimensions of the central strip, the gap, the thickness and permittivity of the dielectric substrate determine the effective dielectric constant, the characteristic impedance and the attenuation of the line.

The gap in the coplanar waveguide is usually very small and supports electric fields primarily concentrated in the dielectric. With little fringing field in the air space, the CPW is a printed circuit analog of the three-wire transmission lines. Like Stripline, CPW has two ground planes, which must be maintained at the same potential to prevent unwanted modes from propagating. Frequency dispersion is generally small for CPW, but there is a small dependence on line dimensions, and narrow lines are less frequency dispersive than wide lines. In addition, to avoid field radiation in the air, the use of high dielectric constant material thin films is a great advantage, in order to have the electromagnetic field mainly concentrated inside the dielectric.

In the context of this study where a high dielectric material (BST) is epitaxially grown on a dielectric substrate (MgO), the coplanar waveguide structure is preferred over the microstrip line structure.

3.1.2. Scattering parameters [66,67]

In telecommunications, waveguide components are described as "Networks" with "ports" corresponding to a certain number of inputs and outputs that connect the microwave circuit to external elements. In the context of network modelization, it is convenient to describe the incident and reflected waves using S-parameters (Scattering parameters) rather than voltages or currents. S-parameters are important in microwave design because they can be easily measured and can be used at high frequencies.
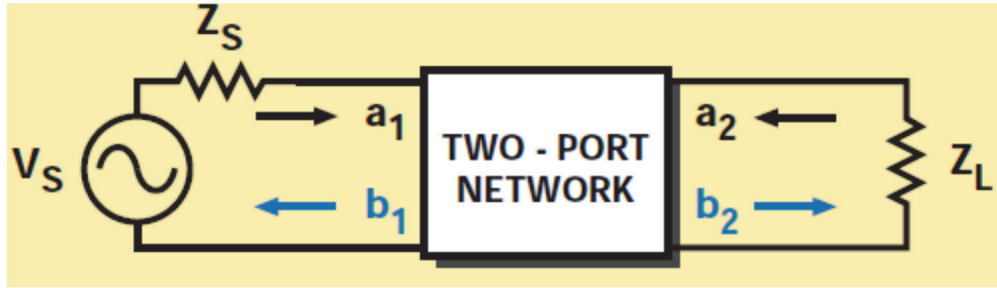
Figure 3.2: Two-port network showing incident waves (a1, a2) and reflected waves (b1, b2) used in s-parameter definitions. [67]

If one assumes a two-port network with ports connected to transmission lines as shown in Fig. 3.2, the complex voltage waves incident on and reflected from the ith port of the network are described by the normalized variables a_i and b_i. They are defined in terms of the terminal voltage V_i, the terminal current I_i, and an arbitrary reference impedance Z_i, where the asterisk denotes the complex conjugate:

$$a_i = \frac{V_i + Z_i I_i}{2\sqrt{|R_e(Z_i)|}} \quad and \quad b_i = \frac{V_i - Z_i^* I_i}{2\sqrt{|R_e(Z_i)|}} \quad \ldots\ldots\ldots\ldots\ldots\ldots\ldots Eq.3.1$$

For most of the measurements and calculations, the reference impedance Z_i is considered to be positive and real ($Z_i = Z_0$).

The independent variables a_1 and a_2 (appearing on Fig 3.2) are the normalized incident voltages, defined as follows:

$$a_1 = \frac{V_1 + I_1 Z_0}{2\sqrt{Z_0}} = \frac{voltage\ wave\ incident\ on\ port\ 1}{\sqrt{Z_0}} = \frac{V_{i1}}{\sqrt{Z_0}} \quad \text{.....................} \quad \text{Eq.3.2}$$

$$a_2 = \frac{V_2 + I_2 Z_0}{2\sqrt{Z_0}} = \frac{voltage\ wave\ incident\ on\ port\ 2}{\sqrt{Z_0}} = \frac{V_{i2}}{\sqrt{Z_0}} \quad \text{....................} \quad \text{Eq.3.3}$$

The variables b_1, and b_2, are the normalized reflected voltages, with:

$$b_1 = \frac{V_1 - I_1 Z_0}{2\sqrt{Z_0}} = \frac{voltage\ wave\ reflected\ on\ port\ 1}{\sqrt{Z_0}} = \frac{V_{r1}}{\sqrt{Z_0}} \quad \text{.....................} \quad \text{Eq.3.4}$$

$$b_2 = \frac{V_2 - I_2 Z_0}{2\sqrt{Z_0}} = \frac{voltage\ wave\ reflected\ on\ port\ 2}{\sqrt{Z_0}} = \frac{V_{r2}}{\sqrt{Z_0}} \quad \text{.....................} \quad \text{Eq.3.5}$$

The linear equations describing the two-port network are then:

$$b_1 = S_{11} a_1 + S_{12} a_2, \quad \text{.....................} \quad \text{Eq.3.6.a}$$

$$b_2 = S_{21} a_1 + S_{22} a_2 \text{..........................} \quad \text{Eq.3.6.b}$$

Where the S-parameters S_{11}, S_{22}, S_{21}, and S_{12} are:

$S_{11} = \frac{b_1}{a_1} \big|_{a2=0}$ =Input reflection coefficient with the output port terminated by a matched

load ($Z_L=Z_0$ sets $a_2=0$) Eq.3.7

$S_{22} = \frac{b_2}{a_2} \big|_{a1=0}$ =Output reflection coefficient with the input terminated by a matched

load ($Z_s=Z_0$ sets $a_1=0$) Eq.3.8

$S_{21} = \frac{b_2}{a_1} \big|_{a2=0}$ = Forward transmission (insertion) gain with the output port terminated

by a matched load. Eq.3.9

$S_{12} = \frac{b_1}{a_2} \big|_{a1=0}$ = Reverse transmission (insertion) gain with the input port terminated by

a matched load. Eq.3.10

Note that: $\quad S_{11} = \frac{b_1}{a_1} = \frac{\frac{V_1}{I_1} - Z_0}{\frac{V_1}{I_1} + Z_0} = \frac{Z_1 - Z_0}{Z_1 + Z_0} \quad$ Eq.3.11

Hence, $Z_1 = Z_0 \frac{(1+S_{11})}{(1-S_{11})}$, ... Eq.3.12

Where $Z_1 = \frac{V_1}{I_1}$ is the input impedance at port 1.

This relationship between the reflection coefficient and the impedance is the basis of the Smith Chart transmission-line calculator, widely used as a graphical representation of microwave measurements.

3.1.3. Material characterization parameters

When a microwave signal passes through a material it will interact in two ways, energy storage in the material (real part of the dielectric constant) and energy loss (imaginary part of dielectric constant).

$$[\varepsilon = \varepsilon' - j\varepsilon'']$$ ……………………………………………………......Eq.3.13

The dissipation factor, also called the loss tangent is defined as

$$\tan\delta = \varepsilon'' / \varepsilon'$$ …………………… Eq.3.14

For a ferroelectric, the tunability, corresponds to the percentage of variation of the dielectric constant for a given applied electric field

$$\Phi(E) = [\varepsilon(0) - \varepsilon(E)]/\varepsilon(0)$$ ……………………………………... Eq.3.15

Where, $\varepsilon(0)$ is the dielectric constant measured without electric field and $\varepsilon(E)$ is the one measured at the applied electric field E

The three dielectric characteristics are the most important in the design of microwave tunable devices, they will determine the geometry of the device and help to predict its performances in terms of signal attenuation and tunability as a function of the applied voltage. Tunability and attenuation being the two main concerns in the context of ferroelectric-based devices, the Figure-of-Merit (FOM) is often used to compare different films together. This parameter represents the trade-off between the tunability and the dielectric losses, and can be easily calculated from the measured $\Phi(E)$ and $\tan\delta$:

$$FOM(E) = \Phi(E) / \tan\delta(0)$$……………………………………………………… Eq.3.16

The microwave characterization of BST thin films requires a method able to accurately extract these thin film microwave characteristics (ε_r, $\tan\delta$, tunability and FOM) from the scattering parameters measurements of a co-planar waveguide (CPW) test structure.

3.2. Thin films characterization method

The CPW circuit on BST thin films, used to guide the microwave signal (illustrated on Fig. 3.3), will have a spacing between the ground planes and the signal line that is typically around 100 µm, in order to obtain a characteristic impedance as close as possible to 50 Ohms. This relatively large gap is not adapted to the application of a polarization voltage, since it will necessitate kV to change the BST dielectric constant.
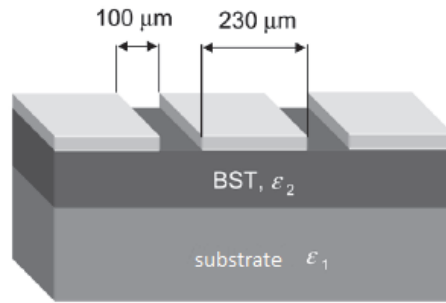
Figure 3.3: Schematic of coplanar waveguide (CPW) (side view).

3.2.1. MW characterization device and method

The BST thin film microwave device used in the BST thin film characterization method is a coplanar interdigital capacitor (IDC). The IDC method consists in measuring at high frequency (from 1 to 20GHz) the calibrated complex capacitance of IDC circuits as a function of an applied voltage. The complex dielectric constant is then extracted from these measurements using a conformal mapping method (CMM) in combination with the partial-capacitance technique (PCT), which provides closed-form formulas for the effective dielectric constant for a given device geometry. Analytical and numerical models were developed in our group to extract the dielectric constant and loss tangent of the ferroelectric thin film.[68,69,70] In this model, the S-parameters measurements can be linked to the intrinsic properties of the film for different applied voltages, which allow to calculate the dielectric tunability and Figure of Merit of the BST films.

The interdigital capacitor (IDC), shown on Fig. 3.4, is a structure where the spacing between the signal and the ground electrode can be reduced to few microns. It is an ideal structure for measuring the film dielectric response as a function of an electric field, since the variation of the capacitance (applied voltage divided by the electrode gap) is directly related to the dielectric constant.

The real and the imaginary parts of the capacitance can be obtained from the S-parameter measurement of the IDC, with the following relation:

$$C_{re} = \frac{1}{2\pi f Z_0} \frac{2\,Im\,\{S_{11}\}}{(1+Re\{S_{11}\})^2+(Im\,\{S_{11}\})^2} \dots\dots\dots \text{Eq.3.17}$$

$$C_{im} = \frac{1}{2\pi f Z_0} \frac{(Re\{S_{11}\})^2+(Im\,\{S_{11}\})^2-1}{(1+Re\{S_{11}\})^2+(Im\,\{S_{11}\})^2} \dots\dots\dots \text{Eq.3.18}$$

The conformal mapping method (CMM) is used to evaluate closed form expressions for computation of IDC capacitances. The calculation is based on the partial capacitance technique (PCT) and takes into account the capacitance between the fingers and the fringing capacitance of the finger ends.[71]
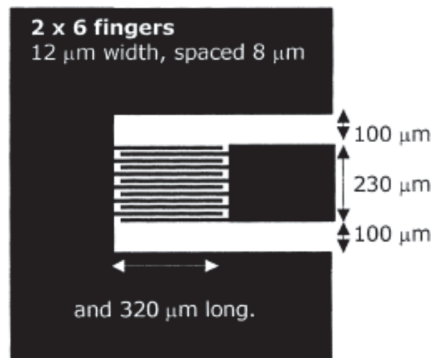
Figure 3.4: Schematic of coplanar interdigital capacitor (IDC) (top view).

91
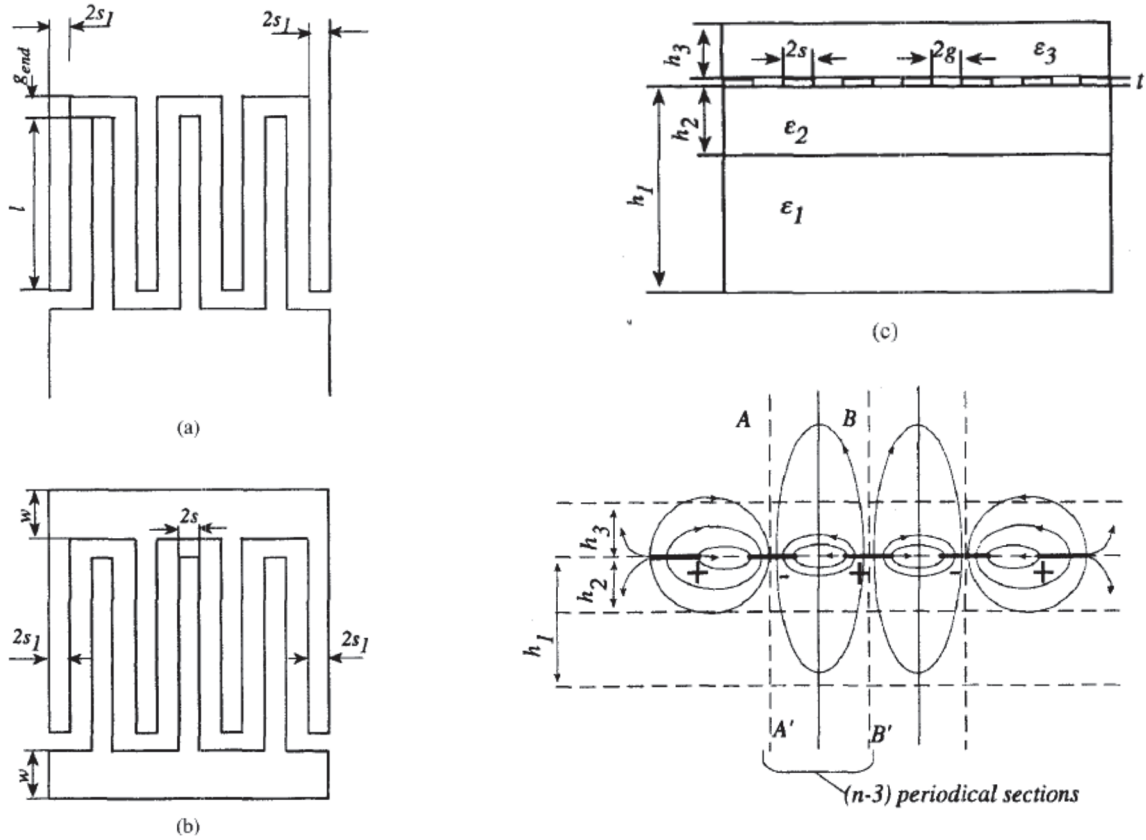
Figure 3.5: a) b) and c) Top and side view of the IDC; d) microwave electric field distribution in IDC.[71]

The total capacitance as decomposed by applying the PCT is:

$$C = C_3 + C_n + C_{end} \ldots\ldots\ldots\ldots \text{Eq.3.19}$$

where n is the total number of fingers of the IDC, C_3, and C_n are respectively the partial capacitance associated with groups of three and of (n-3) fingers, C_{end} is the end to end finger capacitance.

Fig 3.4 and 3.5 show the schematic of the structure and the physical dimensions used in the equations. The capacitance C_n can be represented by:

$$C_n = (n-3)\varepsilon_0\varepsilon_{en}\frac{K(k_0)}{K(k_0')}l \ldots\ldots\ldots\ldots \text{Eq.3.20}$$

where,

$$\varepsilon_{en} = 1 + q_{1n}(\varepsilon_{r1} - 1) + q_{2n}(\varepsilon_{r2} - \varepsilon_{r1})\ldots\ldots\ldots\ldots \text{Eq.3.21}$$

92

$$q_{in} = \frac{1}{2}\frac{K(k_{in})}{K(k'_{in})}\frac{K(k'_0)}{K(k_0)}, \text{ for i = 1 (substrate), 2 (thin film).} \ldots\ldots\ldots \text{Eq.3.22}$$

$$k_0 = \frac{S}{S+g} \ldots\ldots\ldots \text{eq.3.23}$$

$$k_{in} = \frac{\sinh\left(\pi S/2h_i\right)}{\sinh\left[\pi(S+g)/2h_i\right]}\sqrt{\frac{\cosh^2\left[\frac{\pi(S+g)}{2h_i}\right]+\sinh^2\left[\frac{\pi(S+g)}{2h_i}\right]}{\cosh^2\left[\frac{\pi S}{2h_i}\right]+\sinh^2\left[\frac{\pi(S+g)}{2h_i}\right]}}, \text{ for i= 1, 2.} \ldots\ldots\ldots \text{Eq.3.24}$$

$$k' = \sqrt{1-k^2}\ldots\ldots\ldots \text{Eq.3.25}$$

$$C_3 = 4\varepsilon_0\varepsilon_{e3}\frac{K(k_{03})}{K(k'_{03})}l \ldots\ldots\ldots \text{Eq.26}$$

where, $\varepsilon_{e3} = 1 + q_{13}(\varepsilon_{r1}-1) + q_{23}(\varepsilon_{r2}-\varepsilon_{r1})\ldots\ldots\ldots$ Eq.3.27

$$q_{i3} = \frac{1}{2}\frac{K(k_{i3})}{K(k'_{i3})}\frac{K(k'_{03})}{K(k_{03})} \text{ for i = 1, 2.} \ldots\ldots\ldots \text{Eq.3.28}$$

$$k_{03} = \frac{S}{S+g}\sqrt{\frac{1-\left(\frac{(S+2g)}{(S+2S_1+2g)}\right)^2}{1-\left(\frac{S}{(S+2S_1+2g)}\right)^2}} \ldots\ldots\ldots \text{Eq.3.29}$$

$$k_{i3} = \frac{\sinh\left(\pi S/2h_i\right)}{\sinh\left[\pi(S+g)/2h_i\right]}\sqrt{\frac{1-\frac{\sinh^2[\pi(S+g/2h_i)]}{\sinh^2[\pi(S+2S_1+2g/2h_i)]}}{1-\frac{\sinh^2[\pi S/2h_i]}{\sinh^2[\pi(S+2S_1+2g/2h_i)]}}}\ldots\ldots\ldots \text{Eq.3.30}$$

$$k'_{i3} = \sqrt{1-k_{i3}^2}\ldots\ldots\ldots \text{Eq.3.31}$$

The end capacitance of n fingers is expressed as:

$$C_{end} = 4ns(2+\pi)\varepsilon_0\varepsilon_{eend}\frac{K(k_{0end})}{K(k'_{0end})}\ldots\ldots\ldots \text{Eq.3.32}$$

where $\varepsilon_{eend} = 1 + q_{1end}(\varepsilon_{r1}-1) + q_{2end}(\varepsilon_{r2}-\varepsilon_{r1})\ldots\ldots\ldots$ Eq.3.33

with $q_{iend} = \frac{1}{2}\frac{K(k_{iend})}{K(k'_{iend})}\frac{K(k'_{0end})}{K(k_{0end})}$ for i = 1, 2. $\ldots\ldots\ldots$ Eq.3.34

$$k_{0end} = \frac{x}{x+2g_{end}}\sqrt{\frac{1-\left(\frac{(x+2g_{end})}{(x+\xi+2g_{end})}\right)^2}{1-\left(\frac{x}{(x+\xi+2g_{end})}\right)^2}} \ldots\ldots\ldots \text{Eq.3.35}$$

In this equation ξ is the terminal length and x is the effective width of the finger end (considered as x=s/2)

$$k_{iend} = \frac{\sinh\left(\pi x/2h_i\right)}{\sinh\left[\pi(x+g_{end})/2h_i\right]} \quad \ldots\ldots\ldots\ldots \text{Eq.3.36}$$

$$k'_{iend} = \sqrt{1 - k^2_{iend}} \ldots\ldots\ldots\ldots \text{Eq.3.37}$$

The effect of the conductor thickness t is considering an effective finger width such as:

$$2s = 2s_g + \frac{t}{\pi}\left[1 + ln\left(\frac{8\pi s_g}{t}\right)\right] \quad \ldots\ldots\ldots\ldots \text{Eq.3.38}$$

where $2s_g$ is the physical dimension of the finger width.

With these equations and knowing the physical dimensions of the IDC and the dielectric characteristics of the substrate, it is hence possible to extract ε_{r2}, the complex dielectric constant of the BST thin film, from the measured C_{eff}. If C_{eff} is measured at different voltages, the dielectric constant and loss can be obtained as a function of the applied electric field and the tunability can be calculated.

3.2.2. MW devices fabrication

In order to perform the dielectric characterization of the BST thin films, CPW calibration circuit and IDC test devices are patterned on BST/MgO samples using photolithography and the lift-off technique. Photolithography is a micro-fabrication process used to transfer a pattern onto a photoresist, with an exposition to UV radiation through a mask. In the case of a positive tone photoresist, the exposed resist is dissolved onto a chemical developer and open areas of the mask are thus transferred as trenches onto the resist. After the photolithography step, as presented on Fig. 3.6, metal is deposited on the trenches of the photoresist (and on top of the patterned photoresist) such that, as the photoresist is removed, the metal left forms the coplanar metallic electrodes according to the pattern design appearing on the photomask. This process of patterning electrodes on top of the substrate is called lift-off.
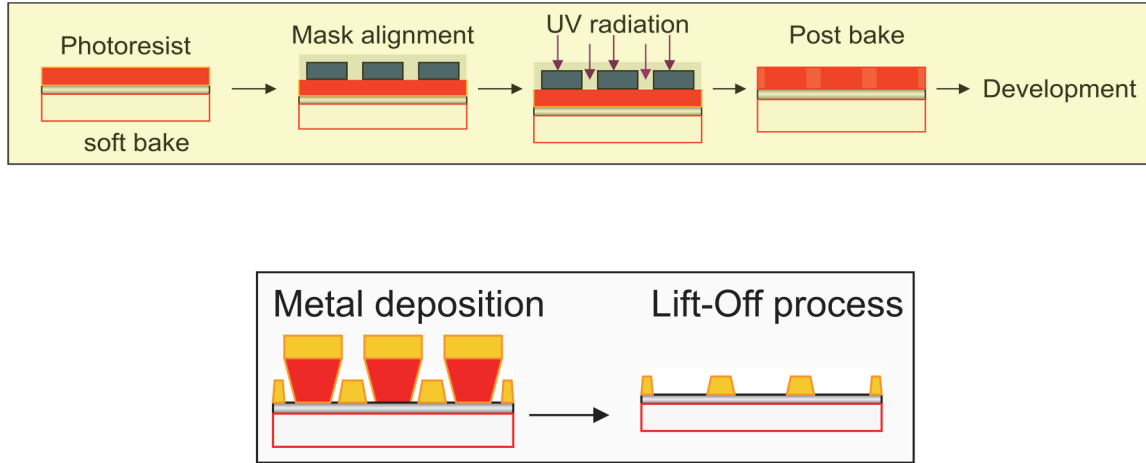
Figure 3.6: Description of the photolithography steps used to fabricate CPW devices on BST/MgO samples.

In the context of microwave measurements, the ohmic losses are function of the "skin effect". In order to decrease the ohmic losses on microwave devices, one must use electrode thickness larger than the skin depth, given by the following equation:

$$d = c\sqrt{\frac{\varepsilon_0}{\pi\sigma f}} \text{ ..... Eq.3.39}$$

where σ is the electrode conductivity and f is the frequency.

For instance, copper electrode ($\sigma = 5.8\times10^7$ [$\Omega^{-1}.m^{-1}$]) have a skin depth of ~2 μm at 1 GHz, which decreases as the frequency increases.

This relatively large electrode thickness required (~2 μm) and the need for small metallic gaps between the finger electrodes of IDCs devices in order to optimize the electric field for a given voltage (typically of few microns) is challenging in terms of micro-fabrication. The photolithography as to be perfectly controlled in order to obtain vertical sidewall on the patterned resist and special care is needed for metal evaporation and the lift-off process in order to obtain high-quality electrodes with high aspect-ratio.

3.2.2a Photolithography process optimization

In order to obtain the proper resist profiles for lift-off, optimization of the UV energy, development time and contact mode was done for the thick photoresist used (SPR220-7

95

from Shipley), the exposition being made on a mask aligner (model EVG 620) using a test pattern of lines with different width.
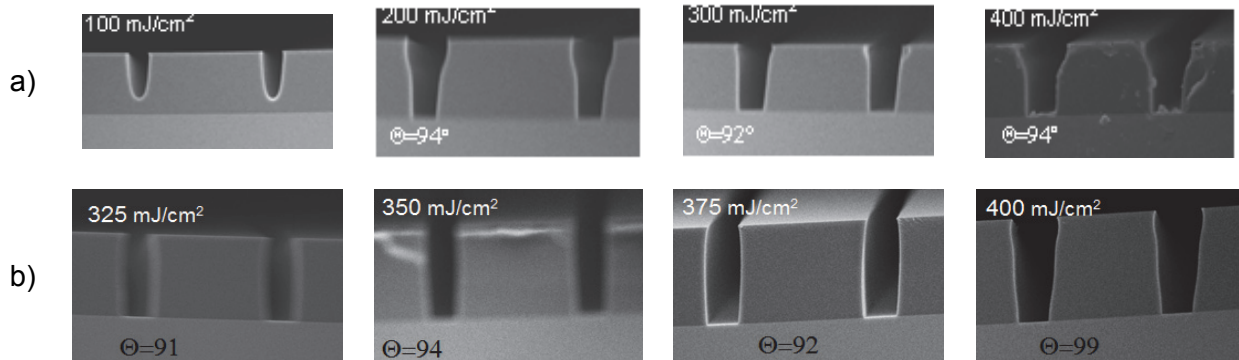
Figure 3.7: Cross section SEM images of SPR220 resist profile exposed with different energy density a) (100, 200, 300 and 400 mJ/cm^2) using hard contact mode and developed for 55s and b) (325, 350, 375 and 400 mJ/cm^2) using vacuum contact mode and developed for 60 sec.

Figure 3.8: Cross section SEM images of SPR220 resist profiles exposed at 300 mJ/cm^2 and developed with different times (40, 50, 55 and 65 s).

Fig.3.7a shows the SEM images of 2 μm width lines exposed into SPR220 resist with an increasing energy density (from 100 to 400 mJ/cm^2) and a fixed development time of 55 sec. The Fig.3.7b shows the same type of characterization but on a smaller energy density range and with a different contact mode on the mask aligner (instead of having the mask mechanically pushed on the surface in the case of the "hard contact" mode, it is pressed by pumping down the air gap between the mask and the resist sample in the case of the "vacuum contact" mode). The measured sidewall angle Θ (angle between the side wall of the photoresist and the bottom of the trench) is indicated on each picture. These SEM images show, first, that the contact mode has a great influence on the resist profile. As "hard contact" mode certainly leaves some space between the resist and the mask that induces larger opening at the top of the profile. Vacuum contact mode creates resist profiles with a curved shape and a slightly smaller opening at the top of the features that is much more adapted to the lift-off process. This figure also shows that for a given development time, there is an energy density range where the resist profile is optimal (between 300 and 375 mJ/cm^2 for a 60 sec development time).

96

The Fig.3.8 shows SEM images of 2 µm width lines exposed at a fixed energy density of 300 mJ/cm^2 and using increasing development times (from 40 to 65 sec). It shows that at 40 sec, the resist development is not completed and above 50sec and up to 65 sec there is no significant change in the resist profile. This proves that the SPR220 resist used as a great process latitude and is perfectly adapted for the fabrication of metallic electrodes in the context of this project.

3.2.2b Microfabrication process

For CPW device patterning on BST samples deposited on MgO, the mask contact being crucial, a first mask was used to clear the resist on the borders of the 1 inch square sample prior to the electrode pattern lithography in order to improve the contact of the mask with the resist surface. The photomasks used for the lithography were prepared using a laser-writer (DWL-66fs from Heidelberg) and etched in a high density plasma etcher using a $Cl_2/O_2/He$ chemistry. The optimized photolithography process used is as follow:

1. The first step consist of cleaning the samples into three consecutive solutions (acetone, isopropanol and methanol) using an ultrasonic bath for 5 minutes to remove organic and solvent traces from the surface. The samples are subsequently blown with nitrogen and dehydrate on a hot plate for 2 minutes at 115°C.
2. An adhesion promoter (HMDS) is spin-coated on the samples prior to the spin-coating of a 6 µm thick positive photoresist layer (SPR220 from Shipley) at 5000 rpm for 30 sec.
3. The resist is soft baked on a hot plate at 115°C for 90 seconds, to eliminate the resist solvents. The resulting resist thickness is 6 µm.
4. The coated samples are then exposed with UV-light at 325 mJ/cm^2 on a mask aligner (model EVG-620) through a photomask. After UV-exposure, the samples are kept on hold for 40 minutes, to avoid the formation of bubbles during the post-bake process.
5. The post-bake allow water (which is necessary to complete the photo-reaction) to diffuse back into the photoresist film. It is done on a hot plate at 115 °C for 90 seconds.

6. The resist development is done in MF-319 (a TMAH based developer), for 55 seconds. Immediately after the pattern development, the samples are rinsed in water to stop the reaction and are dried with a nitrogen gun.
7. Patterns are inspected using an optical microscope.

Finally, the metallization and lift off processes is performed on the optimum photoresist profile.

The metallization is done using an e-beam evaporation system (model AXXIS from Kurt J. Lesker) and three consecutive metal layers deposition that form a 2 μm thick metal electrode. The base pressure of the system being 5×10^{-7} Torr, the metal is heated and evaporated to condense on a rotating sample holder and forms a uniform metal layer. The metal electrode is composed by 50 nm Titanium at the bottom (that acts as an adhesive layer) and a consecutive 1.9 μm thick Copper layer that compose the electrode (Cu was chosen because of its high conductivity of $5.8 \ 10^7$ S/m at 20°C). In order to prevent the oxidation of copper and improve the contact of the measurement probes on the CPW circuit, a 50 nm top layer of Gold layer is used. The total thickness of the metal is 2 μm which is 3 times lower that the thickness of the photoresist in order to facilitate the lift off process.

The samples covered with the metals (Ti - Cu - Au) is immersed into 1165 remover heated at 40°C for few hours in order to remove the photoresist and the excess of metal. Ultrasonics at low power can be used during this step to help the detachment of metallic foils from the substrate. The samples are then rinsed in DI water, dried with N_2, and inspected under an optical microscope. Fig 3.9 shows examples of the different IDC circuits (with gaps from 3 μm to 12 μm on the same sample) fabricated using this process. The Fig 3.10 shows a detailed view of the smaller IDC gap of 3 μm observed under a scanning electron microscope. These pictures show a perfect definition of the electrodes for all the dimensions. The SEM observation proves that the 2 μm thick electrode has a very smooth surface and no defects on the electrode fringe (that could induce electric field non uniformity or even arcs during the microwave measurements under an applied voltage).
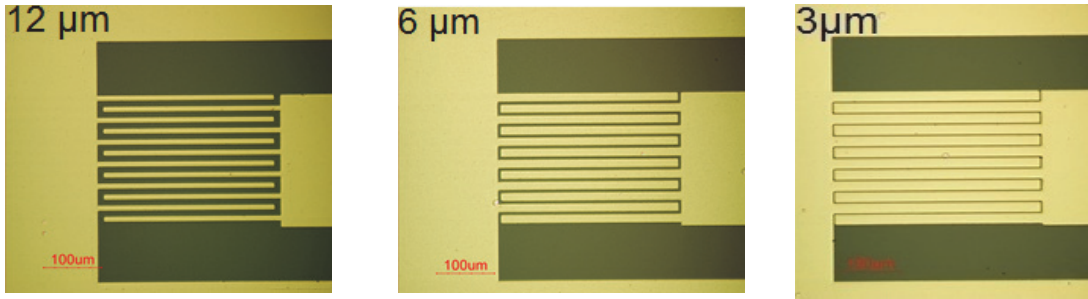
Figure 3.9: Optical microscope image of IDC circuits with different gaps of 3, 6 and 12 μm fabricated on a BST/MgO sample.
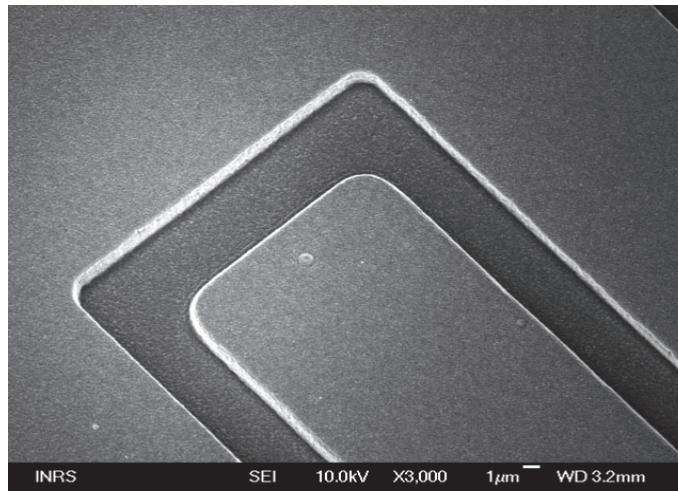
Figure 3.10: SEM image of a 2 μm thick IDC finger with a 3 μm gap fabricated by lift-off on top of a BST thin film.

3.2.3. MW diagnostic calibration

The measurement method used for the determination of the permittivity and loss tangent of dielectric thin films involves three steps: first calibration of the Vector Network Analyzer (VNA) using CPW circuits patterned on the sample, the measurements of the scattering parameter on test circuits (IDCs) and then the thin film dielectric permittivity and loss tangent computation using appropriate models.

TRL calibration

For the microwave characterization the devices must be tested on a probe station (Summit 9000 Cascade from Microtech) using microprobes with a ground/signal/ground

99

(GSG) configuration, connected to the VNA (Vector Network Analyzer, model HP8510C) through coaxial cables. A CCD camera and a monitor are used to accurately position the measurement probes on the devices using micropositioners acting in the x, y and z directions. The measurements are subject to systematic errors mainly due to match, directivity, cross talk, and frequency response errors that can be corrected by a proper calibration.[72] In particular, in the case of the IDC measurements, in order to obtain a precise measurement of the capacitances, the effect of the measurement lines has to be eliminated up to the entrance of the IDC fingers. The calibration method used here is the Thru-Reflect-Line (TRL) method,[73] accomplished by measuring a set of reference circuits that can be easily designed, fabricated, and characterized.

The Fig.3.11 shows the configuration of the three standard circuits used for the TRL calibration:

- a line of length l (Thru)
- an open circuit (Reflect) of length l/2 and
- a line of length (l + $\lambda_g/$ 4) (Line) where, λ_g (electrical length) corresponds to $\lambda_g = c/(f\sqrt{\varepsilon_{eff}})$.

Ideally, since λ_g depend on the ε_{eff} of the device to be characterized, it should be calculated for each sample using a value that is the one that we are looking for. Moreover, the CPW impedance has to be as close as possible to 50 Ohms, a characteristic that also depend on the BST/MgO ε_{eff} and the CPW geometry. In order to overcome this difficulty, both the length difference and CPW geometry were chosen according to an average BST dielectric constant of 700 and a central operating frequency of 10 GHz. The calibration being valid upon a great range around the right value, this choice guarantee the calibration to be valid for large variations of the BST dielectric constant (that has a smaller impact on the ε_{eff}), and can be even used to accurately measure the dielectric constant of the substrate itself.
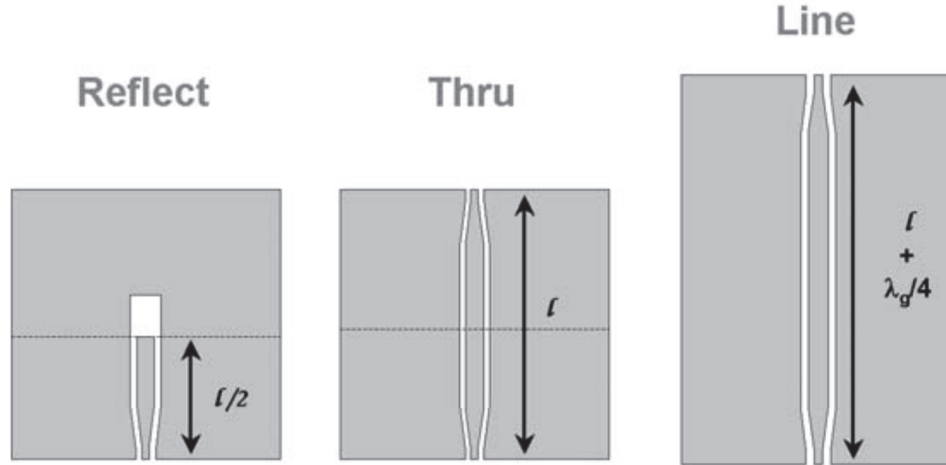
Figure 3.11: the patterns for TRL calibration (thru, reflect, and line).

For all the measurements, the Thru, Reflect and Line devices (with W=230 µm, S=100 µm and $\lambda_g/4$= 3 mm) are patterned on the samples and use as a calibration kit for each of them. Measurements are done and calibrated with an HP 8510C network analyzer. The calibrated measurements of IDCs (single port reflection coefficient S_{11}) are measured at different dc bias ranging from 0V to 40 V and are saved for future data analysis using the IDC method (measurement of the dielectric constant and loss tangent as a function of the applied voltage).

3.2.4. IDC Microwave characterization of BST thin film

As a detailed example, the set of BST thin films deposited at different laser repetition rate (2, 20, 50 Hz) presented in the section 2.4.2 was characterized using the IDC microwave diagnostics. The results are presented in details in order to show the diagnostic capabilities and limitations.

a. Frequency characteristics

Fig 3.12 shows the real and imaginary parts of the 3 µm gap IDC capacitance, calculated from the S_{11} parameter measurements performed on the different BST samples. Fig 3.13 shows the dielectric constants and losses as a function of frequency, extracted from the C(f) measurements using the IDC model (based on CMM and PCT).

101
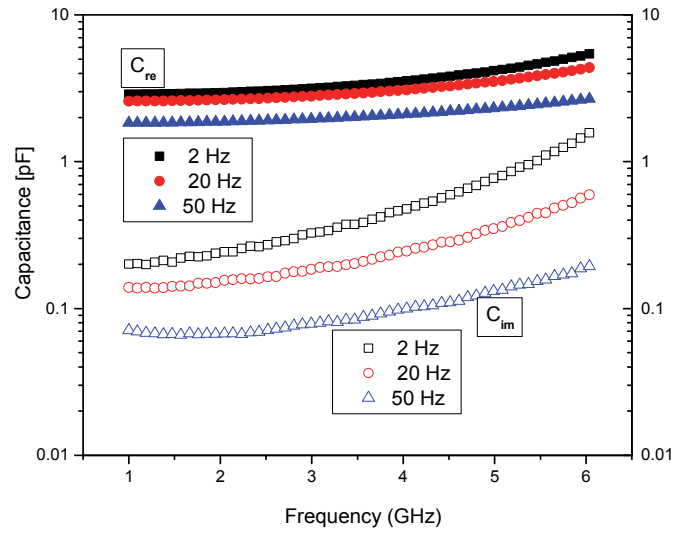
Figure 3.12: real and imaginary capacitance of IDC as a function of frequency and laser repetition rates, at zero bias.
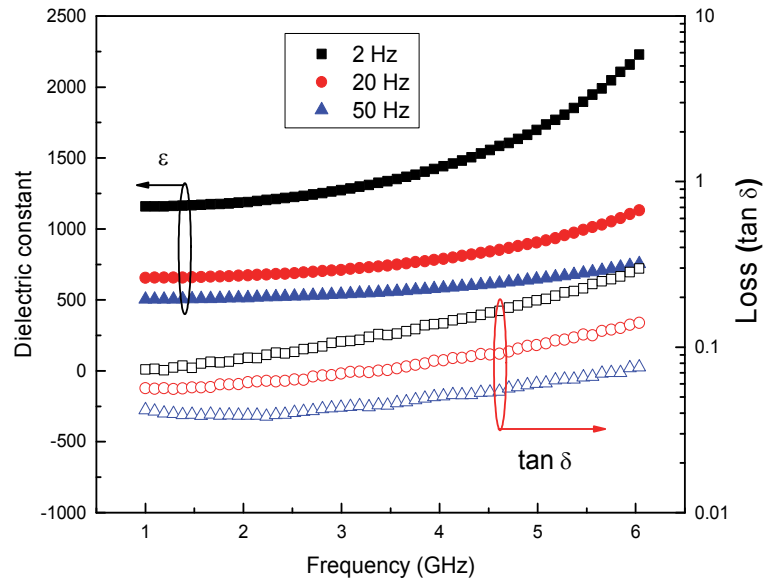
Figure 3.13: dielectric constant and the BST Loss tangent as function of frequency for different laser repetition rates, at zero bias voltage.

The dielectric constant and loss tangent being directly related to the real and imaginary parts of the capacitance, there is a close relation between the variations of ε_r and C_{re} ($\tan\delta$ and C_{im}) as a function of the frequency. The capacitance values show an increase as a function of the frequency that is related to a resonance of the IDC circuit at about 7-8 GHz (corresponding to $\lambda_g/4$ and inversely proportional to ε_{eff}). Hence the apparent increase in the dielectric constant and dielectric loss of BST, extracted from the capacitance values, is only an artifact of the measurements. This is the reason why this diagnostic is only relevant around 2-3 GHz and below, i.e. far enough from the capacitance resonance to be able consider it as a quasi-static case.

Between the different samples (2, 20 and 50 Hz laser repetition rate) without applied voltage, the dielectric constant is decreasing from 1160 to 660 and 550. At the same time, the dielectric losses of the film are decreasing from 0.07 to 0.055 and 0.04. These variations can be related to the change in the cristallinity of the material going from epitaxial to polycristalline as the laser repetition rate increases. It proves that the IDC diagnostic is capable of measuring the dielectric characteristics of the BST films over large range of variation in the dielectric constant and losses. Different IDC geometries are fabricated on each sample with different electrodes gaps, the extracted dielectric constant and loss values are consistent from on geometry to the other.

b. MW properties as a function of the applied voltage

Fig 3.14 shows the extracted dielectric constant and loss tangent as a function of frequency at 0 and 40 V applied voltage for the film deposited at 20 Hz laser repetition rate. This figure shows a large effect of the applied voltage on the measured parameters: the dielectric constant at 2 GHz decreases from 660 at 0V to 290 at 40V whereas the dielectric losses go from 0.055 to 0.045. The capacitance being measured at different voltages, the tunability can be easily plotted as a function of the applied voltage, as presented on the Fig. 3.15. This figure indicates that the tunability variation is the same for the 1 and 3 GHz measurements whereas the values obtained at 6 GHz are higher. Again, this effect is an artifact of the measurement due to the resonance of the IDC capacitance.

Different IDC circuits are fabricated on the same sample with IDC gaps of 3, 4, 8 and 10 μm. In order to compare the different tunability, the extracted measurements as a function of the applied voltage have to be converted to the applied electric field. The result of the different measurements (at 2 GHz) is shown on Fig 3.16. One can note that there is a very similar trend of the tunability as a function of the electric field for the different IDC gaps: it increases almost linearly up to 3 V. μm^{-1} and then tends to reach saturation for higher electric fields. Obviously, for a given range of applied voltages (here from 0 to 40 V, limited by the VNA), the accessible range of electric field increases as the gap decreases. Electric fields as high as 13.3 V. μm^{-1} (133 kV.cm^{-1}) can be applied on the BST film without breakdown with the 3 μm gap configuration whereas the applied field for the larger gap (10 μm) is limited to 4 V. μm^{-1}. For a given electric field, the measured tunability shows some discrepancy that may have different origins. First, the error on the gap size has more incidences on the effective electric field for smaller gaps. Secondly, the area (or volume) of material exposed to an electric field decreases as the gap decreases and the field distribution is also affected which may change the accuracy of the capacitance simulation by Conformal Mapping Method (that is used to extract the dielectric constant from the capacitance measurement) and under-estimate the dielectric constant.
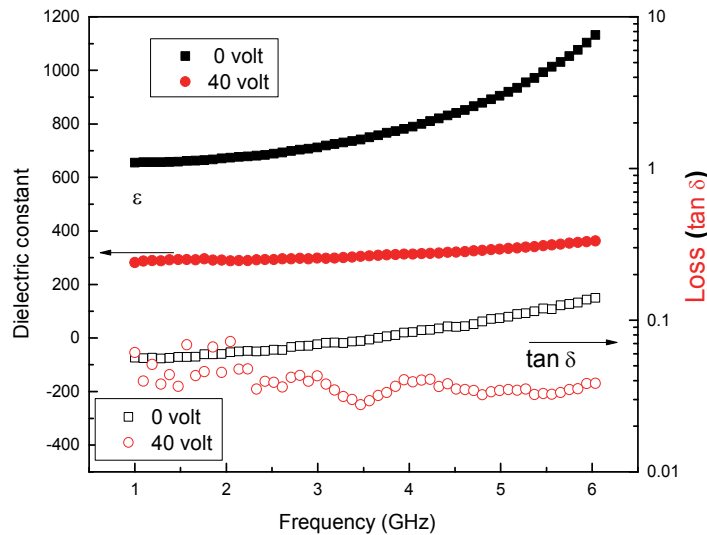
Figure 3.14: BST dielectric constant and Loss tangent of IDC as function of frequency, and applied voltages of 0 and 40 V.
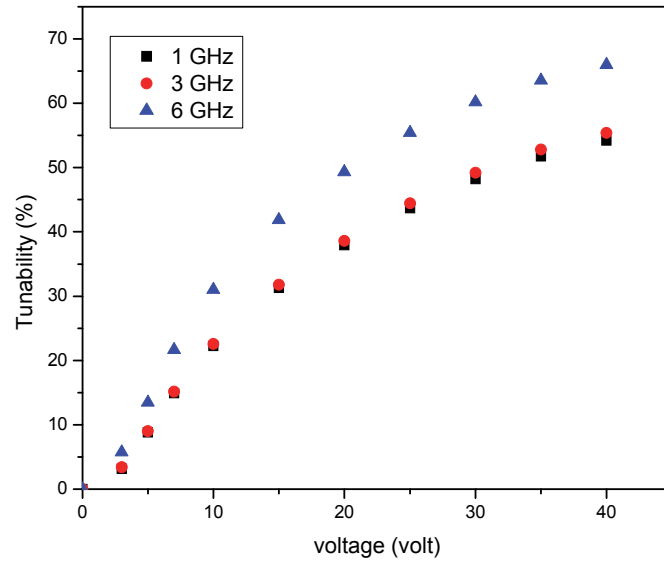
Figure 3.15: Calculated tunability as a function of the applied voltages at different frequencies (1, 3, 6 GHZ), for a BST film deposited at 20 Hz laser repetition rate and an IDC with 3 μm gap.
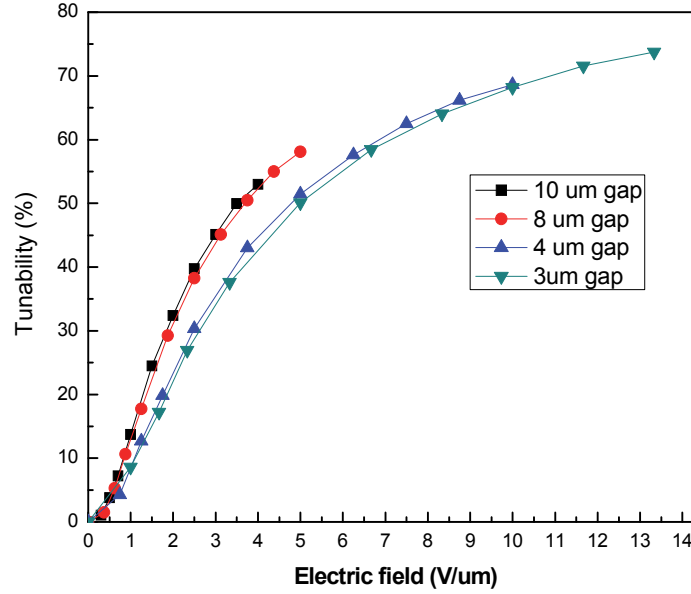
Figure 3.16: Tunability (measured at 2 GHz) as a function of the applied electric field for IDC circuits fabricated on the same BST sample with different gaps (3, 4, 8, 10 μm).

All this considered, the measured tunability at 4 V. µm^{-1} varies only from 53% to 44% depending on the gap size which gives a good indication of the error bars that should be associated with these measurements.

3.3. PLD parameters optimization (MW properties)

The circuit fabrication and the microwave characterization process being well established, all the samples presented in the section 2.4 will be analyzed in order to find a correlation between the structural and electrical characteristics of the material.

3.3.1. Effect of the Laser fluence

3.3.1.a. Varying the laser spot area
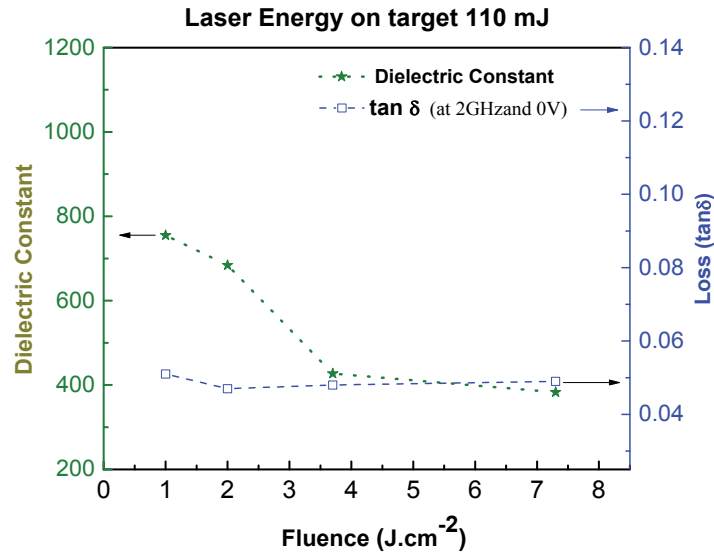
Figure 3.17: Dielectric constant and loss tangent (at 2GHz and 0V) as a function of the laser fluence at constant laser energy.

Fig.3.17 shows the dielectric constant and loss tangent (at 2 GHz and 0 V) as a function of the laser fluence, the fluence being varied by varying the laser spot area. Fig.3.18 shows the calculated tunability and Figure of Merit (at 2 GHz and 10 V.µm^{-1}) as a

function of the laser fluence. While the loss tangent does not show significant change with increasing laser fluence, being around 0.05 for all conditions, the dielectric constant shows a large increase as the fluence decrease from 7.5 to 1 J.cm^{-2}. The tunability and the FOM shows the same behavior, both being maximum at the lowest fluence, 49% and 9.6 respectively, and decreasing down to 26% and 5.3 respectively at 7.5 J/cm^2.
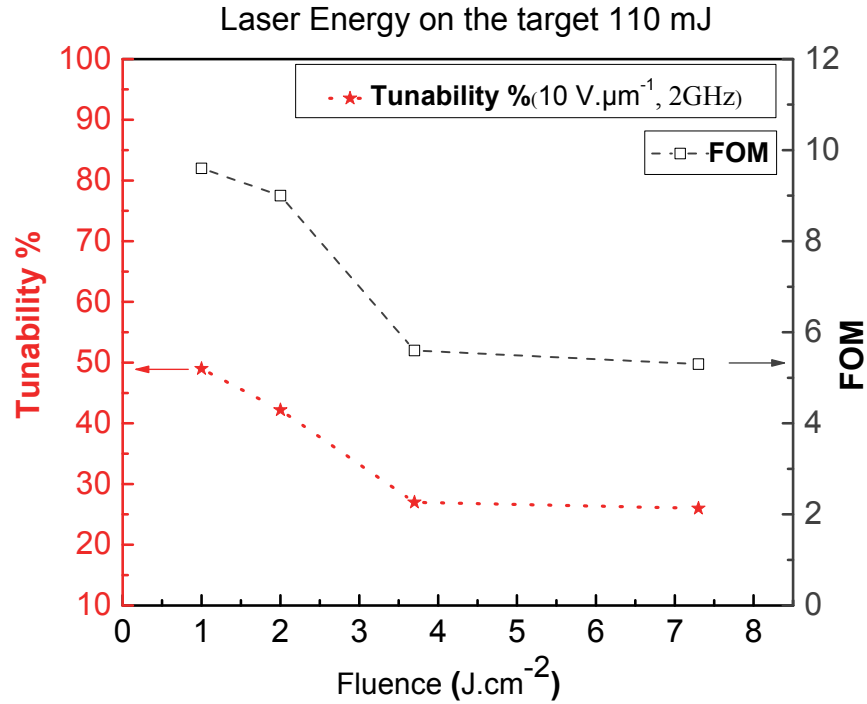
Figure 3.18: Tunability (at 2GHz, 10 V.µm^{-1}) and FOM as a function of the laser fluence at constant laser energy.

3.3.1.b. Varying the laser energy

Fig.3.19 shows the dielectric constant and loss tangent (at 2 GHz and no applied voltage) as a function of the laser fluence at constant spot size. As observed at constant laser energy, the dielectric constant decreases with increasing the laser fluence while the loss tangent only slightly increases as the laser fluence increases. Fig. 3.20 shows the tunability (at 2 GHz and 10 V.µm^{-1}) and the calculated FOM as a function of laser

fluence. Both parameters decrease from 49 % and 9.6 to 15% and 2.5 respectively with increasing the laser fluence from 1 to 4 J/cm^2.
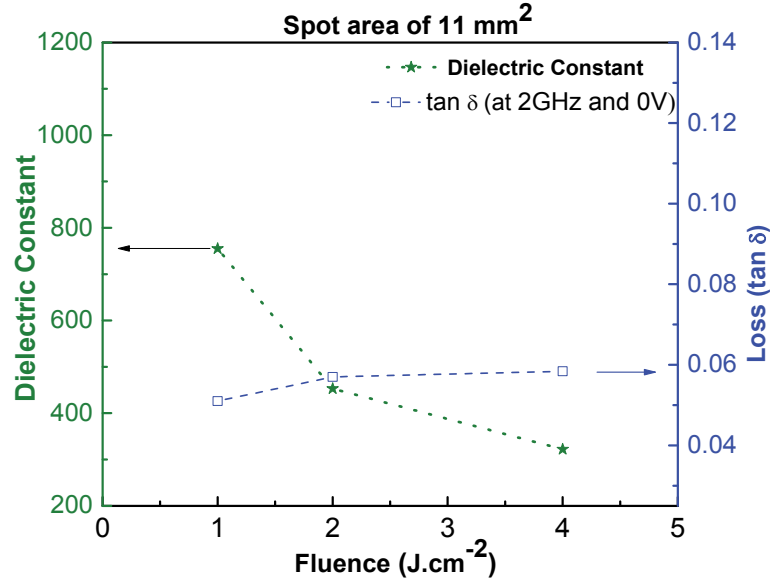
Figure 3.19: Dielectric constant and loss tangent (at 2 GHz, 0 V.μm^{-1}) as a function of the laser fluence at constant spot size.
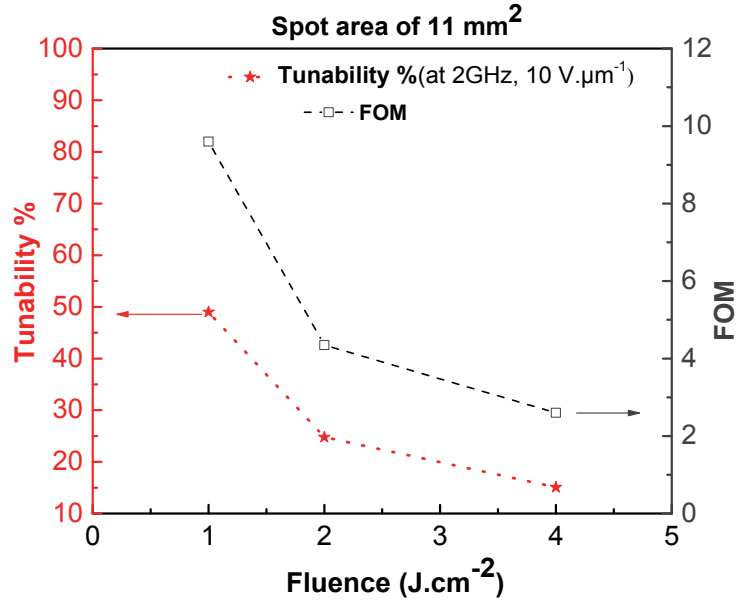
Figure 3.20: Tunability (at 2 GHz, 10 V.μm^{-1}) and FOM as a function of the laser fluence at constant spot size.

3.3.1.c. Constant laser fluence (1 J/cm^2)

The last experiment on laser fluence was done at fixed laser fluence (of 1 J/cm^2) while both the laser spot area and laser energy are varied. Fig. 3.21 shows the influence of the laser energy/spot size on the loss tangent (measured at 2GHz and no applied voltage) and the tunability (measured at 2 GHz and 10 V.μm^{-1}). The corresponding FOM is indicated on the figure for each condition. This figure demonstrates that the specific values of laser energy and spot size used to obtain a certain laser fluence are of great importance for the dielectric characteristics of the films. The tunability and FOM present a maximum value of 50% and 9.6 respectively for the film that is deposited with a 110 mJ laser energy and 11 mm^2 spot size. The films deposited at high energy (and large spot size) exhibit a comparable dielectric loss (of 0.05) but with a much smaller tunability (of 20%). The one deposited at small spot size (and lower energy) show smaller dielectric loss (of 0.04) and a much lower tunability (of 15%). This result in a comparable Figure of Merit for the two extreme conditions, with a value around 4, which is two times less than the maximum.
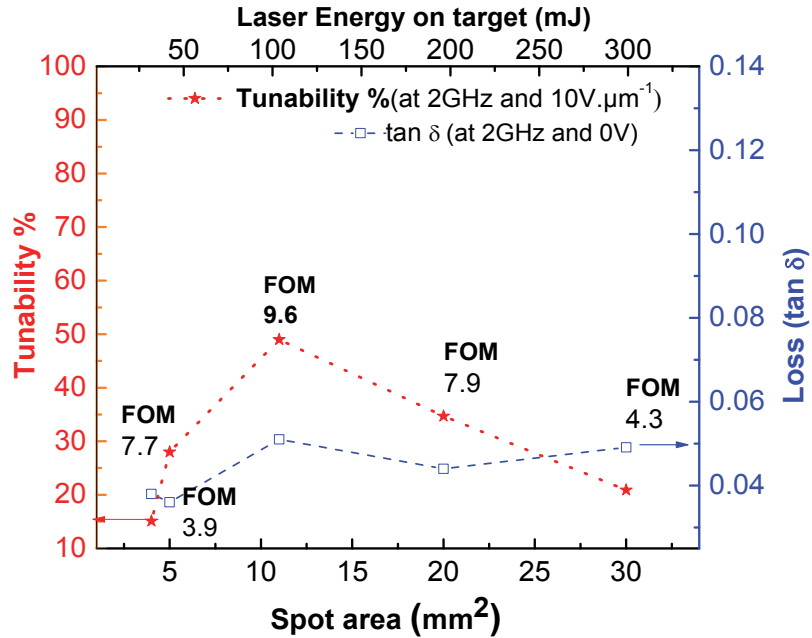
Figure 3.21: The tunability%, loss and FOM at 2GHz as a function of the laser (spot size, energy) values keeping the laser fluence at 1 J/cm^2.

Since the main influence of the laser fluence on the structural characteristics is on the lattice parameter (section 2.4.1.a), these results suggest that the BST dielectric constant and tunability are closely related to the lattice parameter of the material. For all the laser fluence conditions explored, it is observed that the closer is the material lattice parameter to the one of the bulk material, the higher are the dielectric constant and tunability. The highest tunability and Figure of Merit are obtained for BST thin films deposited with a low fluence (1 J/cm^2) obtained with a laser spot area of 11 mm^2. This film exactly corresponds to the one that posses the lattice parameter closer to the bulk value.

There is no clear correlation for the dielectric loss, it is only observed that losses are generally higher for high tunabilities. It is also interesting to note that the lowest dielectric losses are not obtained for the film presenting the best crystallinity or the closer lattice parameter to the bulk, but for the film obtained with the smallest spot size.

3.3.2. Effect of Laser Repetition Rate

This section reports the microwave measurements of the films obtained at different laser repetition rate, deposition condition are the one presented in the section 2.4.2 (these results were partially exposed during the microwave dielectric characterization method, section 3.2.4). Fig.3.22 shows the measured dielectric constant and loss tangent (at 2 GHz, 0 V.µm^{-1}) as a function of the laser repetition rate. Fig.3.23 shows the tunability and FOM measured at 2 Ghz, and 10 V.µm^{-1}. It appears clearly on these figure that as the laser repetition rate increases from 2 Hz to 50 Hz, the dielectric constant decreases from 1200 to 515 and the tunability decreases from 72.5% to 32.5%. At the same time, the loss tangent decreases almost linearly from 0.08 to 0.039. Since the tunability only slightly decreases between 2 and 10 Hz, the FOM is maximum at 10 Hz with a value of 10.1.

If we compare these results with the structural characteristics of the samples (Fig. 2.22.b), it shows again a correlation between the lattice parameter and both the dielectric constant and tunability: the closer the BST lattice parameter from the bulk value, the higher are ε_r and $\Phi(E)$. For the dielectric losses, they seem to decrease as the crystal quality decrease.
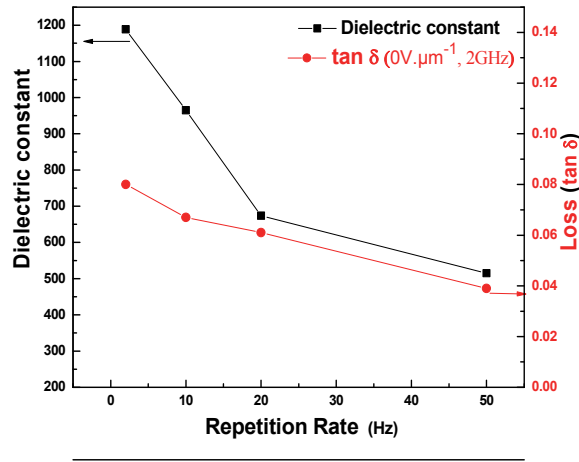
Figure 3.22: Dielectric constant and loss tangent (at 2 GHz, 0 V) as a function of the laser repetition rate.
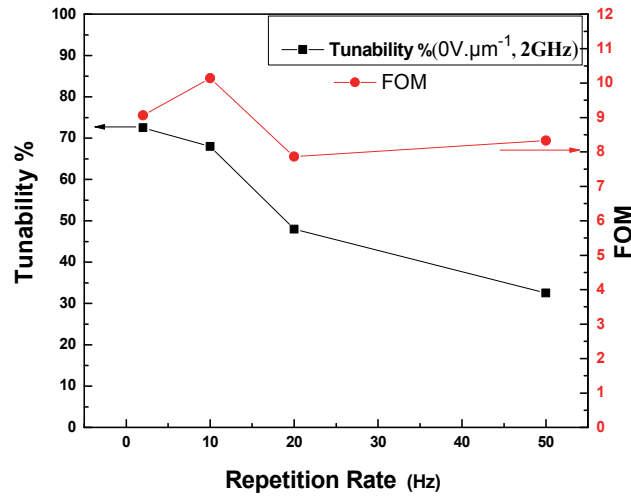
Figure 3.23: Tunability (at 2 GHz and 10 V.µm^{-1}) and FOM as a function of the laser repetition rate.

3.3.3. Effect of BST-x Composition (x=0, 0.3, 0.5, 0.6, 0.7, 1)

Different PLD targets were used to obtain BST-x films with composition going from x=0 to 1, the deposition condition being the one presented in the section 2.4.3. Fig. 3.24 shows the dielectric constant and loss tangent (both measured at 2 GHz and 0 V.µm^{-1}) of these films: BTO, BST-0.7, BST-0.6, BST-0.5, BST-0.3, and STO. One can see on this figure that both dielectric constant and loss tangent are minimum at x=0 (STO, with

respective values of 250 and 0.017) and present a maximum as a function of the film composition. Whereas the dielectric constant is maximum for x=0.6 (ε_r of 965) and decreases down to 600 for x=1, the dielectric losses are maximum for x=0.7 and remain about the same at x=1 (tanδ of 0.11).
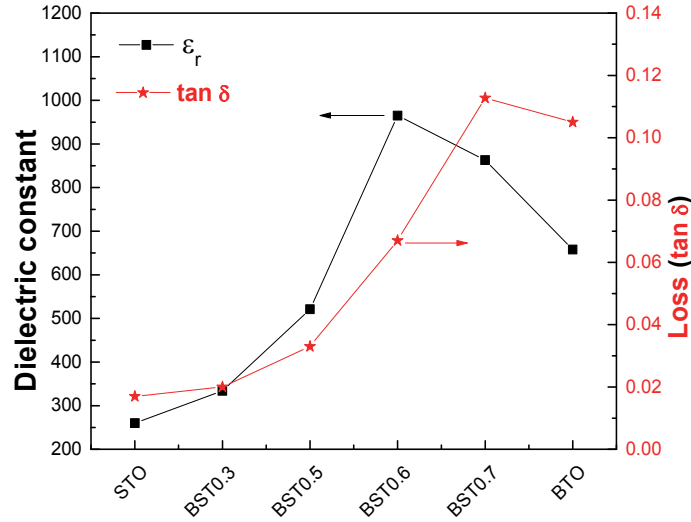
Figure 3.24: Dielectric constant (at 2 GHz, 0 V.µm^{-1}) and loss tangent (at 2 GHz, 0 V.µm^{-1}) of BTO, BST-0.7, BST-0.6, BST-0.5, BST-0.3, and STO thin films grown on MgO substrate.

Fig. 3.25 shows the tunability and the calculated Figure of Merit (at 2 GHz and 0 V.µm^{-1}) for the same films. It is observed that the tunability increases from 3% for STO to 68% for BST-0.6 and remains about the same for BST-0.7 and BTO (60 and 69% respectively). Since the loss tangent drastically increases between x=0 and x=0.7, the FOM presents a maximum of 10 for the composition x=0.6. For STO, the dielectric losses are very low but the tunability is also very low, resulting in a poor Figure of Merit of 1.6. For high concentration of barium, both the tunability and losses are high, resulting also in a low Figure of Merit (of 5.3 and 6.5 respectively for BST-0.7 and BTO).

It is well known that ferroelectric phase present a high level of dielectric loss at room temperature, hence the ferroelectric nature of BST-0.7 and BTO films could be responsible for the degradation of the Figure of Merit for these two compositions. The very high FOM value for BST-0.6 indicates that its Curie temperature is certainly, as expected, very close to room temperature (BST-0.6 has a Curie temperature of 5 °C, and is expected to be in the paraelectric state at room temperature).[74,75,76] Being close to

the dielectric maximum, the dielectric constant and its variation are maximum for this composition.
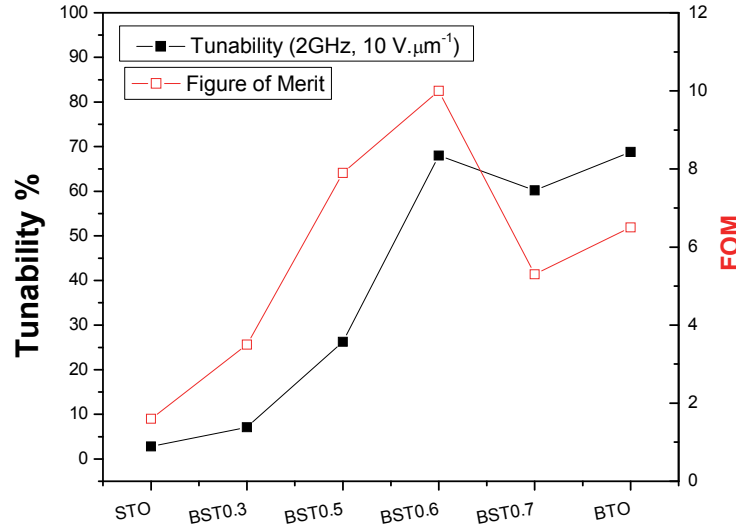
Figure 3.25: Tunability (at 2 GHz, 10 V.µm^{-1}) and Figure of Merit (FOM) of (BTO, BST-0.7, BST-0.6, BST-0.5, BST-0.3, and STO) thin films grown on MgO substrate.

These results indicate that the optimum BST-x / MgO thin film composition for microwave application is the composition x= 0.6 (Ba$_{0.6}$Sr$_{0.4}$Ti O$_3$), which exhibits the highest dielectric constant (ε_r =965), tunability (68%), and FOM (10). However, the loss tangent is still relatively high (0.067) and needs to be improved for microwave applications.

3.3.4. Effect of substrate temperature

Fig. 3.26.a and 3.26b show the dielectric constant, loss tangent (at 2 GHz, 0 V.µm^{-1}), tunability (at 2 GHz, 10 V.µm^{-1}), and FOM of BST-0.6 thin films as a function of the deposition temperature. On the first one (Fig. 3.26.a), it appears that the dielectric constant and loss have almost the same behavior with the temperature: both parameters being minimum and almost constant (ε_r = 500-600 and tanδ = 0.02-0.03) up to 700°C deposition temperature. Between 750 and 950°C deposition temperature, a

clear peak is observed in both the dielectric constant and loss tangent at 850°C, having respective values of 1075 and 0.075.

Fig. 3.26.b shows that this temperature dependence is almost the same for the tunability. Films deposited at temperatures lower than 700°C, exhibit tunabilities lower than 30%, and 850°C corresponds to an optimal deposition temperature for the film tunability that reaches a value as high as 70.5% (at 2 GHz and 10 V.μm^{-1}). From 850 to 900°C, the tunability falls down to 55%.
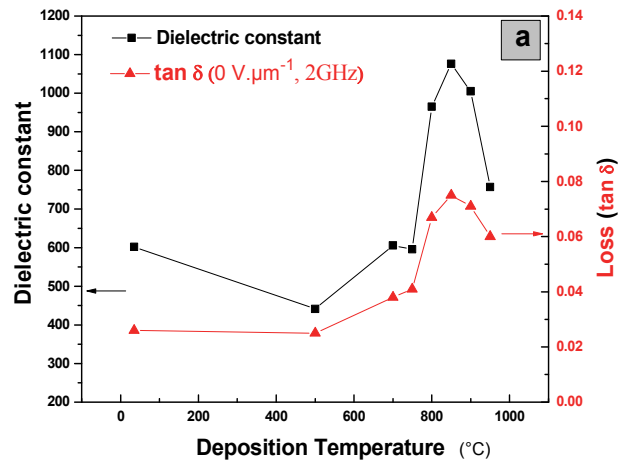
Figure 3.26.a: dielectric properties of BST-0.6 thin film, dielectric constant and loss tangent (at 2 GHz, 0 V.μm^{-1}) as a function of deposition temperature.
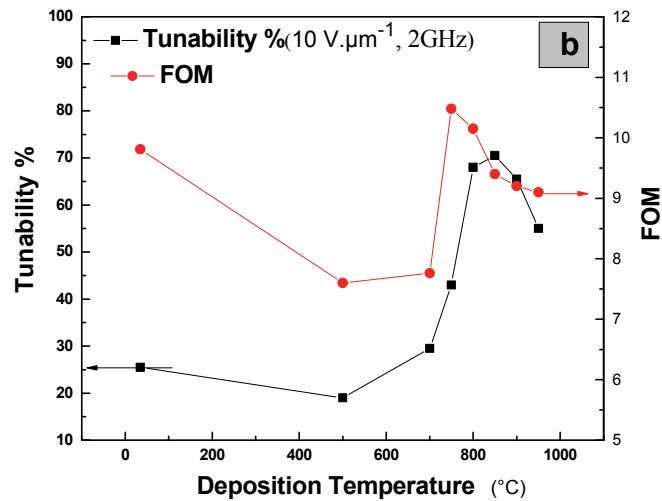
Figure 3.26.b: Tunability (at 2 GHz, 10 V.μm^{-1}) and FOM as a function of deposition temperature.

Looking to the FOM values variation on the same figure, it appears that the optimal deposition temperature for microwave application is around 750-800°C rather than 850°C: this corresponds to lower tunability values but with dielectric losses of 0.04 (compared to 0.075 for the maximum tunability at 850°C). Interestingly, there is another condition where the FOM reaches a value close to 10, it is the film deposited at room temperature that has a relatively low tunability (around 25% at 2 GHz and 10 V.μm^{-1}) but with the lowest dielectric losses (of 0.025).

Putting in parallel the microwave and structural characteristics of the films (presented on Fig. 2.22 and 2.23) highlights again the relation between the crystal structure and the film tunability. On one hand, the maximum tunability (of ~70%) is obtained for the two conditions leading to the best epitaxial quality. Between the two conditions (800 and 850°C), the best overall properties are obtained for the film having the lattice parameter closest to the bulk value (850°C). On the other hand, as compared with the fully polycrystalline film deposited at room temperature, these films certainly exhibit a much larger stress due to the mismatch between the film and the MgO substrate. This leads to high dielectric losses for the perfect crystals and low ones for the polycrystalline film.

This may indicate a different mechanism between the microwave losses and tunability: whereas the dielectric constant and tunability appear to be linked to the thin film lattice parameter, it seems that the dielectric losses are somehow related to the layer stress. The presences of defects that locally relax the stress are beneficial for the dielectric losses of the material. This yield to comparable Figure of Merit between highly epitaxial and polycrystalline films as observed by Chang *et al.*[77] for BST thin films deposited on MgO.

3.3.5. Effect of oxygen background pressure

Table 3.1 reports the dielectric constant, loss tangent (at 2 GHz, 0 V.µm^{-1}), tunability (at 2 GHz, 10 V.µm^{-1}), and FOM at 10, 50 and 100 mTorr deposition pressure.

Table 3.1: BST-0.6 dielectric constant, loss tangent (at 0 V), tunability and FOM (at 10 V.µm^{-1}), of thin films grown under different oxygen pressures.

Oxygen pressure (mTorr)	Dielectric constant	Loss tangent	Tunability% at 10 V.µm^{-1}	FOM
10	755	0.051	49	9.60
50	530	0.029	29	10
100	563	0.041	33	8.04

It is observed that the overall BST characteristics are close for the three samples, the Figure of Merit being between 8 and 10. The respective dielectric loss and tunability are just changing from one condition to the other, the lowest tunability and loss tangent being obtained at 50 mTorr. These results are in agreement with the sample structural characterization (section 2.4.5) where no big differences were observed between the samples except the crystallinity (going from nearly epitaxial at 10 mTorr, to polycrystalline for 50 and 100 mTorr). As exposed for the temperature study, the stress relaxation for the 50mTorr sample (when going from epitaxial to polycrystalline) may explain its lower losses, and it seems that lower losses are always coupled to lower tunabilities.

3.3.6. Effect of substrate material and orientation

Substrates material

Fig. 3.27.a compares the dielectric constant and loss tangent (at 2 GHz, 0 V.µm^{-1}) obtained for BST-0.6 thin films grown on different substrate material: MgO, LaAlO$_3$ and Sapphire crystals, and polycrystalline Alumina. Fig. 3.27.b shows the measured tunability (at 2 GHz, 10 V.µm^{-1}) and FOM for the same samples. This comparison shows that the dielectric properties of BST films deposited onto different substrate materials are significantly different. Dielectric constant is about the same on MgO and LAO (about

900-950), and much lower for the film deposited on Sapphire (550) and Alumina (400). The tunability follows exactly the same trend with values around 70% for films deposited on MgO and LAO, 40% for the film on Sapphire and 25% for the film on alumina. The main difference between the film deposited on MgO and LAO is for the dielectric loss value: while the film on MgO exhibit moderate losses of 0.065, the film deposited on LAO exhibit a high value of 0.11. Losses for the films on Sapphire and Alumina are respectively of 0.046 and 0.036. This result in comparable overall microwave characteristics for films on LAO and Alumina (FOM=6.5), a value that is significantly lower than the one obtained for the films deposited on sapphire (FOM=9) and MgO (FOM=10).

If these results are compared with the structural characteristics of the films, it confirms that tunability and dielectric constant are correlated to the material lattice parameter, whatever the crystal nature of the BST. Again, the losses seem to be linked to the BST films crystallinity, certainly through its role on the film stress. It is observed that BST-0.6 on LAO, which exhibit the best crystallinity (rocking curve FWHM of 0.27) is also the one exhibiting the highest level of dielectric losses. Moreover, the polycrystalline films that are stress-relaxed compared to epitaxial or highly-oriented films, exhibit a much lower level of dielectric losses.

MgO substrate orientation

Table 3.2 reports the dielectric properties of (100), (110), and (111) oriented BST-0.6 thin films grown respectively on (100), (110), and (111) MgO substrates (the structural characterization of these samples was presented in the section 2.4.6.b). One can note that the microwave properties of the (100), (110) and (111) films are very similar, with only slightly higher values for the (110) film, and slightly lower values for the (111) film. Since the Figure of Merit is the ratio between the tunability and the dielectric losses, this results in very close overall microwave characteristics for the different films: FOM=10 for (100) and (111) BST films and 8.7 for the (110) BST film (at 2 GHz and 10 V.μm^{-1}).
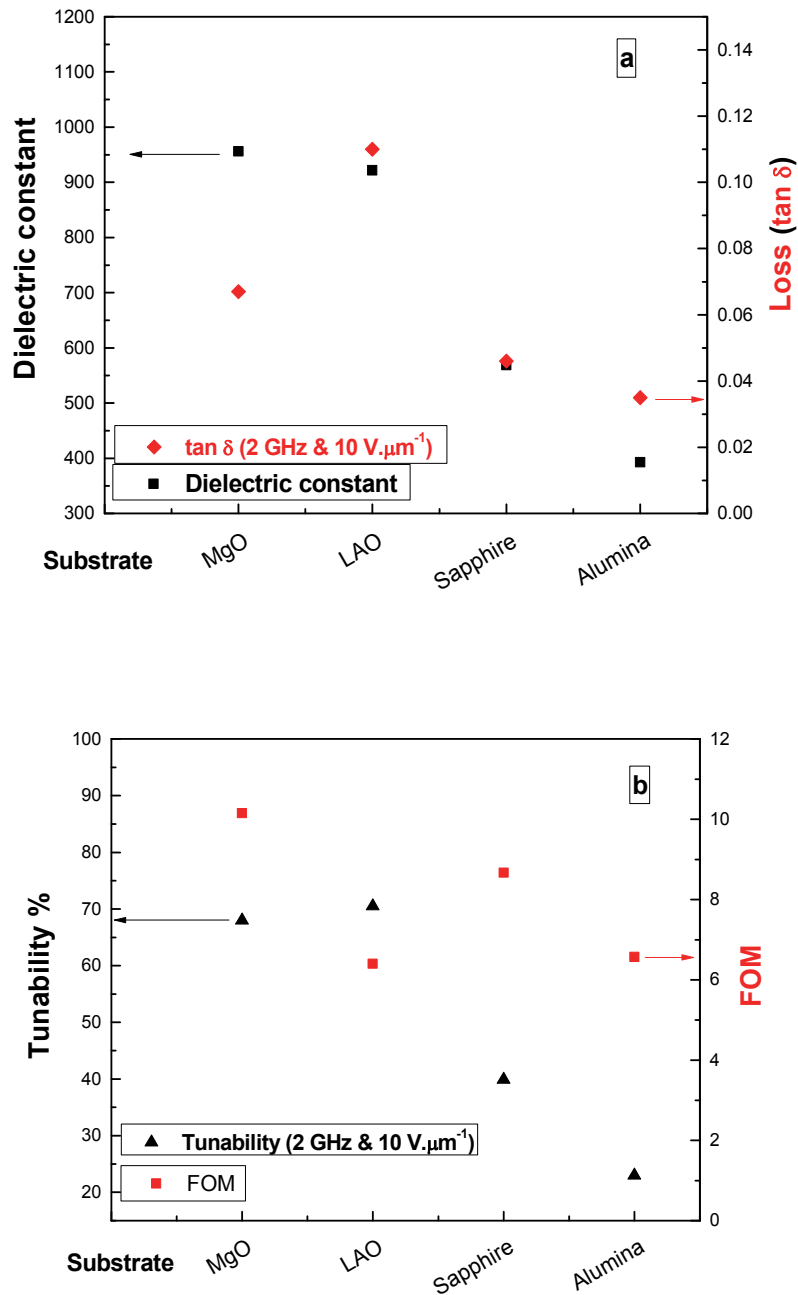
Figure 3.27: a) Dielectric constant and loss tangent (at 2 GHz, 0 V.µm⁻¹) and **b)** Tunability (at 2 GHz, 10 V.µm⁻¹) and FOM of BST-0.6 thin films grown on different substrate types: MgO, LAO and Sapphire crystals, and polycrystalline Alumina.

Many groups have investigated the influence of the substrate on the microwave dielectric properties of BST thin films. Moon *et al.*[78] found a strong correlation between the microwave dielectric properties and the orientation of BST thin films grown by pulsed

laser deposition on various oriented MgO single crystal substrates. Noda *et al.*[79] studied a microwave tunable device based on BST film operating at 20 GHz, they reported an increase of the device figure-of-merit by a factor of 3 between MgO (100) and MgO (111) substrates. They noted that the differences in BST films permittivity and tunability are closely related to the difference in the film strain. Yang *et al.*[80] studied the growth of BST-0.6 on sapphire with and without a TiO_x buffer layer. They found that the film with buffer layer shows highly oriented BST (111), with high permittivity and superior microwave properties.

Table 3.2: Dielectric properties of BST-0.6 thin films grown on different MgO substrate orientations (100), (110), and (111).

Substrate	Dielectric constant	Loss tangent (at 0 V)	T% (at 10 V.μm^{-1})	FOM
MgO (100)	956	0.067	68	10.15
MgO (110)	1021	0.083	72	8.67
MgO (111)	891	0.06	59.5	9.9

In our case, only small differences are observed for the different film orientations on MgO substrates. Large differences appear between the different types of substrates materials that seem to be more related to the material strain than to its quality.

Table 3.3 summarizes the structural and the dielectric properties of epitaxial BST thin film, and shows that the highest obtained FOM is 10.

Table 3.3: structural and dielectric properties of epitaxial BST thin film.

Lattice parameter (A°)	w-scan FWHM (°)	Dielectric constant	Tunability % at 10 V.μm^{-1}	Losses	FOM
3.97	0.3	955	65	0.065	10

Conclusion

In this chapter, we first described the microwave method used for the characterization of BST thin film at high frequency. This method requires the fabrication of thick electrodes (2 µm) with small gap (3 µm) that are used for the measurement of microwave characteristics as a function of the applied electric field (tunability). The device microfabrication process being challenging due to the high aspect ratio and quality requirement on the electrodes, an optimization of the process was carried out. This was done by adjusting the exposition parameters to improve the photoresist profile. A robust process was defined to obtain, on the same wafer and for the different circuit dimensions, resist profiles suitable for an easy and effective metal lift off process. Different CPW devices were then patterned on BST/MgO samples and the circuits are measured on a probe station with a network analyzer. The obtained characteristics are treated through a quasi-static model in order to extract the dielectric constant, dielectric loss and tunability of the BST films up to 10 V.μm^{-1} applied electric field at a frequency of about 1 to 3 GHz.

A microwave diagnostic was used to characterize all the deposited samples presented in the previous chapter. This study includes the different processing parameters, namely the laser fluence, the repetition rate, the substrate temperature, the oxygen pressure, the BST-x composition and the type of substrate. From this extensive study, it is observed that, in general, the closer is the material lattice parameter to the bulk value, the higher is the dielectric constant and tunability of the thin film, whatever its crystal nature (epitaxial, highly oriented, polycrystalline). On the other hand, the higher is the crystal quality, the higher are the losses of the material.

For the laser fluence study, it appears clearly that the highest BST dielectric constants and tunabilities are obtained for films having a lattice parameter as close as possible to the bulk material value. The highest Figure of Merit is obtained for BST-0.6 deposited with a low fluence (1 J/cm^2) obtained with a laser spot area of 11 mm^2. This film corresponds to the one that posses the closest lattice parameter to the bulk value. Concerning the dielectric loss, there is no direct correlation found; it is only observed that they are generally higher for high tunabilities. On the other hand, the lowest

dielectric losses are not obtained for the film presenting the best crystallinity or the best lattice parameter.

For the BST-x target composition study, it shows again a correlation between the lattice parameter and both the dielectric constant and the tunability. It is also observed that the dielectric losses seem to decrease as the crystal quality decreases. According to these results the optimum BST-x / MgO thin film composition for microwave application is the composition x= 0.6 ($Ba_{0.6}Sr_{0.4}Ti\ O_3$), which exhibits the highest dielectric constant (ε_r =965), tunability (68% at 10 V.μm^{-1}), and FOM (10). However, the loss tangent of this sample is relatively high (0.067) and requires improvement for microwave applications.

For the deposition temperature study, it shows that, on one hand, the maximum tunability (of ~70%) is obtained for the two conditions leading to the best epitaxial quality. The best overall properties are obtained for the film having the lattice parameter closest to the bulk value (obtained at 850°C). On the other hand, fully polycrystalline film deposited at room temperature exhibits much lower losses and a comparable Figure of Merit as the nearly perfect crystals thin film deposited at the optimal condition (high temperature).

For the films deposited at different oxygen pressures, it is observed that the overall BST characteristics are close, the Figure of Merit being between 8 and 10. The respective dielectric loss and tunability are just changing from one condition to the other, the lowest tunability and loss tangent being obtained at 50 mTorr. These results are in agreement with the sample structural characterization where no big differences are observed between the samples except the crystallinity (going from nearly epitaxial at 10mTorr, to polycrystalline for 50 and 100 mTorr). As observed for the temperature study, the stress relaxation for the 50mTorr sample (when going from epitaxial to polycrystalline) may explain its lower losses.

Finally, for the BST films obtained on different substrates, only small differences are observed for the different film orientations (100), (110) and (111) on MgO substrates. Large differences appear between the different types of substrate materials (MgO, LAO, Sapphire and Alumina) that seem to be more related to the material strain than to its quality. Whereas the highest tunability is obtained for the film deposited on LAO (that is the one having the lattice parameter closest to bulk BST-0.6), its very high loss tangent (0.11) makes its overall characteristics smaller than the one obtained on MgO. It is also

121

interesting to note that the Figure of Merit of the polycrystalline film obtained on Sapphire (FOM=9) is comparable to one of the highly oriented film obtained on MgO (FOM=10).

These results may indicate a different mechanism driving the microwave losses and the tunability: whereas the dielectric constant and tunability seems to be linked to the thin film lattice parameter (i.e. how close is the material from its bulk form), the dielectric losses are somehow related to the layer stress. It is expected that the epitaxial nature of the film induce large strain on the material compared to lower crystal quality that allow stress relaxation through defects across the grown layer. This stress relaxation is certainly related to the lower losses observed for polycrystalline films. This leads to comparable figures of merit between epitaxial and high-quality polycrystalline films. These correlations between structural and microwave characteristics will be studied in more details in the next chapter, by presenting a synthesis of all the results presented in the chapters 2 and 3.

Chapter 4: Correlation between microstructure and microwave properties of BST thin films

Lots of different BST-0.6 deposition conditions have been explored and their structural and electrical characteristics were presented in Chapter 2 and Chapter 3 respectively. These results will be synthesized in this chapter to draw a general correlation between structural and microwave properties of BST thin film. Such correlation will help to understand the mechanisms of loss and tunability and, in the second part of this chapter, try to improve the BST thin film characteristics using specific design of experiments.

Table 4.1: **Description of the sample sets. For each set the values of the studied parameter are specified and the typical values used for the deposition of the other sets are underlined.**

Set #	Variable parameter	Values of the variable parameter
1	Substrate temp.	RT, 500, 700, 750, <u>800</u>, 850, 900, 950°C.
2	Oxygen pressure	<u>10</u>, 50, 100 mTorr.[a] @ 700°C
3	Substrate	<u>MgO (100)</u> @ 800°C, MgO (110) @ 800°C, MgO (111) @ 800°C, LAO(100) @ 800°C, sapphire@ 700°C, Alumina @ 500°C.[b]
4	Laser fluence	1 J/cm^2 (40, 50, <u>110</u>, 200, 300 mJ). [a] @ 700°C
5	Laser repetition rate	2, <u>10</u>, 20 and 50 Hz.
6	BST-x Composition	x=0, 0.3, 0.5, <u>0.6</u>, 0.7, 1

[a] **Deposited at 700°C**

[b] **Deposited at 800, 800,800,800, 700 and 500°C respectively.**

These different experiments were first regrouped in different sets, as described in Table 4.1. Otherwise mentioned, deposition are done with a repetition rate of 10 Hz, a laser fluence of 1 J/cm^2 (obtained with a 11 mm^2 spot size), an oxygen background pressure of 10 mTorr (10 sccm flow) and a substrate temperature of 800 °C. The obtained BST films are post annealed in a furnace at 1050°C under an oxygen flux for a period of 3 hours in order to improve the crystal quality and remove possible oxygen vacancies.

4.1. Synthesis of BST results

4.1.1. Correlation between lattice parameter and FWHM of rocking curve

The BST- 0.6 bulk lattice parameter being 3.960 Å and the one of MgO substrate being 4.212 Å, there should be a relation between the BST thin film crystal quality and its lattice parameter due to the stress induced by the lattice mismatch. The Fig. 4.1 shows the ω scan FWHM (crystal quality) plotted as a function of the lattice parameter for the different sets (except the set#6 that corresponds to different materials). The figure is separated in 3 zones, according to the nature of the crystal. As observed on the XRD spectra: from 0.2 to 0.45 degree FWHM, the films are found to be epitaxial, whereas between 0.45 and 1.4 degrees they are generally textured and above 1.4 degree the films are polycrystalline. It appears on Fig. 4.1 that, in general, as the crystal quality increases (Δω decreases), the out-of-plane lattice parameter gets closer to the BST bulk value (3.96 Å). Moreover, this range corresponds to epitaxial films obtained from different experimental sets. The second observation is that it seems that going from epitaxial to polycrystalline, the films reach a kind of saturation of the lattice around 3.98 Å (the value obtained for polycrystalline films). The dispersed value for the textured films is mainly coming from the set#4 corresponding to the variation of the fluence, where it was observed a modification of the stoechiometry.

124
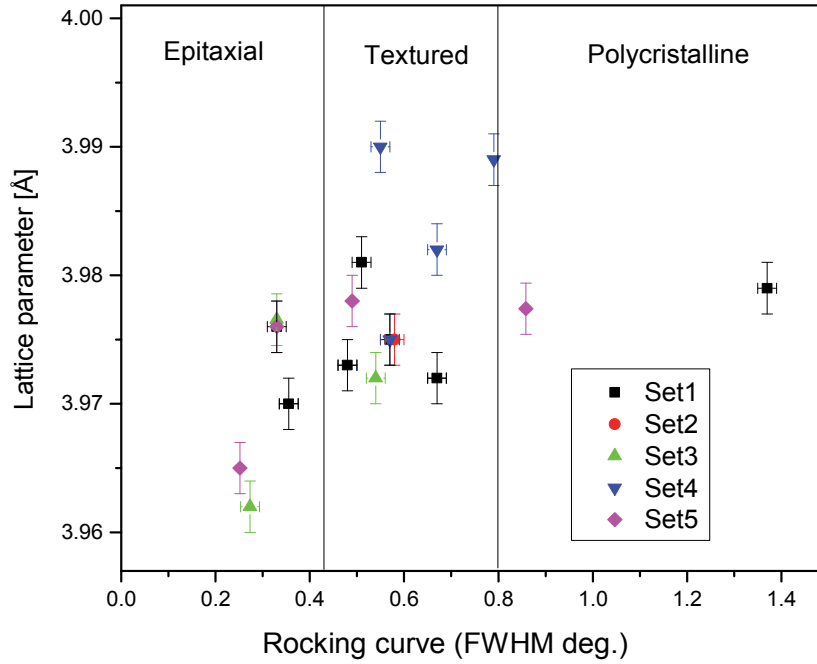
Figure 4.1: Omega Rocking curve (FWHM) as a function of Lattice parameter for the different sets presented in Table 4.1 of BST-0.6.

4.1.2. Correlation between FWHM of rocking curve and tunability

Fig. 4.2 shows the BST tunability as a function of the ω-scan FWHM for the different experimental sets. As for the previous figure, the increase in ω-scan FWHM corresponds to evolution from epitaxial to textured and polycrystalline films (as indicated on the figure). This figure shows that a correlation exists between the crystal quality ($\Delta\omega$) and the tunability: as the crystal quality increases ($\Delta\omega$ decreasing from 0.8° to 0.2°), the tunability (at 2 GHz and 10 V.μm^{-1}) is increasing, going from 25 % for polycrystalline films to values as high as 72.5 % for the best crystal quality obtained ($\Delta\omega$ of 0.25°).

This general trend may be linked to the observed relation between the lattice parameter and the crystal quality (presented on Fig. 4.1). As exposed on the chapter 2, the tunability can be linked to the lattice parameter using the Landau-Devonshire model [81,82]
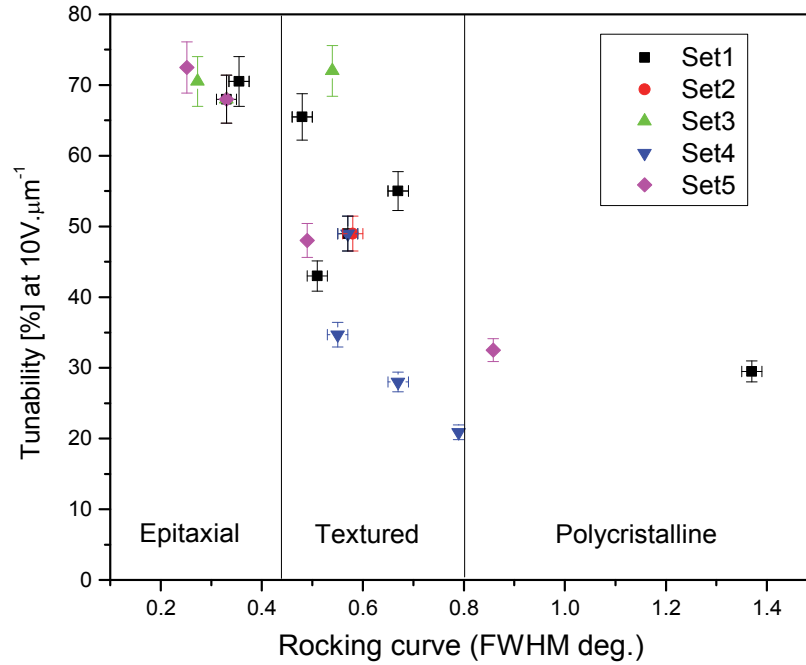
Figure 4 2: BST-0.6 tunability(at 2 Ghz, and 10 V/μm) as a function of the Omega rocking curve FWHM for the different sets presented in Table 4.1.

4.1.3. Correlation between lattice parameter and tunability (Landau–Devonshire model)

One of the recurrent observations, when comparing BST-0.6 films microwave characteristics compared to their structural characteristics (chapter 3) is that the BST tunability is maximum when the material lattice parameter is close to the bulk value. This correspond to the Landau-Devonshire model prediction [81,82] (presented on chapter 1), that shows a maximum of the dielectric constant and tunabiltity as a function of the lattice mismatch. Different groups have found experimental validation of the Landau-Devonshire model [20,27,83] where the tunability is generally plotted as a function of the thin-film stress or misfit strain. A good correlation was also found by our group[30] between the tunability of polycrystalline BST-0.5 films deposited on alumina substrates and the BST-0.5 out-of-plane lattice parameter. This correlation was well fitted using this theoretical model, the misfit strain being replaced by the corresponding BST lattice parameter value, a_{BST}, such as:

$a_{BST} = a_{bulk} (1+u_m)$ .... Eq. 4.1

The Fig. 4.3 presents such a correlation for the different sets of BST-0.6 deposited on MgO. The theoretical tunability calculated for BST-0.6 using the Landau-Devonshire model is also presented on the same figure. The result shows exactly the same trend as the one observed for the BST-0.5, for BST-0.6 films on a single-crystal substrate with film structures going from epitaxial to polycrystalline. This figure shows that, except for some points of the set#1 and 3, the correlation between the tunability and the lattice parameter follows the general trend described by the model. The highest tunability values are generally obtained for films that possess a lattice parameter as close as possible to the BST-0.6 bulk value. This is an indication that, more than the crystal quality, the lattice parameter (or film strain) is the main parameter driving the thin film tunability.
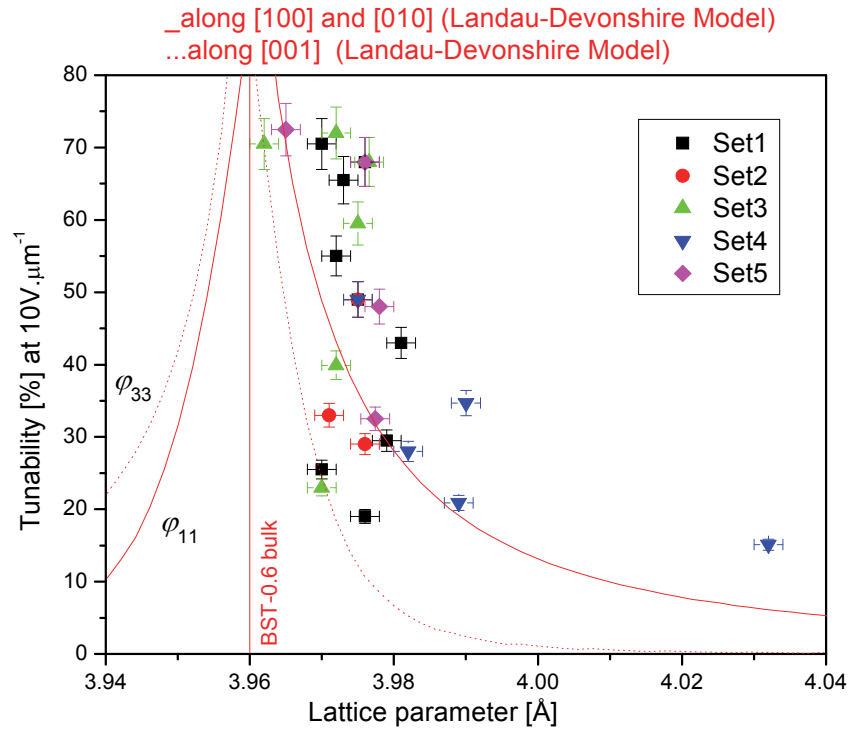
Figure 4.3: **BST-0.6 tunability (at 2 GHz, and 10 V/ μm) as a function of the measured lattice parameter for the different sets presented in Table 4.1. The continuous and dotted lines correspond to the theoretical in-plane and out-of plane tunability (φ_{11} and φ_{33}) calculated for epitaxial films, using the Landau-Devonshire model.**

4.1.4. Correlation between dielectric loss and tunability

The other observation, reported in chapter 3, and in most of the papers published on the subject, is that the BST tunability is usually linked to dielectric losses: usually, the higher is the tunability, the higher are the losses. Plotting the measured tunability as a function of the losses is rarely found in the literature but the results is surprisingly clear. Fig. 4.4 presents this correlation for all the sets investigated (the tunability and tan δ being both measured in the GHz range).

This figure shows that the losses are almost linearly linked to the tunability, with the lower losses associated with the lower tunability, and vice-versa, yielding to a Figure of Merit (FOM) that is comparable for epitaxial and polycrystalline films. For example, the film of set#1(deposition temperature) grown at 500°C is polycrystalline with a low tunability of 19%, but it also possesses the lowest tanδ (of 0.025) and a FOM of 7.6. The best crystal quality film ($\Delta\omega$ of 0.25°) has the highest tunability (72.5%) but also very high tanδ (0.08) yielding to a Figure of Merit of 9.
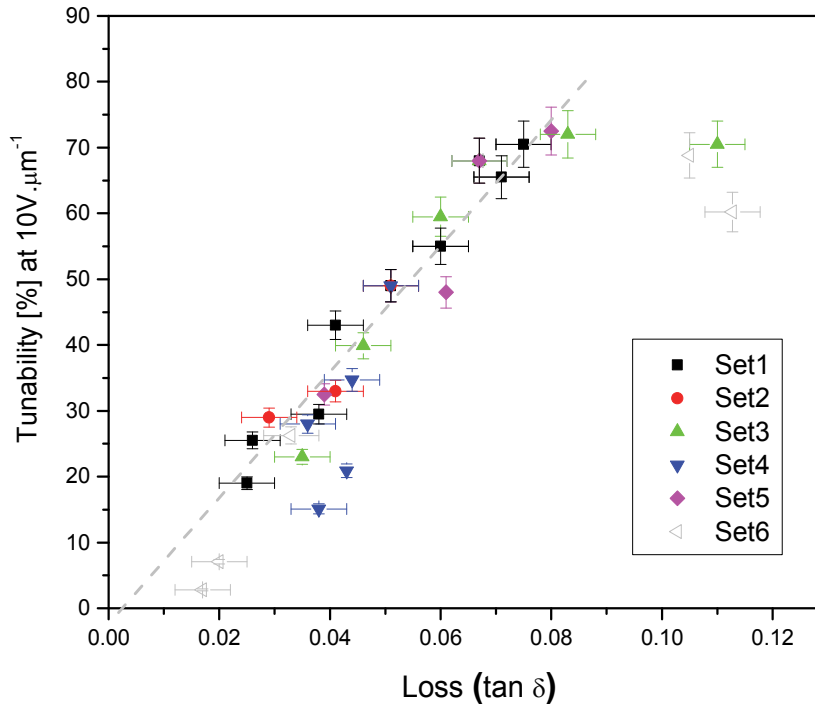
Figure 4.4: BST-0.6 tunability (at 2 Ghz, and 10 V/ µm) as a function of the measured dielectric loss for the different sets presented in Table 4.1.

The other interesting result is that different BST material compositions (set #6), also plotted on this graph, seem to follow the same trend. At least for the materials in the paraelectric state: STO, BST-0.3, BST-0.5 and BST-0.6 are all following the linear dependence, whereas BST-0.7 and BTO, that are supposed to be in the ferroelectric state exhibit very high losses and tunability that seem to decrease as the losses increases. Moreover, the ferroelectric state characteristics correspond to the result obtained for the film deposited on LaAlO$_3$ (isolated point from the set#3, exhibiting tunability of 70% and losses of 0.11).

4.1.5 Interpretation

Some groups have investigated ways to obtain low loss BST thin films while keeping the tunability as high as possible. It is observed that the decrease of the material losses also reduces its tunability and vice versa. Crystal orientation, crystal defects, misfit strain and thin film stress may be the main factors influencing the BST characteristics. Stress and strain effects are among the suspected causes for extrinsic dielectric loss.[27,84] For example the strain can significantly change the dielectric properties and cause large change in the Curie temperature.[85] Large compressive strain also decreases the out-of-plane dielectric constant and degrades the ferroelectric properties.[23] Furthermore the presence of misfit strain can adversely affect the tunability[22,86] and modify the phase diagram of epitaxial ferroelectrics, change the order of the transition, and shift transition temperatures.[87]

Many groups have tried to pinpoint the origins of dielectric degradation in thin films. Yamada *et al.*[88] found a correlation between the dielectric constant and the tunability of BST thin films. They used the strain in the epitaxial films to control the dielectric constant of the films grown on LaAlO$_3$ substrate. They observed that under strong compressive strain, the dielectric constant is significantly lower than that one of unstrained films; higher tunability is obtained for film showing higher dielectric constant. Their conclusion was that lowering dielectric constant of BST (by strain, temperature and/or Ba/Sr composition) can cause the same effect, inducing a reduction of the tunability.
Catalan *et al.*[89,90] studied the effect of strain gradient on the dielectric properties of epitaxial BST films. Gradient terms (of strain, composition, and defects) can cause reduction in the dielectric constant. Their recommendation was to avoid strain gradients

in order to prevent degradation of the ferroelectric response in thin films, where relaxation of strain in epitaxial films is associated with the appearance of internal strain gradients. Also, they studied the impact of flexoelectric coupling on the dielectric and polarization properties of ferroelectric thin films. Flexoelectric effect is a strain-gradient-induced polarization, they show that flexoelectricity can play an important role in decreasing the maximum dielectric constant of ferroelectric thin films under inhomogeneous in-plane strain. They showed that as the film thickness decreased, the dielectric peak decreases and shifts up in temperature, while the polarization increases due to the flexoelectric contribution.

Moeckly *et al.*[91] prepared a variety of STO films on various substrates, with different thicknesses and under different conditions. They found a clear relation between the dielectric constant and the dielectric loss of STO films and between the dielectric loss and the tunability. The correlation found is very similar to the one we found here, where the tunability of STO films is almost linearly dependent on to the dielectric loss of the films.

From our observations, it seems that the BST material tunability properties are only related to its lattice dimensions: for a given BST composition, whatever the way used to change the material lattice parameter (deposition temperature, pressure, substrate type, etc..) the maximum tunability is obtained only for lattice parameter values close to the bulk material value. It is also observed that the crystal quality has little or no direct influence on the tunability value.

On the other hand, it is observed that the losses are linearly linked to the material tunability. It is difficult to conclude if this limitation is intrinsic to the material or if it is related to another phenomenon. A lot of papers are attributing losses to the presence of charged defects, grain boundaries or dislocations,[92,93] but the general trend of Fig. 4.4 may point to another mechanism. In the present study, the films with the best crystal quality are the one that present the higher losses and these losses are decreasing as the films microstructure goes from epitaxial to textured and polycrystalline. For sure, maximum tunability values are obtained for very high quality crystal having large interfacial stress, since BST-0.6 has a 6% mismatch with MgO. Hence, the interfacial stress is not affecting the tunability value but may be the main parameter affecting the dielectric losses.

4.2. Optimization of BST properties

In the previous section, it was found that two different mechanisms may drive the tunability and the losses of BST-0.6 thin films: the tunability is related to the material lattice parameter whereas the dielectric losses are either intrinsically linked to the tunability or influenced by the interfacial stress of the film. In order to further study this phenomenon, one needs to try separating these two effects. In this context two ways were explored: the use of buffer layers and material doping. Thin layers of $Ba_xSr_{1-x}TiO_3$ (with x=0 to 1) were used as buffer layers for the deposition of BST thin film. Buffer layers are used to decrease the interfacial stress between the BST-0.6 layer and the MgO substrate and study its impact on the dielectric loss and dielectric tunability of the material. Another experimental study was carried out on the effect of doping on the dielectric and structural properties of the BST thin films. Two different ways of doping BST were used: the first one using incorporation of doping material (Mg, Ni, Mo, Fe, and Ti) during the deposition and the other one using ion implantation of Mg on deposited films with different doses.

4.2.1. Effect of a buffer layer on BST thin film properties

4.2.1a. Literature review

Chang *et al.*[77] deposited BST thin films on MgO with BST buffer layer with 200 mTorr oxygen background pressure. The films were observed to be strain relieved and show better dielectric properties at 8 GHz compared to strained BST thin films. They observed further improve in the dielectric properties in strain-relieve BST thin films mixed with MgO and strain-relieved BST thin films doped with W.

Wei *et al.*[94] also used BST buffer layer between BST film and the $Pt/Ti/SiO_2/Si$ substrate. They found that the buffer layer has a crucial role during crystallization. Comparing thin films with and without buffer layer, they observed that the grain size was enlarged from 50 to 100 nm, and that the electric properties can be improved by using a buffer layer.

Peng *et al.*[95] deposited BST-0.6 thin films without and with homo- and hetero-buffer layer on MgO substrates using BST-0.8 and BST-0.6 as buffer layer materials. They

found that the films with homo-buffer layer slightly enhanced the dielectric constant, and reduced the dielectric loss.

Park *et al.* [16] epitaxially grown BST-0.6 thin films on MgO substrates. They were able to manipulate the degree of the stress in BST-0.6 films by inserting BST-x (x = 0.1– 0.7) buffer layers. The variation of the chemical composition of the buffer layer allows them to control the lattice distortion of the BST-0.6. They found that the small variations of lattice distortion can result in significant changes in dielectric properties. They also observed that BST-0.6 film grown on a BST-0.7 buffer layer shows larger dielectric values (permittivity of 1180, tunability of 61% at 80 kV/cm) than the one grown on a BST-0.5 buffer layer (permittivity of 840, tunability of 46%).

Furthermore Tang *et al.*[96] deposited BST thin films on Pt (111)/Ti/SiO$_2$/Si (100) substrates with and without LaNiO$_3$ (LNO) buffer layer. They found that the dielectric constant of the BST films was slightly higher with LNO buffer layer (1010 at 1 MHz, compared to 851 without).

4.2.1b. Effect of BTO buffer layer thickness on epitaxial BST thin film properties

A set of experiment was conducted on the influence of the buffer layer thickness on the BST-0.6 properties. Different BaTiO$_3$ (BTO) buffer layer thicknesses (of 20, 50, 100 nm) were deposited on MgO prior to the deposition of a (580, 550, 500 nm respectively) thick BST-0.6 layer. Deposition of BST-0.6 and BTO layers was done at a substrate temperature of 800°C with an O$_2$ background pressure of 10 mTorr.

i. Structural properties

X-ray diffraction spectra show that the BST films are epitaxially grown on the BTO/MgO. The variation of the BST-0.6 lattice parameter as a function of the BTO buffer layer thickness is shown on Fig. 4.5. It is found that as the buffer layer thickness increases, the BST-0.6 lattice parameter decrease down to values very close to the BST-0.6 bulk value (*a* $_{BST-0.6}$ = 3.96 °A). The FWHM of the rocking curve (Fig. 4.6) exhibits a slight decrease as the BTO buffer layer thickness increases whereas the FWHM of the phi scan is almost unchanged (except for the 50 nm buffer layer thickness where it seems overestimated since the rocking curve doesn't show the same tendency).
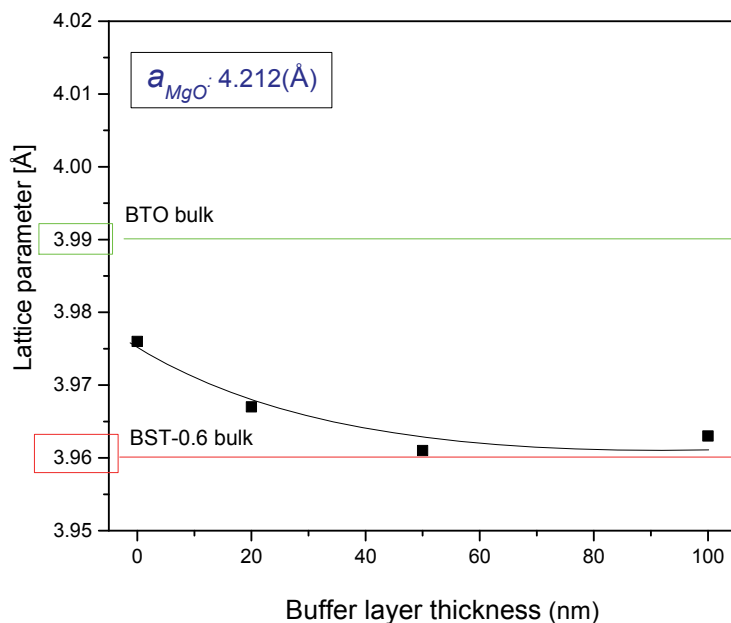
Figure 4.5: Lattice parameter of BST-0.6 thin films grown on MgO substrate with different thickness of BTO buffer layer (20nm, 50nm, and 100nm).
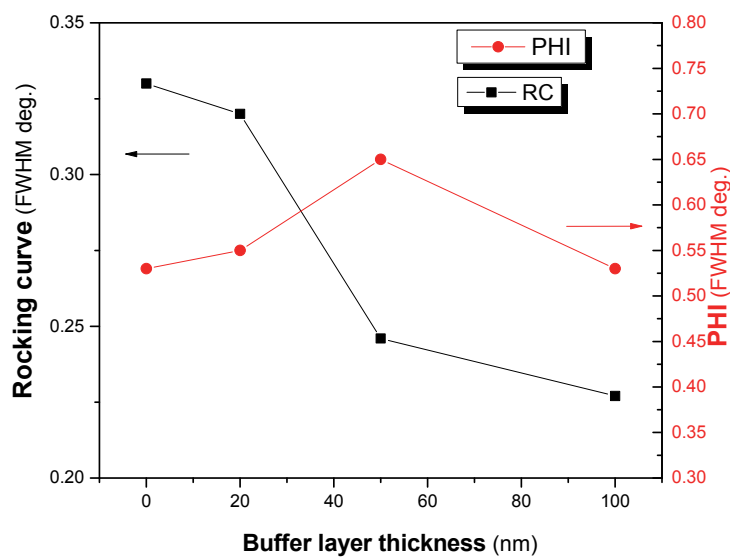
Figure 4.6: ω Scan (rocking curve) FWHM and Phi scan FWHM of BST-0.6 thin films grown on MgO substrate with different thickness of BTO buffer layer (20 nm, 50 nm, and 100 nm).

ii.   Microwave properties

Fig. 4.7 shows the dielectric constant and loss tangent (at 2 GHz, 0 V.μm^{-1}) of BST-0.6 grown on BTO buffer layer with different thicknesses (20 nm, 50 nm, and 100 nm). It shows that the dielectric losses of the BST-0.6 are greatly affected by the thickness of the buffer layer whereas the dielectric constant is not significantly changing. As the thickness of the buffer layer (BTO) increases from 0 to 50 nm the dielectric loss increases from 0.067 to 0.115. In the same range, the dielectric constant only slightly increases from ~900 to 1200. Fig. 4.8 is showing the effect of the BTO buffer layer thickness on the tunability and FOM (at 2 GHz, 10 V.μm^{-1}). As for the dielectric constant, the tunability is only slightly increasing with the buffer layer thickness going from 65% without buffer layer to 75% with a 100 nm buffer layer. Since the dielectric losses increase a lot in the same range, the FOM is decreasing as the buffer layer thickness increases (from 10 without buffer layer to about 6.5 for the 100 nm thick buffer layer).
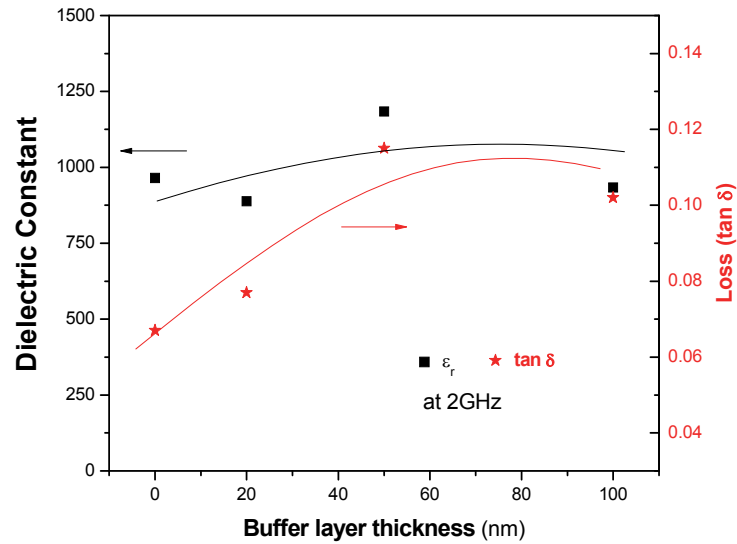
Figure 4.7: Dielectric constant and loss tangent (at 2 GHz, 0 V.μm^{-1}) of BST-0.6 thin films grown on MgO substrate with different thickness of BTO buffer layer (20 nm, 50 nm, and 100 nm).
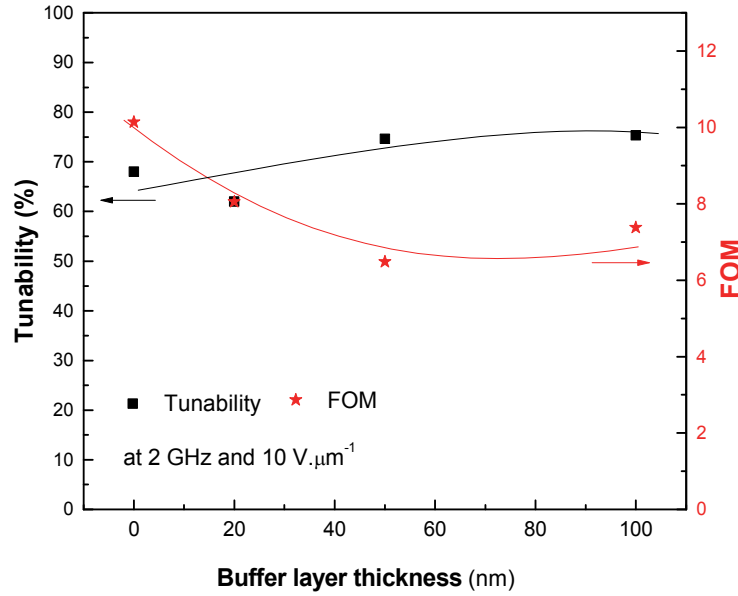
Figure 4.8: Tunability and Figure of Merit (at 2 GHz, 10 V.µm-1) of BST-0.6 thin films grown on MgO substrate with different thickness of BTO buffer layer (20 nm, 50 nm, and 100 nm).

iii.   Discussion

The results obtained for the influence of the buffer layer thickness on the properties of BST-0.6 thin films follows exactly the previous tendency observed for BST-0.6 thin films: as the FWHM of the rocking-curve decreases and the lattice parameter gets closer to the BST-0.6 bulk value as the BTO buffer layer thickness increases, it is observed that, on one hand, the dielectric constant and tunability increase as the buffer layer thickness increases. On the other hand, the dielectric losses greatly increase as a function of the BTO buffer thickness (influenced by the improvement in crystal quality but also by the dielectric losses of the BTO layer itself) which makes the FOM decrease. Interestingly the BST-0.6 with 50nm BTO buffer layer has the same lattice parameter as the bulk ceramic ($a_{BST-0.6}$ = 3.96 Å), and very low rocking curve FWHM (0.24). This sample exhibit very high tunability (74.5%),[77,97] but low FOM (6.5) due to the high level of dielectric loss measured in that case (0.12). It may be better to use buffer layers with lower dielectric losses but, unfortunately, this corresponds to BST compositions having a lower lattice parameter. There may be a tradeoff between the layer stress and the buffer layer lattice parameter that can be found using a specific buffer layer composition.

4.2.1c. Effect of buffer layer material (BST-x with x=0 to 1)

The Table.4.2 reports the different lattice parameters of bulk ceramics and thin films deposited on MgO (as exposed in section 2.4.3). According to these values and the fact that the strain in heteroepitaxial BST films is mainly caused by the lattice mismatch,[16,98] the effect of the buffer layer should go from compressive strain for the BST-x composition going from x=0 to 0.5 and tensile stress for x=0.6 to 1.

Table 4.2: Bulk ceramic and thin films deposited on MgO lattice parameter (a_{bulk} and a in Å).

x	0	0.3	0.5	0.6	0.7	1
Material	STO	BST-0.3	BST-0.5	BST-0.6	BST-0.7	BTO
Bulk ceramic a_{bulk} (Å)	3.90	3.93	3.95	3.96	3.97	a=3.99 c=4.03
thin films on MgO a (Å)	3.915	3.943	3.967	3.976	3.985	4.012

A series of samples was prepared using BST buffer layers of different compositions in order to change the degree of strain on the deposited BST-0.6 films. A series of 550nm thick BST-0.6 thin films were deposited on MgO substrate with different buffer layer materials of 50 nm thick. The typical PLD deposition conditions have been used for both the buffer layer and the epitaxial BST-0.6 films (at 800°C with an O_2 background pressure of 10 mTorr). The two layers have been deposited consecutively in the PLD system, the PVD3000 allowing to choose between three different targets for the deposition.

i. Structural properties

The XRD (θ–2θ) characterizations revealed that BST-0.6 film grown on all buffer layers are epitaxial, except the one grown on STO which is polycrystalline. Fig. 4.9. shows the rocking curves of [BST-0.6/BST-0.3/MgO], [BST-0.6/BST-0.7/MgO], and [BST-0.6/BTO/MgO]. One can observe that the rocking curve of BST-0.6 is shifted to lower angle and a slight decrease of the peak FWHM as the x composition of the buffer layer increases. This indicates a shift of the BST-0.6 lattice parameter to lower values and improvement in the crystal quality as the buffer layer lattice parameter increases. This effect can be clearly seen on Fig. 4.10, that reports the measured BST-0.6 lattice parameters values for the different buffer layers, and Fig. 4.11, that shows ω Scan (rocking curve) FWHM values and Phi scan FWHM values of BST-0.6 for the same samples.

It is observed that both the crystal quality and the lattice mismatch between the buffer and the BST-0.6 layer has an influence on the deposited thin film. As x increases, it has been observed that the buffer layer lattice parameter and crystal quality increase (section 2.4.3 and Table 4.2). The same effect is observed for the crystal quality of BST-0.6 thin film grown on the buffer layer: both the buffer layer and the BST-0.6 are polycrystalline for x=0 (STO) and epitaxial above x=0.3, with a FWHM that improves up to x=1. For the lattice parameter, the effect is reversed compared to the BST-x layer alone: as x increases, the BST-0.6 lattice parameter decreases down to values very close the BST-0.6 bulk values. Since the measured parameter corresponds to the out of plane lattice parameter measurements, this may indicate that the crystal unit cell is elongated along the z-axis (whereas the in-plane lattice parameter decreases, the material out-of-plane lattice parameter increases in order to keep a constant cell volume). This effect may also come from the contribution of the buffer layer peak position that is convoluted to the BST-0.6 peak. In the XRD data analysis, the position of this peak and its intensity directly influence the BST-0.6 position and hence its deduced lattice parameter.
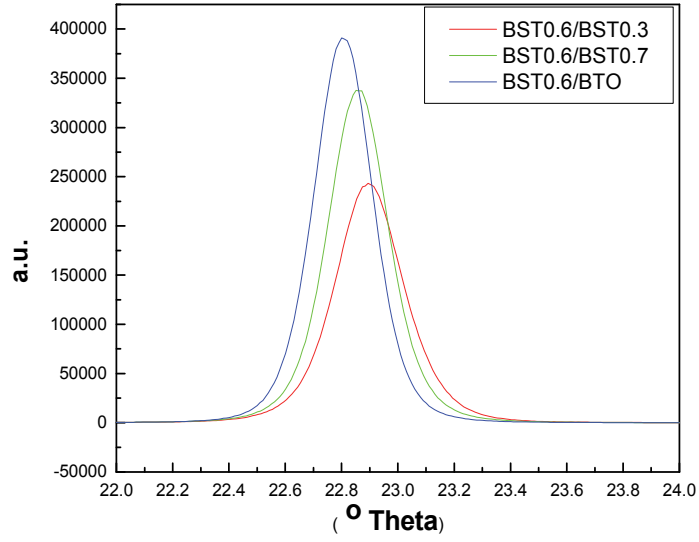
Figure 4.9: Rocking curve of BST-0.6 thin films grown on MgO substrate with different buffer layer materials (BTO, BST-0.7, and STO).
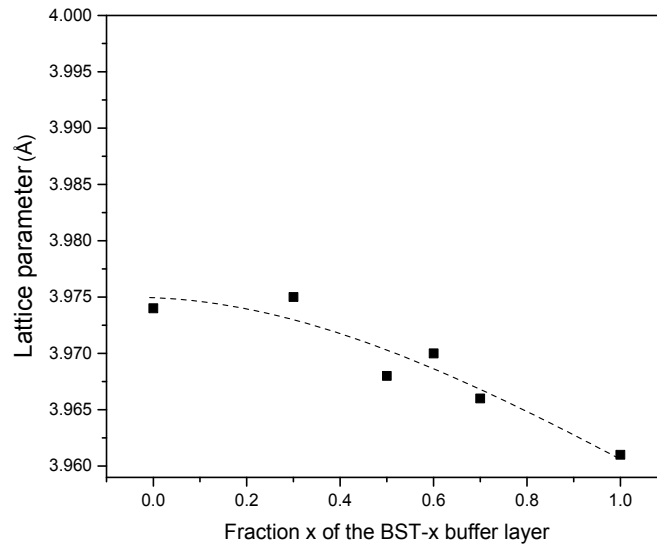
Figure 4.10: lattice parameter of BST-0.6 thin films grown on MgO substrate with different material of the buffer layer (BTO, BST-0.7, BST-0.5, BST-0.3, and STO).
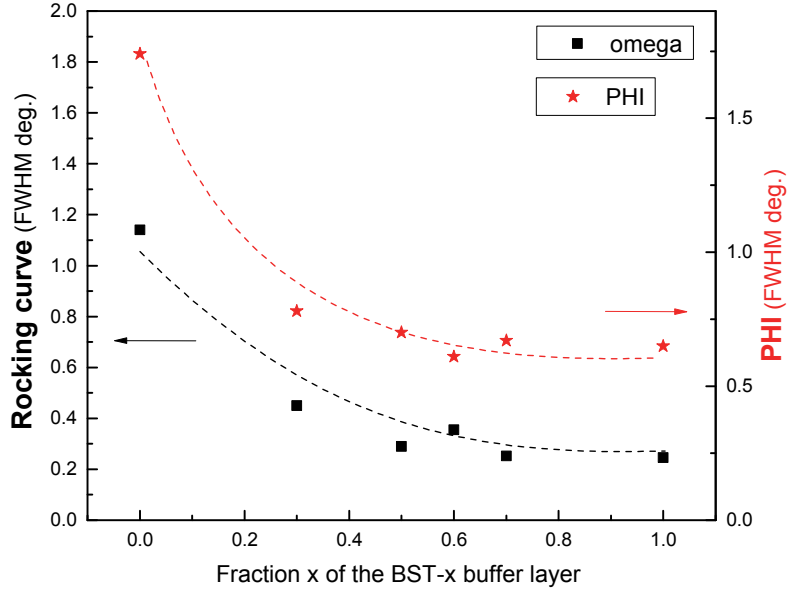
Figure 4.11: ω Scan (rocking curve) FWHM and Phi scan FWHM of BST-0.6 thin films grown on MgO substrate with different material of the buffer layer (BTO, BST-0.7, BST-0.5, BST-0.3, and STO).

ii. Microwave properties

Fig. 4.12 shows the dielectric constant and loss tangent (at 2 GHz, 0 V.µm^{-1}) of BST-0.6 grown on the different buffer layer materials. The typical results obtained for BST-0.6 thin films deposited without buffer layer, is reported on the same graph. It shows that both ε_r and tan δ increase as the fraction x increases from 0 to 1 (from STO to BTO). BST-0.6 on BTO buffer layer is found to have the highest dielectric constant (1184) and the highest loss (0.115), whereas the lowest dielectric constant (523) and the lowest loss (0.025) are observed for BST-0.6 on STO buffer layer. Fig. 4.13 shows the tunability and FOM at 2 GHz and 10 V.µm^{-1}, of BST-0.6 grown on different buffer layer materials. It indicates that the tunability follows the same trend as the loss tangent and the dielectric constant: it increases as a function of x, the highest tunability (of 74.6) being obtained for BST-0.6 on BTO buffer layer and the lowest tunability (22.1) for BST-0.6 on STO buffer layer.
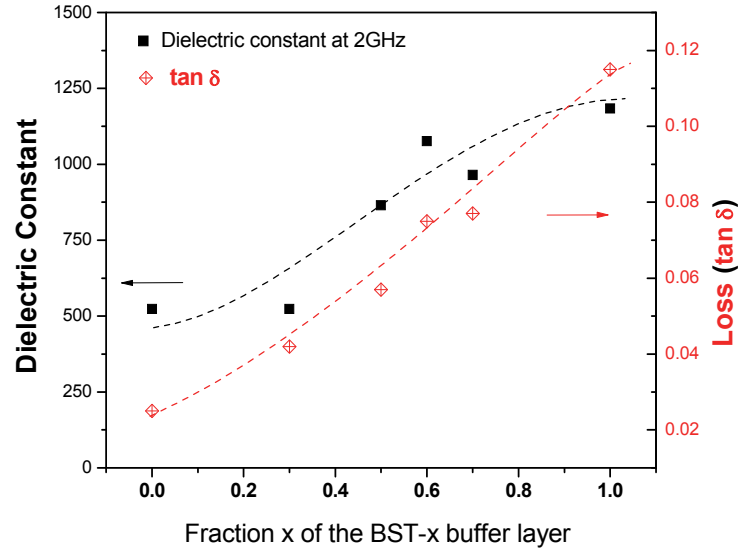
Figure 4.12: **Dielectric constant and loss tangent (at 2 GHz and no bias) of BST-0.6 thin films grown on MgO substrate with different buffer layer materials (BST-x, with x=0, 0.3, 0.5, 0.7and 1).**
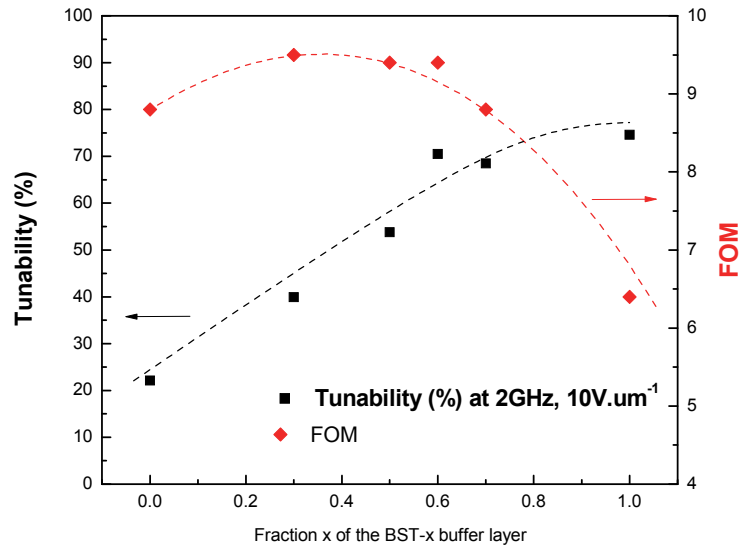
Figure 4.13: **Tunability and the Figure of Merit (at 2 GHz, 10 V.µm^{-1}) of BST-0.6 thin films grown on MgO substrate with different buffer layer materials (BST-x, with x=0, 0.3, 0.5, 0.7 and 1).**

Since the dielectric losses are increasing more rapidly than the tunability, the Figure of Merit presents a maximum for intermediate values of x, the FOM for x=0.3, 0.5 and 0.6 are all close to 9.5.

iii. Discussion

With increasing the fraction x of BST-x buffer layer from 0 to 1 (i.e. from STO to BTO) the lattice parameter gets closer to the bulk ceramic value of BST-0.6 (from 3.974 Å to 3.961 Å). As observed previously, this induces an increase of both the dielectric constant and tunability as x increases. At the same time, the crystal quality increases as x increases (FWHM of the rocking curve goes from 1.14° for STO to 0.246° for BTO) which induces a degradation of the material losses. This observation also corresponds to the general trend reported previously. A part of this increase in the material loss could also come from the buffer layer itself that possess increasing losses as x increases. Since the dielectric losses increase faster than the tunability, the best overall microwave characteristic corresponds to the film deposited on BST-0.3 and BST-0.5 buffer layer, the obtain FOM (~9.5 at 2 GHz and 10 V.µm^{-1}) is very close to the one of BST-0.6 deposited on MgO.

Table 4.3 shows the dielectric properties of the two samples that shows the highest FOM. The results of the FOM may suggest that when the BST-0.6 film experiences a small compressive stress it exhibits higher FOM value, as observed by other groups.[18,99]

Table 4.3: Dielectric properties of (BST0.6/ BST0.3/ MgO), and (BST0.6/ BST0.5/ MgO).

Best FOM sample	Dielectric constant	Loss tangent	Tunability(T%)	FOM
BST0.6/ BST0.3/ MgO	523	0.042	39.9	9.5
BST0.6/ BST0.5/ MgO	865	0.057	53.8	9.4

4.2.2. Doping with different materials

4.2.2a. Literature review

One of the most promising ways to reduce BST dielectric losses is the introduction of a dopant into BST. The objective is to reduce the loss tangent while maintaining a large tunability, considering that the high level of losses measured in BST thin films are due to oxygen vacancies. The oxygen vacancies can be represented as:

$$O_o^x \rightarrow \frac{1}{2}O_2 + V_o^{\cdot\cdot} + 2e^{'} \ldots\ldots\ldots\ldots\ldots\text{Eq. 4.2}$$
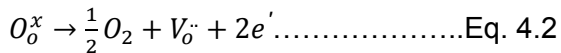
where O_o^x is the oxygen and $V_o^{\cdot\cdot}$ is the oxygen vacancy in the BST unit cell.[18]

The generated electrons reduce Ti^{4+} to Ti^{3+} and produce n-type semiconducting materials, which will increase the dielectric loss.

Acceptor dopants, such as Mg, Ni, Mo, Fe, Mn, Al, Cr, etc... are ions with lower valence than the ion to be replaced. These acceptor-type dopants occupy the B sites of the BST perovskite structure (ABO_3), and trap electrons. In the case of BST, B site are occupied by Ti atoms and dopant are expected to prevent the reduction of Ti^{4+} to Ti^{3+} and improve the dielectric loss.[100,101]

Introduction of dopants also plays a role on the material lattice parameter and stress, through the reduction or increase of the unit cell (due to lower or larger diameter ions) or the formation of oxide phases that exhibit low dielectric losses. For instance, the introduction of Mg, Zr or Al is expected to create oxides such as MgO, ZrO_2 and Al_2O_3 which are low-loss dielectric materials.

In the literature, lots of different groups studied the effect of doping on the structural and electrical characteristics of BST films.

Cole *et al*.[102] studied the characteristics of polycrystalline BST thin films doped with Mg. They observed that Mg is an effective way to reduce oxygen vacancies concentration and lower the losses of BST films. They also found that Mg doping limits the grain growth of BST and plays an important role in the reduction of BST dielectric constant.

Seo *et al.*[103] found that doping of BST thin film deposited at room temperature with Ni significantly reduced the losses. Khalfallaoui *et al.*[104] studied BST thin films with various dopants (Bi, Mg, K and Fe) up to 1 MHz on platinised silicon. Their results showed that Mg reduced the dielectric losses down to 0.008 at 1 MHz. They also found that Potassium, inducing a tunability increase (up to 36% at 1 MHz) is also an attractive

dopant. Unfortunately, their characterization up to 15 GHz on MgO substrates did not show any differences between the different films, the loss tangent being about 0.04 for all the films.

Liu *et al.*[105] epitaxially grown undoped and Mn doped BST thin films on LAO substrates. Their results revealed that Mn doping can reduce the loss tangent from 0.055 to 0.023 (at 15 GHz) with a specific Mn doping concentration of 0.5%.

Balzar *et al.*[85] did the same kind of investigation (W and Mn doped BST epitaxially grown on LAO substrate) and found that doping affects both the elastic and inhomogeneous strains in the films. Using the Landau-Devonshire model, the measured strain is correlated with the change in the Curie-Weiss temperature that can qualitatively explain the observed changes in extrinsic dielectric losses.

Doping with Co ions also decreases the dielectric loss of BST thin films from 0.17 for undoped films to 0.036 for 0.5% doped films. These films, deposited on Sapphire by Xiao *et al.*[106] were characterized at 17 GHz.

4.2.2b. Doping with different elements

In order to investigate the influence of doping on the structural and microwave properties of BST-0.6 films deposited on MgO, a series of BST-0.6 films doped with Mg, Fe, Ni, Mo and Ti were prepared by PLD. Doping in these experiments was achieved by covering part of the target with a foil of the metal (Ni, Fe, Mo, Ti) and, in case of magnesium doping, a piece of MgO substrate was used. The metal foil or the piece of MgO substrate covered 5% of the total target surface. Undoped and doped BST-0.6 films were deposited on MgO single crystal substrates by using KrF excimer laser (λ=248nm) with laser repetition rate 10 Hz. In order to ablate both the ceramic BST target and the metal foil covering it, the laser fluence was raised up to 3.5 J/cm^2. The substrate temperature was fixed at 800°C and the oxygen pressure was maintained at 10 mTorr. After deposition, all the films were annealed in O$_2$ background at 1050°C for 3h.

i. Structural properties

XRD patterns (θ/2θ scan) of epitaxial undoped and doped BST-0.6 thin films deposited on MgO substrate showed that BST doped with Mg and Ni have secondary phase of MgO and NiO respectively, while Ti, Fe, and Mo have no evidence of secondary phase formation. Mg, Fe, Ni and Mo are all acceptors that are expected to replace Ti atoms in the BST lattice and hence should have 4 covalent bonds with Oxygen atoms. Table 4.4 shows ionic radius of Mg^{2+}, Ni^{2+}, Mo^{4+}, Fe^{4+}, and Ti^{4+} ions and indicates that Mo^{4+}, and Fe^{4+} ions have smaller ionic radii than Ti. The influence of these ionic radii on the lattice parameter of the BST is difficult to predict, since the stress and the presence of secondary phase will also strongly influence the lattice parameter value. One other important factor is the difference in ablation rate between the different materials that will change the doping level present in each BST layer.

Fig 4.14 shows the lattice parameter of Mg, Ni, Mo, Fe, Ti doped BST thin films grown on MgO substrates, compared with the value of undoped BST. One can note that the lattice parameter of Mg doped BST is lower than the undoped BST, while Ni, Mo, Fe, and Ti doped BST have higher lattice parameter than the undoped BST.

Table 4.4: ionic radius of Mg, Ni, Mo, Fe, and Ti.

Ion	Mg^{2+}	Ni^{2+}	Mo^{4+}	Fe^{4+}	Ti^{4+}
Crystal Ionic radius (pm)	86	83	65	72.5	74.5
Effective Ionic radius (pm)	72	69	65	58.5	60.5
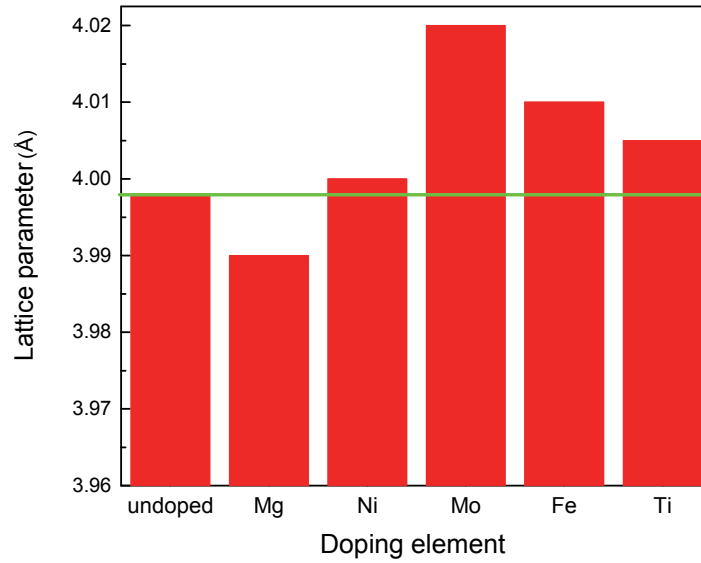
Figure 4.14: The lattice parameter of undoped BST and (Mg, Ni, Mo, Fe, Ti) doped BST thin films grown on MgO substrate, the green line corresponds to position of undoped BST.

ii.   Microwave properties

Fig. 4.15 shows the dielectric constant and loss tangent (at 2 GHz, 0 $V.\mu m^{-1}$) of undoped BST and (Mg, Ni, Mo, Fe, Ti) doped BST thin films grown on MgO substrates, and Fig. 4.16 shows the tunability (at 2 GHz, 10 $V.\mu m^{-1}$) and FOM of the same samples. It is observed that the dielectric loss of Mg, Ni, Mo, and Fe doped BST thin films are lower than the undoped BST thin film (0.034) while Ti doped BST show the same dielectric loss as undoped BST thin film. Mg doped BST thin film presents the lowest dielectric loss (0.028) with a dielectric constant very close to the one of undoped BST thin film (~500). For Ni, Mo, and Ti doped BST thin films show slightly lower dielectric constant than undoped BST thin film, and Fe doped films exhibit a dielectric constant that is almost divided by two compared to the undoped layer.

The tunability follows almost the same trend as the dielectric constant, the tunability of Mg doped films being the same as undoped films, whereas tunabilities of Ni, Mo and Ti doped films are all lower and divided by two for the Fe-doped sample.

145

iii.   Discussion

These preliminary results indicate that Mg, compared to the other elements, is the most promising dopant for BST-0.6 films deposited on MgO. While Ni, Mo, Fe and Ti all increase the lattice parameter of BST, which is not a good thing in regard to the overall dielectric properties of the films, Mg doping is decreasing the lattice parameter down to values closer to the BST-0.6 bulk value. This phenomenon is certainly related to the formation of a very low-loss secondary phase that allows relaxation of the film stress without degrading the tunability of the material. The suppression of oxygen vacancies may also be responsible for both the reduction of the lattice parameter and the reduction of losses in the material.

One of the drawbacks of the deposition technique used (that offers the possibility to obtain different level of doping by varying the area of MgO used) is that it forces to work at higher fluences in order to ablate MgO.
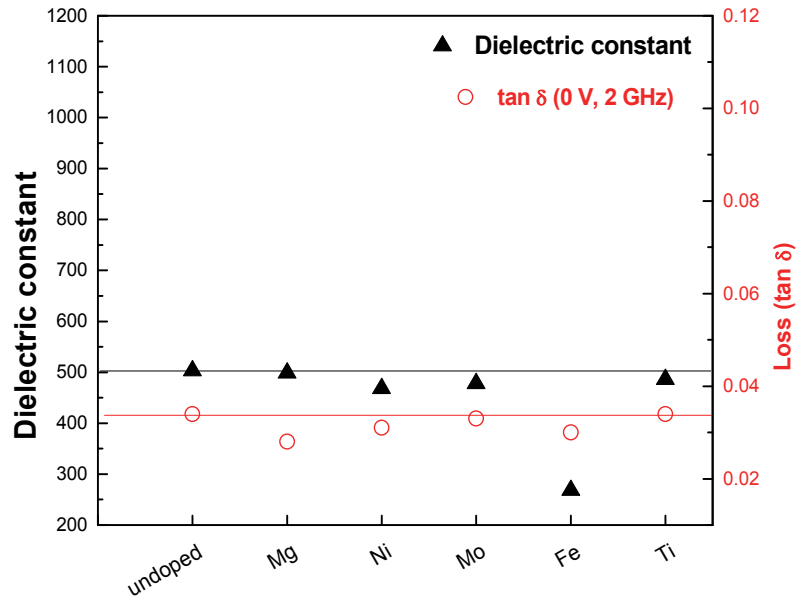
Figure 4.15: Dielectric constant and loss tangent (at 2 GHz, 0 V.μm^{-1}) of undoped BST and (Mg, Ni, Mo, Fe, Ti) doped BST thin films grown on MgO substrate, the black and red lines correspond to position of undoped BST.
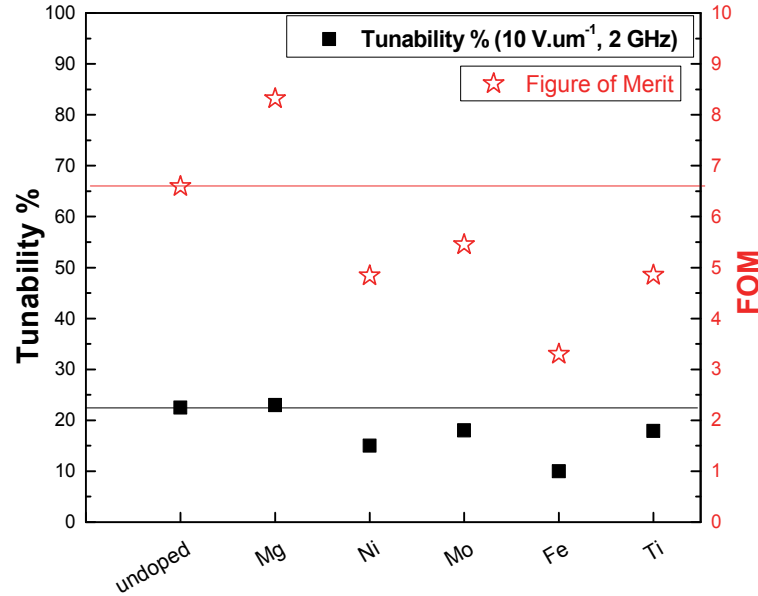
Figure 4.16: Tunability (at 2 GHz, 10 V.μm^{-1}) and FOM of undoped BST and (Mg, Ni, Mo, Fe, Ti) doped BST thin films grown on MgO substrate, the black and red lines correspond to position of undoped BST.

4.2.3. Doping with Mg using ion implantation

In order to further study the influence of Mg doping while using optimized BST deposition conditions we decided to use the implantation technique. Implantation is a doping technique used to introduce controllable element concentrations at a precise depth below the surface of a material. Mg was chosen because it showed the most promising improvement of the BST characteristics according to the preliminary tests presented in the previous section.

4.2.3.a. Literature review

Very few groups reported studies of ion implantation on BST thin film. Only three papers were found on the subject and only one reporting the influence on dielectric properties (at low frequency):

Dietrich *et al.*[107] studied the lattice damage caused by the implantation of ^{111}In (with energies of 60 and 400 keV) of epitaxial $BaTiO_3$ thin films deposited on $SrTiO_3$ single

crystal substrate. They monitored the recovery of the lattice after the implantation by perturbed angular correlation (PAC) spectroscopy.

Gao *et al.*[108] had shown that N-doped BST-0.6 by implantation can be effectively eliminating the oxygen vacancies at lower implantation energy. On the other hand when enhanced implantation energy is used the oxygen vacancies increased. In addition the refractive index decreased largely with nitrogen implantation.

Horng *et al.*[109] studied the effect of ion implantation (with Ar+, N^+ and F^+) on the properties of BST-0.7 thin films. They found that the implantation of F^+ ions improved the losses of BST films and modified its refractive index (compared to implantation with Ar^+ and N^+ and non-implanted films). The optimum F^+ implantation dose (of 5×10^{14} cm^{-2}) exhibits a dielectric constant of 515 which is higher than the non-implanted film. The observed change is attributed to a reduction of –OH contaminant into the sol-gel film.

In the present work, Mg was implanted in epitaxial BST thin film in order to study its influence on the structure and microwave properties of BST films, a study that was never explored by any group.

4.2.3.b. Experimental conditions

A series of epitaxial BST-0.6 films were deposited on MgO single crystal substrates by PLD technique using the optimized deposition conditions determined previously: a laser repetition rate of 10 Hz and a fluence of 1 J/cm^2 (obtained with 110 mJ laser energy and 11 mm^2 laser spot area), the substrate temperature being fixed at 800 °C with background oxygen pressure 10 mTorr. After deposition, all the films were annealed in O_2 background at 1050°C for 3h. The obtained epitaxial BST-0.6 films were then used for ion implantation experiments using a modified Varian CF3000 implanter (model IMC-200 from Ion Beam Services) available at the Laboratory of Micro and Nanofabrication of the INRS. It is a system that has available energies ranging from 1 keV to 200 keV (400 keV for double charge) with medium current (up to 1 mA depending on species) and the ability to work with gas, solid or liquid sources.

Different experiments were conducted with Mg implantation, in order to study its effect on the dielectric properties of BST thin films, our objective is to improve the dielectric loss and the FOM while maintaining high tunability.

Fig 4.17 shows a typical doping profile (obtained by ERDA) of Mg implanted in BST-0.6 thin film at 50 keV energy and 1×10^{15} Mg$^+$ ion /cm^2 dose. The measurement was done after annealing in an oxidizing atmosphere for 30 minutes in furnace at 1000°C (used to reduce the defects generated by the implantation). The implantation profile presents a Gaussian distribution with a maximum (of 20 at.%) at about 80nm below the sample surface (the layer thickness being about 500 nm) and present no significant amount of Mg below 160 nm.
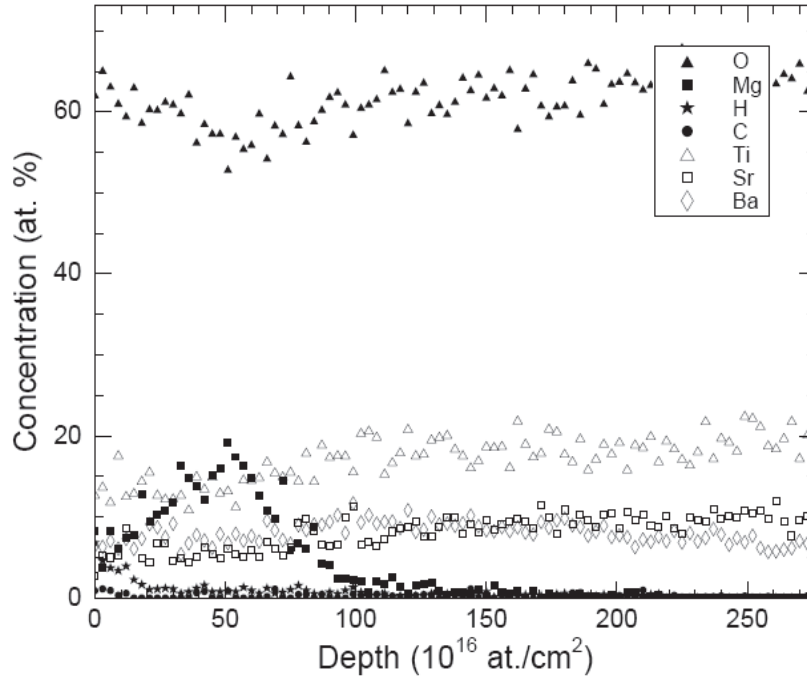
Figure 4.17: **ERDA results of Mg implanted 500nm thick BST-0.6 thin film at 50 KeV energy and 1X 10^{15} Mg$^+$ ion /cm^2 dose.**

4.2.3.c. Effect of the post-implantation annealing

In ion implantation, sufficient energy transfer exist through elastic collisions to displace an atom from its lattice site. This leads to a distribution of vacancies, interstitial atoms and other types of lattice disorder. Hence annealing is important after ion implantation to repair lattice damage and put dopant atoms on substitutional sites. Implantation damage depends on implanted species (heavy ions produce more damage); energy (more energy, more damage); and dose. At low dose, the implantation creates point defects such as vacancies and interstitials defects. At high dose, extended defects are created, and even amorphization can take place.[110] The recovery of such defects is important to enhance the structural and dielectric properties. If ion implantation damages an epitaxial thin film and/or produces an amorphous layer, it is possible to re-grow this disordered layer by an appropriate choice of annealing conditions to repair the epitaxial layer.[111]

In order to study the effect of post implantation annealing on the material properties, epitaxial BST-0.6 were prepared by PLD with optimized deposition conditions. These samples, implanted with Mg at 50 keV and a dose of 1x 10^{14} Mg$^+$ ion/cm^2, were then annealed at different temperatures for characterization. Different samples were annealed in a furnace in an oxidizing atmosphere at 900°C, 1000°C and 1150°C respectively for 30 min. An as implanted sample was kept as a reference and results were compared with those obtained for epitaxial BST films prepared in the same conditions (a_{BST} = 3.97 Å, ω-scan FWHM = 0.3°, ε_r =1000, tanδ = 0.06 and T% = 60).

i. **Structural properties**

Fig 4.18 shows variation of the lattice parameter and the rocking curve (FWHM) as a function of post implantation annealing temperature. The results are compared to the undoped and non-implanted film (open symbols) and un-annealed films (left point of the curve). This figure shows, without too much surprise, that the effect of implantation degrades the epitaxial quality of the film and increases its lattice parameter. Increasing post-implantation annealing temperature is able to repair implantation damages on the crystal as the rocking-curve FWHM decreases down to a value very close to the one of undoped and non-implanted film. The lattice parameter first increases at 900°C and decreases below the value of undoped and non-implanted film, getting closer to the value of the bulk for 1000 and 1150°C.

ii. Microwave properties

Fig 4.19 shows the dielectric constant and loss tangent (at 2 GHz, 0 V.μm^{-1}), and Fig 4.20 shows the tunability and the Figure of Merit (at 2 GHz, 10 V.μm^{-1}) of BST-0.6 epitaxial films as a function of post implantation annealing temperature. The evolutions of dielectric constant and losses are a bit more unexpected. It is observed that the un-annealed sample have almost the same dielectric losses as the undoped and non-implanted film, but with a two times lower dielectric constant and a 30% lower tunability. As the annealing temperature increases, the dielectric constant reaches the value of the undoped and non-implanted film for 900 and 1150°C (~1000) whereas the value at 1000°C is a bit lower (~800). The dielectric losses present the same trend but with larger variations: at 900°C, tanδ value goes higher than the one of undoped and non-implanted film (0.07 compared to 0.06), then presents a minimum of 0.035 at 1000°C before increase again up to 0.05 at 1150°C post-implantation annealing temperature.
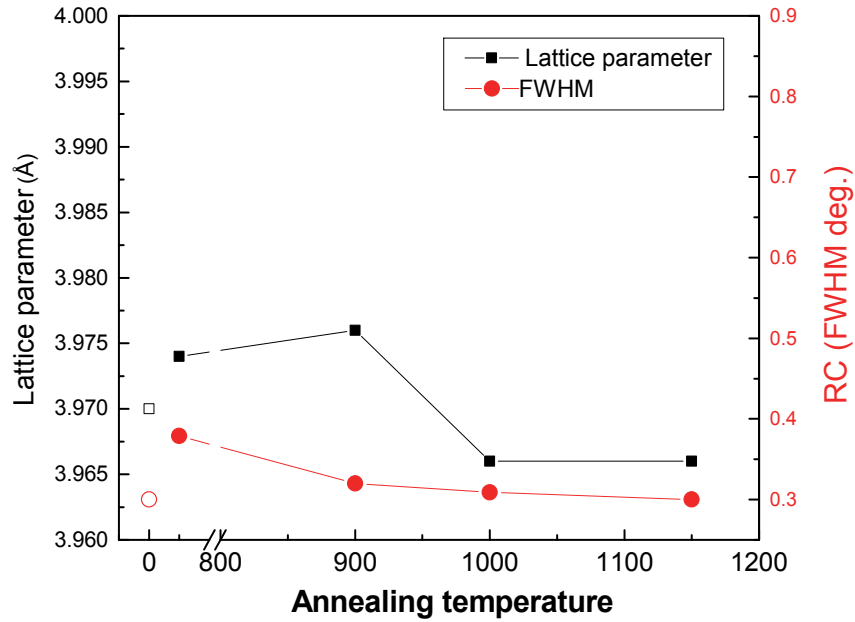
Figure 4.18: lattice parameter and rocking curve FWHM of Mg implanted BST-0.6 thin films with different post implantation annealing temperature (as implanted, 900°C, 1000°C, and 1150°C).
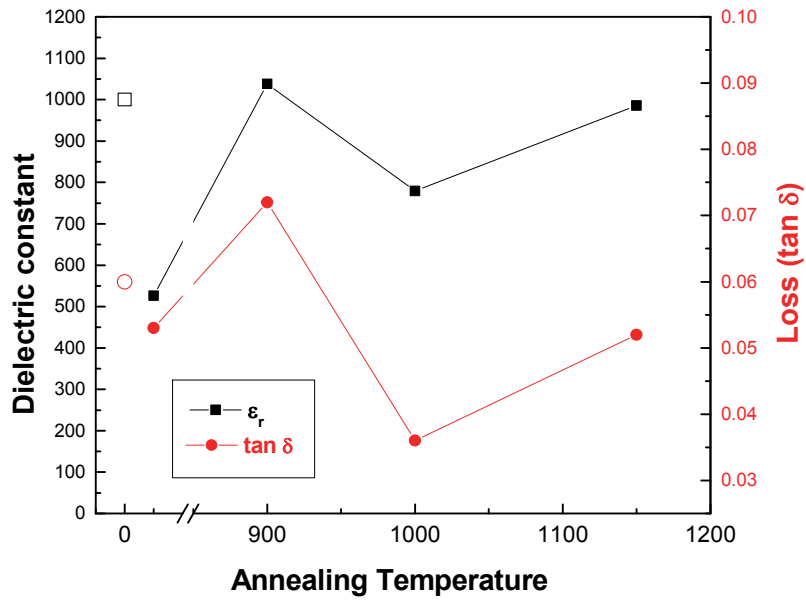
Figure 4.19: Dielectric constant and losses of Mg implanted BST-0.6 thin films with different post implantation annealing temperature (as implanted, 900°C, 1000°C, and 1150°C).
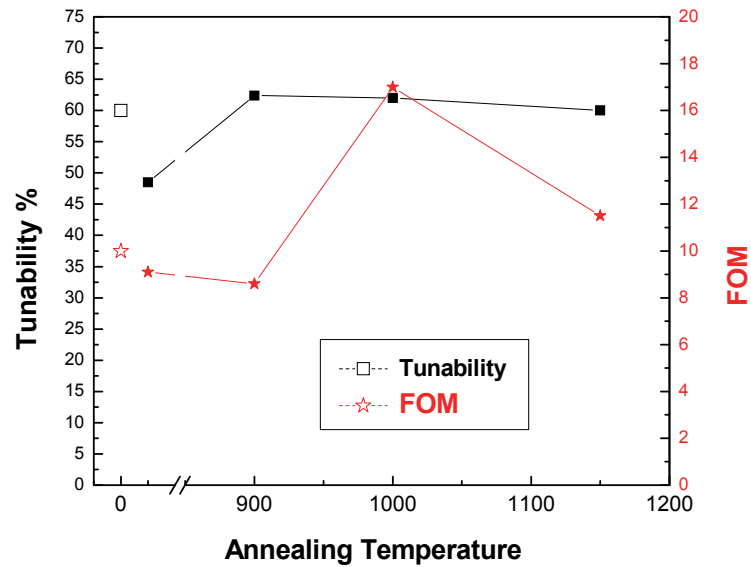
Figure 4.20: Tunability and FOM of Mg implanted BST-0.6 thin films with different post implantation annealing temperature (as implanted, 900°C, 1000°C, and 1150°C).

The tunability presents almost the same value (~60% at 2 GHz and 10 V.μm^{-1}) for the three annealing temperature, it only slightly decrease from 900 to 1150°C. Since the losses varies a lot in the same range (and is minimum at 1000°C), the Figure of Merit presents a maximum of 17 at 1000°C post-implantation annealing temperature, almost two times higher than the 900°C condition.

iii. **Discussion**

Looking at these results, the first observation is that the material modification mechanism behind the implantation process seems to present large differences compared to all the previous results. First, the correlation between the lattice parameter and the tunability is less evident but the largest difference concerns the link between the tunability and the dielectric losses: for all the previous set of experiments, and whatever the deposition parameter are, it was always observed that any improvement of the tunability led to a degradation of the dielectric losses and vice-versa. Here, for epitaxial BST films implanted with Mg at 50 keV and a dose of 1x 10^{14} Mg^{+} ion/cm^2, the post-implantation annealing temperature gives optimum tunability (of about 60%) at 900°C, 1000°C and 1150°C, but induces a large variation of the dielectric losses; tanδ going from 0.07 at 900°C to 0.035 at 1000°C and then increasing again up to 0.05 at 1150°C. Moreover, the Figure of Merit of the implanted but un-annealed sample is not far away from the non-implanted sample, with comparable tunability and dielectric loss. This variation may indicate that for low damage conditions and implantation of Mg very close to the BST surface, the creation of a low-loss and low dielectric constant layer close to the surface has a great influence on the measured losses whereas the tunability and dielectric constant measurements are not really affected by this change.

The annealing temperature is expected to give mobility to the implanted species and help to repair implantation damages. Magnesium having a boiling point of 1090°C, it is hence possible that at higher annealing temperature some implanted species evaporates from the layer surface. An annealing temperature of 1000°C, just below the Mg evaporation temperature, certainly represents the best tradeoff between crystal defects repair and the spreading of Mg into the BST layer.

4.2.3.d. Effect of Mg implantation Energy

In order to study the effect of the implantation energy, Mg ions were implanted in BST-0.6 at room temperature with implantation energy 50 keV and 100 keV and implantation dose of 1×10^{14} Mg^{2+}/cm^2. The implantation energy affects the Mg depth profile in BST: with increasing implantation energy the Mg profile is expected to become deeper and broader. The obtained samples were annealed in an oxidizing atmosphere for 30 minutes in furnace at $1000°C$.

i. **Structural properties**

Typical XRD (θ–2θ) spectra of Mg implanted epitaxial BST-0.6 thin films grown on MgO substrate with implantation energy 50 keV, and 100 keV showed epitaxial films with no sign of secondary phases. XRD analysis give a lattice parameters of 3.966 Å and 3.980 Å, with a rocking curve full width at half maximum (FWHM) of 0.309° and 0.42° for the samples implanted with 50 keV and 100 keV energy respectively. If we compare these values to the non-implanted and undoped samples (typical lattice parameter of 3.97 Å and ω FWHM of 0.3°), it shows that implantation at 50 keV slightly improves the BST lattice parameter (which gets closer to the bulk value) without degrading too much the material crystallinity, whereas 100 keV implantation degrades both parameters.

ii. **Microwave properties**

Table 4.5 summarizes the dielectric properties of Mg implanted epitaxial BST-0.6 thin films with 50 keV and 100 keV implantation energy compared to the non implanted and undoped film. As expected from the different structural characteristics of the samples, it is observed that large differences exist between the different thin film microwave characteristics. The sample with Mg implantation at 50 keV energy shows lower dielectric constant (780), similar tunability (62%) and much lower dielectric loss (0.036) that the non-implanted and undoped BST, whereas the sample implanted at 100 keV exhibit lower dielectric constant and higher losses. This results show a very high FOM for the BST implanted at 50 keV (17) compared to the non-implanted and BST implanted at 100 keV (with FOM of ~10 and ~7 respectively).

Table 4.5: Dielectric properties of Mg implanted BST-0.6 thin films with implantation energy, 50 keV, and 100 keV.

Implantation	Dielectric constant	Loss tangent (at 0 V & 2 GHz)	T% (at 10 V. μm^{-1} & 2 GHz)	FOM
None	1000	0.065	65	10
50 keV	779	0.036	62	17
100 keV	639	0.068	46.3	6.8

iii. **Discussion**

Since implantation energy plays a role on the implantation depth and on the damages created inside the implanted material, it is expected that implantation at 100 keV will cause higher damages close to the surface and introduction of Mg deeper inside the layer with a broader distribution.[112] The larger damage at higher energy may explain the decrease of the crystal quality between 50 keV and 100 keV, but it is not clear how Mg implantation influences the lattice parameter. The role of Mg in the ABO_3 unit cell is complex since it can substitute to A and B sites at the same time and be coupled with a change in the oxygen vacancy behavior.[113] In the case of homogenous distribution, these concurrent effects yield to a decrease of BST lattice parameter for small amount of Mg (up to 1 at. %) and an increase of the lattice parameter for higher concentrations. Here what is observed is that a Mg distribution close to the surface (with a maximum of ~20 at.% 80nm below the surface) corresponds to BST with a smaller lattice parameter, higher tunability and smaller losses whereas Mg implantation profile with a broader and deeper distribution (100 keV case) corresponds to larger lattice parameter, larger dielectric losses and a lower tunability. Here, the variation of tunability is coherent with the variation of material lattice parameter and the differences in material losses may point to a mechanism associated with either material damage and/or oxygen vacancies.

4.2.3.e. Effect of Mg implantation dose

In order to study the influence of Mg implantation dose, epitaxial BST-0.6 thin films were implanted at 50 keV with doses ranging from 1×10^{14} Mg ion cm^{-2} to 5×10^{17} Mg ion cm^{-2}. After the implantation, the films were annealed in an oxidizing atmosphere for 30 minutes at 1000°C.

i. **Structural properties**

XRD results (θ–2θ, omega, and phi scans) confirm the epitaxial structure of BST after implantation and annealing, with no sign of secondary phases. For high implantation doses (1×10^{16} & 5×10^{17} Mg ion cm^{-2}) a broadening of XRD (θ–2θ) FWHM peaks is observed compared to low doses (1×10^{14} Mg ion cm^{-2}) which certainly indicates higher stress in the film. Fig 4.21 shows lattice parameter of 50 keV Mg implanted BST-0.6 thin films as a function of Mg implantation doses (1×10^{14}, 1×10^{15}, 1×10^{16}, 1×10^{17} and 5×10^{17} Mg ion cm^{-2}). All the implanted samples have lattice parameter closer to the bulk value (3.96 Å) than the non-implanted film (3.97 Å), except for the 1×10^{16} dose which exhibits a higher value (close to 3.974 Å).
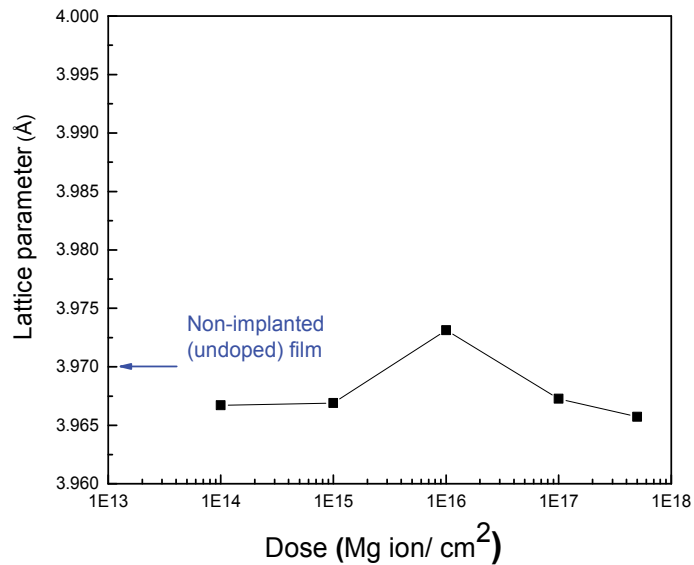
Figure 4.21: lattice parameter of Mg implanted BST-0.6 thin films grown on MgO substrate with different implantation doses.

ii. Microwave properties

Fig 4.22 shows the dielectric constant and loss tangent (at 2 GHz, 0 V.µm^{-1}), and Fig 4.23 shows the tunability and the Figure of Merit (at 2 GHz, 10 V.µm^{-1}) of BST-0.6 epitaxial films as a function of the implantation dose. It is observed that the dielectric loss increases as the implantation dose increases, reaching a value of 0.066 at $5{\times}10^{17}$ Mg ion cm^{-2}, whereas the dielectric constant presents a maximum at $1{\times}10^{16}$ ion cm^{-2}. The tunability slightly decreases as the implantation dose increases, and presents a drop for the sample implanted with very high implantation dose (5×10^{17} Mg ion cm^{-2}, tunability = 42%) that could result from the accumulated damage caused by the implantation. These damages or the presence of higher stress could also be at the origin of the dielectric loss increase. The decrease in tunability and increase in dielectric losses induces a quasi-constant decrease of the overall microwave characteristics of the films as a function of the implanted dose (FOM decreases from 17 for the $1{\times}10^{14}$ Mg ion cm^{-2} dose down to 6 for the 5×10^{17} Mg ion cm^{-2} dose).
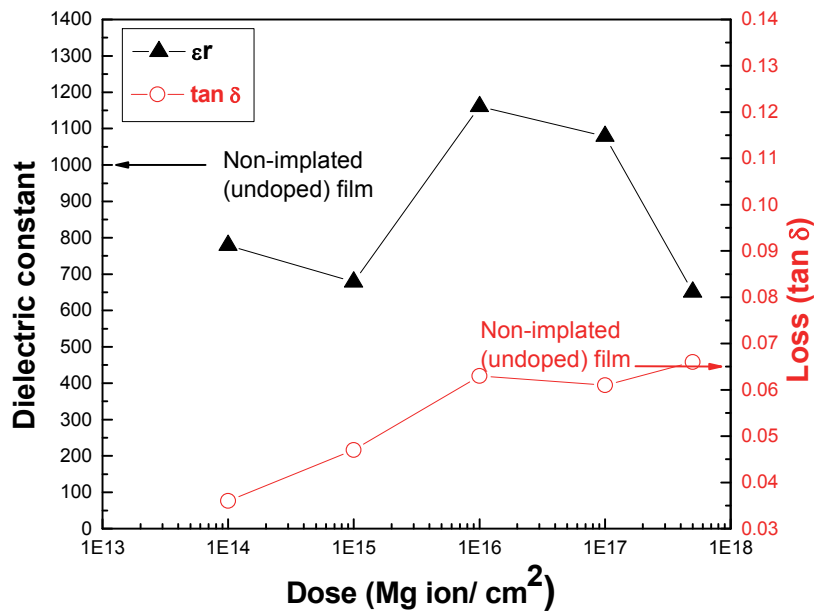
Figure 4.22: Dielectric constant and loss tangent (at 2 GHz, 0 V.µm^{-1}) of BST-0.6 thin films grown on MgO substrate as a function of the implantation dose.
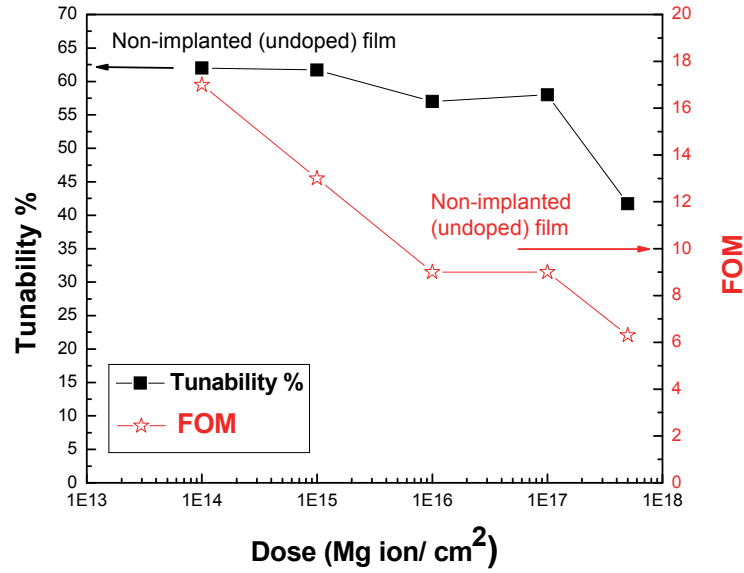
Figure 4.23: Tunability and FOM (at 2 GHz, 10 V.µm^{-1}) of BST-0.6 thin films grown on MgO substrate as a function of the implantation dose.

iii. Discussion

In all the previous experiments, it was observed that the BST dielectric constant presents almost the same trend as the tunability and that tunability was closely linked to the material lattice parameter (the closer the lattice parameter to the one of the bulk, the higher the dielectric constant and tunability). Here the effect of Mg implantation does not follow the same trend: there is no clear correlation between the tunability and lattice parameter and high ε_r do not correspond to higher tunability. This reveals (as for the influence of the implantation energy) an unexpected change in the material characteristics specifically related to the implantation. Since no evidence of secondary phase is observed (contrary to conventional BST doping technique), and that Mg is implanted after the material crystallization (and not during as for conventional doping) the main effect of implantation seems to include damages in the material. It is not clear how Mg is included in the BST unit cell but it may be substitution with A or B sites or simply bonds with oxygen at random sites.

What is sure is that higher implantation dose creates more damage in the material and annealing will leave more and more defects as the implantation dose increases. This was observed in the case of Mg-implanted epitaxial GaN, where unexpected lattice parameter

change is observed at high implantation doses.[114] In the case of epitaxial BST films, the presence of defects can be a way to relax the stress present in the films but, at the same time, the inclusion of another element into the BST matrix should increase the material stress. These contradictory effects make it difficult to interpret the influence of Mg implantation on the material characteristics and especially on the microwave properties. What is observed is that, for a 30min annealing time (at 1000°C in an oxidizing atmosphere), low implantation dose improves a lot the material properties in contrast with dose higher than $1x10^{16}$ Mg ion cm^{-2}, the overall microwave properties decrease below the one of non-implanted films mainly because of a rapid increase in the material losses. This effect may be due to implantation damages that annealing can not repair.

4.3. General Synthesis of BST results

In order to draw a general conclusion on the BST-0.6 results, the last experiments were added to the previous correlation found on the experimental sets (presented on section 4.1). The Table 4.6 summarizes the different sets of conditions investigated in chapter 4, namely the buffer layer study (section 4.2.1), doping material (section 4.2.2), and Mg^+ Implantation (section 4.2.3).

Table 4.6: Description of the sample sets. For each set the values of the studied parameter are mentioned and the typical values used for the deposition of the other sets are underlined.

Set #	Variable parameter	Values of the variable parameter
7	Buffer layer	None, STO (50 nm), $BST_{0.3}$ (50 nm), $BST_{0.5}$ (50 nm), $BST_{0.7}$ (50 nm), BTO (20, 50, 100 nm).
8	Doping material	None, Mg, Ni, Mo, Fe. *
9	Mg^+ Implantation (500 μA)	• None, 50 keV (1×10^{14}) no annealing, 900°C, 1000°C and 1150°C annealing • 50 keV, 100 keV for 1×10^{14} ions/cm^2 (annealed at 1000°C) • 50 keV, Dose : 1×10^{14}, 1×10^{15}, 1×10^{16}, 1×10^{17}, 5×10^{17} ions/cm^2 (annealed at 1000°C)

* **Laser fluence of 3.5 J/cm^2 (315 mJ on 9 mm^2 spot size)**

4.3.1. Correlation between lattice parameter and tunability (Landau–Devonshire model)
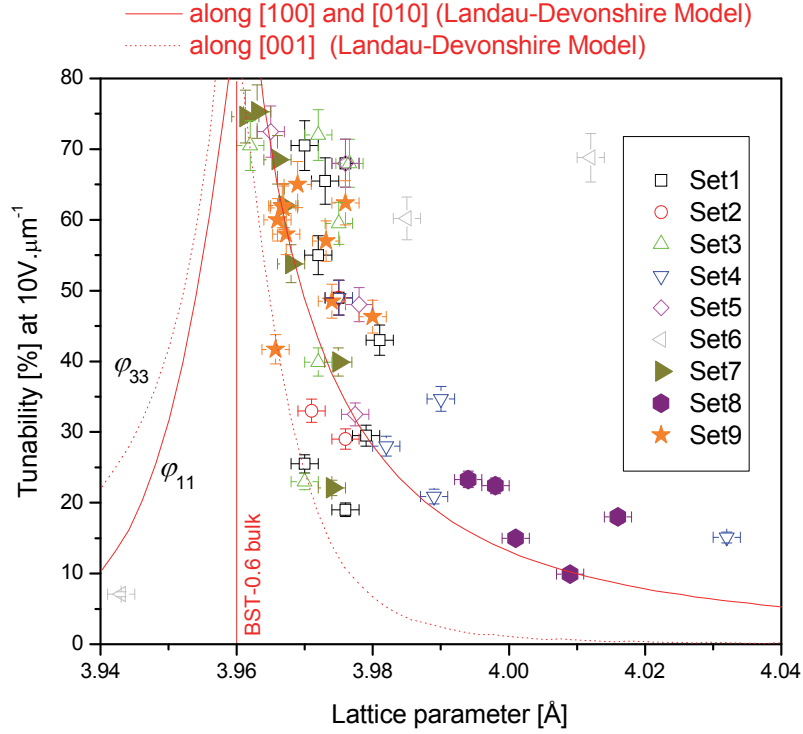
Figure 4.25: BST-0.6 tunability (at 2 Ghz, and 10 V/ μm) as a function of the measured lattice parameter for the different sets presented in Table 4.1 and 4.6. The theoretical in-plane and out-of plane tunability for epitaxial films (φ_{11} and φ_{33}), calculated using the Landau-Devonshire model, are plotted for comparison.

The Fig. 4.25 presents the compilation of all the experimental sets presented in this thesis. The sets 1 to 6 (open symbols) are the same as the one presented at the beginning of the present chapter (Fig. 4.3) with the addition of Set #6 (BST synthesis with different Barium content); the set 7 to 9 (filled symbols) correspond to the new experimental conditions presented in the previous section (4.2). As for Fig. 4.3, the experimental data of BST tunability as a function of the lattice parameter are compared with the theoretical calculation based on the Landau-Devonshire model.

It is observed that the new sets are very close to the previous trend and are following the variation of the calculated tunability. The experimental values from samples with different buffer layers (set #7) are almost directly on the $\varphi_{11}(a_{BST})$ curve whereas the samples from doping and

implantation experiment (Set#8 and 9) are regrouped around the theoretical curve with values close to the bulk and high tunability for the Set #9 and large lattice parameters with low tunability for the Set #8.

Points completely outside the general trend are from the Set #6 which regroups different BST-x material. This comes from the fact that the theoretical curve depends on both the Curie temperature of the BST-x considered and the curve maximum is directly related to the bulk BST-x lattice parameter value.

4.3.2. Correlation between dielectric loss and tunability

The Fig. 4.26 presents, on the same graph, all the experimental sets presented in this thesis. The sets 1 to 6 (open symbols) are the one presented at the beginning of this chapter (Fig. 4.4) and the set 7 to 9 (filled symbols) correspond to the new experimental conditions presented in the section 4.2. As for the sets 1 to 6, the BST tunability of sets 7 and 8 present an almost linear dependence on the dielectric losses. Above 70% tunability BST-0.6 presents a saturation of the tunability that may be attributed to intrinsic limitations, the losses being about 0.08 at this point. Above this value the tunability does not improve much but the material losses can reach values as high as 0.12. This is exactly the trend observed for the previous sets (#1 to 6).

The experimental data that are completely outside this curve are all from the set #9 (Mg implantation), which confirms the very particular characteristics of implanted samples. This phenomenon reveals that a completely different mechanism, particularly affecting the losses, plays an important role on the losses of implanted samples: whereas the tunability as a function of the measured lattice parameter is coherent with the other sets (and follows the theoretical Landau-Devonshire model), the set #9 is the only one where some samples exhibit high tunability and low losses at the same time. Since the dielectric losses can be divided by almost two with implantation (compared to the best BST-0.6 epitaxial film), without affecting the tunability, the best Figure of Merit is obtained for a film implanted at low energy, low dose (50 keV and $1x10^{14}$ ions.cm^{-2}) and annealed at 1000°C.
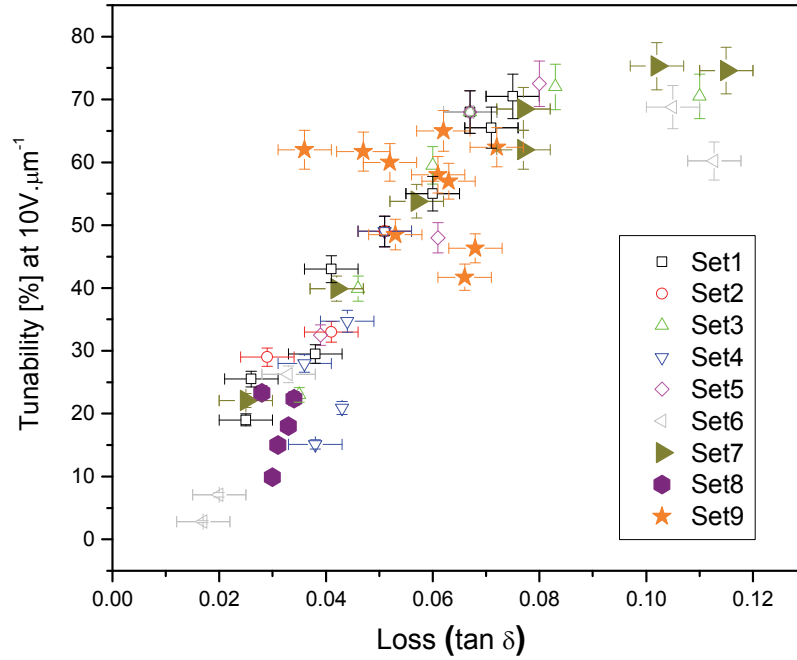
Figure 4.26: **BST-0.6 tunability (at 2 GHz, and 10 V/ µm) as a function of the measured dielectric loss for the different sets presented in Table 4.1.and 4.6**

4.3.3. Observations

A lot of papers are attributing losses to the presence of charged defects, grain boundaries or dislocations, [92,93] but the general trend of Fig. 4.26 may point to another mechanism: in the present study, the films with the best crystal quality are the one that present the higher losses and these losses are decreasing as the films microstructure goes from epitaxial to textured and polycrystalline.

The dielectric losses do not seem to be degraded by the average film strain either: this strain, induced by the lattice mismatch between MgO and BST-0.6 (a = 4.212 Å and 3.960 Å respectively) is supposed to relax as the film lattice parameter gets closer to the BST-0.6 bulk value. What is observed here is the contrary: dielectric losses are decreasing as the lattice parameter increases (as values are getting closer to MgO bulk value). It is also interesting to note that the lattice parameter stretching is not accompanied by an asymmetric variation of ε (E)

162

and larger losses, characteristic of films in the ferroelectric state, as one could expect from film with a lattice parameter close to the one of $BaTiO_3$ (a = 4.02 Å).

The intrinsic microwave losses of the BST-0.6 being about 0.01-0.02 (microwave loss value for bulk ceramic),[115] the extrinsic losses of the material are mainly driven by the thin film interfacial stress more than the presence of defects, the quality of the crystal or the grain boundaries as it is commonly admitted.

As reported by G. Catalan *et al.*[90], strain gradient due to misfit strain can induce degradation of the ferroelectric dielectric properties due to the presence of large flexoelectric coefficients. In the proposed model (section 1.2.5), strain gradient is splitting the bulk Curie temperature (T_c) into three distinct temperatures: the strain modified Curie temperature T_{c^*}, the temperature of the maximum dielectric constant T_m, that are both increasing with stress gradient, and the ferroelectric transition temperature, T_{ferro}, that is decreasing with stress gradient (with $T_m > T_c^* > T_c > T_{ferro}$). The flexoelectric coefficient is particularly large in BST [116] and reaches a maximum near the ferroelectric phase transition.

We can suspect from our experimental results that the tunability is linked to T_m whereas $\tan\delta$ values are linked to the ferroelectric transition T_{ferro} (the dielectric losses of the ferroelectric state being much larger than the one of paraelectric state in ceramics). For strain – relieved films that possess large interfacial stress gradient (as the one having lattice parameters close to the BST bulk value), T_m and T_{ferro} will be close to room temperature with the presence of a large flexoelectric coefficient. The dielectric constant (and hence the tunability) and $\tan\delta$ will be maximum, the value of the losses being well above the intrinsic loss value due to the presence of a large stress gradient at the substrate interface.

In the case of thin film with large stress but low interfacial stress gradient (case of films with lattice parameter close to the one of MgO), the ε (T) peak will be broaden and its maximum decreased with the position of T_m shifted to lower temperatures, the room temperature tunability will hence decrease. The $\tan\delta$ peak will certainly also broaden and shift to higher temperatures, hence lowering the room temperature extrinsic losses to level comparable to bulk ceramics.

What is observed in the case of Mg implanted samples is more complex and certainly related to the formation of a lower loss, lower dielectric constant layer with gradual composition going from Mg-rich layer ~50 nm below the surface of the BST layer to very low Mg content few hundred nm below the surface. It is not clear how this layer affects the dielectric losses but an important

decrease of the dielectric losses is observed without significant decrease of the tunability for an Mg implantation process with low implantation energy and low dose and post-implantation annealing just below Mg boiling point.

Table 4.7. Comparison of the dielectric properties (losses, tunability, and FOM) of this work and recently published works of BST thin-film in GHz frequency range.

Reference	Losses	Tunability%	E (V.µm^{-1})	FOM
Ki-Byoung Kim, *et al.,* 2004.[117]	0.09	28	0.4	3
P. M. Suherman, *et al.,* 2006.[118]	0.043	50	3.2	11.5
M. W. Cole, *et al.*, 2008. [119]	0.039	15	177	4
H. Wang, *et al.,* 2013. [120]	0.17	17	7	1
F. Stemme, *et al.,* 2013. [121]	0.09	35	50	4
A. Ghalem, *et al.*, 2013. [122]	0.024	45	15	19
Kyoung-Tae Kim, *et al.*, 2014. [123]	0.02	41	10	20
Z. Q. Zeng, *et al.*, 2015. [124]	0.02	13	4	6.5
This work	0.035	60	10	17

In terms of Figure of Merit (FOM), the best obtained results in this work were for the epitaxial BST implanted with Mg, with a FOM of 17 (tunability of 60% and losses of 0.035). A comparison between the dielectric properties (losses, tunability, and FOM) of BST thin films in the GHz frequency range reported in this work and those reported in other recent works [refs 117-124] is provided in Table 4.7. It is seen that the FOM obtained in our study is comparable to the highest FOM of 20 reported by "Kyoung-Tae Kim et al."[123].

Conclusion

In this chapter, we first established general correlations between microstructural properties and the microwave properties of BST-0.6 thin film of the different sets of samples synthesized by PLD (all the results reported through chapter 2 and 3). Different correlations were found between i) the lattice parameter and rocking curve FWHM, ii) rocking curve FWHM and tunability, iii) lattice parameter and tunability and iv) dielectric loss and tunability.

(i) It is observed that, in general, as the crystal quality increases, the out-of-plane lattice parameter gets closer to the BST bulk value (3.96 Å) and that the films reach a kind of saturation of the lattice around 3.98 Å (the value obtained for polycrystalline films) going from epitaxial to polycrystalline.

(ii) As the crystal quality increases ($\Delta\omega$ decreasing from 0.8° to 0.2°), the tunability (at 2 GHz and 10 V.μm^{-1}) is increasing, going from 25 % for polycrystalline films to values as high as 72.5 % for the best crystal quality obtained ($\Delta\omega$ of 0.25°).

(iii) The correlation between the tunability and the lattice parameter shows that, the highest tunability values are generally obtained for films that possess a lattice parameter as close as possible to the BST-0.6 bulk value. This general trend corresponds to the calculated tunability as a function of the lattice parameter obtained from the Landau-Devonshire model.

(iv) Finally, plotting the tunability as a function of the losses demonstrates a linear dependence between the two material characteristics. The lower losses are associated with the lower tunability, and vice-versa, yielding to a Figure of Merit (FOM) that is comparable for epitaxial and polycrystalline films. For example, the film of set#1(deposition temperature) grown at 500°C is polycrystalline with a low tunability of 19%, but it also possesses the lowest tanδ (of 0.025) and a FOM of 7.6. The best crystal quality film ($\Delta\omega$ of 0.25°) has the highest tunability (72.5%) but also very high tanδ (0.08) yielding to a Figure of Merit of 9.

From these different correlations, it appears that two different mechanisms drive the tunability and the losses of BST-0.6 thin films: the tunability is found to be related to the material lattice parameter whereas the dielectric losses are either intrinsically linked to the tunability or influenced by the interfacial stress of the film. In order to further study this phenomenon, two different ways were explored: the use of buffer layers and material doping. For the study on buffer layers, thin layers of $Br_xSr_{1-x}TiO_3$ (with x=0 to 1) were used to decrease the interfacial

stress between the BST-0.6 layer and the MgO substrate and study its impact on the dielectric loss and dielectric tunability of the material. The other experimental study was carried out on the effect of doping on the dielectric and structural properties of the BST thin films. Two different doping methods were BST were used: the first one using a conventional incorporation of doping material (Mg, Ni, Mo, Fe, and Ti) during the deposition and the other one using ion implantation of Mg on deposited samples, a technique that was never studied on BST.

For the study on the effect of a buffer layer, two main aspects were studied: the effect of the buffer layer thickness (using BTO) and the influence of the material used as a buffer layer (using BST-x). It was found that the properties of BST-0.6 thin films follows exactly the modifications of BST-0.6 thin films structures: on one hand, the dielectric constant and tunability increases as the buffer layer thickness increases, which is correlated to a decrease of the rocking curve FWHM and a BST lattice parameter that gets closer to the BST-0.6 bulk value as the BTO buffer layer thickness increases. On the other hand, the dielectric losses greatly increase as a function of the BTO buffer thickness (influenced by the improvement in crystal quality but also by the dielectric losses of the BTO layer itself) which makes the FOM decreases. Interestingly the BST-0.6 with 50nm BTO buffer layer has the same lattice parameter as the bulk ceramic ($a_{BST-0.6}$ = 3.96 Å), and very low rocking curve FWHM (0.24). This sample exhibit very high tunability (74.5%), but low FOM (6.5) due to the high level of dielectric loss measured in that case (0.12).

The effect of the buffer layer material (BST-x with x=0 to 1) is also obeying to the general trend reported previously. With increasing the fraction x of the BST-x buffer layer from 0 to 1 (i.e. from STO to BTO) the lattice parameter gets closer to the BST-0.6 bulk ceramic value (going from 3.974 Å to 3.961 Å) and this induces an increase of both the dielectric constant and tunability as x increases. At the same time, the crystal quality increases (the rocking curve FWHM going from 1.14° for STO to 0.246° for BTO) which corresponds to a degradation of the material losses as x increases. Since the dielectric losses increase faster than the tunability, the best overall microwave characteristic corresponds to the film deposited on BST-0.3 and BST-0.5 buffer layer, the obtain FOM (~9.5 at 2 GHz and 10 V. μm^{-1}) is very close to the one of BST-0.6 alone deposited on MgO. A part of the increase in the material loss could also come from the buffer layer itself that posses increasing losses as x increases. Unfortunately, the BST compositions having the lowest lattice mismatch with the MgO substrate is also the one exhibiting the largest dielectric losses.

All these results put a new light on the mechanism associated with dielectric losses in BST thin films. A lot of papers are attributing losses to the presence of charged defects, grain boundaries or dislocations, but in the present study, the films with the best crystal quality are the ones that present the higher losses and these losses are decreasing as the films microstructure goes from epitaxial to textured and polycrystalline. The dielectric losses don't seem to be degraded by the average film strain either: this strain is supposed to relax as the film lattice parameter gets closer to the BST-0.6 bulk value. What is observed here is the contrary: dielectric losses are decreasing as the lattice parameter increases (as values are getting closer to MgO bulk value). For sure, maximum tunability values are obtained for film having large interfacial stress, since BST-0.6 has a 6% mismatch with MgO. Hence, the interfacial stress gradient (mainly due to the lattice mismatch at the interface with the substrate) is not affecting the tunability but may play an important role on the dielectric losses.

The study on the effect of doping on the properties of BST-0.6 may be the key to understand the loss mechanism. The preliminary results on the co-deposition of BST and a doping material by PLD indicate that Mg, compared to the other elements investigated (Ni, Mo, Fe and Ti), is the most promising dopant for BST-0.6 films deposited on MgO. While Ni, Mo, Fe and Ti all increase the lattice parameter of BST, Mg doping is decreasing it down to values closer to the BST-0.6 bulk value. The obtained film exhibits relatively high tunability and much lower losses than the BST-0.6 films deposited in the same conditions. This phenomenon is certainly related to the formation of a very low-loss secondary phase that allow relaxation of the film stress without degrading too much the tunability of the material. But the deposition method used for doping requires high laser fluences (in order to ablate the doping element) that does not lead to optimized BST properties. Another doping strategy was then explored: doping using implantation of Mg element on films epitaxially grown with optimized conditions.

A series of epitaxial BST-0.6 films were deposited on MgO single crystal substrates by PLD technique using the optimized deposition conditions (laser repetition rate of 10 Hz and a fluence of 1 J/cm^2, the substrate temperature being fixed at 800°C with background oxygen pressure 10 mTorr). These samples was implanted with Mg$^+$ at different energies and doses and annealed at different temperatures. What is remarkable with this set of experiments is that the properties are, for the first time, outside of the general trend observed for all the other sets. For epitaxial BST films implanted with Mg at 50 keV and a dose of 1x 10^{14} Mg$^+$ ion/cm^2, the post-implantation annealing temperature gives optimum tunability (of about 60%) at 900°C, 1000°C and 1150°C, but with large variations of the dielectric losses (tanδ going from 0.07 at 900°C to 0.035 at

1000°C and then increasing again up to 0.05 at 1150°C). In the case of high implantation damages (high dose or high energy), the resulting films present a degradation of both the tunability and dielectric losses that is certainly related to defects that annealing can't repair. Finally, for a 30min annealing time (at 1000°C in an oxidizing atmosphere), low implantation doses improves a lot the material properties but for doses higher than $1x10^{16}$ Mg ion cm^{-2}, the overall microwave properties decrease below the one of non-implanted films (mainly due to a rapid increase of the material losses).

What is observed in the case of Mg implanted samples is certainly related to the formation of a lower loss, lower dielectric constant layer with gradual composition going from Mg-rich layer ~50 nm below the surface of the BST layer to very low Mg content few hundred nm below the surface. This low-loss and low dielectric constant layer close to the surface has a great influence on the measured losses whereas the tunability and dielectric constant measurements are not really affected by this change. It is not clear how this layer affects the dielectric losses but, for an Mg implantation process inducing the less damage possible and post-implantation annealing just below Mg boiling point (50keV and $1x\ 10^{14}$ Mg^+ ion/cm^2, annealed at 1000°C for 30min), an important decrease of the dielectric losses is observed without significant decrease of the tunability. In these conditions, the properties of the films (FOM) is comparable to the best reported to date for a BST film [Table 4.7], its Figure of Merit of 17 at 2 GHz and 10 V. μm^{-1} (with tunability of 60% and losses of 0.035), nearly two times higher than the best Figure of Merit for BST-0.6 alone (~10), which makes it suitable for microwave applications.

CONCLUSION AND PERSPECTIVES

Future mobile and wireless networks require high performances tunable microwave devices, such as tunable resonators, filters, and phase shifters. In this context, ferroelectric material such as Barium Strontium Titanate (BST) is a promising candidate for tunable telecommunications devices. The integration into such technologies requires high quality BST thin films with "optimized dielectric properties", which starts with a better understanding of the material properties and, at the same time, improvement of device designs.

The three important characteristics for the integration of BST into microwave devices are the dielectric constant, the tunability and the dielectric loss. High dielectric constant allows reducing the size of the devices, large tuning (tunability) allows operation at low voltages and low dielectric loss (tan δ) allows minimizing the signal attenuation. The typical required values for these three parameters are a dielectric constant of 500-1000, a tunability of more than 50% for few $kV.cm^{-1}$ and tan δ lower than 0.01 at microwave range of frequencies (300 MHz to 300 GHz).

The subject of this thesis was to study BST thin films deposited on MgO single crystal substrate using pulsed laser deposition and, more specifically, to investigate the relation between the material structural properties and its microwave characteristics. In order to reach this goal epitaxial, textured and polycrystalline BST films were prepared using a large range of different deposition conditions. The obtained thin films were characterized in terms of microstructure and microwave dielectric properties to obtain the lattice parameter, ω and phi-scan values (stœchiometry in some cases) of the films and their dielectric constant, tunability and loss. The synthesis of this work lead to clear correlations between tunability and lattice parameter on one hand and between tunability and losses on the other hand, showing that BST thin films deposited on MgO seem to exhibit fundamental limitations due to contradictory effects between the need of a lattice parameter as close as possible to the bulk value and the necessity to minimize the film stress in order to reduce the losses.

These observations were used to elaborate a design of experiment toward the improvement of BST microwave characteristics.

Summary of research

In this work we aimed to deposit high quality of epitaxial, textured, and polycrystalline BST thin films for microwave applications. For that objective, we started our experimental work with optimizing BST thin film microstructure through the optimization of the PLD parameters such as laser fluence, laser repetition rate, substrate temperature, oxygen background pressure, substrate material type and orientation, and BST target composition.

Furthermore we aimed to study the influence of the PLD parameters on the dielectric properties of the deposited BST thin films, to obtain low dielectric loss (tan δ) for BST thin film and at the same time to obtain large tunability (a trade-off expressed by the Figure-of-Merit (FOM), corresponding to the ratio between tunability and loss).

The first PLD parameter studied was the laser fluence, varying the laser energy only, the laser spot area only or both parameters at the same time while keeping its value constant. The obtained results showed that the laser fluence has a direct effect on the stœchiometric transfer of BST-0.6 and hence on the dielectric properties of the films. It was also found that with the microstructure goes from polycrystalline to epitaxial depending on the fluence. The best deposition conditions found, in terms of film stœchiometry, lattice parameter, and crystal quality is at a fluence around 1 J.cm^{-2} obtained with a 110 mJ laser energy and a 11 mm^2 laser spot size. In these conditions, BST growth is epitaxial with a lattice parameter of 3.975 Å, a (Ba+Sr)/Ti ratio close to one and an ω-scan FWHM of 0.56°. These films present a tunability of 50% and dielectric loss of 0.05, corresponding to the best Figure of Merit (FOM) of 9.5. At higher fluences, BST films crystal quality degrades and stœchiometry deviates from the correct value.

Laser repetition rate is also an important PLD parameter because it affects the growth mechanism. The experiment done with different repetition rates shows that the rocking curve FWHM and the lattice parameter both increase as the laser repetition rate increases. The films obtained with low repetition rate of 2 Hz exhibit a rocking curve FWHM of 0.25° and lattice parameter of 3.965 Å, which correspond to high tunability (of 72.5%) and high dielectric loss (of 0.08), corresponding to a FOM of 9. For high laser repetition rate (50 Hz) the film is textured with 0.86° rocking curve FWHM and a lattice parameter of 3.977 Å and exhibit lower tunability and dielectric loss (of 32.5% and 0.039 respectively). The resulting FOM of the high laser repetition rate film is 8.3, which is comparable to the FOM obtained at 2 Hz. These results show

that the variation of growth kinetics through laser repetition rate has a direct effect on the microstructure of the film, with a crystal quality that degrades as the repetition rate increases, which affect the tunability and losses of the films, that both decreases. This suggests that the presence of defects may reduce the film stress but lead to lattice parameter larger than the one of the bulk. This induces opposite effects on the tunability and losses of the films and, hence, leads to comparable overall microwave properties for highly epitaxial and textured films.

Different x concentrations of $Ba_xSr_{1-x}TiO_3$ solid solution were deposited on MgO. Results show that the higher is the x concentration of Ba into the BST solid solution, the better is the epitaxial quality, the higher is the tunability but the losses increases drastically as the material goes from paraelectric (x=0 to 0.6) to ferroelectric (x=0.7 to 1). The highest Figure of Merit (FOM=10) is found for the composition BST-0.6, which exhibits high tunability (68%) but with relatively high dielectric loss (0.067) that will require improvement for actual microwave applications.

The influence of substrate temperature on microstructure and dielectric properties of the deposited film was also studied. The substrate temperature was varied from room temperature to 950°C and annealed at 1050°C. It is observed that the obtained crystal quality of these films change from completely polycrystalline to textured and high quality epitaxial films as the deposition temperature increases. A transition temperature between polycrystalline and epitaxial films is observed at 750°C and while the lattice parameter values of all deposited films are higher than the BST-0.6 bulk value, the film obtained at room temperature (completely polycrystalline film) and at 850°C (best epitaxial film obtained) have a lattice parameter value very close to bulk BST. Concerning the dielectric properties, it is found that the epitaxial BST thin film (deposited at 800°C with a rocking curve FWHM of 0.33°), showed high tunability and high dielectric loss (of ~70% & 0.065 respectively, yielding to a FOM of 10) while the lowest dielectric loss (0.025) is obtained for polycrystalline BST thin film deposited at 500°C with tunability of 19% and FOM of 7.6. The deposition conditions corresponding to the highest FOM (~10.5) are textured BST thin film deposited at 750°C (exhibiting tunability and dielectric loss of ~ 45% & 0.04 respectively). It is interesting to note that polycrystalline films deposited at room temperature exhibit a comparable Figure of Merit as the epitaxial films deposited at high temperature.

For the films deposited at different oxygen pressures, it is found that as the pressure increases the BST films go from textured to polycrystalline with a lower degree of crystallization. This is certainly coming from energy of the atoms landing on the substrate surface going from high to

low energy as the pressure increases. This causes the growth mechanism to change from highly ordered to disordered growth. Interestingly, there are no big differences between the samples except the crystallinity (going from nearly epitaxial at 10mTorr, to polycrystalline for 50 and 100 mTorr). The Figure of Merit is changing between 8 and 10 for the different conditions. Epitaxial growth of the BST films occurs at 10 mTorr, the tunability and dielectric loss of these films are ~50% and 0.05 respectively. The lowest tunability and loss are obtained at 50 mTorr (polycrystalline film) and may be explained by the low level of crystallization and stress relaxation of the film obtained at this deposition pressure.

The last investigation of these preliminary experiments concerned the type of substrate. Different crystal substrates (MgO, LAO, Sapphire and Alumina) and different MgO substrate orientations were used to investigate their influence on BST structural and electrical properties. It was found that the film structure is going from polycrystalline (for polycrystalline substrates) to epitaxial films (for single crystal substrates). The highest tunability is obtained for the film deposited on LAO (~71%) but it also exhibit very high dielectric loss (0.11), making its FOM much lower than the one obtained on MgO (6.4 for LAO compared to 10 for MgO). It is interesting to note that the FOM of the polycrystalline film obtained on Sapphire (FOM=9) is comparable to one of the highly oriented film obtained on MgO. For the different MgO substrate orientation, it is found that the obtained film orientation follow exactly the one of the substrate with a small degradation of the epitaxial quality going from (100) to (010) and (111). Only small differences exist between the different film orientations, the highest FOM being obtained for the (100) oriented BST-0.6 obtained on (100) MgO.

These preliminary experiments shows that the best deposition conditions for epitaxial BST thin film are obtained for MgO (100) with a 1 J/cm^2 laser fluence, 10 Hz laser repetition rate, 800°C substrate temperature and 10 mTorr oxygen pressure. From all the microstructural and microwave properties of the obtained BST films, different correlations were found:

i)   Between the lattice parameter and rocking curve FWHM: as the crystal quality increases, the out-of-plane lattice parameter gets closer to the BST-0.6 bulk value (3.96 Å).

ii) Between the Rocking curve FWHM and the tunability: as the crystal quality increases, the tunability increases (from 25 % for polycrystalline films to 72.5 % for the best epitaxial film).

iii) The first two correlation leads to a third one between the lattice parameter and the

tunability, which is confirmed by the Landau-Devonshire theory: the tunability presents a maximum as a function of the lattice parameter, this maximum correspond to the BST-0.6 value (3.96 Å).

iv)   Finally, the dielectric loss is found to depend almost linearly on the material tunability: lower losses are associated with the lower tunability, and vice-versa, yielding to FOM that is comparable for epitaxial and polycrystalline films.

From these observations, it appears that it is really important, in order to optimize the tunability to obtain a BST lattice parameter as close as possible to the bulk value (3.96 Å). But this creates a large stress at the interface between the MgO (4.02 Å) and the BST layer that is certainly at the origin of the large dielectric losses observed (and, by extension, the relation between the tunability and the losses). In an attempt to reduce the interfacial stress while keeping a BST-0.6 lattice parameter as close as possible to the bulk value, two main strategies were explored : i) the use of a BST buffer layer and ii) the use of a doping material.

The use of a BTO buffer layer with different thicknesses shows that as the buffer layer thickness increases the rocking curve FWHM decreases (down to 0.22°) and BST-0.6 lattice parameter gets closer to the BST bulk value. In agreement with the observed relation between the lattice parameter and the tunability, this improvement increases the tunability of the material (up to 74.5% for a 50 nm BTO buffer layer). Unfortunately, the dielectric losses greatly increase as the buffer layer thickness increases, certainly because of the lossy nature of the ferroelectric BTO material.

By changing the fraction x of the BST-x buffer layer material from 0 to 1, it is observed that the the lattice parameter gets closer to the BST-0.6 bulk ceramic value and the dielectric constant and tunability are both increasing. The crystal quality also improves (the rocking curve FWHM going from 1.14° for STO to 0.24° for BTO), but the overall material losses increases, especially for x compositions higher than 0.6. This makes the BST-0.3 and BST-0.5 buffer layer the best buffer layer materials but with overall microwave characteristic being almost the same as BST-0.6 without any buffer layer. Unfortunately, in order to decrease the lattice parameter of BST-0.6 close to the bulk value, the more suitable BST buffer layer are also the one that present the higher losses, which completely annihilate the advantage of using them.

The second approach consisted in exploring the doping of BST by small amount of metal elements (Mg, Ni, Mo, Fe and Ti). A first study was done using co-deposition of BST and the

doping material using PLD at a slightly higher fluence than the optimized conditions (in order to be able to ablate both the BST target and the piece of Ni, Mo, Fe, Ti or MgO placed on the target). It was found that Mg doping decreases the lattice parameter down to value close to the BST-0.6 bulk value, while other elements are all increasing the BST lattice parameter (compared to the undoped case). The obtained Mg-doped BST is found to exhibit better overall dielectric properties, with slightly lower losses than the undoped BST deposited in the same conditions. This could be due to the formation of a low-loss secondary phase which also allows relaxation of the film stress. But the obtained characteristics (FOM of ~9) are still just equivalent to the films obtained with optimized BST deposition conditions (that can't be use with the experimental setup because of the larger fluences needed to ablate MgO).

Another way of doping with Mg was then investigated: BST thin films were deposited using the optimized deposition conditions and then implanted with Mg ions before annealing the films in a furnace. These experiments, which are the first of their kind on BST, brought very interesting and encouraging results. Different parameters such as the ion energy, implantation dose and post-implantation annealing conditions were studied in order to investigate their influence on both the structural and electrical characteristics of the films. It was found that epitaxial BST films implanted with Mg ions at low implantation energy (50 keV), low implantation doses ($1x\ 10^{14}$ Mg+ ion/cm^2), and annealed at 1000°C show significantly lower dielectric loss (0.035) while maintaining high tunability (~ 60%). The resulting FOM is hence greatly improved compared to undoped films, up to ~17 (at 2 GHz and 10 V. µm^{-1}). This value is nearly two times higher than the best epitaxial BST film (FOM~10). This improvement seems to be related to the formation of a low loss, low dielectric constant layer close to the surface that has a great influence on the measured losses whereas the tunability and dielectric constant are almost unaffected.

The studies on the use of a buffer layer and on BST doping were also analyzed in the light of the previous correlations observed between the lattice parameter and the tunability and between the dielectric loss and the tunability. While the use of a buffer layer (set #7) and doping with different materials during the deposition of BST (set #8) are following the same tendency as the one observed for the previous sets, the BST samples implanted with Mg are clearly following another path in terms of dielectric losses. It is observed for this set (#9) that the tunability doesn't drastically change for the different implantation conditions explored (and compared to the un-implanted sample) but the corresponding dielectric losses are found to decrease by a factor of almost 2 with low dose implantation (going from 0.065 for un-implanted films to 0.035 for Mg implantation dose of $1x\ 10^{14}$ ions/cm^2 at 50 keV). This material modification

makes possible to improve the overall microwave characteristics of BST from a FOM of 10 (at 2 GHz and 10 V. µm^{-1} for the best un-implanted film) to 17, which is a remarkable improvement. This proves the great potential of ion implantation in order to reduce the losses of BST thin films while maintaining the tunability as high as possible. The role of ion implantation on the dielectric properties of BST may certainly require an extended investigation in a future work. What can be concluded from the implantation of BST with Mg ions is that the improvement in BST dielectric properties is certainly related to the formation of a low-loss and low dielectric constant layer close to the surface that has a great influence on the measured losses whereas the BST tunability and dielectric constant are not really affected by this change. The generation of defects into the BST lattice structure that help to relax the thin film stress may also have an influence on the observed improvement of the BST dielectric properties.

This extensive study on the dielectric properties of BST-0.6 films grown on MgO for microwave applications, with films going from epitaxial with one of the best quality obtained so far to polycrystalline films, represent the only study comparing microwave properties of films with such a broad range of structural properties. More importantly, this work draws clear correlations between the structural properties and microwave characteristics of BST films that should apply to other BST thin films deposited on various substrates. It put some new lights on the importance of the BST lattice parameter and stress control on the degradation of BST microwave characteristics compared to bulk ceramics. The reduction of the dielectric losses while preserving high tunability of the material using ion implantation is also an important new avenue that may help to solve the squaring of the circle between high tunability and low loss that is observed for more than a decade by all the groups working on ferroelectrics.

A continuation of this work will surely require a better understanding of how the Mg ion is included in epitaxial BST thin films. This requires characterization with X-ray photoelectron spectroscopy (XPS) in order to get information on the oxidation state of the metal. In addition, characterization techniques such a transmission electron microscopy (TEM) can be employed for investigating presence of MgO clusters. Moreover, further studies are required to understand the influence of ion implantation on the dielectric loss and FOM of BST thin films, using lower implantation doses, or other implantation materials such as nitrogen (N), for example. In addition, one can also study the role of a low-loss layer close to the interface between the BST and the microwave electrodes. We also recommend studying the effect of high oxygen background pressure of PLD (above 100 mTorr) on the epitaxial growth and quality of the produced BST thin film and its corresponding microwave characterization. Along with this study,

one would investigate the plasma dynamics at different background gas pressure (using spectroscopic techniques) and the influence of the plasma dynamics on the film growth. A systematic chemical composition study could also be interesting in order to correlate the chemical composition of BST thin film with the microwave properties.

For further improvements to reduce the losses, one may optimize the BST thin film structure by combining buffer layer and ion implantation strategies. It could also be worth to investigate the role of the interfacial stress on the losses by studying, for example, the effect of the epitaxial BST thin film thickness.

Based on the improvement of the dielectric properties of epitaxial BST thin film doped by Mg via ion implantation reported in this study, it is possible and also interesting to develop Mg doped BST based tunable filters, phase shifters and agile antennas. Since telecommunication technologies are evolving toward higher working frequencies and the hybridization of microwave technology with optical devices, application of highly epitaxial BST material to hybrid or photonic devices such as frequency modulators is also a field that merits investigation. The better understanding of loss mechanisms in ferroelectric materials enable potential applications in the fields of active systems such as smart phones and tablets.

Résumé

Les applications des télécommunications sans fils, particulièrement la téléphonie cellulaire, les tablettes intelligentes et les systèmes GPS ont littéralement envahi notre quotidien dans les dernières années. Cette expansion remarquable est encore en plein essor aujourd'hui car la téléphonie sans fil est en train de fusionner complètement avec un autre domaine majeur des télécommunications : les technologies Internet. Ainsi, les téléphones intelligents actuels permettent non seulement de transmettre la voix mais aussi de s'échanger du texte, des images, de la vidéo, de la musique et de naviguer sur Internet, et ainsi de se déplacer n'importe où à travers le monde avec des milliards d'informations à portée de main. La nouvelle génération de téléphones cellulaires, entièrement numériques, qui finit de remplacer progressivement les derniers survivants de l'ère analogique, a fait évoluer la téléphonie classique vers l'Internet et le multimédia mobiles grâce à l'échange de données à beaucoup plus hauts débits. Cette révolution a été rendue possible grâce à l'émergence de recherches pluridisciplinaires regroupant des domaines tels que la microélectronique, les télécommunications sans fil et les technologies Internet, et le décalage progressif des fréquences d'opération vers les hautes fréquences (>GHz).

Le fonctionnement multibande, multimode et haut débit des systèmes de télécommunications mobiles actuels et futurs ainsi que l'opération à des fréquences d'opération de plus en plus élevées demandent le développement de nouveaux dispositifs actifs qui feraient un bond énorme, pour le traitement des signaux, s'ils intégraient de plus en plus de matériaux dits « intelligents ». Les matériaux intelligents, et particulièrement les matériaux polaires, connus depuis le début du 20e siècle pour leur capacité à modifier spontanément leurs propriétés physiques, ouvrent une nouvelle ère dans l'histoire de l'évolution de ces technologies. D'abord développés sous forme de céramiques pour la conception de capteurs et d'actionneurs, la possibilité d'utiliser ces matériaux sous forme de couches minces actives a permis d'envisager de nouvelles applications pour les télécommunications et suscité de nombreux travaux de recherche. La classe des matériaux ferroélectriques a particulièrement retenu l'attention des chercheurs. Dotés d'une polarisation spontanée pouvant être inversée sous l'application d'un champ électrique, ces derniers rendent possible d'une part le stockage d'information binaire de façon permanente et cela en quelques nanosecondes. D'autre part, leur très haute constante diélectrique relative (ε_r, de l'ordre de 500-1000) peut avantageusement remplacer le SiO_2 ou le

SiN (ε_r égal à 7 et 6 respectivement) pour assurer l'isolation du drain (« gate ») dans les MOSFET. Dans le cas des capacités intégrées, cette propriété permet aussi de diminuer de 50 fois la taille des capacités tout en consommant moins d'énergie et surtout d'opérer à très hautes fréquences (> GHz).

Ce ne sont là que les premières applications des matériaux ferroélectriques car, plus intéressant encore, ils pourraient permettre de diminuer la taille de toutes sortes de guides d'ondes de type MMIC (Monolithic Microwave Integrated Circuits) utilisés dans les télécommunications et d'êtres exploités pour leur variabilité dans des dispositifs actifs. Les composants tels que les filtres, les déphaseurs ou les oscillateurs utilisés dans les dispositifs MMIC pour le traitement de signaux hautes fréquences sont composés de circuits métalliques reposant sur des substrats diélectriques. Dans cette configuration, la taille des circuits est proportionnelle à la longueur d'onde du signal dans le milieu utilisé $\lambda_g = c/f\sqrt{\varepsilon_{eff}}$ où ε_{eff} est la constante diélectrique effective du substrat et f est la fréquence du signal. Ainsi, pour une fréquence donnée, l'emploi de matériaux ferroélectriques (ε_r de l'ordre de 500-1000) comparativement à un substrat conventionnel ($\varepsilon_r \sim 10$) rend théoriquement possible de diminuer jusqu'à 10 fois la taille des circuits actuels.

Par ailleurs, pour les applications MMIC, la variation de la constante diélectrique des matériaux polaires sous l'application d'un champ électrique est particulièrement intéressante, car elle permet d'envisager une nouvelle gamme de dispositifs accordables. La longueur électrique des circuits (λg) devient en effet ajustable en fonction de la tension si ε_{eff} varie en présence d'un champ électrique. Cette caractéristique des matériaux ferroélectriques est appelée « variabilité » (« tunability » en anglais) et correspond au pourcentage de variation de la constante diélectrique relative du matériau. La variabilité, pour un champ électrique E donné, est définie comme étant la quantité $\Delta\varepsilon_r/\varepsilon_r = 1-\varepsilon_r[E]/\varepsilon_r[0]$, exprimée en pourcent. Si l'on considère, par exemple, un filtre passe-bande fabriqué sur un substrat entièrement ferroélectrique (ε_{eff} est alors proportionnel à ε_r), une variabilité de 50 % du matériau ferroélectrique permet un déplacement théorique de la fréquence centrale du filtre (proportionnelle à $1/\sqrt{\varepsilon_{eff}}$) de 40 % vers les hautes fréquences.

C'est le souhait de bien des concepteurs de circuits hautes fréquences de disposer de ce nouveau type de composant qui serait non seulement 10 fois plus petit qu'un composant conventionnel mais dont les propriétés pourraient aussi être ajustées par l'application d'une

tension électrique. Si le principe est simple, la réalisation de ce type de dispositif ne l'est pas forcément car les caractéristiques globales de tels composants sont fortement liées aux caractéristiques électriques du matériau polaire lui-même. Le premier défi est donc de trouver un matériau polaire en couches minces dont la constante diélectrique est relativement élevée (ε_r > 300), dont les pertes diélectriques sont faibles (tan δ < 0.03), et dont la variabilité est la plus grande possible dans le domaine des GHz.

Depuis le début des années 1990, de nombreux groupes se sont lancés à la recherche de ce matériau. Le Titanate de Baryum et de Strontium (BST) a été désigné comme étant le matériau le plus prometteur pour ce type d'applications et n'a pas vraiment trouvé de remplaçant depuis. Un des obstacles majeurs à son intégration à grande échelle dans les dispositifs micro-ondes vient de l'impossibilité apparente d'obtenir une grande variabilité diélectrique du BST tout en ayant de faibles pertes. C'est à la compréhension de ce phénomène que ce travail de recherche s'est attaché. En effet, l'objectif de cette thèse est d'étudier le lien entre les caractéristiques structurelles et électriques de couches minces de BST déposées sur des substrats de MgO (un substrat permettant d'obtenir le matériel sous forme tant épitaxié que polycristalline) afin d'essayer de comprendre le lien existant entre la variabilité et les pertes tant au niveau des propriétés diélectriques que structurales du matériau.

La qualité structurale des couches minces de BST ayant une forte incidence sur ses propriétés électriques, il est primordial de bien contrôler le dépôt de BST. Pour ce faire, nous avons utilisé comme technique de dépôt l'ablation laser en milieu réactif (R-PLD) et déterminé différentes conditions de dépôt afin d'obtenir sur des substrats de MgO orientés [100] des couches minces de BST aux propriétés très diverses.

Résultats de la recherche

La technique de dépôt l'ablation laser en milieu réactif (R-PLD) permet de déposer des couches minces de BST-0.6 sous forme épitaxiée, texturée ou polycristalline et ainsi d'étudier en détail la relation entre propriété structurales et diélectriques des couches minces. Pour atteindre cet objectif, nous avons commencé ce travail par l'optimisation des paramètres de dépôt par ablation Laser tels que la fluence laser, le taux de répétition, la température du substrat, la pression d'oxygène, le type de substrat et son orientation, ainsi que la composition de la cible.

L'influence de ces paramètres sur les propriétés structurales et diélectriques des couches minces a été mesurée afin de chercher à atteindre une faible constante de perte (tan δ) tout en conservant une grande variabilité du matériau, un compromis exprimé par la Figure de Mérite du BST (représentée par le rapport entre la variabilité et les pertes). Le paramètre de maille, la cristallinité et, dans certains cas, la stœchiométrie ou l'aspect de surface des couches minces déposées ont été évalués par diffraction des rayons X (XRD), détection des reculs élastiques (ERD), Microscopie électronique à balayage (MEB) ou Microscopie à force atomique (AFM). La constante diélectrique, la tangente de perte et la variabilité diélectrique dans le domaine des GHz ont été mesurés à l'aide d'un diagnostic développé par notre groupe.

Le premier paramètre de dépôt étudié en détail a été la fluence laser, variée soit à tâche focale constante, soit à énergie constante, soit en variant les deux en même temps afin de conserver une fluence constante. Les résultats obtenus montrent que la fluence laser a un impact direct sur la stœchiométrie des films déposés et ainsi sur leurs propriétés électriques. Il a aussi été observé que la structure des films allait de polycrystalline à épitaxiale suivant la fluence. Les meilleures conditions de dépôt trouvées, en terme de stœchiométrie, paramètre de maille et qualité crystalline correspondent à une fluence de 1 J.cm^{-2} obtenue avec une énergie laser de 110 mJ et une tâche focale de 11 mm^2. Dans ces conditions, la croissance des films de BST est épitaxiale avec un paramètre de maille de 3.975 Å, un ratio (Ba+Sr)/Ti proche de 1 et une largeur à mi-hauteur du ω-scan de 0.56°. Ces films présentent une variabilité de 50% (à 2 GHz et 10 V. µm^{-1}), des pertes diélectriques de 0.05 correspondant à la meilleure valeur de figure de mérite (rapport de la variabilité sur les pertes, de 9.5). À plus haute fluences, la qualité cristalline des couches minces de BST se dégrade et la stœchiométrie dévie de la valeur normale.

Le taux de répétition Laser est aussi un paramètre important de la PLD car il influence le mécanisme de croissance des couches minces. Les films obtenus à différents taux de répétition montrent que la largeur à mi-hauteur (FWHM) des pics de « rocking curve » (indicateur de la qualité cristalline des films, dénoté RC-FWHM) et le paramètre de maille des couches minces de BST augmentent à mesure que le taux de répétition diminue. Les films obtenus à un taux de répétition de 2Hz sont épitaxiés avec une très haute qualité cristalline (un RC-FWHM de 0.25°) et un paramètre de maille de 3.965Å (soit légèrement au-dessus des 3.96Å du BST-0.6 massique), une grande variabilité (de 72.5% à 2 GHz et 10 V. µm^{-1}) et des pertes importantes

(0.08), correspondant à une figure de mérite de 9. Pour des hauts taux de répétition laser (50 Hz), les films sont texturés avec un RC-FWHM de 0.86° et un paramètre de maille de 3.977 Å, de plus faibles variabilités et pertes (respectivement de 32.5% et 0.039). La figure de mérite des films déposés à 50 Hz est ainsi comparable à ceux obtenus à 2 Hz (8.3 comparativement à 9) alors que les qualités cristallines des films sont très différentes. Ces résultats montrent que la variation des mécanismes de croissance des couches minces due à la variation du taux de répétition laser a une incidence directe sur la microstructure des films qui détériore la variabilités du BST à mesure que le taux de répétition augmente mais améliore sa constante de perte. Cela suggère que la présence de défauts de structure diminue les contraintes des couches minces mais entraine aussi un paramètre de maille plus élevé que celui du matériau massique. Cela entraine un effet opposé sur la variabilité et les pertes, et ainsi l'obtention de propriétés diélectrique globales similaires (la figure de mérite étant le rapport des deux quantités).

Différentes concentrations x de $Ba_xSr_{1-x}TiO_3$ ont été déposées sur MgO dans les mêmes conditions d'ablation laser. Ces dépôts montrent qu'à mesure que la concentration x de Ba dans la solution solide de BST augmente, la qualité cristalline et la variabilité du BST augmentent. Dans le même temps, les pertes diélectriques augmentent de façon importante à mesure que le matériau passe de paraélectrique (x=0 to 0.6) à ferroélectrique (x=0.7 to 1). La plus grande figure de mérite (FOM=10) est obtenue pour la composition x=0.6, qui présente une variabilité de 68% mais avec des pertes relativement importantes (0.067), un peu trop élevées pour les applications micro-ondes.

L'influence de la température de dépôt sur la microstructure et les propriétés diélectriques des films de BST a ensuite été étudiée. Celle-ci a été variée de 20 à 950°C alors que les films étaient recuits à 1050°C après le dépôt afin d'améliorer la cristallisation et combler les lacunes d'oxygène potentielles. Cette étude montre que la structure cristalline de ces films passe de polycristalline à texturée puis épitaxié à mesure que la température de dépôt augmente. Une température de transition de polycristallin à épitaxié est observée autour de 750°C et alors que tous les films déposés ont un paramètre de maille supérieur au BST massique, le film obtenu à température ambiante (complètement polycristallin) et celui obtenu à 850°C (le meilleur film épitaxié obtenu) ont un paramètre de maille très proche de la valeur massique. Pour ce qui est des propriétés électriques de ces films, il apparait que les films épitaxiés (déposés à 800°C et ayant un RC-FWHM de 0.33°) ont une grande variabilité accompagnée de fortes pertes (de ~70% et 0.065 respectivement, menant à une FOM de 10) alors que les plus faibles pertes

(0.025) sont obtenues pour le BST polycristallin, déposé à 500°C, qui ont par ailleurs une variabilité de 19% et une FOM de 7.6. La plus forte valeur de FOM (~10.5) est obtenue pour des films de BST texturés déposés à 750°C (qui présentent une variabilité de 45% et des pertes de 0.04). Il est intéressant de noter que les films polycristallins déposés à température ambiante ont une figure de mérite comparable aux films épitaxiés déposés à haute température.

Pour les films déposés à différentes pressions d'oxygène, il est constaté qu'à mesure que la pression de dépôt croît les films de BST passent de texturés à polycristallin avec un degré de cristallisation moindre. Cela est certainement dû à l'énergie décroissante des atomes arrivant sur le substrat à mesure que la pression augmente qui entraîne un changement du mécanisme de croissance, passant de fortement ordonné à désordonné. Étonnamment, il n'y a pas de différence marquée au niveau des propriétés diélectriques de ces échantillons (qui passent de quasi épitaxié à 10mTorr à polycristallin à 50 et 100 mTorr), la figure de mérite ne changeant que de 8 à 10 pour les différentes conditions. La croissance épitaxié des films de BST se situe autour de 10 mTorr, conditions pour lesquelles la variabilité et les pertes sont respectivement de ~50% et 0.05. La plus faible variabilité accompagnée des plus faibles pertes est obtenue pour l'échantillon déposé à 50 mTorr (polycristallin) et provient certainement du plus faible degré de cristallisation et du relâchement du stress dans ces conditions.

Le dernier volet de cette étude préliminaire concernait l'influence du type de substrat utilisé. Différents matériaux (monocristaux de MgO, LAO, Saphir et Alumine polycristalline) et différentes orientations de substrats de MgO ont été utilisés pour évaluer l'influence du substrat sur les propriétés structurales et électriques des couches minces de BST. Cette étude a permis de constater que l'orientation des films de BST obtenus sur MgO et LAO suivait celle des substrats utilisés alors que les films obtenus sur Al_2O_3 (Saphir er Alumine) étaient polycristallins. La plus forte variabilité a été obtenue pour le BST déposé sur LAO (~71%) mais celle-ci est accompagnée de très fortes pertes (0.11), aboutissant à une figure de mérite beaucoup plus basse que celle obtenue sur MgO (6.4 sur LAO comparé à 10 sur MgO). Il est intéressant de noter que la FOM des films obtenus sur Saphir (FOM=9) est du même ordre que celle obtenue pour les films avec orientation préférentielle ou épitaxiés sur MgO. Pour les différentes orientations de substrats de MgO, il apparaît que l'orientation des films déposés suit exactement celle des substrats utilisés avec une légère dégradation de la qualité épitaxiale de (100) à (110) et (111). Seulement de légères différences sont observées entre les propriétés

diélectriques de ces différents films, la plus forte FOM étant obtenue pour le film de BST (100) obtenu sur MgO (100).

Ces travaux préliminaires montrent que les meilleures conditions de dépôt par ablation laser du BST sur MgO (100) sont obtenues pour une fluence de 1J/cm^2, un taux de répétition de 10Hz, une température de dépôt de 800°C et une pression d'oxygène de 10 mTorr. À partir des propriétés structurales et électriques des différents films obtenus, plusieurs corrélations apparaissent :

i)   Entre le paramètre de maille et la qualité cristalline (RC-FWHM). Il est en effet trouvé qu'à mesure que la qualité cristalline augmente le paramètre de maille des films de BST se rapproche de la valeur du BST-0.6 massique (3.96 Å)

ii)   Entre la qualité cristalline et la variabilité : il est constaté qu'à mesure que la valeur de RC-FWHM diminue (correspondant à une augmentation de la qualité cristalline), la valeur de la variabilité augmente. Alors que cette dernière est de 25% pour les films polycristallins, elle atteint 72.5% pour le meilleur film épitaxié obtenu (RC-FWHM, $\Delta\omega$ de 0.25°).

iii) Ces deux premières corrélations mènent ainsi à une troisième dépendance entre le paramètre de maille et la variabilité des films de BST-0.6 qui est confirmée par un calcul théorique issu de la théorie de Landau-Devonshire. Dans ce modèle, la variabilité présente un maximum en fonction du désaccord de paramètre de maille (exprimé par le paramètre de maille de la couche mince elle-même) correspondant à la valeur du paramètre de maille du BST-0.6 massique (3.96 Å).

iv)   Enfin, il apparaît que les pertes diélectriques dépendent de façon quasi-linéaire de la variabilité : plus les pertes diélectriques sont faibles, plus la variabilité est faible (et inversement). Cela fait en sorte que, de façon générale, quelles que soient les conditions de dépôt les films obtenus ont une figure de mérite similaire, qu'ils soient épitaxiés ou polycristallins.

À partir de ces observations, il apparaît que le point le plus important pour optimiser la variabilité des films de BST est de se rapprocher le plus possible de conditions de dépôt où le paramètre de maille correspond à celui de la forme massique du matériau. Cependant, cela crée un stress très important à l'interface entre le substrat de MgO et le BST à cause du désaccord de maille des deux matériaux (3.96 Å pour le BST vs. 4.02 Å pour le MgO). Ce

stress est certainement à l'origine d'une forte dégradation des pertes diélectriques du BST et incidemment de la relation observée entre les pertes diélectriques et la variabilité. Dans l'optique de réduire ce stress d'interface (et donc les pertes diélectriques) tout en conservant un paramètre de maille proche de la valeur massique (et donc maximiser la variabilité), deux stratégies ont été explorées : i) l'utilisation d'une couche tampon et ii) l'utilisation d'un matériau dopant.

Dans le cas de l'utilisation d'une couche tampon de BaTiO3 (BTO), il apparait qu'à mesure que l'épaisseur de la couche tampon augmente, la qualité cristalline du BST-0.6 augmente (RC-FWHM atteignant 0.22° pour 50 nm) et le paramètre de maille se rapproche de la valeur du matériau massique. Tel qu'attendu, cela permet d'augmenter la variabilité du BST, atteignant 74.5% lorsque déposé sur 50nm de BTO. Malheureusement, les pertes diélectriques augmentent fortement à mesure que l'épaisseur de la couche tampon augmente, certainement en raison des pertes de plus en plus importantes induites pour le BTO lui-même (qui, dans l'état ferroélectrique, est très dispesif).

Une autre étude a été menée en fonction de la composition de la couche tampon BST-x (avec x=0, 0.3, 0.5, 0.7 et 1). Celle-ci montre qu'en passant du STO (x=0) au BTO (x=1) pour la couche tampon, le paramètre de maille de la couche de BST-0.6 déposée au-dessus se rapproche de la valeur massique et la constante diélectrique et la variabilité de la couche mince augmentent toutes deux de façon significative. La qualité cristalline augmente elle aussi, RC-FWHM passant de 1.114° pour la couche tampon de STO à 0.24° pour la couche tampon de BTO. Dans le même temps les pertes diélectriques augmentent, en particulier pour les compositions supérieures à x=0.6, c'est à dire lorsque la nature de la couche tampon passe de paraélectrique à ferroélectrique et deviens donc beaucoup plus dispersive. Au regard de la figure de mérite, la meilleure composition de couche tampon se situe entre x=0.3 et x=0.5 mais avec seulement très peu de gain par rapport à une couche de BST-0.6 seule. Il apparaît donc que les couches tampons de BST les plus à même de rapprocher la valeur du paramètre de maille du BST-0.6 près de la valeur massique et diminuer le stress d'interface sont aussi celle qui sont le plus dispersives et cette contribution annule complètement l'avantage de les utiliser pour les applications micro-ondes.

La seconde approche consistait à explorer l'effet du dopage du BST avec une faible quantité d'un élément métallique (Mg, Ni, Mo, Fe and Ti). Un premier travail a été mené en utilisant la co-déposition par ablation Laser (PLD) du BST et de l'élément dopant en utilisant une fluence

plus élevée que pour le BST seul (afin d'être en mesure d'ablater le BST et une surface de Ni, Mo, Fe, Ti ou MgO placé sur la cible de BST). Il a été constaté que seul le dopage par Mg permettait de diminuer la valeur du paramètre de maille du BST-0.6 jusqu'à une valeur proche de sa valeur massique alors que tous les autres éléments l'augmentait (comparativement au BST-0.6 seul). De plus, le BST-0.6 dopé avec du Mg présente de meilleure propriétés diélectriques avec de plus faibles pertes que le BST seul déposé dans les mêmes conditions. Cela semble être dû à la formation d'une phase secondaire très peu dispersive qui permet de diminuer les pertes globales de la couche mince et, dans le même temps, d'en relâcher les contraintes. Le seul point négatif réside dans le fait que la figure de mérite obtenue (FOM de 9) n'est qu'équivalente à la FOM du BST-0.6 déposé dans des conditions optimales (plus basse fluence, qui ne peut être utilisée ici pour ablater le MgO servant au dopage).

Une autre façon de doper les couches minces de BST-0.6 avec du Mg a alors été explorée : l'implantation ionique. Pour ce faire, des couches épitaxiées de BST ont préparées dans les conditions optimales définies précédemment puis implantées avec du Mg et recuite dans un four (afin de réduire les dommages créés par l'implantation). Ces expériences, uniques en leur genre pour le BST, ont menées à des résultats intéressants en termes de propriétés diélectriques haute-fréquences.

Différents paramètres tel que l'énergie des ions, la dose d'implantation et la température de recuit ont été étudiés afin de déterminer leur influence respective sur les propriétés structurales et électriques des couches minces. Il a été observé que les films implantés avec du Mg à basse énergie (50 keV), basse dose (1x 10^{14} Mg+ ion/cm^2), et recuits à 1000°C présentaient des pertes diélectriques beaucoup plus basses (0.035) tout en présentant une variabilité élevée (60%). La figure de mérite de ces films est donc significativement plus élevée que tous les films épitaxiés obtenus dans cette étude (FOM de ~17 à 2 GHz and 10 V. µm^{-1}), puisqu'elle est près de deux fois plus élevée que le meilleur résultat obtenu pour un film épitaxié non dopé (FOM~10). Cette amélioration semble reliée à la formation d'une couche très peu dispersive près de la surface du BST qui a une grande influence sur les pertes diélectriques alors que la constante diélectrique et la variabilité ne sont que légèrement affectées.

Ces résultats sur l'utilisation d'une couche tampon et le dopage in-situ ou obtenu par implantation ionique ont été analysés à la lumière des corrélations trouvées précédemment (corrélations entre le paramètre de maille et la variabilité, ainsi qu'entre la variabilité et les pertes). Alors que les résultats obtenus pour le BST-0.6 avec couche tampon (set#7) et le

dopage in-situ (set#8) suivent les mêmes tendances que celles observées précédemment, les résultats des couches implantées avec du Mg (set#9) dévient clairement de la tendance générale pour ce qui est des pertes diélectriques. Il est en effet observé que la variabilité ne change pas de façon significative pour les différentes conditions d'implantation utilisées (ou même par rapport à l'échantillon non-implanté) mais que les pertes diélectriques de ces échantillons sont près de deux fois plus faibles pour les échantillons implantés à faibles doses (allant de 0.065 pour le film non-implanté comparativement à 0.035 pour le film implanté au Magnésium avec une dose de 1x 10^{14} ions/cm^2 et à 50 keV). Cette modification du matériau rend possible une amélioration remarquable des propriétés hautes fréquences du BST, passant d'une figure de mérite de 10 (à 2 GHz et 10 V.µm^{-1} pour le meilleur résultat des films non implantés) à 17 pour le meilleur film implanté. Cela montre l'intérêt de l'implantation pour réduire les pertes du BST-0.6 tout en gardant des valeurs élevées de variabilité. Ce qui se dégage de cette première étude, est que la diminution des pertes diélectriques du matériau sont certainement liées à la présence d'une fine couche riche en Mg près de la surface du BST. Cette couche de quelques nm doit être à la fois de faible constante diélectrique et peu dispersive, et possède une grande influence sur les pertes diélectriques de la couche mince de BST-0.6 alors que la variabilité n'en est que très peu affectée. La présence de défauts dans la structure cristalline du BST, induits par le processus d'implantation, qui relâcherait les contraintes de la couche mince pourrait aussi être à l'origine de la diminution des pertes diélectriques. L'étude complète des mécanismes entrainant ce gain significatif en terme de propriété diélectriques demanderait une étude approfondie qui dépasse les limites de cette thèse mais pourra certainement faire l'objet d'une recherche future.

Cette étude sur les propriétés diélectriques du BST-0.6 pour des applications dans le domaine des hautes fréquences représente la seule étude comparant de façon aussi exhaustive les propriétés de couches minces déposées sur substrats de MgO. Les propriétés structurales des films obtenus couvrent en effet une large gamme allant du matériau polycristallin à la couche mince possédant une qualité épitaxiale parmi les plus hautes obtenues pour ce matériau. Plus important encore, ce travail permet de tracer une corrélation claire entre les propriétés structurales et diélectriques des couches minces de BST qui devrait s'appliquer à d'autres compositions de BST déposées sur des substrats variés. Cette corrélation met en lumière l'importance du paramètre de maille du BST et du contrôle des contraintes sur les propriétés hautes fréquences des couches minces comparativement au matériau massique et marque les limitations de ce matériau pour les applications micro-ondes. La réduction des pertes

diélectriques du matériau, obtenue tout en gardant des variabilités élevées grâce à l'utilisation d'implantation ionique de Mg est aussi un résultat important qui pourrait aider à mieux comprendre le mécanisme associé aux pertes diélectriques et briser la quadrature du cercle entre haute variabilité et faibles pertes, observée depuis plus de 10 ans par les groupes de recherche œuvrant dans ce domaine. La poursuite de ce travail nécessiterait de mener une étude approfondie de l'influence de l'implantation ionique sur les pertes diélectriques et la figure de mérite du BST en utilisant de plus faibles doses, l'utilisation d'autres éléments tels que le Mn par exemple, et l'étude du rôle de la couche d'implantation située très près de la surface du BST sur les propriétés diélectriques obtenues. Puisque le domaine des télécommunications évolue vers des fréquences d'opération de plus en plus élevées et l'hybridation de circuits micro-ondes avec des dispositifs optiques, l'utilisation de BST épitaxié dans des dispositifs hybrides ou photoniques tels que les modulateurs de fréquences est aussi un domaine de recherche qui mériterait que l'on s'y attarde et pour lequel ce travail constituerait une base appréciable. Car si les mécanismes associés aux pertes diélectriques des matériaux ferroélectriques pouvaient être mieux compris et maitrisés afin de rapprocher les propriétés hautes fréquences des couches minces de celles du matériau massique, cette classe de matériaux trouverait une place de choix dans les dispositifs actifs des futures générations de tablettes et de téléphones intelligents.

References

1 Plunkett's Telecommunications Industry Almanac, 2014.

2 M. T. Sebastian, "Dielectric Materials for Wireless Communications", Elsevier Ltd., 2008.

3 L. F. Chen, C. K. Ong, C. P. Neo, V. V. Varadan and V. K. Varadan, "Microwave Electronics (Measurement and Materials Characterization)", John Wiley & Sons Ltd, 2004.

4 H. Sobol, "Milestones of Microwaves", IEEE Transactions On Microwave Theory And Techniques, Vol. 50 (3), p. 594-611, 2002.

5 P. Bao, T. J. Jackson, X. Wang and M. J. Lancaster, "Barium strontium titanate thin film varactors for room-temperature microwave device applications", J. Phys. D: Appl. Phys. 41, 063001, 2008.

6 N. Setter, D. Damjanovic, L. Eng, G. Fox, S. Gevorgian, S. Hong, A. Kingon, H. Kohlsted, N. Y. Park, G. B. Stephenson, I. Stolitchnov, A. K. Tagantsev, D. V. Taylor, T. Yamada, S. Streiffer "Ferroelectric thin films: Review of materials, properties, and applications", J. Appl. Phys. 100, 051606, 2006.

7 U. S. Modani, G. Jagrawal, "A survey on Application of Ferroelectric Materials for Fabrication of Microstrip Patch Antennas", International Journal of Recent Technology and Engineering (IJRTE), Vol. 1 (5), pp. 65-72, 2012.

8 E. Kaxiras, "Atomic and Electronic Structure of Solids", Cambridge University Press, 2003.

9 C. L. Chen, H. H. Feng, Z. Zhang, A. Brazdeikis, Z. J. Huang, W. K. Chu, C. W. Chu, F. A. Miranda, F. W. Van Keuls, and R. R. Romanofsky, Y. Liou, "Epitaxial ferroelectric Ba0.5Sr0.5TiO3 thin films for room-temperature tunable element applications", Appl. Phys. Lett., 75 (3), pp. 412-414, 1999.

10 J. Xu, W. Menesklou, and E. Ivers-Tiffee, "Investigation of BZT Thin Films for Tunable Microwave Applications", Journal of the European Ceramic Society, 24, pp. 1735–1739, 2004.

11 A. L. Campbell, R. R. Biggers, G. Subramanyam, G. Kozlowski, R. A. Kleismit, H. N. Zate, S.C. Hopkins, B. A. Glowacki, B. D. Riehl, and T. L. Peterson, "Microwave characterization of nanostructured ferroelectric Ba0.6Sr0.4TiO3 thin films fabricated by pulsed laser deposition", Nanotechnology,19, 485704, 2008.

12 L. Pardo, J. Ricote, M. Alguero, M. L. Calzada, "Handbook of Low and High Dielectric Constant Materials and Their Applications" Vol. I, chapter 10, "Ferroelectric Materials Based On Lead Titanate", pp. 457-499, 1999.

13 R.Waser,U. Böttger, and S.Tiedke, "Polar Oxides (Properties, Characterization, and Imaging)", Edited by WILEY-VCH Verlag GmbH & Co., 2005.

14 Y Poplavko and N-I Cho, "Clamping effect on the microwave properties of ferroelectric thin films", Semicond. Sci. Technol. 14, p. 961, 1999.

[15] K. Chi Kao, "Dielectric phenomena in solids", Elsevier Academic Press, 2004.

[16] B. H. Park, E. J. Peterson, Q. X. Jia, J. Lee, X. Zeng, W. Si, and X. X. Xi, "Effects of very thin strain layers on dielectric properties of epitaxial Ba0.6Sr0.4TiO3 films", Appl. Phys. Lett., Vol. 78 (4), pp. 533-535, 2001.

[17] S. Gevorgian, "Ferroelectrics in Microwave Devices, Circuits and Systems Physics, Modelling, Fabrication and Measurements", Springer, 2009.

[18] X. Zhu, J. Zhu, S. Zhou, Z. Liu, N. Ming, S. Lu, H. Lai-Wah Chan, and C.-L. Choy, "Recent Progress of (Ba,Sr)TiO3 Thin Films for Tunable Microwave Devices", Journal of Electronic Materials, Vol. 32 (10), pp. 1125-1134, 2003.

[19] A.K. Tagantsev, V.O. Sherman, K.F. Astafiev, J. Venkatesh & N. Setter, "Ferroelectric materials for microwave tunable applications", Journal of Electroceramics, 11, pp. 5–66, 2003.

[20] W. Chang, C. M. Gilmore, W.-J. Kim, J. M. Pond, S. W. Kirchoefer, S. B. Qadri, D. B. Chirsey, and J. S. Horwitz, "Influence of strain on microwave dielectric properties of .Ba,Sr.TiO3 thin films", J. Appl. Phys., Vol. 87 (6), pp. 3044-3049, 2000.

[21] T. M. Shaw, Z. Suo, M. Huang, E. Liniger, R. B. Laibowitz and J. D. Baniecki, "The effect of stress on the dielectric properties of barium strontium titanate thin films", Appl. Phys. Lett., 75, 2129, 1999.

[22] H. Li, A. L. Roytburd, S. P. Alpay, T. D. Tran, L. Salamanca-Riba, and R. Ramesh, "Dependence of dielectric properties on internal stresses in epitaxial barium strontium titanate thin films", Appl. Phys. Lett., Vol. 78 (16), 2354, 2001.

[23] B. Xiao, V. Avrutin, H. Liu, E. Rowe, J. Leach, X. Gu,Ü. Özgür, H. Morkoç, W. Chang, L. M. B. Alldredge, S. W. Kirchoefer, and J. M. Pond, "Effect of large strain on dielectric and ferroelectric properties of Ba0.5Sr0.5TiO3 thin films", Appl. Phys. Lett. 95, 012907, 2009.

[24] X. H. Zhu, B. Guigues, E. Defaÿ,C. Dubarry, and M. Aïd, "Thermal strain-induced dielectric anisotropy in Ba0.7Sr0.3TiO3 thin films grown on silicon-based substrates", J. Appl. Phys. 106, 024109, 2009.

[25] S. Ito, H. Funakubo, I. P. Koutsaroff, M. Zelner, and A. Cervin-Lawry ,"Effect of the thermal expansion matching on the dielectric tunability of (100)-one-axis-oriented Ba0.5Sr0.5TiO3 thin films", Appl. Phys. Lett. 90, 142910, 2007.

[26] Z.-G. Ban and S. P. Alpay, "Optimization of the tunability of barium strontium titanate films via epitaxial stresses", J. Appl. Phys., Vol. 93 (1), 1, 2003.

[27] W. Chang, L. M. B. Alldredge, S. W. Kirchoefer, and J. M. Pond, "microwave dielectric properties of strained BST-0.5 films with and without strain-induced permanent polarization", J. Appl. Phys. 102, 014105, 2007.

[28] D. M. Potrepka, S. Hirsch, M. W. Cole, W. D. Nothwang, S. Zhong, and S. P. Alpay." Effect of strain on tunability in BST-0.6 thin film on Pt-Si substrates", J. Appl. Phys. 99, 014108, 2006.

[29] A. Sharma, Z.-G. Ban, and S. P. Alpay, J. V. Mantese, "The role of thermally-induced internal stresses on the tenability of textured barium strontium titanate films", Appl. Phys. Lett., Vol. 85 (6), p. 9, 2004.

[30] S. Delprat, C. Durand, J.H. Oh, M. Chaker, K. Wu "Correlation between the lattice parameter and the dielectric tunability in nonepitaxial Ba0.5 Sr0.5 Ti O3 thin films", Appl. Phys. Lett., Vol. 91 (6), 063513, 2007.

[31] G. Catalan, L. J. Sinnamon, and J. M. Gregg, "The effect of flexoelectricity on the dielectric properties of inhomogeneously strained ferroelectric thin films", J. Phys.: Condens. Matter 16, 2253, 2004.

[32] W. Ma and L. E. Cross," Flexoelectric polarization of barium strontium titanate in the paraelectric state", Appl. Phys. Lett., Vol. 81 (18), 2002.

[33] J. Petzelt, T. Ostapchuk, I. Gregora, I. Rychetský, S. Hoffmann-Eifert, A. V. Pronin, Y. Yuzyuk, B. P. Gorshunov, S. Kamba, V. Bovtun, J. Pokorný, M. Savinov, V. Porokhonskyy, D. Rafaja, P. Vaněk, A. Almeida, M. R. Chaves, A. A. Volkov, M. Dressel, and R. Waser, "Dielectric, infrared, and Raman response of undoped SrTiO3 ceramics: Evidence of polar grain boundaries", Phys. Rev. B 64, 184111, 2001.

[34] K. F. Astafiev, V. O. Sherman, A. K., Tagantsev, N. Setter, T. Kaydanova , and D. S. Ginley," Intrinsic and Extrinsic Loss Contributions in SrTiO3 Thin Films at Microwave Frequencies", Integrated Ferroelectrics, 66, pp. 179–186, 2004.

[35] A. Vorobie, P. Rundqvist, S. Gevorgian, "Microwave loss mechanisms in Ba0.25Sr0.75TiO3 films", Materials Science and Engineering B 118, pp. 214–218, 2005.

[36] X. H. Zhu, B. Guigues, E. Defaÿ, and M. Aïd, "Modeling of the evolution of dielectric loss with processing temperature in ferroelectric and dielectric thin oxide films", J. Appl. Phys. 104, 074118, 2008.

[37] L. B. Freund, S. Suresh, "Thin Film Materials, (Stress, Defect Formation and Surface Evolution)", 2003.

[38] J. Palisaitis, and R. Vasiliauskas, based on the lecture of Prof. Gabriel Ferro, Physics of Advanced Materials Winter School, 2008.

[39] C. J. Forst, C. R. Ashman, K. Schwarz, and P. E. Blochl, "The interface between silicon and a high-k oxide", Nature 427, p. 53, 2004.

[40] R. Eason, "Pulsed Laser Deposition Of Thin Films Applications-Led Growth Of Functional Materials", John Wiley & Sons, Inc., Hoboken, New Jersey, 2007.

[41] E.K. Hollman, O.G. Vendik, A.G. Zaitsev and B.T. Melekh, "Substrates for high-Tc superconductor microwave integrated circuits", Supercond. Sci. Technol. 7 (9), p. 609, 1994.

[42] J. S. Horwitz, W. Chang, W. Kim, S. B. Qadri, J. M. Pond, S. W. Kirchoefer and D. B. Chrisey, "The Effect of Stress on the Microwave Dielectric Properties of Ba0.5Sr0.5TiO3 Thin Films", Journal of Electroceramics 4:2-3, pp. 357-363, 2000.

[43] L. B. Freund, S. Suresh, "Thin Film Materials Stress, Defect Formation and Surface Evolution", Cambridge University Press, New York, 2004.

[44] K. Wasa, M. Kitabatake, and H. Adachi, "Thin film materials technology, sputtering of compound materials", by William Andrew, Inc., 2004.

[45] H.M. Smith and A.F. Turner, Appl.,Opt. 4, p. 147, 1965.

[46] R. Eason, "Pulsed Laser Deposition of Thin Films Applications-Led Growth Of Functional Materials", John Wiley & Sons, Inc., Hoboken, New Jersey, 2007.

[47] P. F. Ndione, "Étude des couches minces de $CaxBa1-xNb2O6$ pour les applications électro-optiques", Ph. D. dissertation, INRS, 2009.

[48] S. D. Bu, B. H. Park, B. S. Kang, S. H. Kang, T. W. Noh, and W. Jo, "influence of the laser fluence on the electrical properties of pulsed-laser-deposited $SrBi2Ta2O9$ thin films", Appl. Phys. Lett., Vol. 75 (8), p. 1155, 1999.

[49] B. Dam, J. H. Rector, J. Johansson, J. Huijbregtse, and D. G. De Groot, "Mechanism of incongruent ablation of $SrTiO3$", J. Appl. Phys., Vol. 83 (6), p. 3386, 1998.

[50] K. B. Han, C. H. Jeon, H. S. Jhon, S. Y. Lee, "Effect of laser fluence on the ferroelectric properties of pulsed laser deposited $(Pb1-xLax)Ti1-x/4O3$ thin films", Thin Solid Films 437, pp. 285–289, 2003.

[51] T. Ohnishi, H. Koinuma, M. Lippmaa, "Pulsed laser deposition of oxide thin films", Applied Surface Science 252, 2466–2471, 2006.

[52] T. Ohnishi, K. Shibuya, T. Yamamoto, and M. Lippmaa, "Defects and transport in complex oxide thin films", J. Appl. Phys. 103, 103703, 2008.

[53] Tsuyoshi Ohnishi, Keisuke Shibuya, Takahisa Yamamoto, and Mikk Lippmaa, "Defects and transport in complex oxide thin films", J. Appl. Phys. 103, 103703, 2008.

[54] D. Saranya, J. Parui, S. B. Krupanidhi, "Effect of laser frequency on pulsed laser grown polycrystalline $0.85Pb (Mg1/3 Nb2/3) O3-0.15PbTiO3$ thin films", J. Nanosci. Lett. 3, 16, 2013.

[55] L. Guan, D.M. Zhang, X. Li, Z.H. Li "Role of pulse repetition rate in film growth of pulsed laser deposition", Nucl. Instr. and Meth. in Phys. Res. B 266 (1), pp. 57-62, 2008.

[56] V. Shelke, V. N. Harshan, S. Kotru, and A. Gupta "Effect of kinetic growth parameters on leakage current and ferroelectric behavior of $BiFeO3$ thin films", J. Appl. Phys. 106, 104114, 2009.

[57] Y. Gim, T. Hudson, Y. Fan, C. Kwon, A.T. Findikoglu, B.J. Gibbons, B.H. Park, Q. X. Jia, "Microstructure and dielectric properties of $BaxSr1-xTiO3$ films grown on $LaAlO3$ substrates", Appl. Phys. Lett., 77 (8), pp. 1200-1202, 2000.

[58] Y.Q. Wang, W.S. Liang, Peter Kr. Petrov, Neil McN. Alford, "Dissociation of misfit and threading dislocations in $Ba0.75Sr0.25TiO3$ epitaxial film", Materials Characterization, 62 (294 – 297), 2011.

[59] C.V. Ramanaa, R.J. Smith, O.M. Hussain, C.M. Julien, "On the growth mechanism of pulsed-laser deposited vanadium oxide thin films", Materials Science and Engineering B 111, pp. 218–225, 2004.

[60] L.Z. Cao, Q.D. Meng, W.Y. Fu, S.F. Wang, M. Lei, B.L. Chenga, Y.L. Zhou, Z.H. Chen, "Effect of annealing on the crystal structure and dielectric properties of Ba0.6 Sr0.4TiO3 thick films", Physica B, 393, 175–178, 2007.

[61] Can Wang, B.L. Cheng, S.Y. Wang, H.B. Lu, Y.L. Zhou, Z.H. Chen, G.Z. Yang, " Effects of oxygen pressure on lattice parameter, orientation, surface morphology and deposition rate of (Ba0.02Sr0.98)TiO3 thin films grown on MgO substrate by pulsed laser deposition", Thin Solid Films 485, 82 – 89, 2005.

[62] X. H. Zhu, Q. D. Meng, L. P. Yong, Y. S. He, B. L. Cheng, and D. N. Zheng, "Influence of oxygen pressure on the structural and dielectric properties of laser-ablated Ba0.5Sr0.5TiO3 thin films epitaxially grown on (001) MgO for microwave phase shifters", J. Phys. D: Appl. Phys., 39, pp. 2282–2288, 2006.

[63] C. Wang, B. L. Cheng, S. Y. Wang, H. B. Lu, Y. L. Zhou, Z. H. Chen, and G. Z. Yang, "Effects of oxygen pressure on lattice parameter, orientation, surface morphology and deposition rate of (Ba0.02Sr0.98)TiO3 thin films grown on MgO substrate by pulsed laser deposition", Thin Solid Films, 485, pp. 82– 89, 2005.

[64] T. Yamada, P. Muralt, V. O. Sherman, C. S. Sandu, and N. Setter, "Epitaxial growth of Ba0.3Sr0.7TiO3 thin films on Al2O3 (0001) using ultrathin TiN layer as a sacrificial template", Appl. Phys. Lett. 90, 142911, 2007.

[65] L. G. Maloratsky, " RF and Microwave Integrated Circuits Passive Components and Control Devices", Elsevier Inc., 2004.

[66] N. Kinayman, and M. I. Aksun, "Modern Microwave Circuits", ARTECH HOUSE, INC., 2005.

[67] HEWLETT PACKARD "Test& Measurement Application Note 95-1 S-Parameter Techniques", 1997.

[68] S. Delprat, "Étude de matériaux ferroélectriques (Ba$_x$Sr$_{1-x}$TiO$_3$) pour la conception de dispositifs hautes fréquences accordables", Ph. D. dissertation, INRS, 2005.

[69] S. Delprat, M. Ouaddari, F. Vidal, M. Chaker, and K. Wu, "Voltage and Frequency Dependent Dielectric Properties of BST-0.5 Thin Films on Alumina Substrates", IEEE Microwave and wireless components letters, Vol. 13 (6), pp. 211-213, 2003.

[70] M. Ouaddari, S. Delprat, F. Vidal, M. Chaker, and K. Wu,"Microwave characterization of ferroelectric thin –film materials", IEEE Transaction on microwave theory and techniques, Vol.53 (4) , pp. 1390-1397, 2005.

[71] S. Gevorgian, T. Martinsson, P. L. J. Linner, and E. L. Kollberg, "CAD models for multilayered substrate interdigital capacitors," IEEE Trans. Microw. Theory Tech., Vol. 44 (6), pp. 896–904, 1996.

[72] L. F. Chen, C. K. Ong, C. P. Neo, V. V. Varadan and V. K. Varadan "Microwave Electronics: Measurement and Materials Characterization" John Wiley & Sons Ltd, 2004.

[73] H. T. Lue and T. Y. Tseng, "Application of on-wafer TRL calibration on the measurement of microwave properties of Ba0.5Sr0.5TiO3 thin films", IEEE Transactions on Ultrasonics, Ferroelectrics, and Frequency Control, 48 (6), p. 1640-1647, 2001.

[74] Y. Gim, T. Hudson, Y. Fan, C. Kwon, A.T. Findikoglu, B.J. Gibbons, B.H. Park, and Q.X. Jia, "Microstructure and dielectric properties of Ba1−xSrxTiO3 films grown on LaAlO3 substrates", Appl. Phys. Lett. 77, p. 1200, 2000.

[75] Q.X. Jia, J.R. Groves, P. Arendt, Y. Fan, A.T. Findkoglu, S.R. Foltyn, H. Jiang, and F.A. Miranda, "Integration of nonlinear dielectric barium strontium titanate with polycrystalline yttrium iron garnet", Appl. Phys. Lett. 74, p. 1564, 1999.

[76] C.M. Carlson, T.V. Rivkim, P.A. Parilla, J.D. Perkins,D.S. Ginley, A.B. Kozyrev, V.N. Oshadchy, and A.S. Pavlov, "Large dielectric constant (ε/ε0>6000) Ba0.4Sr0.6TiO3 thin films for high-performance microwave phase shifters", Appl. Phys. Lett. 76, p. 1920, 2000.

[77] W. Chang, S. W. Kirchoefer, J. M. Pond, J. S. Horwitz, and L. Sengupta, "Strain-relieved BST thin films for tunable microwave applications", J. Appl. Phys. Vol. 92 (3), p.1528, 2002.

[78] S. E. Moon, E.-K. Kim, M.-H. Kwak, H.-C. Ryu, Y.-T. Kim, K.-Y. Kang, and S.-J. Lee, "Orientation dependent microwave dielectric properties of ferroelectric Ba1-xSrxTiO3 thin films", Appl. Phys. Lett., Vol. 83 (11), pp. 2166-2168, 2003.

[79] M. Noda, T. Yamada, K. Seki, T. Kamo, K. Yamashita, H. Funakubo, and M. Okuyama, "Comparison of BST Film Microwave Tunable Devices Based on (100) and (111) MgO Substrates", IEEE Transactions on Ultrasonics, Ferroelectrics, and Frequency Control, Vol. 57 (10), pp. 2221-2227, 2010.

[80] L. Yang,F. Ponchel, G. Wang, D. Rémiens, J.-F. Légier, D. Chateigner, and X. Dong, "Microwave properties of epitaxial (111)-oriented Ba0.6Sr0.4TiO₃ thin films on Al₂O₃ (0001) up to 40 GHz", Appl. Phys. Lett. 97, 162909, 2010.

[81] N. A. Pertsev, V. G. Kukhar, H. Kohlstedt, and R. Waser, "Phase diagrams and physical properties of single-domain epitaxial Pb(Zr1-xTix)O3 thin films", Phys. Rev. B 67, 054107, 2003.

[82] Z.-G. Ban and S. P. Alpay, "Phase diagrams and dielectric response of epitaxial barium strontium titanate films: A theoretical analysis", J. Appl. Phys. 91, pp. 9288-9296, 2002.

[83] D. M. Potrepka, S. Hirsch, M. W. Cole, W. D. Nothwang, S. Zhong, and S. P. Alpay. "Effect of strain on tunability in BST-0.6 thin film on Pt-Si substrates", J. Appl. Phys. 99, 014108, 2006.

[84] A. Sharma, Z.-G. Ban, and S. P. Alpay, and J. V. Mantese, "The role of thermally-induced internal stresses on the tunability of textured barium strontium titanate films", Appl. Phys. Lett., Vol. 85 (6), p. 9 2004.

[85] D. Balzar, P. A. Ramakrishnan, P. Spagnol, S. Mani, A. M. Hermann and M. A. Matin, "Influence of Strains and Defects on Ferroelectric and Dielectric Properties of Thin-Film Barium–Strontium Titanates", Jpn. J. Appl. Phys. Vol. 41, pp. 6628-6632, 2002.

[86] K. V. Saravanan, M. G. Krishna, and K. C. J. Raju, "Effect of misfit strain and surface roughness on the tunable dielectric behavior of Ba0.5Sr0.5TiO3 thin films", J. Appl. Phys. 106, 114102, 2009.

[87] N. A. Pertsev, A. G. Zembilgotov, A. K. Tagantsev, "Effect of Mechanical Boundary Conditions on Phase Diagrams of Epitaxial Ferroelectric Thin Films", Phys. Rev. Lett. 80, p. 1988, 1998.

[88] T. Yamada, V.O. Sherman, A. Noth, P. Muralt, A.K. Tagantsev, and N. Setter, "Tunable ferroelectric thin films with enhanced responses through nano-structural control", Proc. of the Sixteenth IEEE International Symposium on Applications of Ferroelectrics (ISAF 2007), pp. 195-197, 2007.

[89] G. Catalan, B. Noheda, J. McAneney, L. Sinnamon, and J. M. Gregg, "Strain Gradients in Epitaxial Ferroelectrics", Phys. Rev. B 72, 020102, 2005.

[90] G. Catalan, L. J. Sinnamon, and J. M. Gregg, "The effect of flexoelectricity on the dielectric properties of inhomogeneously strained ferroelectric thin films", J. Phys.: Condens. Matter 16, 2253, 2004.

[91] B. H. Moeckly and Y. Zhang, "Strontium Titanate Thin Films for Tunable $YBa_2Cu_3O_7$ Microwave Filters", IEEE transactions on applied superconductivity, 11 (1), pp. 450-453, 2001.

[92] A. Vorobiev, P. Rundqvist, K. Khamchane, and S. Gevorgian, "Microwave loss mechanisms in Ba0.25Sr0.75TiO3 thin film varactors",J. Appl. Phys. 96, p. 4642, 2004.

[93] A. K. Tagantsev, V. O. Sherman, K. F. Astafiev, J. Venkatesh, and N. Setter, "Ferroelectric Materials for Microwave Tunable Applications", J. Electroceram. 11, p. 5, 2003.

[94] Z. Wei, H. Xu, M. Noda, M. Okuyama, "Preparation of $Ba_xSr_{1-x}TiO_3$ thin films with seeding layer by a sol–gel method", Journal of Crystal Growth, 237–239, pp. 443-447, 2002.

[95] D. Peng, Z. Meng , "Influence of buffer layer on dielectric properties of $(Ba_{1-x}Sr_x)TiO_3$ thin films", Microelectronic Engineering 66, pp. 631–636, 2003.

[96] X.G. Tang, H.F. Xiong, L.L. Jiangc, H.L.W. Chan, "Dielectric properties and high tunability of (100) and (110)-oriented (Ba0.5Sr0.5)TiO3 thin films prepared by pulsed laser deposition", Journal of Crystal Growth 285, pp. 613–619, 2005.

[97] A. R. James and X. X. Xi, "Effects of buffer layer thickness and strain on the dielectric properties of epitaxial SrTiO3 thin films", J. Appl. Phys., Vol. 92 (10), p. 6149, 2002.

[98] B.H. Park, E.J. Peterson, J. Lee, X. Zeng, W. Si, X.X. Xi, and Q.X. Jia, "Dielectric properties of Ba0. 6Sr0. 4TiO3 thin films with various strain states", Integr. Ferroelectr.39 (1-4), p. 271-280, 2001.

[99] L.B. Kong, S. Li b, T.S. Zhang, J.W. Zhai, F.Y.C. Boey, J. Ma, "Electrically tunable dielectric materials and strategies to improve their performances", Progress in Materials Science 55, pp. 840–893, 2010.

[100] X. Liang, Z. Meng, and W. Wu, "Effect of Acceptor and Donor Dopants on the Dielectric and Tunable Properties of Barium Strontium Titanate", J. Am. Ceram.Soc., 87 (12), pp. 2218–2222, 2004.

[101] S. Hoffmann, and R. Waser, "Dopant Influence on Dielectric Loss, Leakage Behaviour, and Resistance Degradation of SrTiO3 Thin Films," Thin SolidFilms, 305, pp. 66–73, 1997.

[102] M.W. Cole, P.C. Joshi, M.H. Ervin, M.C. Wood, R.L. Pfeffer, "The influence of Mg doping on the materials properties of $Ba_{1-x}Sr_xTiO_3$ thin films for tunable device applications", Thin Solid Films 374, pp. 34-41, 2000.

[103] H. Seo,Y.-B. Kim, G. Lucovsky, I.-D. Kim, K.-B. Chung, H. Kobayashi, and D.-K. Choi, "Enhanced leakage current properties of Ni-doped Ba0.6Sr0.4TiO3 thin films driven by modified band edge state", J. Appl. Phys. 107, 024109, 2010.

[104] A. Khalfallaoui, G. Vélu, L. Burgnies, J. C. Carru, "Characterization of doped BST thin films deposited by sol-gel for tunable microwave devices", IEEE Transactions on Ultrasonics, Ferroelectrics, and Frequency Control, Vol. 57 (5), pp. 295-298, 2010.

[105] M. Liu, C. Ma, G. Collins, J. Liu, C. Chen, L. Shui, H. Wang, C. Dai, Y. Lin, J. He, J. Jiang, E. I. Meletis, and Q. Zhang, "Microwave Dielectric Properties with Optimized Mn-Doped Ba0.6Sr0.4TiO3 Highly Epitaxial Thin Films", Crystal Growth & Design, Vol. 10 (10), pp 4221–4223, 2010.

[106] Li Xiao, Kwang-Leong Choy, Ian Harrison, "Co-doped BST thin films for tunable microwave applications", Surface & Coatings Technology 205 (8-9), pp. 2989-2993, 2011.

[107] M. Dietrich, Ch. Buchal, J.G. Correia, M. Deicher, M. Schmid, M. Uhrmacher, U. Vetter, U. Wahl, "Annealing of BaTiO3 thin films after heavy ion implantation", Nucl. Instr. and Meth.in Phys. Res. B 216, pp. 110–115, 2004.

[108] Y. H. Gao, H. Shen, J. H. Ma, J. Q. Xue, J. L. Sun, X. J. Meng, and J. H. Chu, "Surface chemical composition and optical properties of nitrogen-doped Ba0.6Sr0.4TiO3 thin films", J. Appl. Phys. 102, 064106, 2007.

[109] R.H. Horng, D.S. Wuu, C.Y.Kung, J.C.Lin, C.C. Leu, T.Y.Haung, S. M. Sze, "Ion- implantation treatment of (Ba, Sr) TiO3 films for DRAM application", Journal of Non-crystalline soilds 280, pp. 48–53, 2001.

[110] A.Yu. Azarov, A. Hallen, B.G. Svensson, X.L. Du, A.Yu. Kuznetsov, "Damage accumulation and annealing behavior in high fluence implanted MgZnO", Nuclear Instruments and Methods in Physics Research B,272, pp. 426-429, 2011.

[111] J. Ranking J. C. McCallum, and L. A. Boatner, "The effect of annealing environments on the epitaxial recrystallization of ion-beam-amorphized SrTiO3", J. Mater. Res., Vol. 7 (3), pp. 717 – 724, 1992.

[112] S. Franssila, "Introduction to Microfabrication", John Wiley & Sons Ltd, Chapter 15, Ion Implantation. 2004.

[113] S.G. Xu, Y.F. Qu, and C. Zhang, "Effect of Mg2+ content on the dielectric properties of $Ba_{0.65-x}Sr_{0.35}Mg_xTiO_3$ ceramics", J. Appl. Phys. 106, 014107231, 2009.

[114] Y. Wei, Z. Xiao-Dong, Z. Li-Min, Y. Zhen, B. Hai, L. Zheng-Min, "Yellow and red luminescence in Mg-implanted GaN epitaxial films", Nuclear Instruments and Methods in Physics Research B 264, p. 41-46, 2007.

[115] J. Zhang, J. Zhai, X. Chou, J. Shao, X. Lu, and X. Yao, "Microwave and infrared dielectric response of tunable Ba1−xSrxTiO3 ceramics", Acta Mater. 57, p. 4491, 2009.

[116] W. Ma and L. E. Cross, "Flexoelectric polarization of barium strontium titanate in the paraelectric state", Appl. Phys. Lett. 81, p. 3440, 2002.

[117] Ki-Byoung Kim, Tae-Soon Yun, Hyun-Suk Kim, Ran-Young Kim, Ho-Gi Kim, and Jong-Chul Lee, "An Interdigital BST Capacitor with High Tunability and Low Loss Tangent" **34"** European Microwave Conference - Amsterdam, 2004.

[118] P. M. Suherman, T. J. Jackson, Y. Y. Tse, I. P. Jones, R. I. Chakalova, M. J. Lancaster, and A. Porch, "Microwave properties of $Ba_{0.5}Sr_{0.5}TiO_3$ thin film coplanar phase shifters", JOURNAL OF APPLIED PHYSICS 99, 104101, 2006.

[119] M. W. Cole, C. V. Weiss, E. Ngo, S. Hirsch, L. A. Coryell, and S. P. Alpay, "Microwave dielectric properties of graded barium strontium titanate films", APPLIED PHYSICS LETTERS 92, 182906, 2008.

[120] Hui Wang, Yanlong Bian, Bo Shen, and Jiwei Zhai, "Comparison of Microwave Dielectric Properties of Ba0.6Sr0.4TiO3 Thin Films Grown on (100) LaAlO3 and (100) MgO Single-Crystal Substrates", Journal of ELECTRONIC MATERIALS, Vol. 42, No. 6, 2013.

[121] F. Stemme, M. Bruns, H. Geßwein, M. Schroeder, M. Sazegar, M. D. Drahus R.-A. Eichel, F. Paul, C. Azucena, J. R. Binder, "Fabrication and characterization of iron and fluorine co-doped BST thin films for microwave applications", J Mater Sci 48:3586–3596, 2013.

[122] Areski Ghalem, Freddy Ponchel, Denis Remiens, Jean-Francois Legier, and Tuami Lasri, "Broadband Dielectric Characterization of Sapphire/TiOx/Ba0.3Sr0.7TiO3 (111)-Oriented Thin Films for the Realization of a Tunable Interdigitated Capacitor", IEEE Transactions on Ultrasonics, Ferroelectrics, and Frequency Control, vol. 60, no. 5, May 2013.

[123] Kyoung-Tae Kim, Cheolbok Kim , David E. Senior, Dongsu Kim, Yong-Kyu Yoon, "Microwave characteristics of sol-gel based Ag-doped (Ba0.6Sr0.4)TiO3 thin films", Thin Solid Films 565, 172–178, 2014.

[124] Z. Q. Zeng, A. Podpirka, S. W. Kirchoefer, T. J. Asel, and L. J. Brillson, "Direct correlation and strong reduction of native point defects and microwave dielectric loss in air-annealed $(Ba,Sr)TiO_3$", Appl. Phys. Lett. 106, 182903, 2015.